UNIVERSITÀ DEGLI STUDI DI PAVIA
DOTTORATO DI RICERCA IN FISICA – XXI CICLO

The unique source inside the RCW103 supernova remnant: a decade of X-ray observations

Silvia Entradi

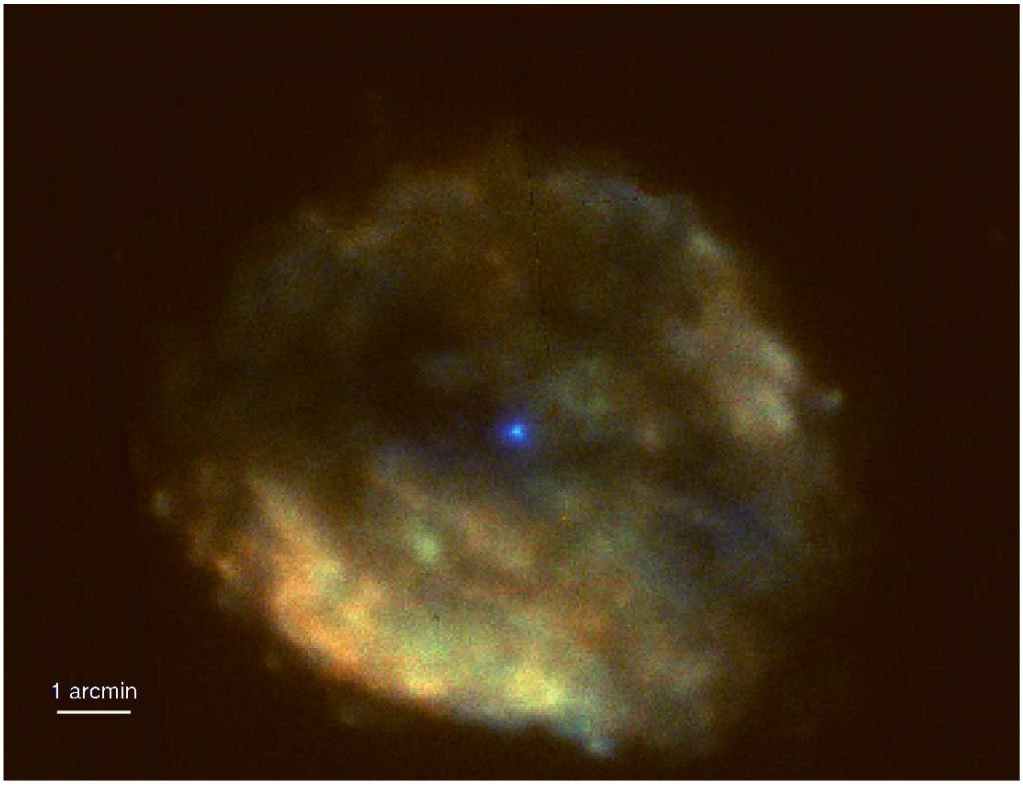

Supervisors: **Prof.** ***A. De Luca***
Prof. ***K. Hurley***

Tesi per il conseguimento del titolo

Università degli Studi di Pavia

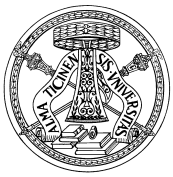

Dipartimento di Fisica Nucleare e Teorica

Istituto Nazionale di Astrofisica

Istituto Nazionale di Fisica Nucleare

University of California, Berkeley

DOTTORATO DI RICERCA IN FISICA – XXI CICLO

The unique source inside the RCW103 supernova remnant: a decade of X-ray observations

Dissertation submitted by

Silvia Entradi

to obtain the degree of

DOTTORE DI RICERCA IN FISICA

Supervisor: **Prof. Andrea De Luca**
Università degli Studi di Pavia, DFNT
INAF-IASF, Istituto Nazionale di Astrofisica
IUSS, Istituto Universitario di Studi Superiore
INFN, Istituto Nazionale di Fisica Nucleare
Prof. Kevin Hurley
University of California, Berkeley, SSL

Referee: **Dr. Roberto Mignani**
University College London, MSSL

Cover

The young SNR RCW 103 and its central source 1E as observed in August 2005 by the EPIC MOS cameras onboard XMM-Newton. Photon energy is color-coded: Red corresponds to the energy range 0.5 to 0.9 keV, green to 0.9 to 1.7 keV, and blue to 1.7 to 8 keV. North is up, east is left.

The unique source inside the RCW103 supernova remnant: a decade of X-ray observations.
Silvia Entradi
PhD thesis – University of Pavia
Printed in Pavia, Italy, November 2008
ISBN: 978-88-95767-18-5

Contents

Thesis overview

Neutron stars are a very variegate class of astrophysical sources that, since their discovery in 1968 by Bell and Hewish, have been extensively studied, and are now catalogued into several classes, that include radio quiet (Central Compact Objects, Soft Gamma Repeaters, Anomalous X-ray Pulsars and X-ray Dim Isolated Neutron Stars) and radio loud neutron stars (Pulsars, Rotating Radio Transients).

Nonetheless, many questions are still unanswered, especially when dealing with the life of a neutron star and the consequent evolution of its emission. For this reason the study of young neutron stars is of fundamental importance.

Young neutron stars are usually found in Supernova Remnants, and thus are generally classified as Central Compact Objects, which is the less homogeneous group. The objects that compose this class are very different from each other, and may represent a sample of how a young star emits. For this reason it is extremely important to study these sources, and the one I chose for my thesis is one of the most puzzling.

1E 161348-5055 is a very peculiar point-like X-ray source, which has been extensively studied in the past years. It is located very close to the geometrical center of the young ($\sim$ 2000 yr) RCW103 Supernova Remnant, 3.3 kpc far away from the Earth.

The source shows a unique behavior: since its discovery in 1980, when it was first detected by *Einstein* as a faint, unresolved source, it was clear that the object did not have a point source radio counterpart, but its emission couldn't be ascribed to a simple thermal cooling, or to the spectrum expected in case of an accreting binary system. This radio quiet source then underwent a period of intense variability: in 1994 its flux increased by a factor 4 (one order of magnitude) from its quiescence value ($\sim 9 \times 10^{-13}$ erg/cm^2 s), recovering the pre-brightening level in four years.

A second, major episode of brightening of 1E 161348-5055 happened in 2000, when it was serendipitously detected by *Chandra* with a very high flux: $\sim 9 \times 10^{-11}$ erg/cm^2 s. A follow up by means of *Chandra*/ACIS was then scheduled. It showed clearly that the flux was decreasing with a smooth trend, yet the origin of the outburst remained unknown, first because the type of

source itself was not understood, second because the peak of the emission was not detected.

The *Chandra* monitoring was integrated with two *XMM-Newton* observations. The first one, obtained in 2001, pointed out how the profile of the lightcurve had dramatically changed as a consequence of the outburst, raising several questions on how traditional models on neutron stars could explain such variability. The second one, made in 2005, was a real breakthrough. This very long observation showed with no uncertainties that 1E 161348-5055 has a period of 24000 s, that corresponds to 6.67 hr, the longest ever detected in case the source were an isolated neutron star.

The comparison between the two *XMM-Newton* observations, which both provided a very abundant statistic, highlighted that the spectral properties of 1E 161348-5055 were varying a lot too: the spectrum of the source was softening, and was clearly a double component model. Unfortunately, though, the lightcurve of the source in 2001 was so complicated and different than the 2005 profile that it was impossible to make a direct comparison between the shapes.

Yet in 2005 it was still unclear which kind of object was hosted at the center of the Supernova Remnant, being at least two possibilities open: an isolated neutron star, likely embedded in a ulta-high magnetic field, where the origin of the outburst would be magnetic, or a neutron star in a binary system, and the brightenings would be driven by accretion episodes. In both cases 1E 161348-5055 was expected to be a unique source: if it were an isolated neutron star, it needs to have a giant magnetic field to power the emission and the brightenings, and to brake it down to such slow spin period. If instead it were confirmed to be a neutron star in a binary system, its geometrical properties have to be very fine tuned.

The anomalous properties of 1E 161348-5055 and the major uncertainties that still affect our knowledge of this source justified a global reanalysis of all the available observations.

The goals of this thesis are first of all to introduce in more detail 1E 161348-5055 and the neutron stars, in chapters 1 and 2. Next, I traced the evolution of the spectral properties of 1E 161348-5055, modeling the time integrated and phase resolved spectrum, in order to derive constraints on the origin of the source (and, as a consequence, of the outbursts), in chapters 3, 4 and 5. Then, I refined the period value and phase connected the huge dataset available, in chapter 6. This strategy has provided an accurate evaluation of the period and period derivative. It has also made possible to compare the pulsed profiles of the source, and draw conclusions on the major variations that the lightcurve underwent. We gained more insight on the physics of the phenomenon that caused the brightening, and we compared the long term evolution of the source with the differences between the spectra of the maximum and the minimum. In the last chapter then I drew the conclusions.

Chapter 1

Introduction

The existence of neutron stars (NS) was first predicted by Baade and Zincky [Baade & Zwicky(1934)] as the end product of supernovae explosion. At that time, soon after the discovery of the neutron, the prediction was striking, and was as a consequence put aside for thirty years, when the first pulsar (rotational powered neutron star) was detected by Bell and Hewish [Hewish et al.(1968)]. For several decades the intense study over the newly discovered class of objects lead the scientific community to believe that neutron stars could only be either pulsars or radio quiet neutron stars.

It is nowadays fair to say that an immense amount of progress has been made in the quest to understand how neutron stars (NS) form and evolve in different stellar systems. In this first chapter I give a brief description of neutron stars and all the classes they are divided into (section 1.1 and relative subsections), and then introduce the object analyzed in this thesis, 1E 161348-5055, from its discovery to now (section 1.2 and 1.3), shortly describing as well the hypothesis available to explain its origin.

1.1 Isolated Neutron Stars

It is widely accepted that neutron stars are remnants of supernovae explosions of massive stars of $\sim 10M_{\odot}$ up to $\sim 20-40M_{\odot}$; at the time of their formation, neutron stars acquire recoil kicks due to asymmetries that develop during the core-collapse process. Typical kick magnitudes inferred from studies of pulsar population kinematics and the formation of binaries with NS are in the range of 100- 300 km/s. NS then are born with birth spin periods of $\sim$ 10 ms and spin down over a time span of $\sim$ 10 Myr; if in binaries they can spin up and reach spin periods of 10 ms or shorter later in their life through accretion of material from their companion.

Today we observe them as magnetically braking pulsars, accreting pulsars in binary systems, isolated cooling blackbodies, sources of astrophysical jets, and emitters of high-luminosity bursts of X-rays. This rich phenomenology led

to the classification of Isolated Neutron Stars (INSs) into different species:

- **Radio Loud**: the radio loud species includes rotation-powered radio Pulsars (PSRs), and Rotating Radio Transients (RRaTs) [McLaughlin et al.(2006)].
- **Radio Quiet**: all the other species are generally radio quiet, and include Anomalous X-Ray Pulsars (AXPs) and Soft Gamma Repeaters (SGRs) [Woods & Thompson(2006)] and [Mereghetti(2008)], Central Compact Objects (CCOs) at the center of supernova remnants [Pavlov et al.(2004)] and [De Luca(2008)], and X-ray Dim Isolated Neutron Stars (XDINS), see for example [Haberl(2007)] and [Kaplan(2008)].

The differences among these INSs are related at least to different properties of their magnetic fields: for instance, AXPs and SGRs are believed to be magnetars, that is neutron stars with ultra high magnetic field, the ultimate source that powers their emission. A unified picture, that includes birth properties and evolution paths connecting of all the isolated neutron stars, though, is still lacking, and in particular the Central Compact Objects are the least understood specie.

In the following I will give a brief description of each class of Isolated Neutron Stars.

1.1.1 Pulsars

Pulsars are isolated neutron stars for which the energy for the observed X-rays is thought to originate from the rotation of the neutron star, or from an internal heat reservoir following formation (for a review see [Kaspi et al.(2004)]). Rotation power can manifest itself as pulsed emission, or as nebular radiation produced by a relativistic wind of particles emitted by the neutron star. Residual heat of formation is observed as soft X-ray emission from young neutron stars. Such thermal radiation, however, can also be produced as a result of reheating from internal or external sources. Rotation-powered pulsed and nebular X-ray emission, as well as thermal emission, can often be observed in a single object simultaneously.

Rotation-powered neutron stars are generally referred to as "radio pulsars" since it is at radio wavelengths that the vast majority of the catalogued population (almost 2000) is observed. However, the radio emission is energetically unimportant, and now it is known that several rotation-powered neutron stars are not detected as radio sources in spite of deep searches.

The total available spin luminosity in a rotation-powered pulsar is given by the rate of loss of rotational kinetic energy:

$$\dot{E} \equiv I\omega\dot{\omega} \equiv 4\pi^2 I\dot{P}/P^3,$$

where I is the stellar moment of inertia and $\omega \equiv 2\pi/P$ is the angular frequency with P the spin period. Thus a simple measurement of P and $\dot{P}$ for an isolated

neutron star determines the available rotational power in a model-independent way, assuming a value for I, typically taken to be 10^{45} g cm^2.

Also generally inferred for these sources are their surface di-polar magnetic fields, $B = 3.2 \times 10^{19} (P\dot{P})^{1/2}$ G (for B on the equator), and their characteristic spin-down ages, via $\tau_c = P/2\dot{P}$. Although these latter two inferences are model-dependent (B because it assumes simple magnetic dipole braking in a vacuum - which is almost certainly not the case - and τ_c because it represents the true physical age only for the same assumption and also for a negligible initial spin period), the important point is that P and $\dot{P}$ provide, in addition to $\dot{E}$, at least estimates of other important physical information.

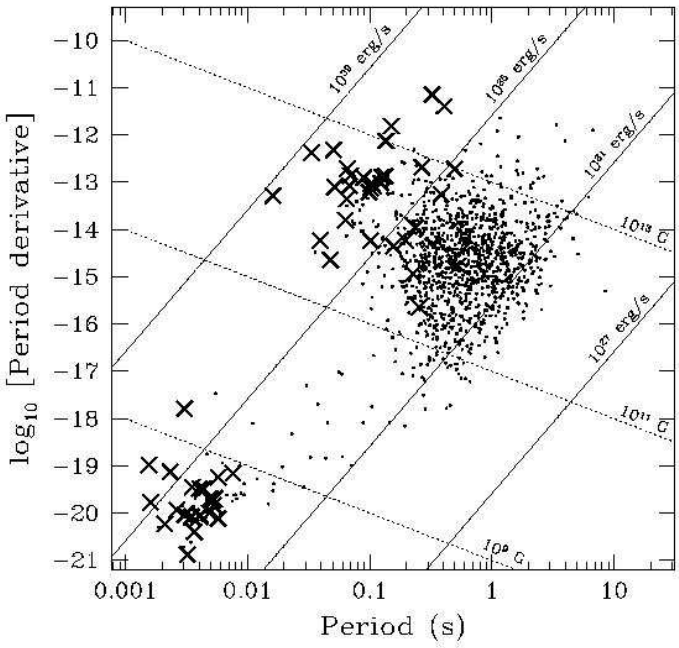

Figure 1.1: P–$\dot{P}$ diagram for the 1403 currently catalogued rotation-powered pulsars. The 66 X-ray detected sources are indicated with an "X." Solid lines show constant $\dot{E}$, and dotted lines show constant inferred surface di-polar magnetic field. "X-ray-detected" means pulsed, unpulsed or nebular emission, be it thermal or non-thermal. X-ray detected sources are generally those with the greatest spin-down luminosity, although the correlation is not perfect because of the wide range of source distances and observational selection effects.

It is for this reason that P–$\dot{P}$ diagrams are so useful. Figure 1.1 shows

the P-$\dot{P}$ phase space, with all catalogued rotation-powered neutron stars with measured $\dot{P}$s indicated as dots. Lines of constant $\dot{E}$ and B are indicated. Note the two different populations of rotation-powered neutron stars: those with periods between ∼16 ms and ∼8 s, having $B \gtrsim 10^{11}$ G, and the lower magnetic field ($B \lesssim 10^{10}$ G), very rapidly rotating class ($P \lesssim 100$ ms), the millisecond pulsars. The division is made particularly obvious when binarity is considered, as the latter sources are mostly in binaries, while the former are only rarely in binaries. The millisecond pulsars are often referred to as "recycled" pulsars as they are thought to be formed in a past episode of mass transfer as part of an accreting X-ray binary phase. Finally, note the absence of sources having $B \gtrsim 10^{14}$ G. Neutron stars having fields higher than this are thought to be "magnetars".

Generally, the X-ray spectra of spin-powered pulsars show a mix of thermal and non-thermal components. Often several thermal components and sometimes even several non-thermal components can be identified. Cleanly separating the non-thermal, or power-law, components from the thermal components can be difficult, especially in sources where the thermal components dominate (e.g. Geminga, PSRs 0656+14 and B1055−52).

Detectors with sensitivity at energies up to at least 10 keV, such as *RXTE, Chandra* and *XMM*, have been able to make the best measurements of non-thermal emission components. This non-thermal emission probably originates from the radiation of particles accelerated in the pulsar magnetosphere, while the thermal emission is the result of the cooling of the neutron star.

1.1.2 Rotating Radio Transients

In 2006 February, a new class of neutron stars, the "Rotating RAdio Transients" (RRATs) was reported [McLaughlin et al.(2006)]: during a large-scale search for radio sources varying on short timescales 11 objects were revealed, characterized by single, dispersed bursts having durations between 2 and 30 ms. The average time intervals between bursts range from 4 minutes to 3 hours, with radio emission typically detectable for $< \mathbf{1}$ s per day. Despite the small number of sources presently detected, their ephemeral nature implies a total Galactic population which significantly exceeds that of the regularly pulsing radio pulsars.

These 11 objects have periods ranging from 0.7 to 7 seconds, identified from an analysis of the burst arrival times, and are located in the Galactic plane at 2 - 7 kpc distances. Their periods are longer than those of most normal radio pulsars and similar to those of the populations of Xray dim isolated neutron stars and magnetars.

For the three sources with the highest pulse detection rates, period derivatives, $\dot{P}$, have been determined. If the measured $\dot{P}$ values are interpreted as due to magnetic dipole spin-down, they imply characteristic ages and magnetic field strengths in the general range of the normal pulsar population, with one having a rather high inferred magnetic field of 5×10^{13} G. There have been

several suggestions put forward on the nature of this new class of neutron star. One obvious suggestion is that the RRATs are related to pulsars which emit "giant pulses" [Knight(2006)]. However, the RRATs with measured period derivatives do not appear to have high values of either magnetic field strength at the light cylinder or spindown luminosity, both suggested as predictors of giant-pulse activity.

All the sources have been reobserved at least nine times at intervals of between one and six months. All have shown multiple bursts, with between four and 229 events detected in total from each object (see table 1.1). As far as we can tell from the limited statistics, the density of sources on the sky appears to be greater towards the Galactic plane, with eight of the 11 having $|b| < 2\,\mathrm{deg}$. Average rates of detected events range from one every three hours for J1911+00 to one every 4 minutes for J1819–1458. The 2 ms to 30 ms-long bursts have peak 1400-MHz flux densities which range from 0.1 to 3.6 Jy. These sources are therefore among the brightest radio sources of the sky after the giant pulses detected from the Crab pulsar and the pulsar B1937+21 [Cordes et al.(2004)]. The distances are inferred from their dispersion measures (DM), positions and a model for the Galactic free electron density[Cordes & Lazio(2002)]. The extremely sporadic nature of the bursts makes localization difficult, with most positions known only to within the 1400-MHz 14-arcminute beam of the Parkes Telescope. For the three sources for which there are measured period derivatives, more accurate positions have been derived through radio timing.

Name	RA (J2000) h m s	Dec (J2000) deg ′ ″	DM pc cm^{-3}	D kpc	w_{50} ms	S_{1400} mJy	N_p/T_{obs} hr^{-1}	N_{det}/N_{obs}
J0848–43	08:48(1)	–43:16(7)	293(19)	5.5	30	100	27/19	9/28
J1317–5759	13:17:46.31(7)	–57:59:30.2(6)	145.4(3)	3.2	10	1100	108/24	23/24
J1443–60	14:43(1)	–60:32(7)	369(8)	5.5	20	280	32/41	17/25
J1754–30	17:54(1)	–30:11(7)	98(6)	2.2	16	160	18/30	10/20
J1819–1458	18:19:33.0(5)	–14:58:16(32)	196(3)	3.6	3	3600	229/13	24/24
J1826–14	18:26(1)	–14:27(7)	159(1)	3.3	2	600	18/17	8/12
J1839–01	18:39(1)	–01:36(7)	307(10)	6.5	15	100	8/13	1/10
J1846–02	18:46(1)	–02:56(7)	239(10)	5.2	16	250	11/10	5/9
J1848–12	18:48(1)	–12:47(7)	88(2)	2.4	2	450	10/8	5/9
J1911+00	19:11(1)	+00:37(7)	100(3)	3.3	5	250	4/13	4/11
J1913+1333	19:13:17.69(6)	+13:33:20.1(7)	175.8(3)	5.7	2	650	66/14	7/10

Table 1.1: Measured and derived parameters for the 11 RRATs. For each, we give the Right Ascension, Declination, dispersion measure (DM), inferred distance, average burst duration at 50% of the maximum, peak 1400-MHz flux density of brightest detected burst, ratio of the total number of bursts detected to the total observation time, and the ratio of the number of observations in which at least one burst was detected to the total number of observations. Estimated 1-σ errors are given in parentheses where relevant and refer to the last quoted digit. Burst durations for each source remain constant, within the uncertainties.

1.1.3 Anomalous X-ray Pulsars and Soft Gamma Repeaters

Soft Gamma Repeaters (SGRs) and Anomalous X-ray Pulsars (AXPs) are two of the most extraordinary evolutionary paths of a neutron star.

Soft Gamma Repeaters were discovered as high-energy transient burst sources. They were originally classified as a subtype of classical Gamma-Ray Burst (GRB), one with a short duration and a soft spectrum [Mazets & Golenetskii(1981)]; some were later found also to be persistent X-ray pulsars, with periods of several seconds, that are spinning down rapidly. Anomalous Xray Pulsars are identified through their persistent pulsations and rapid spin down; some have also been found to emit SGR-like bursts. In spite of the differing methods of discovery, this convergence in the observed properties of the SGRs and AXPs has made it clear that they are, fundamentally, the same type of object. What distinguishes them from other neutron stars is the likely source of energy for their radiative emissions, magnetism. The cumulative behavior of SGRs and AXPs is now best described by the magnetar model, in which the decay of an ultra-strong magnetic field ($B > 10^{15}$ G) powers the high-luminosity bursts and also a substantial fraction of the persistent X-ray emission.

The main observational properties that led to the recognition of the AXPs as a separate class were: lack of evidence of companions and luminosity larger than the spin-down power, that together excluded more conventional explanations; spin period in the 5-12 s range and secular spin.down on timescales of $10^3 - 10^5$ yr, soft X-ray spectrum and, in some cases, association with a supernova remnant. Later it was found that AXPs show long term variability, and can have radio emission. Most of these properties apply also to the counterparts of SGRs, but they have generally harder spectra and probably are younger than the AXPs.

As said before, the SGRs were discovered because of their bursting activity, that can be of different types and origins:

- **Short bursts**: they have peak luminosity up to $\sim 10^{42}$ erg s^{-1} and durations typically in the range ∼0.01-1 s, with a lognormal distribution peaking at ∼0.1 s [Hurley et al.(1994)]. Most of the bursts consist of single or a few pulses with fast rise times, usually shorter than the decay times. The waiting time between bursts is also distributed lognormally and no correlations exist between the bursts intensity and waiting time. SGR bursts occur randomly distributed in rotational phase. The discovery that also AXPs can emit short burst [Kaspi et al.(2003)], similar to those of the SGRs, confirmed the link between these two classes of objects and supported the application of the magnetar model also to the AXPs.

- **Giant flares:** Giant flares have been observed so far only from three SGRs (see table 1.2). They are characterized by the sudden release

of an enormous amount of energy ($\sim$(2–500)$\times 10^{44}$ ergs), a fraction of which escapes directly as a relativistically expanding electron/positron plasma, while the remaining part is gradually radiated by a thermal fireball trapped in the magnetosphere. This gives to the giant flares a unique spectral and timing signature consisting of a short hard spike followed by a longer pulsating tail. Other features that could be observed only in some cases are a precursor and a long lasting afterglow.

The energy emitted in the pulsating tails of the three giant flares was roughly of the same order ($\sim 10^{44}$ ergs), while the energy in the initial spike of SGR 1806−20 (a few 10^{46} ergs) was at least two orders of magnitude higher than that of the other giant flares (see table 1.2). Since the tail emission is thought to originate from the fraction of the energy released in the initial spike that remains trapped in the neutron star magnetosphere, forming an optically thick photon-pair plasma [Thompson & Duncan(1995)], this indicates that the magnetic field in the three sources is similar. In fact the amount of energy that can be confined in this way is determined by the magnetic field strength, which is thus inferred to be of several 10^{14} G in these three magnetars.

Source	**SGR 0526−66**	**SGR 1900+14**	**SGR 1806−20**
Date	March 5, 1979	August 27, 1998	December 27, 2004
Assumed distance	55 kpc	15 kpc	15 kpc
		Initial Spike	
Duration (s)	$\sim$0.25	$\sim$0.35	$\sim$0.5
Peak luminosity (erg s^{-1})	3.6 10^{44}	$>$8.3 10^{44}	(2÷5) 10^{47}
Fluence (erg cm^{-2})	4.5 10^{-4}	$>$1.2 10^{-2}	0.6÷2
Isotropic Energy (erg)	1.6 10^{44}	$>$1.5 10^{44}	(1.6÷5) 10^{46}
		Pulsating tail	
Duration (s)	$\sim$200	$\sim$400	$\sim$380
Fluence (erg cm^{-2})	1 10^{-3}	9.4 10^{-3}	5 10^{-3}
Isotropic Energy (erg)	3.6 10^{44}	1.2 10^{44}	1.3 10^{44}
Spectrum	kT$\sim$30 keV	kT$\sim$20 keV	kT$\sim$15–30 keV
Pulse Period (s)	8.1	5.15	7.56
QPO Frequencies (Hz)	43	28, 54, 84, 155	18, 30, 92.5, 150, 625, 1480

Table 1.2: Comparison of the three giant flares from SGRs, from [Mereghetti(2008)].

1.1.4 X-ray Dim Isolated Neutron Stars

While almost 2000 isolated neutron stars have now been discovered as radio pulsars, the total number in the Galaxy is much larger. Radio pulsars emit pulsations for $\sim 10^7$ yr and are visible due to radio beams that subtend 1–10% of the sky, so the total number of neutron stars of all ages just in the local region of the Galaxy (where radio pulsars are detectable) should be $\gtrsim 10^6$ [Faucher-Giguère & Kaspi(2006)].

For years astronomers have proposed that a large fraction of these objects would be visible through one of two mechanisms: accretion or cooling. The first mechanism could revive old, dead pulsars, while the second would primarily work for younger sources. Both mechanisms, however, make the neutron stars visible in the soft X-ray regime, not in the radio regime that had dominated the study of neutron stars.

In [Kaplan(2008)] a review of this class of object is presented: these neutron stars should be identifiable by:

1. Largely thermal emission peaking in the soft X-ray or far-UV band, requiring small hydrogen column densities to remain visible
2. The absence of bright optical counterparts
3. Significant ($\gtrsim 0.1$ arcsec yr^{-1}) proper motions
4. Preferred locations in the Galactic plane

The first two criteria relate to the spectra of the neutron stars, and serve to rule out the active galaxies and stars that dominate X-ray surveys. The third criterion reflects the proximity of the sources (with maximum distances of ~ 1 kpc) and the large space velocities of known neutron stars. The final criterion comes from the Galactic nature of the sources, and is similar to the distribution of radio pulsars.

Only seven of these objects are known, all of them discovered by the *ROSAT* All Sky Survey; their properties are those anticipated by [Treves & Colpi(1991)], albeit with smaller numbers. Their X-ray spectra are reasonably close to soft black bodies with kT in the range of 40 to 100 eV, attenuated by a small amount of interstellar absorption. There is no sign of any non-thermal X-ray power-law such as those seen in the spectra of most radio pulsars. Most of the XDINS, however, have spectra that appear with significant absorption features at low energies. The measured column densities, along with a map of the local interstellar medium, were used to infer distances: the objects were found as nearby ($\lesssim 500$ pc, generally).

All but one of the INS show gentle, largely sinusoidal X-ray pulsations, although some may be double-peaked. The periods are all tightly clustered (compared to radio pulsars) between 3 and 11 s, and the pulsed fractions vary from $\sim 1\%$ to almost 20%. Through repeated X-ray observations it was found that these objects spin-down with rates of $\sim 10^{-13}$ s s^{-1}. With

the period derivatives, the usual pulsar quantities were calculated: dipolar magnetic field $B_{\rm dip} = 2.4$ and 3.4×10^{13} G, characteristic age $\tau = 1.9$ and 1.5 Myr, and spin-down energy loss rate $\dot{E} = 4.7$ and 4.0×10^{30} erg s^{-1} for for RX J0720 and RX 1308, respectively (see [Kaplan & van Kerkwijk(2005)] and [Kaplan & van Kerkwijk(2005)]). Table 1.3 summarized the properties of the seven XDINS.

RX J	**Spin**[a]			**Spectrum**[b]				
	P (s)	$\dot{\mathbf{P}}$ (10^{-14})	**PF** (%)	$\mathbf{n_{H,20}}$ (cm^{-2})	**kT** (keV)	PN (s^{-1})	$\mathbf{E_{abs}}$ (keV)	$\mathbf{m_B}$ (mag)
1856.5−3754	7.06	...	1	0.8	62	8.3	...	25.2
0720.4−3125[c]	8.39	7	11	1.0	87	7.6	0.3	26.6
1605.3+3249	...	...	< 3	0.8	93	5.6	0.5(0.6,0.8)	27.2
1308.6+2127	10.31	11	18	1.8	102	2.5	0.2(0.4)	28.4[d]
2143.0+0654	9.44	...	4	3.6	102	2.0	0.7	> 26[e]
0806.4−4123	11.37	...	6	1.1	92	1.8	0.3(0.6)	> 24
0420.0−5022	3.45	...	17	2.1	45	0.2	0.3	26.6

[a]The spin-period, period derivative, and rms pulsed fraction are given.

[b]The hydrogen column density (units 10^{20} cm^{-2}, blackbody temperature, *XMM-Newton* EPIC-pn count-rate, central energy of any absorption features in the X-ray spectrum, and B-band magnitude are given, together with the energies of any secondary lines, if known.

[c]The spectral parameters are average quantities.

[d]Inferred from STIS 50CCD.

[e]Inferred from V and r' bands.

Table 1.3: Observed Properties of the Seven X.ray Dim Isolated Neutron Stars. From [Kaplan(2008)] and references therein.

1.1.5 Central Compact Objects

CCOs (see table 1.4 for a list of the seven members of the class) are a handful of sources positioned close to the center of young SNRs. They show lack of radio/IR/optical counterparts, as well as of surrounding diffuse, non-thermal nebulae, and are characterized by constant, unpulsed X-ray emission ($L_X \sim 10^{33}$ erg s^{-1}) with thermal-like spectrum. The spectral properties are unique among neutron stars: CCOs are characterized by high temperatures (0.2-0.4 keV) over a very small emitting area (few % of the expected NS surface).

The lack of counterparts excludes that CCOs are pulsars, while the spectral and timing characteristics distinguish them from the AXPs and SGRs. In fact, the only property shared by all the CCOs is the strong association with a SNR, for the rest the identification of a source as a CCO is more a result of an elimination process rather than a recognisation of common properties. This is of course a consequence of the lack of knowledge of these sources: it is not

even certain that CCOs are isolated neutron stars: for sure they are young and quite common among the results of a supernova explosion. In fact, inspecting all the SNRs within 5 kpc from the solar system, one finds 14 radio PSRs (among which 3 are revealed by the presence of a surrounding nebula, their emission being beamed away from us), 6 CCOs and 1 AXP [De Luca(2008)].

To have a better idea on how inhomogeneous the CCO specie is, consider that the objects listed in table 1.4 are very different from each other:

- 1E 161348-5055 in RCW103, that will extensively be studied in the next chapters, is likely to be a braked magnetar.
- 1E 1207.4-5209 in G296.5+10.0 and CXOU J185238.6+004020 in Kes 79 are weakly magnetized INSs (see [Gotthelf & Halpern(2007)] and [Halpern et al.(2007)]).
- CXOU J232327.9+584843, at the center of Cas A [Fesen et al.(2006)], instead, could be a dormant magnetar, whose spectrum is consistent with that of transient AXPs in quiescence, and SGRs in low luminosity state [Mereghetti et al.(2006)].
- RX J0852.0-4622, the central source in Puppis A [Hui & Becker(2006)], together with 1WGA J1713.4-3949 [Lazendic et al.(2003)] in the SNR G347.3-0.5 (very bright at TeV energies [Aharonian et al.(2004)]) and the central source in Vela Jr [Becker et al.(2006)], shares spectral properties with the other CCOs: it has thermal spectrum, lacks of any counterpart and shows no variability of the few month time scale.

SNR	Age (ky)	Distance (kpc)	Luminosity	Variability	Period	Pulsed fraction
RCW103	2	3.3	1.1-80	factor 100	6.67 hour	12-50%
G296.5+10.0	7	2.2	1.2	$< 5\%$	424 ms	$\sim 10\%$
Kes 79	7	7.1	3	$< 15\%$	105 ms	$\sim 80\%$
Cas A	0.3	3.4	2	Flares?	...	$< 13\%$
Puppis A	3.7	2.2	5	$< 5\%$	...	5%? ($< 7\%$)
G347.3-0.5	2	1.3	0.6	$< 5\%$	...	$< 7\%$
VelaJr.	1	1	0.25	$< 5\%$	...	$< 7\%$

Table 1.4: List of the seven "confirmed" CCOs and of their basic X-ray properties. Flux is in the 0.5-8 keV energy range and in 10^{-12} erg cm^{-2} s^{-1} units; the bolometric luminosity is computed for a purely thermal model (either single or double blackbody) and in 10^{33} erg s^{-1} units. See text for references.

The information collected until now on these objects point to the picture of CCOs as an heterogeneous sample of intrinsically different objects: weakly magnetized neutron stars, as well as magnetars (braked or dormant), that is the two opposite wings of the distribution of newly born neutron stars as a function of their magnetic fields.

1.2 1E 161348-5055 history

1E 161348-5055 is an X-ray source discovered in 1980 when it was first detected by *Einstein* as a faint, unresolved source located near the center of the Supernova Remnant (SNR) RCW103 [Tuohy & Garmire(1980)], at a distance ~ 3.3 kpc [Caswell et al.(1975)]. Already at the time of the detection it was clear that the object did not have a point source radio counterpart, and was very close to the geometrical center of the remnant (1E 161348-5055 was located within better than one third of arcmin from the centroid, calculated by fitting the boundary of the SNR with a circle).

The logical conclusion was the association of the source with the Supernova Remnant RCW103, and tentative interpretations of the emission with the thermal cooling of the surface of a neutron star since the time of the explosion ($\sim$ 2000 yr [Nugent et al.(1984)]), or with the powerlaw spectrum expected from a pulsar (like the case of the Crab and the Vela). Against this latter hypothesis was the lack of radio detection from 1E 161348-5055.

The first spectral parameters of 1E 161348-5055 were derived through X-ray observations with ASCA: Gotthelf et al. [Gotthelf et al.(1997)] found the source with unabsorbed X-ray luminosity $L \sim 10^{34}$ erg/s (0.5-10 keV, for an assumed distance of 3.3 kpc), from a blackbody model fit to the source with temperature kT = 0.6 keV. In the cited paper, though, it is pointed out that the three models taken into consideration for the source (cooling neutron star, accreting binary or plerionic origin) are not completely satisfactory: the isolated neutron star emitting through cooling shows discrepancy between the measured values for the luminosity and blackbody, and the predicted parameters for a star of such age. The inferred temperature is too high for an object of age a few times 10^3 y. Moreover, the luminosity and the blackbody temperature imply an effective emitting area of only 1 km^2, a rather small hot spot, corresponding to $\sim 0.1\%$ of the surface area of an NS. This in turn is surprising since the source shows no rotational modulation (down to $\sim 13\%$).

For what concerns the plerionic origin, the morphology of RCW103 is inconsistent with a plerion dominated by synchrotron emission, such as is observed from Crab-like composite remnants. The central sources in these young SNRs are copious radio emitters with highly polarized extended synchrotron nebulae driven by a radio pulsar [Dickel et al.(1994)], while 1E 161348-5055 lacks of radio emission. Last, the evidence against an accreting binary is equally compelling: the luminosity range for a typical accretion-driven low-mass X-ray binary (LMXB) is $10^{36} - 10^{38}$ ergs/s, implying a distance for 1E 161348-5055 far behind that estimated for RCW103 of 3.3 kpc. Moreover, for a binary origin one would expect to find an optical companion, perhaps with ultraviolet excess from an accretion disk.

The authors then propose alternative explanations: the properties of RCW103 along with its compact source are quite similar to other radio-quiet compact X-ray sources found near the center of SNRs. The luminosity and age of 1E 161348-5055 are also consistent with an isolated pulsar radiating thermal en-

ergy.

This not completely clear framework was further complicated by subsequent ASCA observations [Gotthelf et al.(1999)], that showed that 1E 161348-5055 manifested an intense variability over 4 years, namely a decrease of one order of magnitude in luminosity, when compared with archival *Einstein* and ROSAT data (see figure 1.2).

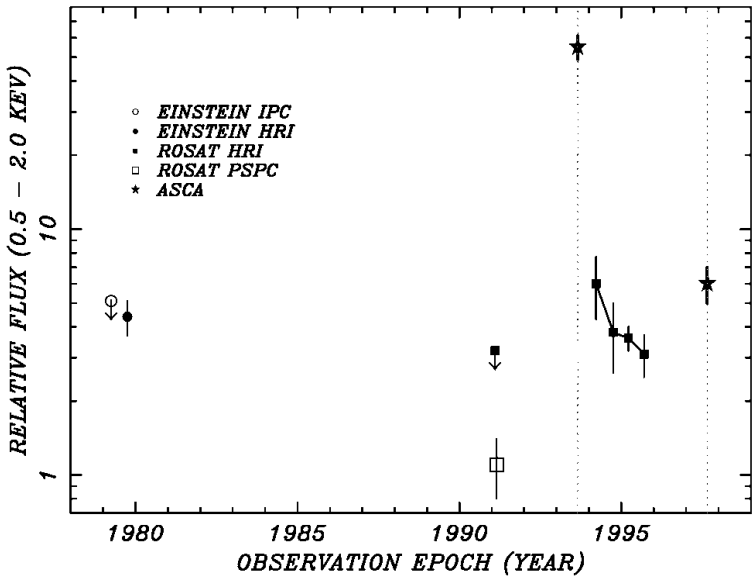

Figure 1.2: Long-term light curve of 1E 161348-5055 in the 0.5-2.0 keV energy bandpass (from [Gotthelf et al.(1999)]). Symbols represent *Einstein* IPC (open circle), *Einstein* HRI (filled circle), ROSAT PSPC (open square) and HRI (filled squares), and ASCA (star). Error bars are 1 σ. The dashed vertical lines indicate the model-dependent uncertainty in the ASCA flux when extrapolated to the 0.5-2 keV bandpass.

The new ASCA observation of 1E 161348-5055, in fact, revealed an order-of-magnitude decrease in its 3-10 keV flux since the previous ASCA measurement 4 yr earlier. That result was difficult to reconcile with suggestions that the bulk of the emission is simple quasi-blackbody, cooling radiation from an isolated neutron star. The spectra from the new data were consistent with no significant spectral change despite the decline in luminosity. No evidence for a pulsed component in any of the data sets was found, with a best upper limit on the pulsed modulation of 13% (no pulsed signal was found between 10 ms and 1000 s).

It is hard for cooling models to address the issue of variability or the dramatic flux reduction observed between the ASCA epochs, unless there is a source for rejuvenating the heating of the NS interior. Such a source could be hypothesized in a superstrong magnetic field [Heyl & Hernquist(1998)], where the energy for impulsive heating of the core could be provided by episodic re-

arrangement of the magnetic field in the stellar interior (this will be treated in more detail in chapter 2).

Instead, an accretion scenario could have been considered, although the relatively low luminosity, lack of any optical counterpart, and young age were inconsistent with a typical accreting NS binary. Accretion from a very low mass companion ($\leqslant 0.1 M_{\odot}$, [Mereghetti et al.(1996)]) or a fossil disk around a solitary NS [van Paradijs et al.(1995)] however, couldn't be ruled out as well. Furthermore, a remarkable similarity of the spectral properties of 1E 161348-5055 to those of the AXPs is present: at the time of the paper, at least two AXPs were reported to vary significantly in flux, by as much as a factor of 5, and AXPs were thought to be consisting of an ultramagnetized star as well. The property of being radio quiet, moreover, is common to all AXPs, soft gamma-ray repeaters, and to 1E 161348-5055. The lack of strong pulsations though argued against this model.

In any case, it was clear that 1E 161348-5055 could share some of the properties of AXPs and SGRs, and even if at its discovery it was taken as the prototype of the evolution of cooling young neutron stars [Tuohy & Garmire(1980)], the new observation properties of 1E 161348-5055 added to the view that young collapsed stars can follow an evolutionary scenario quite distinct from those of Crab-like pulsars.

The breakthrough came in February 2000, when Garmire et al. [Garmire et al.(2000)] found 1E 161348-5055 by chance with a flux 100 times higher than the *Einstein* or ASCA quiescent detections: 1E 161348-5055 had passed from $\sim 8 \times 10^{-13}$ erg/cm^2 s to $\sim 7 \times 10^{-11}$ erg/cm^2 s, that at a distance of 3 kpc corresponds to $L = 10^{33}$ to $L = 10^{35}$ erg/s. This exceptional event required a monitoring campaign to follow the decay in flux: it was asked and obtained by the Garmire High Energy Astrophysics Group in Penn State University, with the *Chandra* X-Ray Observatory. Several monitoring observations were obtained (see chapter 4), and some timing observations as well. They show the smooth decay in flux of 1E 161348-5055, will allow later on to study the timing properties of the source, together with the changes in the profile of the emission (see chapter 6).

Two additional observations, carried out with *XMM-Newton* in 2001 and 2005, helped to study the spectral properties of 1E 161348-5055, and especially the last one showed a strong, unambiguous periodic modulation at 6.67 ± 0.03 hr [De Luca et al.(2006)] (see figure 1.3). That was the first time that pulsations were clearly detected, and a period measurement was carried out: the observation was long enough to cover more than three complete periods, and this left no space to doubts. The value of the period is totally unexpected for an object classified as a Central Compact Object, that is some kind of a neutron star. It is so long and so unusual that 1E 161348-5055 deserves a special place among CCOs.

In their paper, De Luca et al. discuss the evolution of 1E 161348-5055 from 2001 to 2005: apart from the changes in the shape of the lightcurve, the

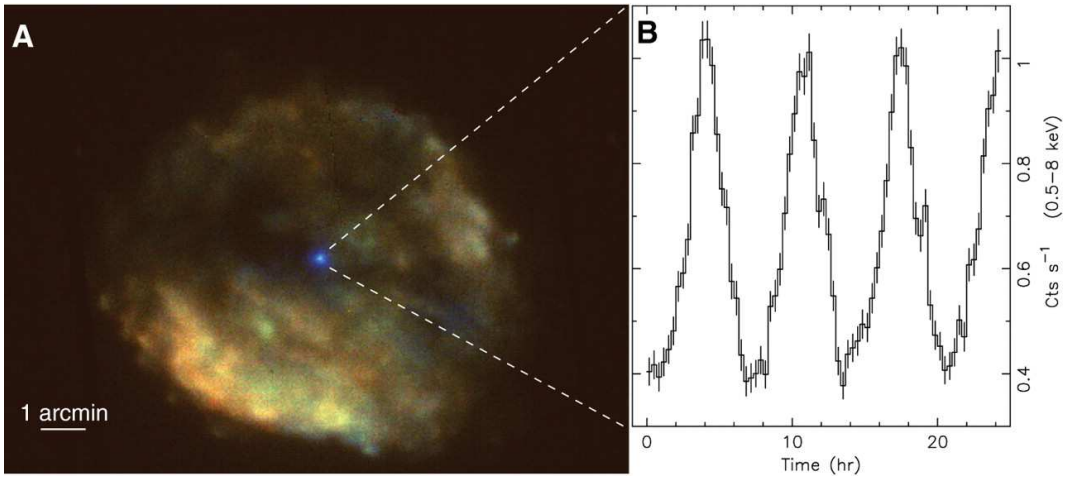

Figure 1.3: (A) The SNR RCW 103 and its central source 1E 161348-5055 as observed in August 2005 by the EPIC MOS cameras onboard *XMM-Newton*. Photon energy is color-coded: Red corresponds to the energy range 0.5 to 0.9 keV, green to 0.9 to 1.7 keV, and blue to 1.7 to 8 keV. (B) Background-subtracted flux evolution of 1E 161348-5055 in the 0.5 to 8 keV energy range, with its unambiguous 6.67 hr periodicity. (From [De Luca et al.(2006)])

periodicity is recognizable also in the 2001 observation, albeit with a larger uncertainty (P = 6.67 ± 0.08 hr), but the pulsed fraction passes from ∼ 12 % to ∼ 44 %, while the pulsed flux remains constant (∼ 2×10^{-12} erg/cm^2 s). The period is compatible with being constant in the four years, but this can not be stated for the spectral properties of the source: the spectrum, that is shown to necessitate of a double component model, evolves from hard to soft with time.

These characteristics, taken all together, rise several questions about the type of source that could be responsible for the emission: two are the main hypothesis:

- Binary system;
- Magnetar.

All the other candidates, in fact, have to be excluded: to explain all the observed properties of 1E 161348-5055 if it were a "normal" neutron star, one should interpret the 6.67 hr period as the precession period and the modulation of the emission as induced by a hot spot, but there is no trace of the faster periodicity related to the neutron star rotation. Moreover, in this scenario the outburst would remain without plausible explanation. Postulating that the observed period is the rotation period of a neutron star means that a huge braking-down mechanism must be invoked. In a classical dipole field approximation, the required magnetic field has to be $B \sim 10^{18}$ G, which is

physically unlikely. If instead one supposes that the star was born with such long rotation period, the X-ray flux variability can not be accounted for.

As mentioned, only two plausible scenarios then remain. In the following, they will be briefly discussed.

1.2.1 Binary system

The binary system hypothesis is the most natural, if one wants to account for the extremely long observed period of 1E 161348-5055. The system should be composed of a compact object, born as a consequence of the supernova explosion, and a faint companion star. Quite stringent limits concerning the companion exist, due to infrared observations (see below, paragraph 1.3): 1E 161348-5055 would be a Low Mass X-ray Binary (LMXB) that must, first of all, have survived the supernova event. An additional complication is that the luminosity range spanned by 1E 161348-5055 ($10^{33} - 10^{35}$ erg/s) is very low when compared to that of LMXB (peak luminosities $\sim 10^{38}$ erg/s, persistent luminosities $\sim 10^{36}$ erg/s); it is only comparable to that of very faint transient LMXB [King & Wijnands(2006)], whose age of $\sim 10^9$ yr though is inconsistent with that of 1E 161348-5055. An explanation can be found in the diverse ages of typical LMXB (10^6 yr) and 1E 161348-5055, assuming of course that it was born in the RCW103 explosion. When the system is newly formed, the donor star has not filled its the Roche Lobe yet, and so mass transfer is not efficient enough to power the usual output from LMXB.

The binary system model meets some more difficulties as well: 1E 161348-5055 long term evolution, the spectral phase variability (see chapter 3) and the orbital modulation necessary to reproduce the pulsations has never been observed in LMXBs, but an explanation could be found in the young age of 1E 161348-5055 system.

Kalogera et al. study [Kalogera(1996)] how a supernova explosion can affect the orbit parameters of a binary system that survives the event:the neutron star, in fact, acquires a kick velocity that can be large enough to disrupt the system. The author assumes that the binary orbits prior to the supernova explosion are circular, and that the kick velocities follow a Maxwellian distribution. This means that the binary system has had enough time during its main-sequence evolution to circularize the orbit, and that the kick velocity is independent from the pre-explosion parameters. In its discussion the author also considers the interaction between the expanding shell and the companion to be weak enough to ignore it, which is generally a good assumption. She finds that the distribution of velocities is similar to that before the supernova event, while the eccentricity of the final orbit is expected to be quite high unless the orbital separation is comparable to that before the explosion.

In a young LMXB, then, one expects to have significant orbital eccentricity, which plays an important role on mass transfer: the exchange of mass is only possible in a narrow range of orbital phases. The material would then start settling into a disk around the compact object; this disk could be responsible for

long term changes in 1E 161348-5055 emission. The wind from the companion star would also be captured with modulation following the orbital motion, and this could be the origin of the 6.67 hr periodicity in 1E 161348-5055 emission.

Once the binary system is formed, one more issue has to be overcome: assuming that the compact object is a neutron star, it passes through several stages in its lifetime that affect greatly the star's capability of emission. They are determined by the mass accretion rate, by the star's magnetic field and by its rotation period. A neutron star undergoes first a stage, called ejector (see figure 1.4), where it behaves like a pulsar, emitting cosmic rays, X-rays and pulsed optical radiation, while the radio emission is absorbed by the stellar wind plasma (see for example [Illarionov & Sunyaev(1975)]). In the course of time, the pressure of the ejected cosmic rays decreases, until it is not effective any more to throw out the surrounding thermal plasma, that begins to penetrate below the light cylinder of the neutron star. As a consequence, the following stage of the neutron star's life is characterized by deceleration of its rotation, which though is still too fast to allow accretion to take place. The star is thus a propeller, that throws away the accreting gas by means of the corotating magnetosphere. Only when rotation becomes slow enough, accretion can be possible to the regions of the magnetic poles, even though only at a small rate because the material comes from the companion wind. The neutron star then emits pulsed X-ray radiation.

Thus X-ray emission through accretion can occur only if both the rotating dipole (ejector) and centrifugal (propeller) barriers can be overcome. This in turn implies that the magnetic field has to be very low, or the rotation period very large. In fact, from [Davies & Pringle(1981)], the onset of the accretion stage is usually taken when the magnetosphere radius r_M is equal to the corotation radius r_Ω. r_M is defined as the radius where the pressure due to the accreting material is equal to the magnetic pressure due to the dipole field of the star. This implies that the period must be longer than the "accretor period" P_A; defining $\dot{M}$ the accretion rate, μ the neutron star magnetic moment ($\mu = B \cdot R_{NS}^3$), one has:

$$P_A = 2^{5/14}\pi(GM)^{-5/7}\left(\frac{\mu^2}{\dot{M}}\right)^{3/7} \text{ s.} \tag{1.1}$$

Using for 1E 161348-5055 the following values

$$\dot{M} = 10^{14} \text{ g}, \quad M = 1.4M_\odot, \quad R_{NS} = 10^6 \text{ cm},$$

gives:

$$B \sim 10^{10} \cdot P^{7/6} \text{ G.} \tag{1.2}$$

Both a long period and such a low magnetic field are unusual for a star whose age (taking for granted that the origin of the neutron star and that of RCW103103 are the same) is $\sim$ 2000 yr: canonical values are period of few tens of milliseconds, and magnetic fields of order $\sim 10^{12}$ G. The only way to achieve the values needed is that already at the time the neutron star was born the spin period was very large, but this is very peculiar (not to say unlikely).

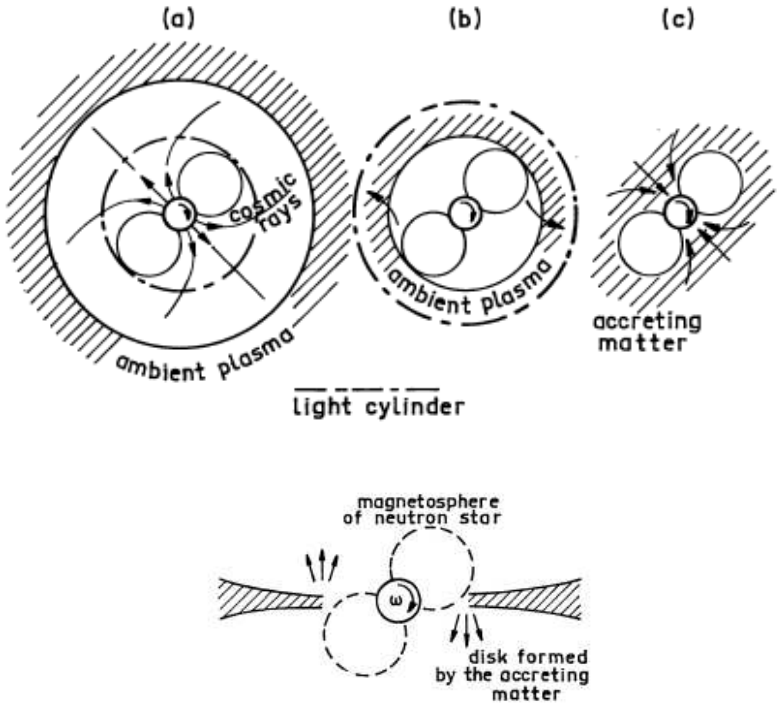

Figure 1.4: Schematic draws (from [Illarionov & Sunyaev(1975)]) of the possible stages of the neutron star life in a detached binary system. Top: the three possible stages. (a) ejector, (b) propeller, (c) accretor. Bottom: a picture that illustrates the interaction of the propeller with the accreting disk.

1.2.2 Magnetar

Already at the time of the ASCA observations, that showed an increase of four time of the flux emitted by 1E 161348-5055, the hypothesis of an ultra magnetized neutron star was taken into account. After the more powerful outburst in 2000, the hypothesis of a magnetar as the compact object inside RCW103 is even more tantalizing. Magnetars are neutron stars with ultra-high magnetic field, up to 10^{15} G [], whose decay powers the emission.

The magnetar origin would explain without ad hoc assumptions the luminosity and spectral characteristics of 1E 161348-5055, and its X-ray variability as well: magnetars, that are classified into Anomalous X-ray Pulsars (AXPs) and Soft Gamma Repeaters (SGRs), commonly show long term variations in flux, spectrum, pulsed fraction and pulse shape. But all magnetar periods are dramatically different than that of 1E 161348-5055: they spin every 5-12 s, typically, which is more than 1000 times faster. The magnetar hypothesis for 1E 161348-5055 has to be supported, then, by a very effective spin down mechanism.

Since a debris disk around AXP was recently found, the probability of a supernova remnant residual disk around an isolated neutron star is not to be

excluded.

Detailed calculations performed in [De Luca et al.(2006)], following [Francischelli et al.(2002)], show that the present spin period of 1E 161348-5055 can be reproduced assuming the star was born with rotation not faster than 0.3 s per cycle, that its surface dipolar magnetic field was 5×10^{15} G, and it was surrounded by a disc of $3 \times 10^{-5} M_{\odot}$. Under these circumstances (see figure 1.5), the early ejector phase is avoided, and the neutron star starts slowing down in the propeller stage. The interaction with the material of the disc is capable of damping down on the period to $P \sim 6.67$ hr in ~ 2000 years.

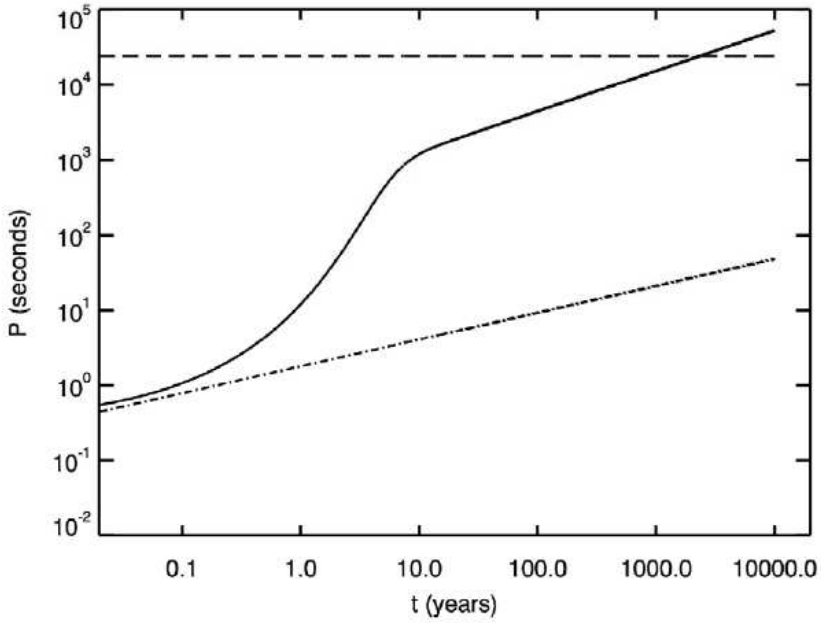

Figure 1.5: Spin down history if 1E 161348-5055, resulting from propeller interaction with the material of a supernova debris disk. The source rotation period is plotted as a black solid line. The dot-dashed line shows the faster spin period at which propeller interaction may occur. For faster rotation rates the pressure of the rotating dipole would exceed the pressure of the infalling material, pushing the disc outside the light cylinder (ejector phase), preventing the propeller effect. From [De Luca et al.(2006)].

An additional comment is required on the birth period of the candidate magnetar: a rotation faster than 0.3 s would imply that the star undergoes an early ejector phase, but this would cause the disk to be pushed away by the radiation pressure of the rotating dipole. Vice versa, with a slower rotation at birth the star would hold back its disk, and immediately begin a very efficient loss of rotational energy.

The birth period $\gtrsim 300$ ms, though, brings some problems to the model: the most widely accepted explanation of the origin of the huge magnetic fields

of magnetars is a dynamo effect [Duncan & Thompson(1992)] in the proto-NS, which requires a birth period much faster than this: $\sim$ 1 ms. However, since there is a possible evidence that not all the magnetars are born with fast initial periods [Vink & Kuiper(2006)], alternative explanations such as the compression of the progenitor field have been proposed ([Vink & Kuiper(2006)] and [Ferrario & Wickramasinghe(2006)]).

This picture of 1E 161348-5055 differentiates it substantially from the more common AXPs and SGRs, mainly for what concerns the period: these objects clearly did not experience a propeller phase, maybe because of a shorter period at birth, or strong gamma-ray bursting activity. There may be a new class of magnetars, whose peculiarity would be a spin history dominated by the supernova debris disk.

A boost to the magnetar interpretation came when Eksi et al showed that in particular geometries (see [Ekşİ & Alpar(2005)]), a debris disk can survive the ejector phase of a neutron star: they derived the electromagnetic energy density for obliquely rotating magnetic dipoles. They showed that the electromagnetic energy density of a rotating dipole makes a broad transition for disk existence across the light cylinder radius, for small inclination angles. In this model, then, the disk could survive beyond the light cylinder even if the radio pulsar activity (ejector phase) turns on.

Li [Li(2007)] examined then to what extent an eventual fallback disk would affect the spin evolution of magnetars: he carried out a simulation on the evolution of 10^6 neutron stars (based on the model by [Lipunov(1992)]), where the stars first pass the ejector phase, then a propeller phase, and last will enter the accretor phase.

He chose an initial neutron star magnetic field B from a lognormal distribution of mean 15 and standard deviation 0.4. He then assumed that all neutron stars were born with a surrounding supernova fallback disk, whose initial masses are distributed as follows: $\log(\Delta M/M_{\odot})$ are uniformly spread between -6 and -2. Mass flow rate through the disk is assumed to decline in a power law with time: $\dot{M} \propto t^{-1.25}$ [Francischelli et al.(2002)], and the initial spin period P and the inclination angles are assumed to be uniformly distributed between 2 and 50 ms, and between and 0°and 90°.

For the propeller torque, Li uses the expression:

$$T_{prop} = \dot{M} R_{in}^2 \left[\Omega_K(R_{in}) - \Omega_s\right],$$

where R_{in} is the inner radius of the disk, $\Omega_K(R_{in})$ is the Keplerian angular velocity at R_{in}, and Ω_s is the angular velocity of the NS. He stopped the calculation at a fiducial time of 2500 yr, to be compatible with the age of RCW103.

In figure 1.6 the histogram of the spin periods for the magnetars are reported. The hatched regions indicate the propeller/accretor (45°) and ejector (45°) systems, respectively. It is noted that most ($\sim$99%)[1] of the magnetars

[1]The percentages are subject to the uncertainties in the initial parameters and the spin-

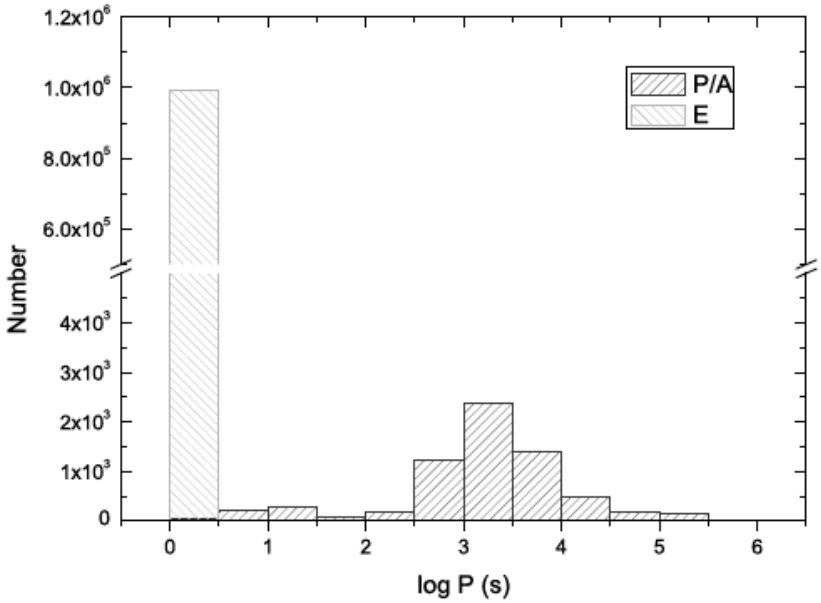

Figure 1.6: Distribution of the spin periods of magnetars at the age of 2500 yr. The hatched regions indicate propeller/accretor and ejector systems. See text for details. From [Li(2007)].

are in the ejector state, having spin periods of a few seconds. These features are consistent with most AXPs and SGRs, which occupy the majority of the magnetar family. The spin periods of the propeller/accretors, which consist of ∼0.6% of the whole population, have a much broader distribution, peaking around a few 10^3 s. 1E 161348-5055 may belong to this latter group. In this case, the puzzling initial spin period P ∼ 300 ms does not appear.

Li then concludes that, in either one of the two possible scenarios (accreting NS or magnetar) for 1E 161348-5055, a supernova fallback disk is favored to explain the observational characteristics of 1E 161348-5055. Other AXPs showed the presence of a disk (4U 0142+61 and 4U 0142+61 [Wang et al.(2006)]), which make this hypothesis not unrealistic. Moreover he shows that in the magnetar interpretation it is possible to model the spin period evolution without exotic assumptions, but only with typical values of the input parameters for a magnetar. The presence of a fallback disk could be confirmed by observations in IR/optical, with the aim to detect the emission from the cooler parts of the disk.

down mechanisms adopted

1.3 Infrared observations

Being 1E 161348-5055 such an interesting and peculiar object, classified as a central compact object but with remarkable features that distinguish it among the other members of the class, with two possibile explanations on its origin, an effort was made in the past to identify a counterpart in optical and infrared observations.

VLT observations of the crowded field of 1E 161348-5055 performed with *FORS1* and *ISAAC* identified a possible counterpart in a very red object (I > 25, J ~ 22.3, H ~ 19.6 and Ks ~ 18.5) located within the *Chandra* error circle [Sanwal et al.(2002)]. The existence of this object was also confirmed by *HST/NICMOS* follow-up observations [Mignani et al.(2004)]. A search for a counterpart in the far IR with the Spitzer telescope was also performed, with negative results [Wang et al.(2007)].

In order to clarify the puzzling picture of 1E 161348-5055, and to acquire evidence that one of the two models could be favored to explain its phenomenology, a deeper infrared observation was carried out with the NACO instrument at the ESO/VLT, [De Luca et al.(2008)], searching for IR counterparts showing the 6.67 hr periodicity, close to the best X-ray position of 1E 161348-5055:

$$\alpha\,(J2000) = 16^h\,17^m\,36.23^s, \quad \delta(J2000) = -51^\circ\,02'\,24''.6$$

with a 1σ uncertainty of $0''.285$ and $0''.185$ in right ascension and declination, respectively.

The images of the field of 1E 161348-5055 are shown in figure 1.7, with the *Chandra* error circle superponed (the two contours are at 68% and 99% CL). The seven objects detected are enumerated in the image, and are all consistent with a point-like source. It is interesting to note that, after refining the X-ray position of 1E 161348-5055, the object proposed by [Sanwal et al.(2002)] as the counterpart falls in the outskirts of the 99% CL region. The field is very crowded, with a source density in the combined *VLT/NACO* K_s image of > 1.1 objects per square arcsec at the sensitivity limit of $K_s \sim 22.1$. The average H-K~ 2 requires a large interstellar reddening, consistent with $A_V \sim 20 - 25$. Such a reddening is much larger than the value of $A_V \sim 3.3 - 6.6$ expected at the distance of the X-ray source according to the n_H measured by [De Luca et al.(2006)].

A search for periodic emission from the seven candidates did not lead to any result: none of the candidate counterparts showed modulation, not in the last observation nor in the reanalysis of the archival observations. For what concerns the long term variability, objects no. 4 and 5 possibly showed a decrease of 0.7 and 1 mag respectively from 2002 and 2006, but they are among the fainter sources (no. 5) or could be contaminated in the earlier observations by the emission from source no. 2, so this evidence should be taken carefully, with caution. In case it proves to be real, the optical vs X-ray flux ratio would remain constant.

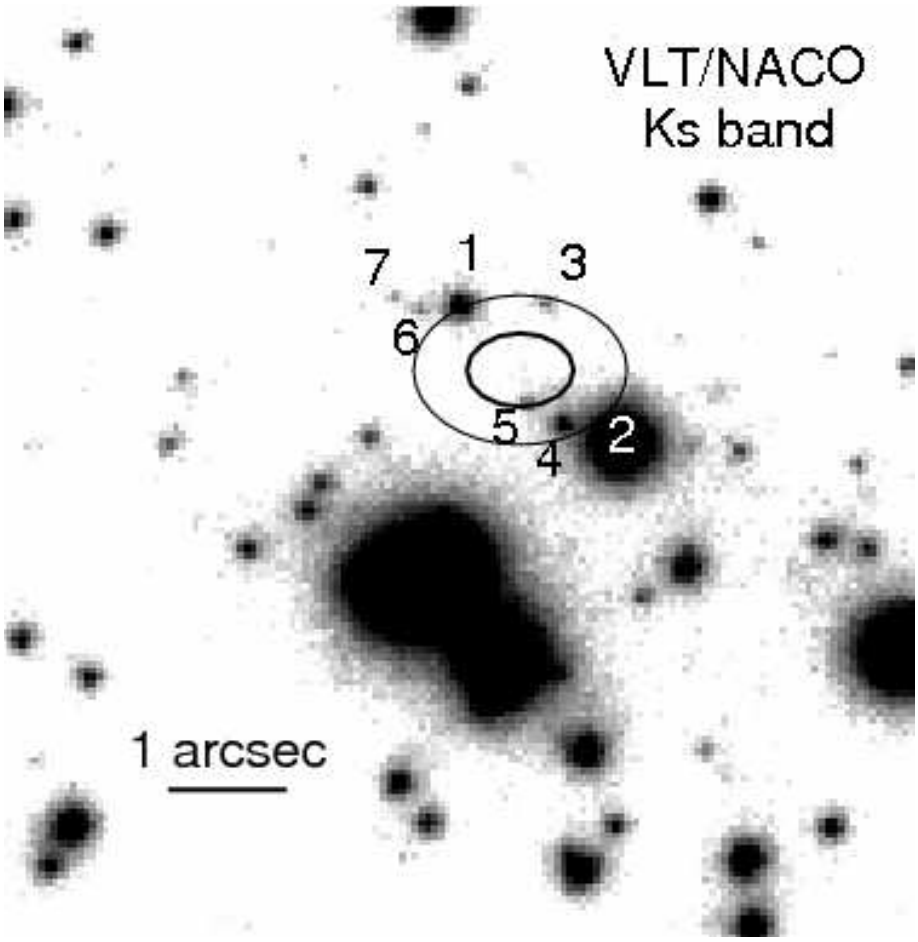

Figure 1.7: Inner part of the field of 1E 161348-5055 as observed by the *VLT/NACO* (K_s band). North to the top, East to the left. In each case, the images are the result of the co-addition of repeated integrations with corresponding total integration time of 40000 s, respectively. The inner ellipse corresponds to the 68% c.l. error region, while the outer ellipse corresponds to the 99% c.l. region. Candidate counterparts detected within or close to the X-ray error region are numbered. Object #1 is the originally proposed counterpart of [Sanwal et al.(2002)]. From [De Luca et al.(2008)].

For all these reasons, De Luca et al. conclude that the IR search did not single out any high confidence candidate for 1E 161348-5055. They consider the hypothesis that any of the possible candidates be the companion of 1E 161348-5055 to be very unlikely. The observed colors and magnitudes would require an unrealistically low temperature for the star ($\sim 1000 - 1500$ K), implying (at a distance of 3.3 kpc and for $A_V = 6.6$), a photospheric radius of (1-2)$\times 10^{11}$ cm, exceeding the Roche lobe dimension ($\sim 4 \times 10^{10}$ cm, assuming a 1.4 $M_\odot$ neutron star, a 0.5 $M_\odot$ companion and an orbital period of 6.67 hours) and comparable to the system orbital separation ($\sim 1.5 \times 10^{11}$ cm under the

same assumptions).

Within the isolated magnetar scenario, it is clear that a debris disk from the supernova explosion is needed. Other AXPs showed the presence of a disk (4U 0142+61 and 4U 0142+61 [Wang et al.(2006)]), but the physics is not fully understood yet, and the present upper limits [Wang et al.(2007)] are not stringent enough.

In the hypothesis that none of the source is the IR counterpart to 1E 161348-5055, De Luca et al. next take into consideration the implications of a source non-detection down to K_s >22.1. Considering the binary scenario, this upper limit is only consistent with an M6-M8 dwarf, but such a small companion is unlikely to power the wind necessary, in the accretion mechanism, to account for the flux modulation of 1E 161348-5055. Moreover, the survival to the supernova explosion is also very unlikely under these conditions. On the other side, the lack of an IR counterpart fits well within the isolated magnetar scenario: the upper limit to the ratio $F_{Ks}/F_X < 1.5 \times 10^{-4}$ (at the epoch of the NACO observation) is fully consistent with the values observed for all magnetars identified in the IR [Fesen et al.(2006)], including 4U 0142+61 [Wang et al.(2006)]. In the isolated magnetar scenario then the possibility that one of the candidate sources is the residual disc surrounding 1E 161348-5055 cannot be ruled out. Nonetheless, since all possible candidates are undistinguishable from normal, background stars, this is an unfavored scenario.

In the future, in case of a rebrightening of 1E 161348-5055 like the one in 2000 (or 1994), prompt infrared observations will be necessary in order to find out the counterpart, that will show a variability resembling the X-ray range. Thanks to the Swift monitoring program, asked and obtained by De Luca, monthly observations of 1E 161348-5055 are performed. They allow to trace the flux evolution of this puzzling source, and will trigger a set of follow up and ToO observations as soon as a new outburst is detected.

From what has been said until now, the magnetar model is favored to explain the complex phenomenology of 1E 161348-5055, so the following chapter 2 will be dedicated to a brief description of the magnetars, and of the binary systems that could be formed of a magnetar plus a small companion star (polar models, [Pizzolato et al.(2008)]). Next, a reanalysis of the *XMM-Newton* and *Chandra* observations cited in this introduction is performed; then it is the turn of the *Swift* observations collected in the past two years of monitoring. Last, having so many observations spanning a 10 years baseline, a timing analysis was possible, in order to derive precisely 1E 161348-5055 period and eventual variations. The last chapter is dedicated to the modelization of the flux decay, and a discussion of the great amount of information collected. For a complete list of the available X-ray observations of 1E 161348-5055, see each chapter dedicated to the various observatories and satellites that observed it.

Chapter 2

Magnetars

Magnetars is the name used to define those neutron stars endowed with ultra-high magnetic field: $B \simeq 10^{14} - 10^{15}$ G, the highest ever detected in the Universe, and very much above the quantum critical value: $B_{QED} = \frac{m^2c^3}{\hbar e} = 4.4\times10^{13}$ G, at which the energy between Landau levels of electrons equals their rest mass. Their magnetic fields are at least 100-1000 times stronger than those of the typical neutron stars observed as radio pulsars powered by the loss of rotational energy, or shining in X-rays thanks to the accretion of matter from binary companion stars. Magnetic field is the ultimate energy source of all the observed emission from magnetars (see [Thompson & Duncan(1995)] and [Thompson & Duncan(1996)]).

As already introduced in chapter 1, magnetars are historically divided in two classes of neutron stars that were independently classified because of their different high-energy emission: the Soft Gamma-ray Repeaters (SGRs) and the Anomalous X-ray Pulsars (AXPs). SGRs were discovered through the detection of short bursts in the hard X-ray/soft gamma-ray range, and initially considered as a subclass of gamma-ray bursts. AXPs were first detected in the soft X-ray range (<10 keV) and thought to belong to the population of galactic accreting binaries; only as more X–ray data accumulated, and deeper optical/IR searches excluded the presence of bright companion stars, their peculiar properties started to appear, leading to their classification as a separate class of pulsars. Observations performed over the last few years led to new discoveries pointing out many similarities between these two classes of objects. Thus, the magnetar model initially developed to explain the extreme properties of the SGRs, difficult to interpret in other models, was applied also to the AXPs.

The basic idea of the model is that the variable X-ray emission - the bursts lasting up to ~ 1000 s and the transient changes in persistent emission observed up to several years - are powered by the decay of the star's magnetic field. A rms field exceeding $\sim 10^{15}$ G is needed to supply an output of 10^{35} erg/s extending over 10^4 yrs.

Isolated neutron stars in fact generally drawn on several sources of energy.

For most observed neutron stars, the dominant source of energy is the rotation of the star:

$$E_{rot} = \frac{1}{2} I \Omega^2 \approx 2 \times 10^{46} I_{45} \left(\frac{P}{1 \text{ s}} \right)^{-2} \text{ erg} \tag{2.1}$$

Magnetars are typically young, highly magnetized neutron stars. The magnetic energy,

$$\mathcal{M} = \frac{1}{8\pi} \int B^2 \, dV \approx 2 \times 10^{47} \, R_6^3 \, B_{NS,15}^2 \text{ erg}, \tag{2.2}$$

exceeds the rotational energy by an order of magnitude. Nearly as large is the thermal energy of the star:

$$U \sim 10^{47} \, R_6^2 \, M_{1.4}^{1/3} \, T_{8.5}^2 \text{ erg}, \tag{2.3}$$

where $M_{1.4}$ and $T_{8.5}$ are the mass and core temperature of the star in units of $1.4 M_\odot$ and $10^{8.5}$ K, respectively, and R_6 is the radius in units of 10 km and $B_{NS,15}$ is the surface magnetic field of the star in units of 10^{15} G.

It is also evident that the rotational energy is not enough to power the outbursts seen from some SGRs (see previous chapter).

The first problem arised by the magnetars is how such a high magnetic field can form in neutron stars. Thompson and Duncan (see for example [Thompson & Duncan(1993)]), first consider that a large dipolar magnetic field can be formed simply via flux conservation in a white dwarf that undergoes accretion-induced collapse. However, the maximum field observed in white dwarves indicate a neutron star field no stronger than 10^{14} G, and even if a sufficiently magnetized white dwarf were to exist, it would be spun down the accretion phase. Thompson and Duncan show that in young neutron stars, during the convective phase, an amplification of their magnetic field is inevitable, and show that fields as strong as $\sim 10^{16}$ G are generated during a period of entropy-driven convection, and that a significative portion of the energy is retained by the star. The situation has some similarities with the solar dynamo, but a few important considerations differentiate them: for the neutron star dynamo it is convection and not rotation that plays the most important role. Being that the convective overturn time of the neutron star is ~ 1 ms, much shorter than the birth spin period, thus rotation plays a less important role and the scale of the resulting amplified field will be smaller than the stellar radius, being the convective cell as small as ~ 1 km. The crustal field will as a consequence be very discontinuous, because the reconnection is inhibited by the stable stratification of the star. Reconnections eventually happen because of diffusive processes in the crust, and they may result in shifts in the spin-down rate. As a result the magnetic field of the neutron star will have a multipolar structure.

Such high magnetic field has as a consequence that magnetars undergo a rapid spin down due to their strong magnetic dipole radiation losses, reaching periods of several seconds in a few thousands years. This rapid evolution

toward the so called "death-line" in the B-P diagram explains why no magnetars are observed at short rotational periods, and possibly why they are not active in radio like normal pulsars. Shortly in their life, magnetars slow down to the point that their magnetic energy,

$$E_{mag} \sim 10^{47} \left(\frac{B}{10^{15}\ \mathrm{G}}\right)^2 \left(\frac{R}{10\ \mathrm{km}}\right)^3 \sim 10^{46} \left(\frac{P}{5\ \mathrm{s}}\right) \left(\frac{\dot{P}}{10^{-11}\ \mathrm{s/s}}\right) \quad \mathrm{erg},$$

is much larger than their rotational energy.

Such a huge energy reservoir is sufficient to power for $\sim 10^4$ years the persistent X-ray emission. The giant flares sporadically emitted by SGRs, during which up to $\sim 10^{46}$ erg can be released, are energetically more challenging. This obviously limits the number of such events that a magnetar can emit in its lifetime.

In the following sections I'll briefly describe the mechanisms that power the X-ray emission in a magnetar.

2.1 X-ray luminosity

2.1.1 Bursting activity

Magnetars (SGRs in particular) can emit both short bursts, and giant bursts. Their typical energetic content is $\sim 10^{41}$ erg for short bursts, while giant flares span a rather large energy range: $10^{44} - 10^{46}$ erg in a single episode. Obviously two trigger mechanisms are needed to account for such diverse energetic. The accepted idea is that giant bursts are due to large scale readjustments of the stellar magnetic field, whereas the **SGR bursts** are triggered when magnetic stresses in a patch of the crust (a few kilometers in radius) build up significantly to crack it [Duncan & Thompson(1994)].

This is possible because the large magnetic field, that diffuses through the stellar interior, eventually causes departures from magnetostatic equilibrium, with the result that crustal stresses build up and crack the neutron star crust. It is important to notice that the higher the magnetic field is, the faster it will decay: thus a stronger field is capable of triggering much more energetic bursts at much smaller ages. From this consideration is the hypothesis that SGRs are younger than AXPs.

Consequence of the crustal crack is that a displacements of the magnetic footpoints happens, thus injecting an Alfvén wave into the magnetosphere directly, or provoking seismic activity that propagates to the magnetic poles, and there is converted into magnetospheric Alfvén waves. What we observe then depends on the magnetic field strength at the outer radius $R_{max} = R_\star + \Delta R$ of the zone into which the Alfvén waves are injected. If $B(R_{max})$ is strong enough to contain the wave energy ΔE in a volume $\sim \Delta R_{max}^3$,

$$\frac{B^2(R_{max})}{8\pi} \gtrsim \frac{\Delta E}{3\,\Delta R_{max}^3}, \tag{2.4}$$

then the Alfvén waves remain trapped on the closed field lines on the dynamical time-scale $\Delta R_{max}/c$, they undergo non-linear damping and ultimately dissipate into a magnetically confined thermal pair plasma.

If instead $B(R_{max})$ is weaker than the limit in equation 2.1.1, then there is a relativistic outflow, that has a characteristic duration R_ν/c, where R_ν is the minimum characteristic dimension of any harmonic excitation of the magnetosphere.

The resulting excitation and trapped plasma are highly asymmetrical, and depend on the magnetic field geometry and the crustal fracture patterns.

For what concerns the onset of **giant flares**, the observed ~ 0.1 s duration of the initial hard transient rules out a magnetospheric origin, because it would release energy on a timescale equal to the magnetospheric Alfvén crossing time of:

$$\frac{R_\star}{c} \sim 3 \times 10^{-5} \quad \text{s.}$$

This consideration pushes towards a mechanism as an interchange instability [Thompson & Duncan(1993)], that leads to an exchange in the positions of the magnetic footpoints. This instability may be originated either by a reduction of the internal or the external magnetic field energy, combined with reconnection of the magnetic field lines, which involves large-scale horizontal motions of the fluid core.

After the onset of reconnection, energetic changes are rapidly accelerated throughout the region of the fluctuating fields. This leads very quickly to the formation of an optically thick photon-pair plasma, trapped in the magnetosphere of the neutron star. The cooling of this cloud powers the pulsating tail emission of giant bursts, because it first heats the outer part of the surface, and after it contracts in volume becomes exposed and glows for a time that is comparable to the duration of the burst [Thompson & Duncan(1995)].

2.1.2 Persistent emission

Different possibilities have been proposed to explain the observed X-ray emission at a level of several $\sim 10^{35}$ erg/s. Magnetic field decay can provide a significant source of internal heating. While ohmic dissipation and Hall drift dominate the field decay respectively in weakly ($\lesssim 10^{11}$ G) and moderately magnetized ($\sim 10^{12} - 10^{13}$ G) neutron stars, the most relevant process in magnetars is ambipolar diffusion, which has a characteristic timescale $t_{amb} \sim 10^4 \times (B_{core}/10^{15}\ \text{G})^{-2}$ years [Thompson & Duncan(1996)]. This internal heating source is conducted from the heated core to the surface and powers an anomalously high X-ray flux, and yields a surface temperature higher than that of a cooling neutron star of the same age and smaller magnetic field. The surface X-ray flux is dependent of course on the surface temperature, which in turn brings a time dependence from the magnetic field decay. Moreover, the X-ray flux is linked to the neutrino luminosity by a tight relation that implies that the X-ray luminosity saturates at $L_X \sim 10^{35} - 10^{36}$ erg/s at an age of

$\sim 10^4$ yr, because of rapid neutrino cooling. This compares favorably with the quiescent emission observed from AXPs and SGRs.

The magnetic field also induces multiple small scale fractures (each of them releasing orders of magnitude less energy than a typical SGR burst): the resulting Alfvén wave luminosity depends sensitively on the the shear modulus μ and on the maximum yield strain θ_{max} [Thompson & Duncan(1996)], whose associate maximum tolerated value of B is:

$$B_\mu = (4\pi\,\mu\,\theta_{max})^{1/2} \sim 2 \times 10^{14} \left(\frac{\theta_{max}}{10^{-3}}\right)\ \text{G}.$$

When $B \gg B_\mu$ the crust undergoes a plastic deformation, and seismic activity is suppressed: the irregularities in the magnetic field are damped directly by crustal yielding.

Furthermore, the enhanced thermal conductivity in the strongly magnetized envelope contributes to increase the surface temperature. An additional effect occurs when the star contains a strong $\sim 10^{15}$ G toroidal magnetic field: the rate of ejection of magnetic helicity from the interior can be high enough to induce a significant twist on the external poloidal field lines. This effect is especially important following periods of X-ray burst activity, and has been suggested as a source of persistent increases in spin-down rate, and as a source of external heating [Thompson et al.(2002)].

2.2 Transient magnetars

Variations in the X-ray flux of magnetars are expected as a consequence of fluctuations in the internal magnetic dissipation rate, but their timescale depends on whether the energy is transported by thermal conduction from the core to the surface, or by low-amplitude Alfvén waves into the magnetosphere [Thompson & Duncan(1996)]: fluctuations in the Alfvén wave flux will almost instantly lead to variations in the X-ray flux. By contrast, the thermal conduction time is quite long: 2×10^7 s for a neutron star with density greater than $\sim 10^{12}$ g/cm^3 and surface temperature of $T = 3 \times 10^6$ K. As a result, small amplitude fluctuations in the core dissipation rate are smoothed out. Large amplitude fluctuations will yield detectable changes in L_X, but only if the total energy released exceeds 10^44 erg, that is comparable to the energy released in giant bursts; the energetic requirements needed by an increase of the Alfvén wave flux, instead, are less severe.

Two mechanisms have been proposed to describe the properties of transient magnetars: deep crustal heating [Lyubarsky et al.(2002)] and currents in the twisted magnetosphere [Thompson et al.(2002)]. The first model considers the effects that a relatively fast energy deposition in the neutron star crust, due for example to a sudden fracture or a gradual plastic deformation, has on the surface thermal emission. The time dependence of the surface "thermal echo"

depends primarily on the thermal properties of the outer crust, as well as on the depth of the energy deposition.

In a twisted magnetosphere, induced by a smooth shearing deformation of the magnetic field, the dissipation outside the star takes two principal forms: impact of the current-carrying charges on the stellar surface, and resonant Comptonization of this surface X-ray flux by the magnetospheric currents. The surface heating provides a minimal radiative output, that is increased as the X-rays undergo multiple scattering. When B_{dipole}, multiplied by the irradiated fraction of the stellar surface, is $\sim 10^4$ G, the surface X-ray flux generated by the twisted magnetosphere is comparable to the equilibrium flux powered by the ambipolar diffusion of a strong internal magnetic field described above ($\sim 10^{25}$ erg). One example of a twisted, self-similar magnetosphere (corresponding to $\Delta\phi_{\rm N-S} = 2$ radians) is depicted in figure 2.1.

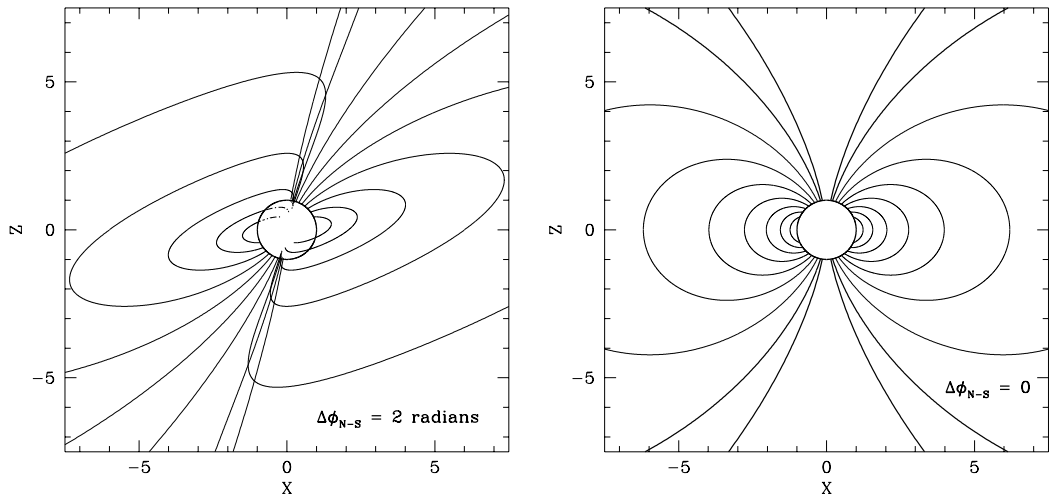

Figure 2.1: An example of a twisted, self-similar, force-free magnetosphere, with net twist angle $\Delta\phi_{\rm N-S} = 2$ radians. Only a small number of field lines are plotted. The field lines protruding from the top right and bottom left corners of the star are anchored in the $X - Z$ plane, at regular intervals. Dashed lines indicate that the field is projected behind the star. A pure dipole is shown for comparison. From [Thompson et al.(2002)].

A simple estimate of the maximum time for the external twist to dissipate completely, in the absence of further sub-surface motions is derived in [Thompson et al.(2002)]. The energy of a twisted magnetosphere exceeds the energy of a pure dipole with the same polar flux density (p is the parameter of self similarity of the flux)

$$\frac{E_B}{E_B(\text{dipole})} = \frac{3}{2(p+1)} \int_0^1 d\mu \left(\frac{dF}{d\mu}\right)^2 > 1, \tag{2.5}$$

and can be approximated by

$$\frac{E_B}{E_B(\text{dipole})} = 1 + 0.17\Delta\phi^2_{\text{N-S}} \tag{2.6}$$

for $\Delta\phi_{\text{N-S}} \lesssim 1$. This works out to (introducing B_{pole} as the field at the magnetic pole)

$$E_B - E_B(\text{dipole}) = 1.4 \times 10^{44}\,\Delta\phi^2_{\text{N-S}} \left(\frac{B_{\text{pole}}}{10^{14}\text{ G}}\right)^2 \left(\frac{R_{\text{NS}}}{10\text{ km}}\right)^3 \text{ erg}, \tag{2.7}$$

for twists $\lesssim 1$ radian. The decay time for the global twist is then

$$t_{\text{decay}} = \frac{E_B - E_B(\text{dipole})}{L_X} \tag{2.8a}$$

$$= 40\,\Delta\phi^2_{\text{N-S}} \left(\frac{L_X}{10^{35}\text{ erg s}^{-1}}\right)^{-1} \left(\frac{B_{\text{pole}}}{10^{14}\text{ G}}\right)^2 \left(\frac{R_{\text{NS}}}{10\text{ km}}\right)^3 \text{ yr}. \tag{2.8b}$$

This gives a timescale for the decay of the external twist, and is somehow linked to the decay of the variability of a magnetar, when it is produced by twisting of the magnetosphere.

The twist of the magnetosphere can be responsible also of changes of pulsed profiles of AXPs and SGRs: for example, SGR 1900+14 pulse profile changed dramatically following the giant flare, simplifying from four or five subpulses to a single sinusoidal pulse [Woods et al.(2001)]. Two alternative explanations of the phenomenon involving a twist are possible:

- If a giant flare results from a sudden change (unwinding) in the internal magnetic field, a twist is implanted into the magnetosphere and at the same time there was an increase in the current density and the optical depth to resonant scattering.

  Multiple scattering of 2-10 keV photons at the electron cyclotron resonance will cause such a change in pulse profile)if the magnetic field is predominantly dipolar at a radius of ~ 100 km) and is a natural consequence of a twisting up of the external field during the flare.

- Alternatively, giant flares may involve a sudden relaxation in the twist outside the star, without the impetus of sudden subsurface motions, in close analogy with Solar flares. This requires that the external magnetic shear build up gradually, and that the outer crust of the neutron star is deformed plastically by internal magnetic stresses. This mechanism has the advantage that the energy stored in the external twist need not be limited by the tensile strength of the crust, but instead by the total external magnetic field energy. In this second scenario the simplified pulse profile would require the elimination of a non-axisymmetric component of the current during the flare.

Transient X-ray sources have always been of great interest since they allow to explore the theoretical models over a large luminosity range and with fixed source parameters such as distance, orientation, and, presumably, magnetic field. In the next paragraph I'll report some cases of AXPs and SGRs that show transient behavior.

2.2.1 XTE J1810-197

XTE J1810-197 is the prototype of a Transient Anomalous X-ray Pulsar (TAXP): it was discovered on January 23, 2003, with RXTE [Ibrahim et al.(2004)] at a flux of $\sim 8 \times 10^{-11}$ erg cm^{-2} s^{-1}, and a posteriori it was realized that XTE J1810-197 was in a high state: its discovery flux was factor 100 higher than that of its quiescent counterpart recovered in archival data.

Since January 2003 its luminosity decreased monotonically and is now approaching the pre-outburst level (see figure 2.2). During the outburst the spectral and timing properties of XTE J1810-197 were similar to those of the persistent AXPs, and short burst were also observed [Woods et al.(2005)].

The outburst that resulted in the detection of the transient AXP occurred sometime between 2002 November and 2003 January. Since then, over the course of a year, regular scans of the region with *RXTE* recorded an exponential flux decay with a time-constant of 269 ± 25 days from a maximum of $F(2-10\mathrm{keV}) \approx 8{\times}10^{-11}$ erg cm^{-2} s^{-1}. In comparison, the previous average quiescent flux, with its softer spectrum, gives $F(0.5-10\mathrm{keV}) \approx 5.5 \times 10^{-13}$ erg cm^{-2} s^{-1}.

XMM-Newton observations carried out during its long outburst decay (see [Gotthelf & Halpern(2005)] and [Halpern & Gotthelf(2005)]) showed a significant evolution of the spectrum and pulse profile. Gotthelf and Halpern (see [Gotthelf & Halpern(2007)]) found that the spectrum is well described by two blackbody components whose luminosity decreases exponentially with different timescales. This is particularly of interest since spectra of AXPs were nominally modeled assuming a two-component power-law plus blackbody model. Instead, in the case of XTE J1810-197 it was found that a two temperature blackbody model gave equally acceptable spectral fits but was better motivated physically. Although the hot blackbody component initially dominated the emission at low energies, it fades more rapidly than the cooler "warm" emission component. The spectrum of XTE J1810-197 can then be thought of as the combined flux from two concentric emitters, "hot spots", whose temperature and size are evolving at different rates, effectively changing the overall shape of the spectrum with time (see figure 2.3.

The temperature of the cooler component, initially at kT$_1$ $\sim$0.25 keV, has been steadily decreasing since mid 2004, while at the same time its emitting area expanded to cover almost the whole neutron star surface. The hotter component cooled from kT$_2$ $\sim$0.7 keV to kT$_2$ $\sim$0.45 keV while its emitting area, initially $\sim$30 km^2, reduced by a factor $\sim$8. This behavior has been interpreted in the framework of the magnetar coronal model [Beloborodov & Thompson(2007)] attributing the high temperature component to a hot spot at the footprint of

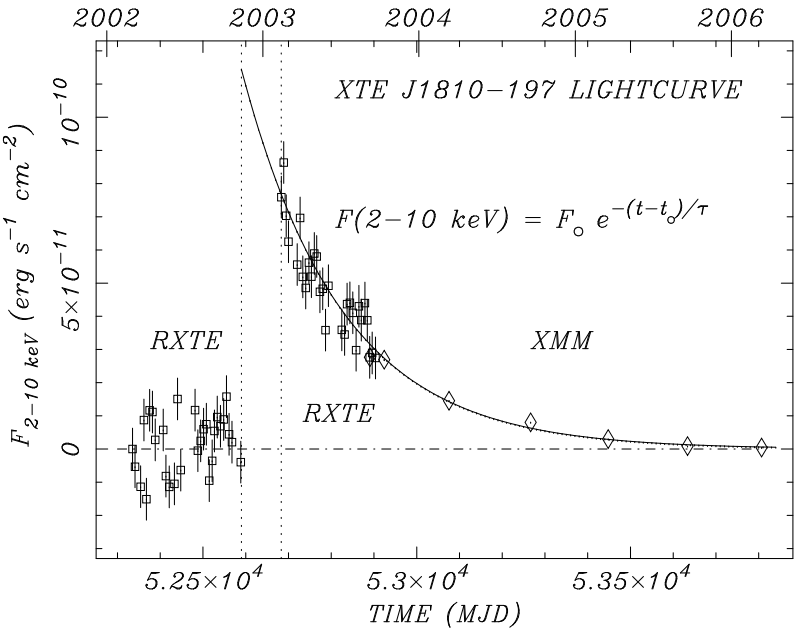

Figure 2.2: Long-term light-curve of XTE J1810-197 using measurements obtained with *RXTE* (*squares*) and *XMM-Newton* (*diamond*). The *solid line* is a best combined fit to an exponential decay model. From [Gotthelf & Halpern(2007)]

an active magnetic loop and the cooler component to deep crustal heating in a large fraction of the star.

Prior to epoch 2004, the spin-down rate derived from the *RXTE* and initial *XMM-Newton* measurements were highly erratic, ranging from $\dot{P} = (0.8 - 2.2) \times 10^{-11}$ s s^{-1} [Ibrahim et al.(2004)]. This temporal behavior is likely associated with the outburst event. The latest period measurements suggest that the spin-down rate has settled down to a period derivative of $\dot{P} = 1.26 \pm 0.04 \times 10^{-11}$ s s^{-1}. The revised X-ray rate implies a nominal characteristic age $\tau_c = 7.0$ kyr, surface magnetic field $B_s = 2.7 \times 10^{14}$ G, and spin-down power $\dot{E} = 2.9 \times 10^{33}$ erg s^{-1}, values typical for a magnetar.

The energy-dependent modulation of XTE J1810-197 has evolved noticeably over time with the declining flux [Gotthelf & Halpern(2007)]. The pulsed fraction has generally decreased with time, most notably at X-ray energies below $E < 2$ keV; at higher energies the trend is less clear due to the large uncertainties derived for those pulsed fractions. Furthermore, at all epochs, the pulsed fraction clearly increases with energy. The broad-band pulse shape is not a simple sine function; the pulse peak is relatively sharp with a broader inter-pulse trough. This effect is more pronounced at higher energy, where the profile is nearly triangular in shape. It is natural to associate the two pulsed components uniquely with the two spectral components, i.e., the triangle shape for the hotter blackbody component, that dominates above 2 keV, and the sinusoidal shape for the cooler one. However, it was found that it is

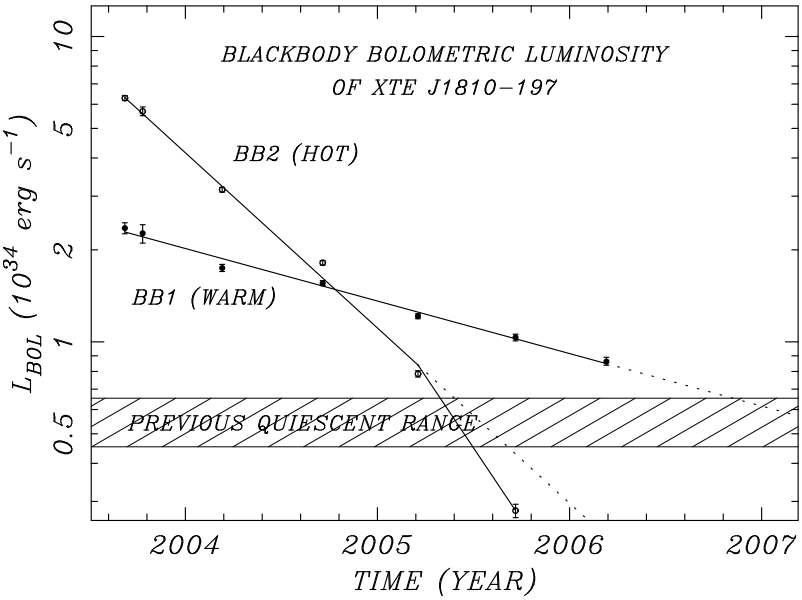

Figure 2.3: A semi-log plot of the bolometric luminosity of XTE J1810-197 as a function of time (*crosses*) for each temperature component of the double blackbody model. The light-curves are fit assuming an exponential decays model (*solid lines*); the corresponding e-folding times is $\tau_1 = 280$ d and $\tau_2 = 870$ d for the warm and hot temperature components, respectively. The most recent data for the hot component now deviates from this model. The fitted quantities have been extrapolated to the (1σ) quiescent range (*cross-hatched area*). From [Gotthelf & Halpern(2007)].

not possible to model all the profiles in a consistent manner with just a simple superposition of these temporal components, based on the implied flux ratio in each energy band [Gotthelf & Halpern(2005)].

2.2.2 CXOU J1647−45

Other transient AXPs have been identified recently: CXOU J1647−45, in the young star cluster Westerlund 1 [Muno et al.(2006)], and 1E 1547-54, likely associated to a possible SNR [Gelfand & Gaensler(2007)]. The first one spanned a dynamical range in luminosity larger than a factor ∼300. 1E 1547-54 was seen to vary only by a factor ∼16 [Camilo et al.(2007)], but it is possible that the peak of the outburst was missed.

CXOU J1647−45 showed an intense rebrightening following a short burst detected by *Swift* and reported in [Israel et al.(2007)]: on September 21, 2006, an intense ($\sim 10^{39}$) erg and short (20 ms) burst was detected by *Swift* BAT at a position consistent with that of the candidate Anomalous X-ray Pulsar CXOU J1647−45 discovered by *Chandra* in 2005. *Swift* follow-up observations began ∼13 hours after the event and found the source at a 1-10 keV flux level of about 4.5×10^{-11} erg/cm^2 s, i.e. ∼300 times brighter than measured 5 days

earlier by *XMM-Newton*.

Together with the burst, large changes in the timing and spectral properties of the persistent component were detected and seen evolving during the subsequent weeks. In particular, the *Swift* XRT monitoring (plus two proprietary *XMM-Newton* and two archival *Chandra* observations) allowed to find the following:

- The pulse phase evolution is consistent with the occurrence of a large glitch ($\Delta\nu/\nu \sim 10^{-4}$), the largest ever detected from a neutron star. The glitch was recovered over a timescale of 1.4 d, though its effects were present in the pulse phases until approximately one week after the glitch epoch. A variable period component in the pulse phases was also detected, corresponding to a $\dot{P} = 9.2(4) \times 10^{-13}$ s s^{-1}.

- The first 1-10 keV *Swift* XRT spectrum was measured ∼13 hours after the burst detection and showed, in addition to a $kT \sim 0.65$ keV blackbody ($R_{BB} \sim 1.5$ km), a $\Gamma \sim 2.3$ power-law component accounting for about 50% of the observed flux.

- The flux decay of CXOU J1647−45 is well described by the function $F \propto t^{\alpha}$, with index α of -0.28±0.05. Moreover, the PL component decays more rapidly (index α of -0.38±0.11; 90% uncertainty) than the BB flux (index α of -0.14±0.10).

- The pulsed fraction of the 10.61 s pulsations was seen to drop from a value of ∼ 80% (as recorded by an *XMM-Newton* observation a few days before the burst) to ∼ 10% a few hours after the BAT event. The spectral and timing analysis clearly show that only the blackbody component is responsible for the pulsed flux (at least during the initial phases of the outburst). The pulsed profile also shows great changes (see figure 2.4, from a nearly sinusoidal profile before the event to a three-peaked profile after.

- Archival *Chandra* data analysis revealed that the modulation in quiescence is 100% pulsed at energies above ∼4 keV and consistent with the (unusually small-size) blackbody component being occulted by the neutron star as it rotates.

A comparison of the properties of CXOU J1647−45 with those of other AXPs which underwent bursting phases and flux variability showed a rather similar behavior, but also underlined that several differences can arise: for example, SGR 1900+14 showed a simplification of the pulsed profile after the giant flare, while CXOU J1647−45 instead changed its pulsed profile to a more complicated shape.

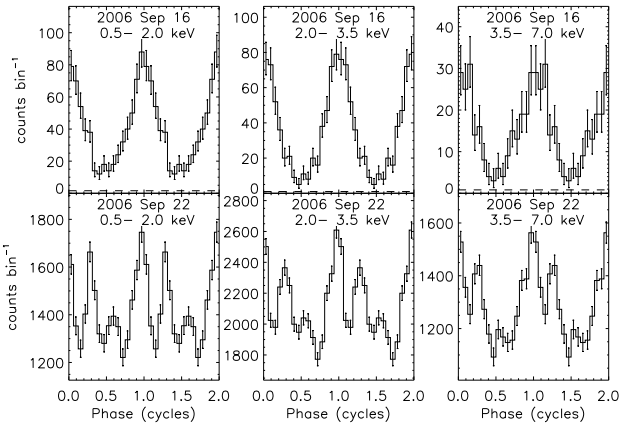

Figure 2.4: Pulse profiles of CXOU J1647−45taken on 2006 September 16 (top panels) and 2006 September 22 (bottom panels), and in three energy bands: 0.5-2.0 keV (left panels), 2.0-3.5 keV (middle panels), and 3.5-7.0 keV (right panels). Two identical cycles are repeated in each panel. The dashed line in the top panel represents the background count rate. From [Muno et al.(2007)].

1E 2259+586

1E 2259+586showed gross changes in the pulsed flux, persistent flux, energy spectrum, pulse profile and spin down [Woods et al.(2004)] as a consequence of an outburst of more than 80 individual bursts, similar to those seen from Soft Gamma Repeaters (SGRs), that was detected in June 2002. For this reason 1E 2259+586is not actually classified as a transient AXP, even though its brightening showed similar properties as those of XTE J1810-197and CXOU J1647−45.

An X-ray flux increase (pulsed and phase-averaged) by more than an order of magnitude was observed having two distinct components. The first component is linked to the burst activity and decays within ∼2 days during which the energy spectrum is considerably harder than during the quiescent state of the source. The second component decays over the year following the glitch according to a power law in time with an exponent -0.22 ± 0.01. The pulsed fraction decreased initially to ∼15% RMS, but recovered rapidly to the pre-outburst level of ∼23% within the first three days. The pulse profile changed significantly during the outburst, and recovered almost fully within two months of the outburst (see figure 2.5).

A glitch of size $\Delta\nu_{\max}/\nu = (4.24 \pm 0.11) \times 10^{-6}$ was observed in 1E 2259+586 that preceded the observed burst activity.

The changes in the persistent emission properties of 1E 2259+586 suggest that the star underwent a plastic deformation of the crust that simultaneously impacted the superfluid interior (crustal and possibly core superfluid) and the magnetosphere.

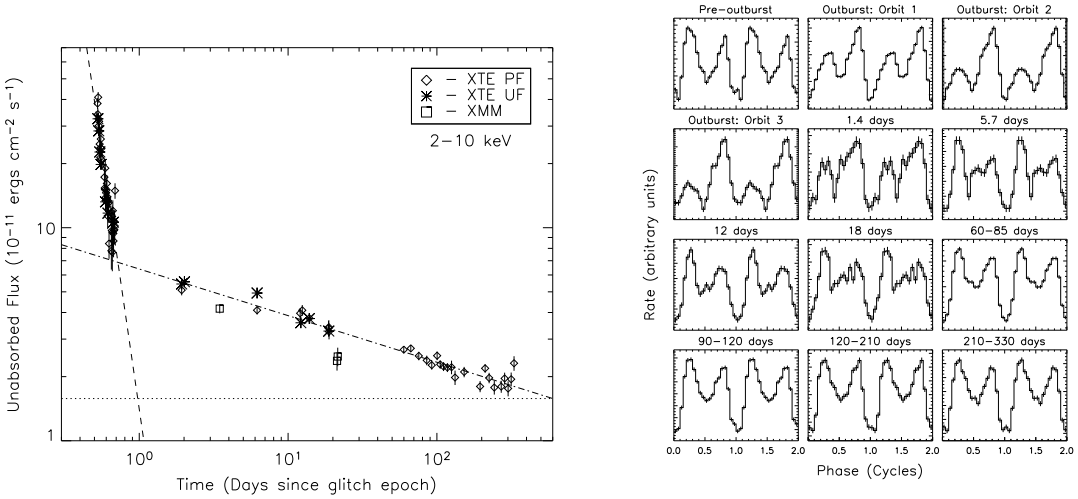

Figure 2.5: **Left**: the time evolution of the unabsorbed flux from 1E 2259+586following the 2002 June outburst. Diamonds denote inferred unabsorbed flux values calculated from *RXTE* PCA pulsed flux measurements. Asterisks and squares mark independent phase-averaged unabsorbed flux values from *RXTE* and *XMM-Newton*, respectively. The dotted line denotes the flux level measured using *XMM-Newton* 1 week prior to the glitch. The dashed line is a power-law fit to the PCA flux measurements during the observations containing the burst activity (<1 day). The dot-dash line marks the power-law fit to all data >1 day following the glitch. **Right**: the time evolution of the 2−10 keV pulse profile of 1E 2259+586through the outburst of 2002. Profiles have arbitrary flux units and two pulse cycles are shown for clarity. Time increases from left to right and top to bottom. From [Woods et al.(2004)].

2.3 Variability in SGRs

2.3.1 SGR 1900+14

As already mentioned before when talking about the twisted magnetosphere of magnetars, SGR 1900+14 underwent major changes in its pulsed profile following the giant flare in 1998, but this was not the only consequence of that event [Woods et al.(2001)].

Following the August 27, 1998, flare, the persistent SGR flux reached a maximum, increasing of a factor ~ 700 (see figure 2.6). This flux enhancement decayed over the next $\sim$40 days as a power-law in time with an exponent -0.71. All measurements of the RMS pulse fraction suggest this parameter remained constant despite the large excursion in the X-ray intensity of the SGR. Finally, the dramatic pulse profile change is independent of the change in luminosity of the source, but appears to be a direct consequence of the August 27$^{\text{th}}$ flare. In fact, following the decay of the flux enhancement the reemergence of the blackbody component is observed; this suggests that the observed radiation comes again directly from the stellar surface. Moreover, the

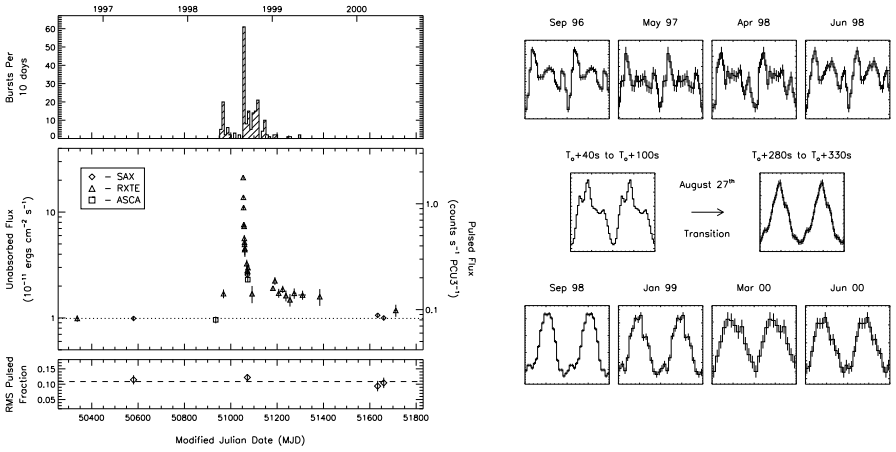

Figure 2.6: Left: burst rate history, flux history and pulsed fraction of SGR 1900+14 covering 3.8 years. Right: evolution of the pulse profile of SGR 1900+14 over the last 3.8 years. The top and bottom rows are integrated over the energy range 2−10 keV. From top-to-bottom, left-to-right, the data were recorded with the RXTE, BeppoSAX, ASCA, RXTE, RXTE, RXTE, BeppoSAX, and RXTE. From [Woods et al.(2001)].

observation of the simple pulse profile in the presence of the thermal component implies that the stellar magnetic field is now predominantly dipolar. Since the pulse profile was observed to change from complex (multi-polar field structure) to simple (di-polar field structure) within the August 27$^{\text{th}}$ flare, this line of reasoning proposed by [Woods et al.(2001)] suggests that the stellar magnetic field underwent a *global* reconfiguration at the time of the giant flare rather then a twist.

2.3.2 SGR 1627−41

SGR 1627−41 was discovered in 1998 by the *Compton Gamma Ray Observatory* [Kouveliotou et al.(1998)] because of the intense bursting phase it entered, emitting more than a hundred bursts in six weeks. Soon after the discovery of the bursts, the persistent X-ray emission of this SGR was detected by *BeppoSAX* at a luminosity of $\sim 10^{35}$ erg s^{-1}, assuming a distance to the source of 11 kpc. The quiescent spectrum was well modeled by an absorbed power law ($N_{\rm H} \approx 8 \times 10^{22}$ cm^{-2} and photon index $\Gamma \approx 2.5$ [Woods et al.(1999)]). No further bursting activity has been reported since then, but several X-ray observations of the persistent counterpart of SGR 1627−41 were obtained in the past ten years. Since its discovery, this persistent emission showed a slow luminosity decay, from about 10^{35} to 10^{33} erg s^{-1}, the lowest value ever observed for an SGR, and a spectral softening from $\Gamma \approx 2$ to 4 [Mereghetti et al.(2006)]. The post-burst cooling trend seen in X-rays is peculiar among SGRs; rather it resembles the behavior of transient anomalous X-ray pulsars (AXPs) . After

a ten year long stretch of quiescence SGR 1627−41 re-activated on 28 May 2008 [Esposito et al.(2008)] with tens of bursts, that were observed by *Swift* XRT with fluxes exceeding the underlying continuum by a factor $> 10^5$. The bursts achieved a maximum luminosity of $\sim 10^{41}$ erg s^{-1} and had a duration of <0.5 s, typical of the bursts detected in SGRs. With respect to the last pre-burst *XMM-Newton* observation, the source was detected in May-June 2008 at a much larger flux level (see figure 2.7) and with a considerably harder spectrum. The correlated spectral hardening/flux increase is in line with what is observed in the long term evolution of other magnetars [Mereghetti(2008)], and expected in models in which the non thermal X-ray emission is due to resonant up-scattering by magnetospheric currents [Thompson et al.(2002)].

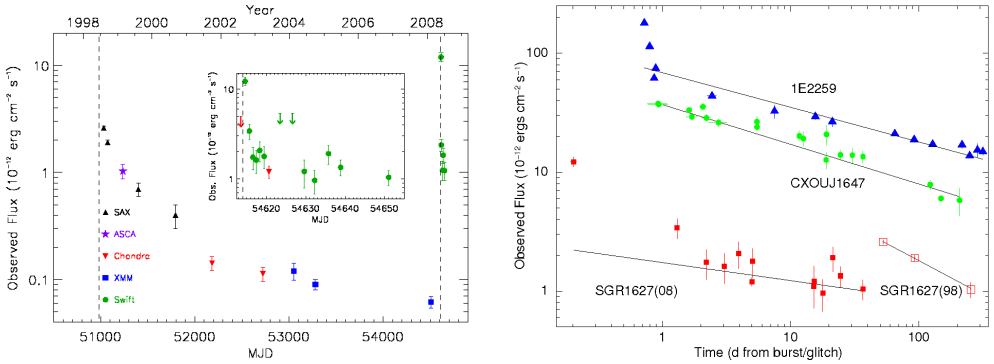

Figure 2.7: Top: long term light-curve of SGR 1627−41. The vertical dashed lines indicate the onset of the two burst-active periods. The inset shows in detail the light-curve around the 2008 reactivation. The down-arrows indicate upper limits at $3\,\sigma$ confidence level. Bottom: comparison among flux decays of SGR 1627−41 for both the 2008 (filled squares) and 1998 (open squares) activation periods, CXOU J164710.2–455216 (filled circles) and 1E 2259+586 (filled triangles). The solid lines represent the power-law best-fits. From [Esposito et al.(2008)]

The right image in figure 2.7 shows a comparison among flux decays of two AXPs and SGR 1627−41. The SGR 1627−41 data taken after more than two days from the May 2008 trigger are well fit by a power-law decay (index ~ -0.2) [Esposito et al.(2008)], but the XRT points at earlier times shows a marked excess over this trend, indicating a very steep initial decay. This behavior closely resembles that of 1E 2259+586: in that case, after the June 2002 bursts active phase the source flux showed a double component decay, with a steep component that decayed rapidly during the first ∼2 days, followed by a slower year-long decay phase. This is also consistent with what was observed in CXOU J164710.2–455216 and SGR 1627−41: in the former case, in which no steep/prompt decay was observed, the bursting activity (if present) was already over at the time of the first observation of the persistent flux. In the latter case, after the activation of June 1998 only a shallow decay

was monitored >60 days from the first bursts.

2.4 Magnetars in a binary system

In this section I am examining the case of a magnetar in a binary system, since the observational evidence did not exclude it for the possible origin of 1E 161348-5055.

The binary scenario is appealing since it provides an easy explanation of the long 6.67 hr periodicity, as due to the orbital period of the system. However, the observed properties of 1E are dramatically different from those of any known LMXB. The system is orders of magnitude dimmer than persistent LMXBs. Moreover, a very peculiar "double accretion" mechanism is required to explain the unusual, large flux and spectral variations along the 6.67 hr cycle as an orbital modulation, as well as the dramatic long term variability.

A comprehensive model for an alternative scenario was developed by Pizzolato et al. [Pizzolato et al.(2008)]: it consists of a neutron star in close orbit with a low mass main sequence star. and the time signature of 6.67 hr is interpreted as the neutron star's spin period. Magnetic or/and material (propeller) torques are needed to spin rapidly the young neutron star down to the asymptotic, equilibrium spin period of 6.67 hr, in close synchronism with the orbital period, similarly to what happens in Polar or strongly magnetized Intermediate Polar Cataclysmic Variables.

Pizzolato et al. assume that 1E is a binary system made by a neutron star (NS) of mass $M_1 = 1.4\,M_\odot$ and a low main sequence star (a red dwarf, RD) of mass $M_2 = 0.4\,M_\odot$ (consistent with the current optical/infrared constraints). In a narrow system like the one proposed, the tidal torques are expected to be quite effective in synchronizing the companion star's rotation with the orbital period and in circularizing the orbit. The companion star is thus expected to be synchronous, with eventually an orbit that may still be moderately eccentric, but since the results are not expected to be too sensitive to the use of a circular orbit approximation, they suppose that the orbit is circular, with the two stars separated by the fixed distance a, given by Kepler's third law:

$$a = 1.5 \times 10^{11} \left(\frac{P_{orb}}{6.67\ \mathrm{hr}}\right)^{2/3} \left(\frac{M}{1.8\,M_\odot}\right)^{1/3} \ \mathrm{cm}, \tag{2.9}$$

Assuming that the interaction between the stars and the accretion flow are dominated by the star's magnetic field, as happens in canonical Polar CVs, requires the condition $R_A \gtrsim a$, where

$$R_A = 1.8 \times 10^{11} \left(\frac{\mu_1}{10^{33}\ \mathrm{G\ cm^3}}\right)^{4/7} \left(\frac{\dot{M}_1}{10^{13}\ \mathrm{g\ s^{-1}}}\right)^{-2/7} \left(\frac{M_1}{1.4\,M_\odot}\right)^{-1/7} \ \mathrm{cm}, \tag{2.10}$$

is the NS's Alfvén radius. The mass accretion rate $\dot{M}_1$ has been normalized to the low state X-ray luminosity L_X of 1E according to $L_X = G\,M_1\,\dot{M}_1/R_1$, being $R_1 = 10^6$ cm the NS's radius. The requirement $R_A \gtrsim a \simeq 10^{11}$ cm implies a NS's magnetic moment $\mu_1 \simeq 10^{33} - 10^{34}\,\mathrm{G\,cm^3}$, or a magnetar-like surface magnetic field $B_1 \simeq \mu_1/R_1^3 \simeq 10^{15} - 10^{16}$ G.

Under these circumstances, the Roche Lobe of the neutron star is totally occupied by the neutron star's magnetosphere, and thus the material that passes from the red dwarf companion through the lagrangian point to the neutron star is accreted straightaway. There is no possibility that an accretion disk can form. The equilibrium condition for the accretion is determined by the magnetic torque, and this translates into the condition on the corotation radius R_{co}:

$$R_{\rm co} = \left(G\,M_1/\omega_1^2\right)^{1/3} \sim R_A, \tag{2.11}$$

where ω_1 is the NS's rotation angular frequency.

The rotation equilibrium condition $R_{\rm co} \sim R_A$ sets the NS's final spin period:

$$P_1 \rightarrow P_{\rm eq} \simeq 6\ \left(\frac{\mu_1}{10^{33}\ \mathrm{G\,cm^3}}\right)^{6/7}\ \left(\frac{|\dot{M}_2|}{3\times 10^{13}\ \mathrm{g\,s^{-1}}}\right)^{-3/7}\ \left(\frac{M_1}{1.4\ M_\odot}\right)^{-5/7}\ \mathrm{hr}. \tag{2.12}$$

The X-ray emission of this system is powered by mass accretion from the secondary (as in standard Polars), but this is not the only mechanism responsible for the luminosity of 1E 161348-5055: in fact, it is likely that the magnetic power endowed in 1E 161348-5055 is in action as well. The spectral properties and temporal variability of this source are remarkably similar to those of AXPs and SGRs. Therefore the decay of the magnetic field could be partially or even totally responsible for the luminosity of 1E 161348-5055, while the role of the companion is to explain the observed time periodicity at 6.67 hr instead of the canonical period of 5-12 s typical for magnetars.

Of course the characteristics of the system as we see them now would be the result of a long dynamical interplay between the magnetar and the companion, explicated by the several torques in action: the spin-down torque, the torque between the magnetic moments of the two stars, the torque that will slow the neutron star down to synchronize its spin with the orbital period, the accretion and propeller torques, plus the tidal torque acting on the companion star and the orbital torques. They are all quantified with an equation that summarizes the interplay, and links the phases of the neutron star and the companion ϕ_1 and ϕ_2:

$$\begin{aligned}
\dot{\phi}_1 &= \omega_1 \\
I_1\,\dot{\omega}_1 = &-\tfrac{\mu_1\,\mu_2}{a^3}\ \Big[2\,\cos(\phi_2-\vartheta)\ \sin(\phi_1-\vartheta) + \sin(\phi_2-\vartheta)\ \cos(\phi_1-\vartheta)\Big] - \\
&-\tfrac{2}{3}\ \tfrac{\mu_1^2}{c^3}\ \omega_1^3 - I_1\ \tfrac{\omega_1-\Omega_{\rm orb}}{\tau_{\rm syn}} + \\
&+|\dot{M}_2|\ (G\,M\,b_1)^{1/2}\ \Big[\tfrac{1}{1+\lambda\,(\omega_1/\Omega_{\rm orb})^2} - \tfrac{\lambda}{2}\,(\omega_1/\Omega_{\rm orb})^2\Big]
\end{aligned} \tag{2.13}$$

where $\theta = \Omega_{orb}\, t$ is the true anomaly. The first part of equation 2.13 is due to the magneto-dipole losses, the second term is the result of the dipole-dipole magnetic interaction torques that act on the stars, the third is the dissipative torque that acts to synchronize the NS spin and the orbital period, and the last term is the consequence of accretion-propeller torque.

Pizzolato et al. show that this equation admits an asymptotical solution, which is the neutron star equilibrium spin period and full synchronism with the orbiting case material torques are absent, while if they are present the spin period assumes a value that is anyway close to that of the orbital period: $P_{eq} \simeq 0.5 - 0.7\ P_{orb}$. With standard assumptions as the neutron star moment of inertia $I_1 = 10^{45}\,\mathrm{g\,cm^2}$, the global equation with null mass transfer rate yields orbital synchronization because of the magnetic torques, within ~ 2000 yr if the synchronization time τ_{syn} is no longer than a few hundred years. In this situation a magnetar-like field and a close orbit are necessary.

If the mass transfer rate is not negligible, the material torques are relevant and lead to the equilibrium period within few hundred years independently on the exact value of the synchronization time. The requirements of a magnetar-like field is still essential for the NS magnetosphere to fill its Roche lobe, but 1E 161348-5055 would be more similar to a young accreting low-mass binary.

2.4.1 Cataclysmic Variables

The above reported model for a magnetar in a close orbit with a red dwarf was inspired by the Polar or Intermediate Polar models. These are subclasses of the Cataclysmic Variables, where the magnetic field of the white dwarf (that plays the role of the magnetar in the above model) is high.

In such systems the magnetic interaction between the components is so strong to lock the white dwarf in synchronous rotation with the orbit, with periods up to few hours (the longest period of a Polar, *V1309 Ori*, is of 8 hr, [Garnavich et al.(1994)]). In addition, the magnetic pressure prevents the formation of a disc around the white dwarf, and the accretion flow is directly channeled from the inner Lagrangian point L_1 to one or both the white dwarf's poles.

Cataclysmic Variables[1] (CVs) are a distinct class of interacting binaries, transferring mass from a donor star to a degenerate accretor, a white dwarf (WD) whose mass, as required by theory for stable mass transfer, has to be of higher mass than the donor. The majority of CVs have orbital periods, P_{orb}, between 75 min and 8 h (see for example [Kuulkers et al.(2006)]) and consist of Roche Lobe-filling main sequence donors and WDs. For longer orbital periods, the donors need to be at least evolved subgiants in order to fill the Roche Lobe. In essence, a CV's gross behavior is determined by the rate of mass transfer from the donor, $\dot{M}_{\mathrm{donor}}$, and the strength of the magnetic moment, μ, of the WD. Other parameters, such as P_{orb}, mass ratio, and chemical abundances,

[1] See [Hack et al.(1993)] and [Warner(1995)] for comprehensive overviews.

have less effect; but the brightness and spectral variations on an orbit time scale can depend strongly on the inclination.

For $\mu \lesssim 10^{31}\,\mathrm{G\,cm^{-3}}$ (corresponding to a magnetic field strength $B \lesssim 10^4\,\mathrm{G}$) the WD is essentially "non magnetic" and mass is transferred from donor to WD via an accretion stream and accretion disk without any significant magnetic influence on the fluid flow. Even for μ up to $\sim 10^{33.5}\,\mathrm{G\,cm^{-3}}$ a stream and accretion disk can form, but the inner regions of the disk are removed by the magnetosphere of the WD, within which fluid flow is magnetically channeled. For larger μ no disk can form at all; the stream flow from the donor couples onto field lines from the WD before the stream can circle around the WD. These configurations, which apply for typical $\dot{M}_{\mathrm{donor}} \sim 10^{-10}$–$10^{-8}\,\mathrm{M_\odot\,yr^{-1}}$, are known as *intermediate polars* (IPs) for the systems with intermediate field strength, and *polars* for those with strong fields. The field in polars is so strong that it couples to the field of the donor and forces the WD to corotate with the binary; it also prevents the formation of an accretion disk, while in IPs the WD does not corotate.

Since 1E 161348-5055 hosts a magnetar, I'll only give a brief description of the X-ray emission from polars and intermediate polars.

X-ray emission from Polars

In polars, the originally free-falling matter couples to magnetic field lines somewhere between the two stars and is guided to one or two accretion regions in the vicinity of the magnetic poles. These are the sources of intensive X-ray radiation, mainly in the soft X-ray regime, and of cyclotron radiation from IR to UV wavelengths. A complete picture therefore requires multi-wavelength observations, preferably obtained contemporaneously because of the inherent high variability on many time scales (from seconds to years).

Matter in the accretion stream is accreted almost vertically on to the magnetic poles of the WD. The accretion process is, therefore, almost always modeled in a one-dimensional quasi-radially symmetric approximation. The presence of, e.g., accretion arcs with corresponding variety of accretion rates and deviations from the radial symmetry due to inclined magnetic field lines is evident from observations. Accretion is governed by three parameters, M_{WD}, the accretion rate per unit area, $\dot{m}$, and B. The balance between those parameters determines, whether the accretion region is heated via a strong hydrodynamic stand-off shock or by particle bombardment, and whether the cooling function is dominated by plasma emission or by cyclotron radiation.

In the "standard accretion model" (see for example [King & Lasota(1979)]) about half of the X-rays and of the cyclotron radiation are intercepted by the WD surface and are reprocessed as soft X-rays. This simple model predicts about equal luminosities in the bremsstrahlung and cyclotron components on the one hand and the soft emission on the other, even though significant deviations from this trend were reported, as high as $F_{soft}/F_{hard} \sim 100$ in the X-ray band.

An alternative scenario applies to the low $\dot{m}$ and high B case (bombardment solution, [Woelk & Beuermann(1996)]). In such an environment cyclotron cooling becomes so efficient that it cools the plasma over a mean free path of the infalling particles, i.e., the shock is resolved and bremsstrahlung is suppressed.

Polars display a rich phenomenology of X-ray light curves despite their rather simple accretion geometry. The light curves offer large diagnostic potential, since they are modulated by the location and the three-dimensional extent of one or several accretion spots, by stellar eclipses (11 out of 70 systems display stellar eclipses), by nonstationary accretion processes, and by absorption of X-rays within the binary. The long-term light curves are affected by shifts of the accretion regions in longitudinal and/or lateral directions, by changes between one- and two-pole accretion modes (which gives those systems a completely different appearance) and by large-scale variations of $\dot{M}$.

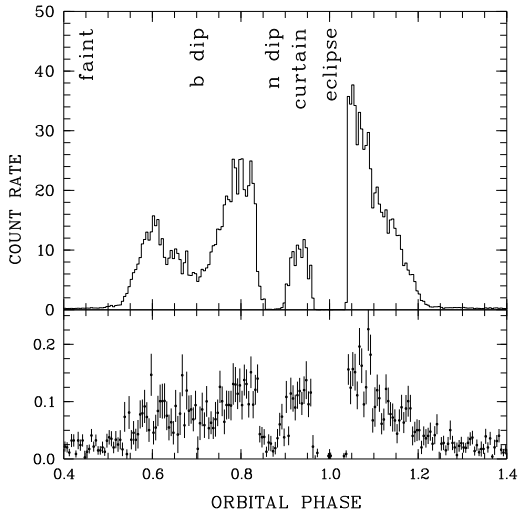

Figure 2.8: *ROSAT* X-ray light curves of the high-inclination polar HU Aqr. The original photon data comprise 36 ksec and were phase-averaged over the 125 min orbital period. The upper panel encompasses the whole spectral band pass (0.1-2.4 keV), the lower panel only the hard X-ray spectral component (0.5–2.0 keV). Several important features around the orbital cycle are indicated. From [Kuulkers et al.(2006)].

For example, in figure 2.8 the lightcurve of HU Aqr is reported (from [Kuulkers et al.(2006)]), and several features are evident: a broad dip ("b dip"), a narrow dip ("n dip"), and eclipse due to self-occultation of the accretion region behind the WD, that appears as an on-off pattern. The narrow dip is

due to absorption in the transient accretion stream, which becomes X-rayed when it has just left the orbital plane. It can be observed in systems in which the orbital inclination exceeds the co-latitude of the accretion spot. Its phase indicates the azimuth and its width the size of the threading region in the magnetosphere. The origin of the broad dip centered at an earlier phase instead remains unclear so far. Its width and X-ray color suggest an origin in warm absorbing matter in close vicinity to the hot accretion spot.

X-ray emission from Intermediate Polars

Intermediate Polars, as anticipated before, are those Cataclysmic Variables where the magnetic field of the WD allows the formation of a disk, but material is channeled from its inner part to the WD along the magnetic field lines and flows towards the magnetic poles forming "accretion curtains" above each pole. Unlike the polars then, the accretion flow impacting the WD in IPs will be more extended, occurring over a greater fraction of the WD surface.

Modulation at the WD spin period is produced by a combination of self occultation and varying photo-electric absorption towards the X-ray emission sites, while also a suite of modulations are expected due to geometry projection. Denoting $\Omega{=}2\pi/P_{\rm orb}$ and $\omega{=}2\pi/P_{\rm spin}$, the frequencies $\omega{-}\Omega$, $\omega{-}2\Omega$, $\omega{+}\Omega$ and $\omega + 2\Omega$ are predicted to occur in the optical range.

The model widely accepted to explain the variety of lightcurves of Intermediate Polars (one is shown as an example in figure 2.9) is the "accretion curtains" model, where the emission region is a tall, thin, arc-shaped curtain and the largest X-ray flux is seen when the curtains are viewed from the side (i.e., when a given pole is pointing *away* from the observer).

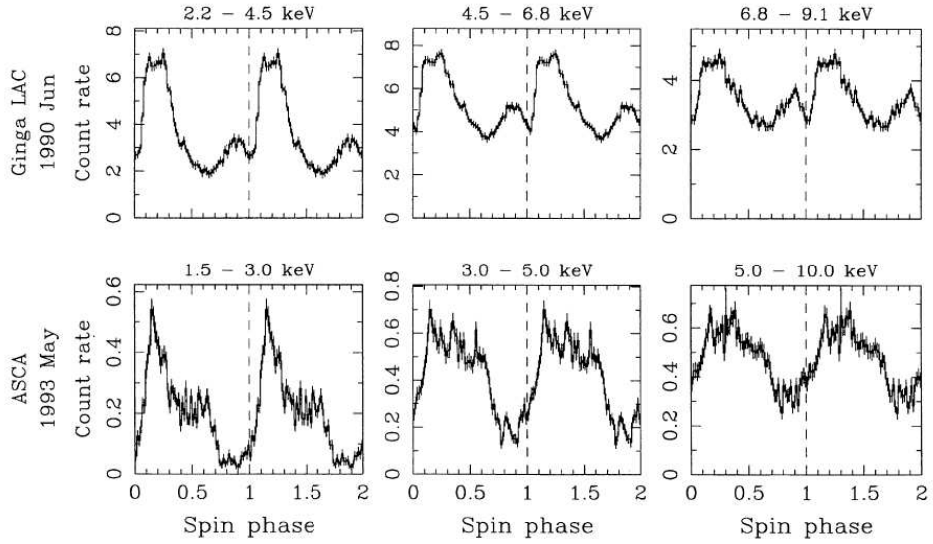

Figure 2.9: X-ray pulse profiles of FO Aqr. From [Kuulkers et al.(2006)].

It has been noted [Norton et al.(1999)] that the IPs exhibiting double-

peaked X-ray pulse profiles are mostly those with short $P_{\rm spin}$. The WDs in these objects therefore probably have weak magnetic fields, so the magnetospheric radius is relatively small. Consequently the footprints of the disk-fed accretion curtains on the WD surface are relatively large. Indeed, two-pole accretion onto smaller regions of the WD surface may be considered the 'normal' mode of behavior in a disk-fed IP with a longer $P_{\rm spin}$ (and therefore a higher field strength), resulting in a single-peaked pulse profile.

IPs sometimes show strong orbital modulations in their X-ray light curves. For example FO Aqr (see figure 2.9) has orbital dips characterized by increased photo-electric absorption around $\phi_{\rm orb}\sim 0.8$.

The X-ray spectra of IP is best modeled by a multi-temperature emission region, with many emission lines.

Chapter 3

XMM data

In this chapter I am dealing with the data analysis of the *XMM-Newton* available observations: in section 3.1 the observations are described, next the background spectral analysis is performed (section 3.2). After the modelization of the background the source time integrated (section 3.3) and phase resolved (section 3.4) spectral analysis is presented.

3.1 Observations

Three *XMM-Newton* observations exists (see table 3.1), two were made in 2001 (observation id: 0113050601, 0113050701) and one in 2005 (0302390101).

Obs ID	Rev.	Start time	Exp. Time (ks)	Observation Mode PN	MOS1	MOS2	Offset
0113050601 (A)	318	2001-09-03 18:51:00.0	19.6	SW	FF	FF	no
0113050701 (B)	318	2001-09-03 10:06:48.0	28.7	TI	FF	FF	yes
0302390101 (C)	1045	2005-08-24 07:53:58.0	87.9	SW	FF	FF	no

Table 3.1: Net exposure time for the three EPIC instruments (in units of ks) during the three observations.

I used only two of them for the spectral analysis: 0113050601 and 0302390101 - respectively observation A and C - because 0113050701 observed the target with a considerable offset, thus being inhomogeneous with the other ones. Moreover, the PN instrument aboard *XMM-Newton* was operated in timing mode. Observation A is a 20 ks long observation in small window mode, while Observation C is 88 ks long: it covers more than three periods of rotation of the source, allowing for phase-resolved spectral analysis to be done. The importance of analyzing also of observation A resides in the fact that 1E 161348-5055 has a secular variation in flux: in 2001 it was in a high state, while in 2005 its intensity had decreased of a factor around 10.

Data reduction was performed using SAS version 7.1.0, with the latest calibration database, and the standard tools.

3.2 Background spectral analysis

The spectral analysis I performed was obtained with Xspec version 11.3.2ad, and the underlying idea is modeling the source together with the Supernova Remnant, because the *XMM-Newton* mirrors are so powerful that the contamination from the SNR is very relevant (it dominates the spectra below $\sim$ 0.8 keV). This was not as easy as we initially thought: RCW103 is a bright remnant, whose properties present spatial variability that has not been studied in detail yet. For this reason, when I extracted the spectra from a circular region centered on 1E 161348-5055, with a radius of 30 arcsec, all the standard models failed to describe the plasma, leaving very important residuals at low energies. They are probably due to abundances, but still need a detailed and space resolved approach (the analysis is currently ongoing).

The solution to this problem was choosing a smaller extraction region: a circle whose radius is 10 arcsec, a third with respect to the previous case. This allowed to dramatically reduce the number of counts from the SNR.

Both observations A and C were not affected by soft protons; as a consequence, all the observation time was useful for data analysis, there was no need for a rejection filter. It must be noticed though that they were affected by diffuse particle background, very visible especially at high energies where all the models tested left big residuals.[1]

They had a simple powerlaw shape, not convoluted with the response of the instrument: it was necessary then to add one more component to the model, a powerlaw/b, having thus a model of phabs(nei)+pow/b for the SNR. This was to be added to the Neutron Star model, making the model extremely complicated and heavy to be fitted. The only thing one could do was fitting the background separately, and use the best fit parameters in the source fit, keeping in mind that the extraction region for the background had to be chosen carefully, seen its marked variability.

[1]The signature modeled as a powerlaw not convoluted with the instrumental response is due to Non X-ray Background in the EPIC detectors. This is analyzed in [De Luca & Molendi(2004)]. I will give here just a brief description.

The signal was generated by the interactions of particles with the detectors and with the surrounding structures; when the incident particles have very high energy ($E \gtrsim$ a few MeV) their signal is automatically filtered out by the data reduction pipeline. Conversely, when the particles accelerated to $E \sim$ a few keV in the terrestrial magnetosphere reach the detector from the mirrors, their interaction with the CCDs generate events that are almost indistinguishable from valid X-ray photons. This signal is very time-dependent, and sometimes has the shape of flares in the lightcurve, thus it can be easily filtered away with a GTI selection. An additional component of background can be generated by a steady flux of low energy particles, reaching the detectors through the telescope optics at a uniform rate. This is the high energy tail that had to be modeled together with the background.

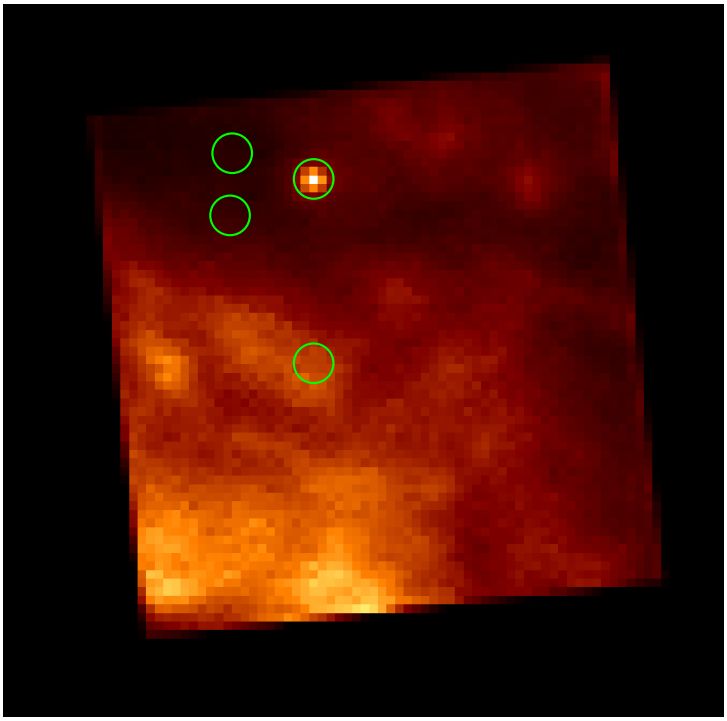

Figure 3.1: Image of the pn field of view, observation C. The source region and the three background regions (10as) used to describe the SNR are superimposed on the image. The two regions closer to the source are homogeneous, while the third shows a significant variation of the n_H.

The aim was finding, as a first approximation, the one parameter whose variability could best reproduce the diversity of the spectra in the regions. The models I chose to try to reproduce the spectra are the Xspec models nei and vnei, standard models for young supernova remnants. They describe non-equilibrium ionization plasmas, with the possibility in the vnei model to let the abundances vary with respect to the solar abundances. As a result I had a list of parameters common to all backgrounds (namely temperature, abundances and, of course, ionization time), while the hydrogen column, instead, proved to be quite variable: it doubles when passing from the less bright region of the SNR to the a more bright one.

In order to minimize the number of free parameters for the fit, then, I extracted several background spectra, in different regions of the SNR (see fig. 3.1), and performed a fit of the background model on all of them. I used three circular regions, whose radius is 10 arcsec, two of them in the less bright part of the supernova remnant and one in the bright halo (see figure 3.1), and two 30 arcsec circular region, one in the dark and one (centered in the same point as the 10 arcsec region) in the bright part.

For a comparison, all the parameters of the fit are listed in table 3.2, and in table3.3. As said at the beginning of the paragraph, the source spectrum was

extracted from a circular 10 arcsec region, so there would have been no reason to study the background spectra of the 30 arcsec regions. This was done, in fact, not for a spectral analysis itself, but for a cross check of the physical parameters (namely the temperature) that have to remain constant even when choosing different sized extraction regions.

Since 1E 161348-5055 is located in the less bright region, I chose to model the SNR with the parameters of the two background regions closest to the source. In figure 3.2, instead, the spectra of the background chosen to reproduce the SNR in the source region are reported, to better visualize the effects of reducing the extraction radius. Top: region of 10 as. Bottom: 30 as. The models are described in detail in tables 3.2 and 3.3, where it is clear that the temperature is consistent in both fits.

Parameter	Value	90% CL error	
		lower	upper
n_H	0.84	-0.04	+0.04
kT	0.57	-0.02	+0.02
Abund	0.38	-0.05	+0.06
Tau	9.43×10^{10}	-1.65×10^{10}	2.05×10^{10}
Redshift	0	0	0
$\chi^2_{red}(DOF)$		1.54 (194)	
N. H. P.		1.8×10^{-6}	

Table 3.2: Best fit parameters for the two regions (radius of 10 as) of the background chosen to parameterize the SNR. The model is: absorbed non equilibrium ionization collisional plasma. No error is given for the frozen parameters. For further details, see the xspec manual description of the models.

The residuals of both spectral fittings show that models nei and vnei are not adequate to perfectly reproduce the data. In particular, the 30as spectrum has one big residual that can eventually be modeled through emission lines (in the source extraction region, the line is at 0.84 keV, a blend of oxygen and iron emission lines around 0.8 keV.). In both the figures the particle background at high energies is clearly visible. By comparing the top and bottom figures, one can note how the intensity of the emission increases with the radius of the extraction region: choosing the 10as region for the fit, we both obtain a more reliable model for the SNR, and a conspicuous reduction of the high energy background.

3.3 Source spectral time-integrated analysis

Having determined the parameters of the background model, we can now perform a combined fit of the SNR and the source.

Since the favorite hypothesis for the object in RCW103 is a magnetar-like

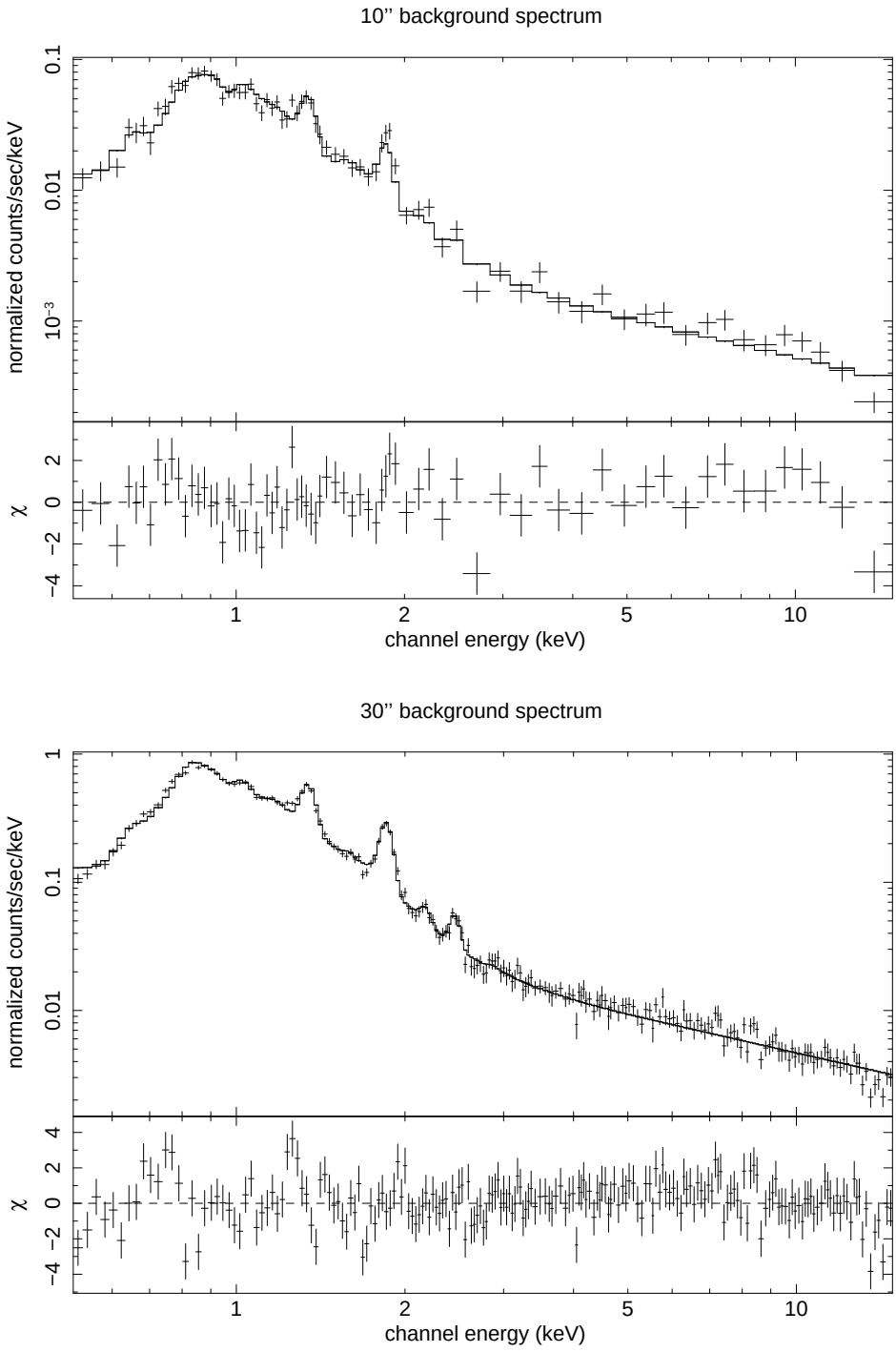

Figure 3.2: Background spectra for different sized extraction regions. It's evident how decreasing the size of the extraction region the number of counts decreases. Nonetheless, some residuals are present even in the 10 arcsec circular region. See text for further details.

Parameter	Value	90% CL error	
		lower	upper
n_H	0.634	-1.29×10^{-2}	2.29×10^{-2}
kT	0.583	-3.29×10^{-3}	1.083×10^{-2}
H	1	-	-
He	4.19	-1.24	0.90
C	0	-	-
N	0	-	-
O	1.10	-0.32	0.57
Ne	0.497	-5.57×10^{-2}	5.39×10^{-2}
Mg	1	-	-
Si	1.4766	-9.24×10^{-2}	4.98×10^{-2}
S	1.62	-0.30	0.27
Ar	1	-	-
Ca	0	-	-
Fe	0.695	-6.35×10^{-2}	6.36×10^{-2}
Ni	0	-	-
Tau	2.391×10^{11}	-4.38×10^{10}	6.44×10^{10}
Redshift	0	-	-
$\chi^2_{red}(DOF)$		1.56 (188)	
N. H. P.		1.3×10^{-6}	

Table 3.3: Best fit parameters for the two regions (radius of 30 as) of the background chosen to parameterize the SNR. The model is: absorbed non equilibrium ionization collisional plasma with variable abundances. No error is given for the frozen parameters. For further details, see the xspec manual description of the models.

star, isolated or in a binary system, I refer to the models most used in literature for this kind of source.

AXPs spectra, which in the X-ray band are soft (below 10 keV), are generally fitted by a combination of a blackbody (temperature kT $\sim$ 0.5 keV) and a steep powerlaw (photon index $\sim$ 3-4) [Mereghetti et al.(2002)]. Nonetheless, some AXP spectra are equally well fitted by a combination of two blackbodies: this is the case, for example, of the Transient Anomalous X-ray Pulsar XTE J1810-197, that also shows X-ray variability (see [Halpern & Gotthelf(2005)] and [Halpern et al.(2005)]) and a spectral evolution whose interpretation as a decay of the a hot spot favors the double blackbody model. This is even more confirmed by the fact that the double blackbody model, when extrapolated to lower energies, does not exceed the optical and near infrared limits.

As expected, a single component model is totally inadequate for this source:

- Blackbody: reduced χ^2 (d.o.f.) = 1.60 (289), with high energy residuals.
- Powerlaw: reduced χ^2 (d.o.f.) = 2.39 (290), with structurate residuals at 1-2 keV, and high energy residuals.

Coherently with the examples present in literature, I used the two canonical

models for 1E 161348-5055: a double blackbody, and a blackbody plus power-law. First I tried to fit the two spectra with the same model parameters, and only an overall normalization factor free to vary, but the fit does not give good results: reduced $\chi^2 = 3.29$ for 295 degrees of freedom. As a second step, then, I let all the parameters of the model free to vary: the results are summarized in table 3.4.

Model	Parameter	Value and 90% CL error 2005	2001
	n_H (10^{22} cm^{-2})	$0.96^{+0.07}_{-0.06}$	$1.25^{+0.08}_{-0.07}$
bbodyrad	kT (keV)	$0.48^{+0.02}_{-0.02}$	$0.49^{+0.03}_{-0.04}$
	norm	$4.85^{+1.04}_{-0.73}$	$26.45^{+8.02}_{-4.96}$
bbodyrad	kT (keV)	$1.22^{+0.32}_{-0.22}$	$0.90^{+0.17}_{-0.11}$
	norm	$1.33^{+3}_{-0.9}\times10^{-2}$	$0.51^{+0.92}_{-0.36}$
Reduced χ^2 (d.o.f.)		0.93 (287)	
N.H.P.		0.786	

Model	Parameter	Value and 90% CL error 2005	2001
	n_H (10^{22} cm^{-2})	$1.57^{+0.21}_{-0.25}$	$1.80^{+0.37}_{-0.30}$
bbodyrad	kT (keV)	$0.48^{+0.02}_{-0.02}$	$0.53^{+0.03}_{-0.04}$
	norm	$3.71^{+1.04}_{-0.73}$	$16.40^{+2.94}_{-3.43}$
powerlaw	PhoIndex	$3.60^{+0.39}_{-0.38}$	$3.63^{+0.38}_{-0.50}$
	norm	$2.4^{+2}_{-1}\times10^{-3}$	$1.3^{+0.6}_{-0.8}\times10^{-2}$
Reduced χ^2 (d.o.f.)		0.95 (285)	
N.H.P.		0.701	

Table 3.4: Free parameters of the model describing 1E 161348-5055. N.H.P. stands for Null Hypothesis Probability.

Both the models give very good results: it is not possible then, from a statistical point of view, to discriminate between them (see tables 3.4): we are facing another situation where the models represent the spectra equally well. But the case of XTE J1810-197, where the spectral evolution is modeled by the decay of a hot spot, makes one think that the double blackbody model should be preferred for 1E 161348-5055 as well, also because it does not overestimate the flux in the infrared range (see par. 3.3.1). Let's note that the n_H value varies with the choice of the second component of the underlying continuum (whether a blackbody or a powerlaw).

Double blackbody model

As we can see from table 3.4, many parameters have comparable values in the 2001 and in the 2005 observations. At first sight, one could reasonably think

that the difference in flux between the two epochs are due to the change in the normalization of the blackbodies, but from a more detailed analysis one can see that the data can be reproduced by linking (see table 3.5) different sets of parameters between the two epochs: for example the temperatures, or the hydrogen column and the cold temperature, or the normalizations.

The meaning of choosing one parameter rather than a different set is the following: reproducing the long term variations of the spectral properties by means of the n_H would imply an accreting scenario, while either the temperatures or the normalizations are compatible with cooling, even though the origin of the temperature increase is not specified. Assuming that only the temperatures vary means hypothesizing that a region of the magnetar surface is heated, and is cooling by radiating thermal energy without changing its size. Conversely, allowing only the normalizations to vary would imply that the heated region is shrinking but is not changing its temperature.

As is evident from table 3.5, we cannot discriminate which of the different scenario is the one physically reproducing the data, since the biggest fraction of the flux is emitted by the cold blackbody, and its physical parameter (the Temperature) is perfectly compatible in all cases.

It is important to notice, in fact, that, despite the low null hypothesis probability of some of the above cases, they all offer a good modelization of the spectra: the low N.H.P. is given by residuals at low energies, and at very high energies (above 7 keV). One should remember that residuals at low energies were present in the fit to the background, so these are likely due to a not perfect yet modelization of the supernova remnant. For what concerns the high energy residuals, the temperatures of the blackbodies are low enough to ensure that the high energy tail is almost exclusively due to the particles incident onto the detectors, and not because of a bad source model. The only unacceptable combination is number 5: this indicates that the warm blackbody is for sure responsible of the flux variation. What the fit results in table 3.5 show is that it is possible to reproduce the spectra allowing a set of only three parameters to vary. From a statistical point of view it is not possible to decide which is the best set to reproduce the flux variations between 2001 and 2005. A hint can come from the fact that if one wants to isolate the parameter that can alone reproduce better the decay, that is the blackbody temperature of the warm blackbody. These considerations are very important in the next chapters, when thanks to the *Chandra* monitoring observations we will try to model the secular decay of the luminosity.

Comptonized blackbody model

The above models are just phenomenological descriptions of the data, but they indicate that the soft X-ray emission is predominantly of thermal origin, but the emerging spectrum is more complex than a simple Planckian. Another possible and more physical choice for the model could then be a comptonized

		1		2	
Model	Parameter	Value and 90% CL error		Value and 90% CL error	
		2005	2001	2005	2001
	n_H (10^{22} cm^{-2})	$0.92^{+0.06}_{-0.06}$	$1.29^{+0.06}_{-0.05}$	$1.15^{+0.06}_{-0.05}$	
bbodyrad	kT (keV)	$0.48^{+0.02}_{-0.02}$		$0.45^{+0.02}_{-0.02}$	
	norm	$4.7^{+1.0}_{-0.8}$	$30.4^{+5.7}_{-4.2}$	$7.4^{+1.8}_{-1.4}$	$24.2^{+6.7}_{-4.9}$
bbodyrad	kT (keV)	$0.91^{+0.12}_{-0.08}$		$1.04^{+0.19}_{-0.14}$	$0.71^{+0.04}_{-0.03}$
	norm	$0.06^{+0.07}_{-0.04}$	$0.52^{+0.56}_{-0.32}$	$0.04^{+0.06}_{-0.03}$	$3.22^{+1.03}_{-0.88}$
Reduced χ^2 (d.o.f.)		0.97 (288)		1.12 (288)	
N.H.P.		0.61		0.07	
		3		4	
	n_H (10^{22} cm^{-2})	$1.29^{+0.06}_{-0.06}$	$1.23^{+0.07}_{-0.07}$	$0.93^{+0.06}_{-0.06}$	$1.06^{+0.04}_{-0.04}$
bbodyrad	kT (keV)	$0.31^{+0.02}_{-0.02}$	$0.48^{+0.02}_{-0.02}$	$0.49^{+0.01}_{-0.02}$	$0.57^{+0.01}_{-0.01}$
	norm	$25.7^{+6.2}_{-4.4}$		$4.7^{+0.8}_{-0.6}$	$14.7^{+1.2}_{-1.1}$
bbodyrad	kT (keV)	$0.63^{+0.04}_{-0.03}$	$0.80^{+0.04}_{-0.04}$	$1.36^{+0.30}_{-0.21}$	
	norm	$1.13^{+0.50}_{-0.38}$		$0.086^{+0.012}_{-0.005}$	
Reduced χ^2 (d.o.f.)		1.12 (279)		1.17 (288)	
N.H.P.		0.07		0.02	
		5			
	n_H (10^{22} cm^{-2})	$0.98^{+0.08}_{-0.07}$	$1.05^{+0.04}_{-0.04}$		
bbodyrad	kT (keV)	$0.47^{+0.02}_{-0.03}$			
	norm	$5.4^{+1.4}_{-1.0}$			
bbodyrad	kT (keV)	$1.10^{+0.28}_{-0.19}$	$0.60^{+0.01}_{-0.01}$		
	norm	$0.024^{+0.054}_{-0.017}$	$10.1^{+0.9}_{-0.8}$		
Reduced χ^2 (d.o.f.)		1.24 (288)			
N.H.P.		3.754×10^{-3}			

Table 3.5: Parameters of the model describing the time-integrated spectra of 1E 161348-5055 for different choices of free parameters. In case 1, the temperatures are linked in the two epochs. Case 2: n_H and one temperature are linked. Case 3: the normalizations are linked. Case 4: the hot blackbody is linked. N.H.P. is Null Hypothesis Probability of each fit.

blackbody[2]; this model will prove later (see chapters 4 and 5) to be a good

[2]The "compbb" model in xspec is based by the work in [Nishimura et al.(1986)]. It extends the previous available models by extending the electronic temperature up to values as high as $\sim$ 200 keV, and is valid for any optical thickness of the electron plasma, while before the model was useful only for optically thick plasma, and not for optically thin. Its only restriction is that the electronic temperature T_e and the photon energy E meet the following requirement:

$$E \lesssim kT_e < mc^2,$$

choice to fit the monitoring observations of 1E 161348-5055.

Model	Parameter	Value and 90% CL error	
		2005	2001
compbb	n_H (10^{22} cm^{-2})	$1.08^{+0.07}_{-0.06}$	$1.29^{+0.05}_{-0.05}$
	kT (keV)	$0.39^{+0.01}_{-0.01}$	$0.46^{+0.01}_{-0.01}$
	kTe (keV)	$1.00^{+0.06}_{-0.00001}$	$2.02^{+0.12}_{-0.12}$
	tau	$4.45^{+0.09}_{-0.06}$	$2.59^{+0.07}_{-0.07}$
	norm	$38.0^{+6.2}_{-5.2}$	$110.8^{+12.7}_{-11.1}$
Reduced χ^2 (d.o.f.)		0.97 (286)	
N.H.P.		0.653	

Table 3.6: Free parameters of the comptonized blackbody model describing 1E 161348-5055. N.H.P. is Null Hypothesis Probability.

3.3.1 Extrapolation to infrared

Previously it was said how the double blackbody model is physically favored over the blackbody plus powerlaw, and one of the reasons is that in this case there is no overestimation of the source flux in the optical and infrared band.

Deep infrared observations of 1E 161348-5055, described in chapter 1 and in more detail in [De Luca et al.(2008)], failed to identify a univocal counterpart in the H and K bands, putting 3σ upper limits at H = 23 mag, and K = 22.1 mag. From the X-ray observations, a visual absorption $A_V \sim 3.3 - 6.6$ was induced (these are very conservative limits: they are compatible to both the n_H of the supernova remnant, and that of the neutron star), that translates into a reddening $\sim 1 - 2$. I used these values to test our best fit model for 1E 161348-5055 from the 2005 observation, described in table 3.4. The overall model now, in addition to the absorbed double blackbody, includes also a reddening component, to extrapolate it to the infrared energy range and check whether the above upper limits are consistent with its extrapolation.

The result is shown in figure 3.3, that shows the extrapolation of model to infrared wavelengths ($\sim 10^5$, with the minimum $E(B-V) = 1$ absorption, that means with the highest predictable flux in infrared. The two red arrows instead indicate the upper limits in the appropriate flux units: $H \sim 6 \times 10^{-8}$ and $K \sim 7 \times 10^{-8}$ photons cm^{-2} s^{-1} $^{-1}$. The model for the neutron star emission predicts an infrared flux well above the sensitivity magnitude reached in the infrared observation, but the eventual debris disk around 1E 161348-5055 (see chapter 1) should have a higher emission in this energy range.

where m is the electron mass, and k is the Boltzmann constant.

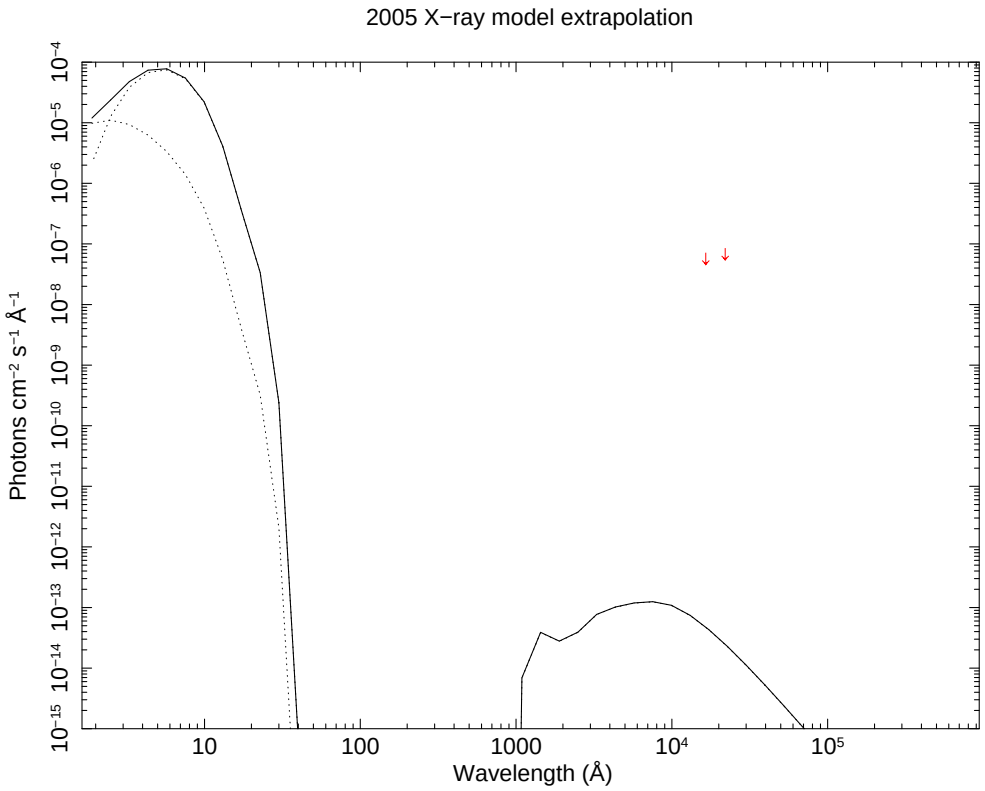

Figure 3.3: Extrapolation of the best fit X-ray model of the 2005 *XMM-Newton* observation of 1E 161348-5055 to the infrared energy range. In red, the upper limits derived in [De Luca et al.(2008)] for the non-identification of an infrared counterpart.

3.4 Phase-resolved analysis

I then proceeded to phase-resolved analysis, to get further insight on the emission mechanism for 1E 161348-5055. As is well known, 1E 161348-5055 spins with the longest period known for a neutron star, $P = 6.67hr =\sim 24000s$.

3.4.1 2001 observation

The *XMM-Newton* on axis 2001 observation isn't long enough to cover at least one period of the source, and moreover the lightcurve shows that the pulsed profile shape is dramatically different than the one in 2005, where 1E 161348-5055 has recovered the pre-outburst shape.

For this reason it's very difficult, if not impossible, to identify the peak and throat of the quiescence profile with one of the peaks and dips that the 2001 lightcurve shows.

This problem was overcome thanks to the accurate timing analysis described in chapter 6: starting with the *Swift* observations and going backwards

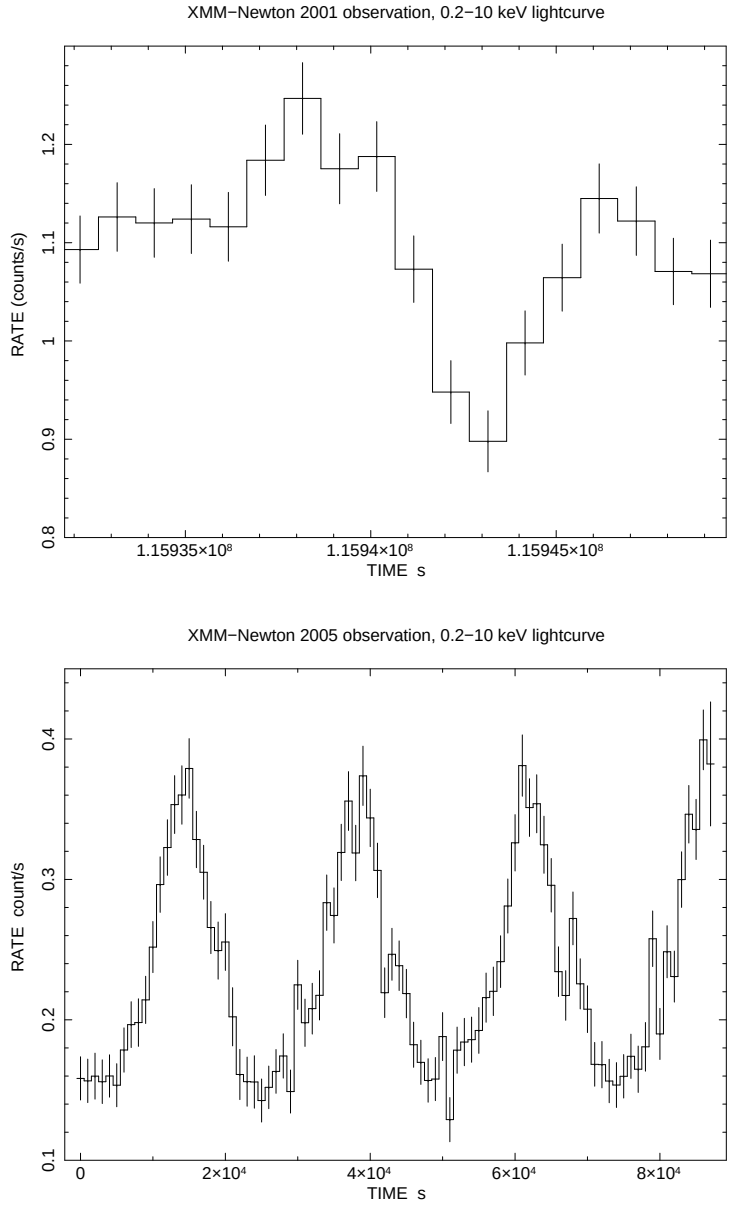

Figure 3.4: Unfolded, background subtracted 0.2-10 keV lightcurves of the 2001 and 2005 *XMM-Newton* observations. It's evident how the 2005 observation covers more than three periods of 1E 161348-5055. The 2001 observation, instead, is shorter than one period and has many substructures. As explained in detail in text, it was possible anyway to identify the highest peak and the minimum next to it as the peak and minimum of the sinusoidal profile, since they are in phase.

until the 1999 *Chandra* observation, we derived a refined value of the period $P = 24030 \pm 1$ s. Such a small error implies that the period value is valid throughout the 9 year old observation baseline, from 1999 to 2008, and in

particular for the *XMM-Newton* 2001 observation.

The phase coherent solution then identifies the sinusoidal peak with the highest peak of the 2001 observation, and the minimum with the narrow dip of the lightcurve. Since the observation lasts less than a period, it was not necessary to fold it, and I just chose two intervals of 2500 s each, covering the selected parts of the lightcurve (see also figure 3.4). The intervals are shorter than a quarter of a period; this is of course due to the fact that choosing longer intervals would mean including more peaks other than those identified as being in phase with the sinusoidal profile. For this reason it seemed more reliable to reduce the temporal interval.

The approach to the analysis was to find out which parameter, in the double blackbody model, is more responsible for the spectral variations between maximum and minimum. The results are reported in table 3.7. It's evident how the major improvement in fitting the spectra is achieved when the normalization of the cold blackbody is let free to vary. The effect of the hydrogen column, or the hot blackbody normalization, free to vary is an improvement of the reduced χ^2, which though is not enough to obtain a good fit. For what concerns the hot blackbody temperature, the fit result is too different from the time integrated spectrum to be considered reliable.

From all these considerations we can state that what is responsible of the spectral variations is the normalization of the warm blackbody.

3.4.2 2005 observation

Being the *XMM-Newton* 2005 observation 88 ks long, it is possible to perform a phase resolved analysis on those data.

I divided the period (see fig. 3.5) into 4 intervals of phase, corresponding to the minimum, maximum, rise and fall of the folded profile of the lightcurve, and in particular I took into account the spectrum extracted from the minimum and maximum, which are expected to be the most different from each other. No rescaling had to be made, since the phase intervals have the same length. I first extracted the spectra from the 10 arcsec source region, in order to avoid the big residuals of the supernova remnant, but the statistic was greatly reduced, so much that there were no differences between the minimum and maximum spectra. I then had to use the 30 arcsec extraction region, with the supernova remnant fitted by the model vnei (see table 3.3 for the parameters), and resulting reduced χ^2 on average quite high, but this was a consequence only of the big SNR residuals at low energies.

As one can see from figure 3.6, the count rate is very reduced compared to the time integrated spectra, leading to the fact that the best fit is now with a one component spectrum for the source. This component has a comparable temperature to that of the cold blackbody in the two components model, which confirms the choice of a simplest model: the reduced statistic affects the spectrum mainly at high energies, as can be expected.

Model	Parameter	Value and 1σ CL error peak	dip	Value and 1σ CL error peak	dip
	n_H (10^{22} cm^{-2})	$1.10^{+0.06}_{-0.07}$	$1.42^{+0.09}_{-0.08}$	$1.23^{+0.07}_{-0.07}$	
blackbody	kT (keV)	0.49		0.49	
	norm	$25.1^{+1.4}_{-1.4}$		$28.3^{+1.8}_{-1.7}$	$21.4^{+1.5}_{-1.3}$
blackbody	kT	0.90		0.90	
	norm	$0.52^{+0.06}_{-0.05}$		$0.52^{+0.05}_{-0.06}$	
Red χ^2 (dof)		1.17 (208)		1.00 (208)	
N.H.P.		0.04		0.481	
	n_H (10^{22} cm^{-2})	$1.20^{+0.07}_{-0.07}$		$1.03^{+0.05}_{-0.05}$	
blackbody	kT (keV)	0.49		0.49	
	norm	$24.0^{+0.8}_{-0.9}$		$10.6^{+1.4}_{-1.5}$	
blackbody	kT	0.90		$0.66^{+0.01}_{-0.01}$	$0.62^{+0.01}_{-0.01}$
	norm	$0.70^{+0.06}_{-0.06}$	$0.39^{+0.06}_{-0.06}$	$5.4^{+0.4}_{-0.6}$	
Red χ^2 (dof)		1.23 (208)		1.28 (207)	
N.H.P.		0.01		0.04	

Table 3.7: Result of the double blackbody model fit to the phase resolved spectra of the 2001 *XMM-Newton* observation, for several combinations of linked parameters. Where no error is listed, the parameter was frozen to the value of the time integrated spectrum.

One blackbody is then enough to describe the spectra. In particular what varies between the maximum and the minimum is the normalization of the blackbody, and the hydrogen column. This is made even more evident when we plot the confidence contour of the n_H versus the temperature: from figure 3.7, there is no overlap between the contour plots for the spectrum of the minimum (on the left) and that of the maximum, at a three sigma level, and complete overlap for the temperatures. It can thus be stated that there is a significative change of the hydrogen column, but not of the temperature, within the maximum and the minimum of the profile. The same result is obtained also using a comptonized blackbody. In table 3.8 the parameters for the phase resolved analysis are listed.

The result of the variation of the n_H in the phase-resolved analysis can rise doubts, since we changed the model from a double blackbody to a single blackbody for the source. To have further inside in this effect, I performed one more analysis on the time-integrated spectra, first modifying them to obtain the same uncertainties as in the phase-resolved spectra. This was done to see if the one component model could be applied to the global spectra with reduced statistic as well, and in that case if a variation of the n_H was again visible. As described at the beginning of this section, one period was divided into 4 phase intervals, thus leading to phase resolved spectra with about a quarter of

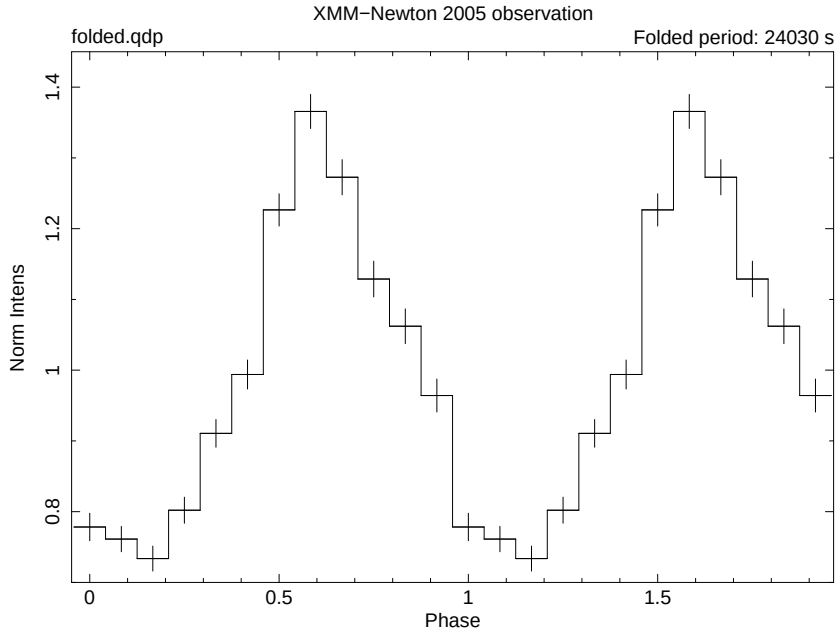

Figure 3.5: Folded lightcurve of 1E 161348-5055, *XMM-Newton* 2005 observation. The intervals chosen to extract the spectra are: [0,0.25] minimum, [0.25,0.50] rise, [0.50,0.75] maximum, [0.75,1] fall.

Model	Parameter	Value and 1σ CL error	
		min	max
compbb	n_H (10^{22} cm^{-2})	$0.23^{+0.12}_{-0.09}$	$1.01^{+0.28}_{-0.22}$
	kT (keV)	$0.48^{+0.05}_{-0.05}$	$0.41^{+0.03}_{-0.04}$
	kTe	1.00	1.00
	tau	4.45	4.45
	norm	$0.40^{+0.23}_{-0.13}$	$2.60^{+1.91}_{-0.96}$
	Red χ^2 (dof) = 1.24 (166)		
	N.H.P. = 0.02		
bbodyrad	n_H (10^{22} cm^{-2})	$0.16^{+0.10}_{-0.08}$	$0.69^{+0.19}_{-0.16}$
	kT (keV)	$0.60^{+0.05}_{-0.04}$	$0.57^{+0.03}_{-0.03}$
	norm	$0.05^{+0.02}_{-0.01}$	$0.19^{+0.07}_{-0.05}$
	Red χ^2 (dof) = 1.21 (166)		
	N.H.P = 0.03		

Table 3.8: Where no error is listed, as for example the electronic temperature, the value was frozen to that of the time integrated spectrum.

the overall counts. As a consequence, the error bars were significantly higher. There are two ways to obtain the same effect in the time integrated spectra:

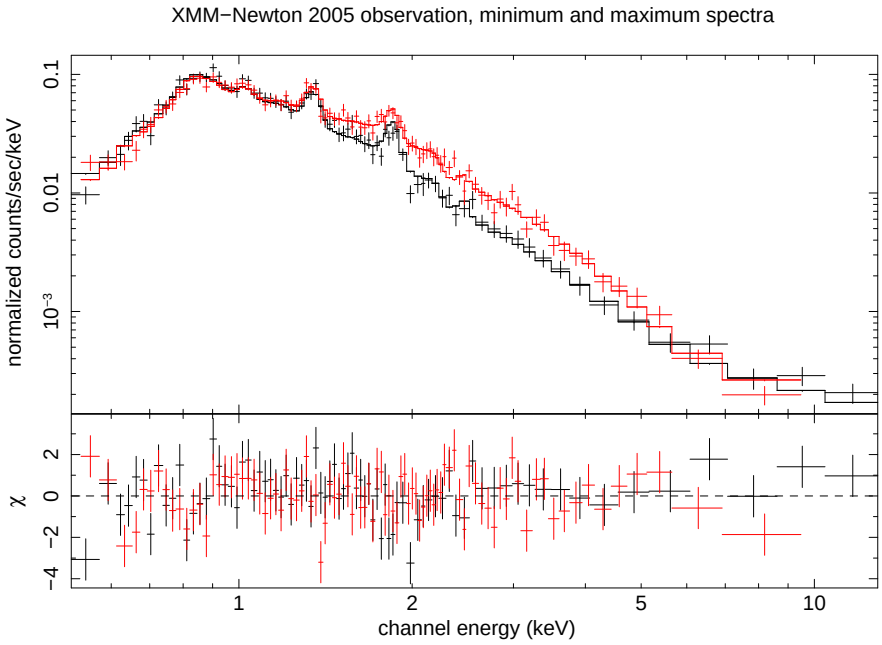

Figure 3.6: *XMM-Newton* 2005 observation. Source spectra in the minimum (black) and maximum (red) interval phase. The differences arise at energies $>$ 1.5 keV, because for lower energies the spectra are dominated by the supernova remnant.

either adding a systematic error component, or building the spectrum using only a quarter of the events, choosing one every four photons. I chose the second option, and applied it to the event file of observations A and C. What I obtained is represented in figures 3.8 and 3.9, and in table 3.9 for the parameters. As in the phase resolved case, the spectra can be well fitted by a one component model, which confirms the fact that only one component is needed when we reduce the statistic. Furthermore, the temperature of the blackbody is compatible with the cold temperature in the two components model.

The difference in n_H in the two observations is visible again: as in the phase resolved spectra, the n_H is the only parameter that can reproduce the variations in flux: as one can see in figure 3.9, the confidence contour plots are completely separated, while the temperature is compatible. This way it is showed that the n_H variation is model dependent, since in the original spectra the flux variation could be reproduced equally well varying different sets of parameters. One quite strange thing emerges: the two values of the n_H, in 2001 and 2005, are the same as those of the minimum and maximum of the phase resolved spectra. This is quite striking! It has no physical meaning, but since both the long term variation (with reduced statistics) and the phase variation of the spectra can be modeled with the variation of the same parameters, one cannot exclude that the underlying phenomenon physically causing the evolution in flux is the same causing the peaks within each period of 1E 161348-

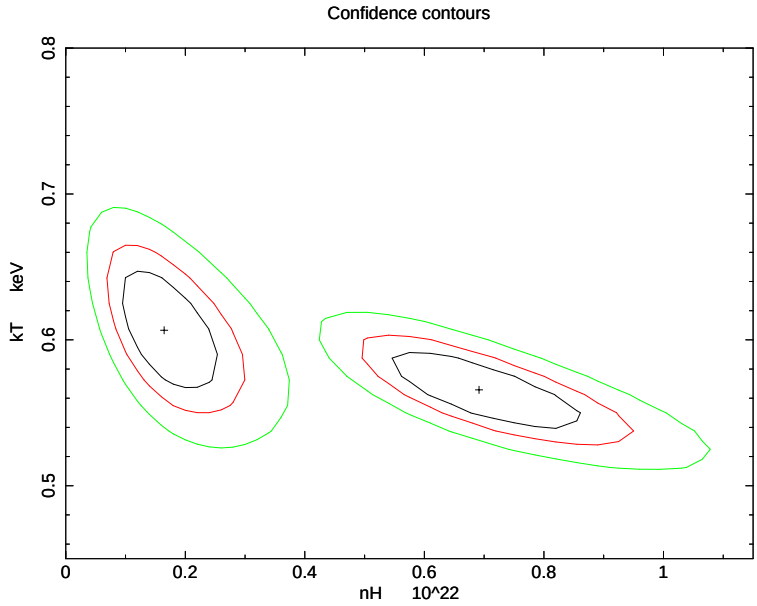

Figure 3.7: Contour plots of the hydrogen column and temperature of the single blackbody fit to the minimum and maximum spectra, 2005 observation. It is immediate to notice how the hydrogen column does not overlap at all, while the temperature is compatible at 1 σ level.

Model	Parameter	Value and 90% CL error	
		2005	2001
bbodyrad	N_h (10^{22} cm^{-2})	$0.20^{+0.10}_{-0.08}$	$0.82^{+0.08}_{-0.07}$
	kT (keV)	$0.61^{+0.05}_{-0.03}$	$0.58^{+0.01}_{-0.01}$
	norm	$0.08^{+0.02}_{-0.02}$	$3.13^{+0.44}_{-0.37}$
Reduced χ^2 (d.o.f.)		0.91 (205)	
N.H.P.		0.815	

Table 3.9: Fit parameters for the *XMM-Newton* 2005 observation, where the dataset was filtered to have a quarter of the overall counts. One blackbody is then enough to model the source spectrum.

5055.

For consistency with the time-integrated analysis, and with the following analysis in the monitoring observations, since the time integrated spectra show the evidence of a second component to the model, I also performed a fit with a double blackbody, but with some parameters linked between the maximum and minimum. This is done both for a statistical reason - this fit does not need the second component, which tends to be normalized to zero, or to have the same temperature as the first one - and in agreement with the following monitoring analysis (see, for example, chapter 4). The fit parameters are summarized in

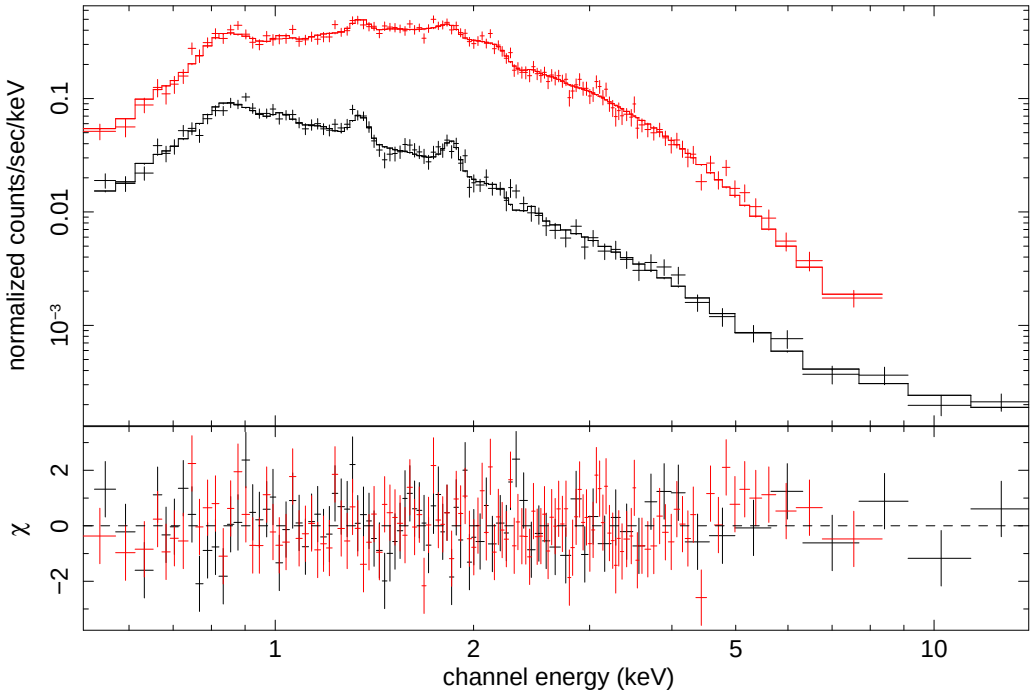

Figure 3.8: *XMM-Newton* 2001 observation (red) and 2005 observation (black) source spectra. The event file was filtered to have a quarter of the overall counts. Notice that no or little residuals are present.

table 3.10. It's evident again a variation of the hydrogen column. The poor statistic is unable to constrain well the hot blackbody, and the variation in the warm blackbody is dropped once on the temperature, and once on the normalization.

Model	Parameter	Value and 1σ CL error min	Value and 1σ CL error max	Value and 1σ CL error min	Value and 1σ CL error max
	n_H (10^{22} cm^{-2})	$0.30^{+0.09}_{-0.07}$	$0.81^{+0.12}_{-0.12}$	$0.23^{+0.10}_{-0.08}$	$0.95^{+0.17}_{-0.15}$
blackbody	kT (keV)	$0.33^{+0.02}_{-0.03}$	$0.41^{+0.07}_{-0.01}$	0.48	
	norm	$0.26^{+0.04}_{-0.01}$		$0.10^{+0.02}_{-0.02}$	$0.39^{+0.05}_{-0.05}$
blackbody	kT	$0.70^{+0.12}_{-0.08}$	$0.70^{+0.08}_{-0.04}$	0.91	
	norm	$0.024^{+0.014}_{-0.016}$		$0.0040\ ^{+0.0012}_{-0.0013}$	$0.0049^{+0.0016}_{-0.0018}$
Red χ^2 (dof)		1.18 (164)		1.23 (166)	
N.H.P.		0.05		0.03	

Table 3.10: Fit parameters for the double blackbody model, for several combinations of linked parameters. Where no error is listed, the parameter was frozen to the value of the time integrated spectrum.

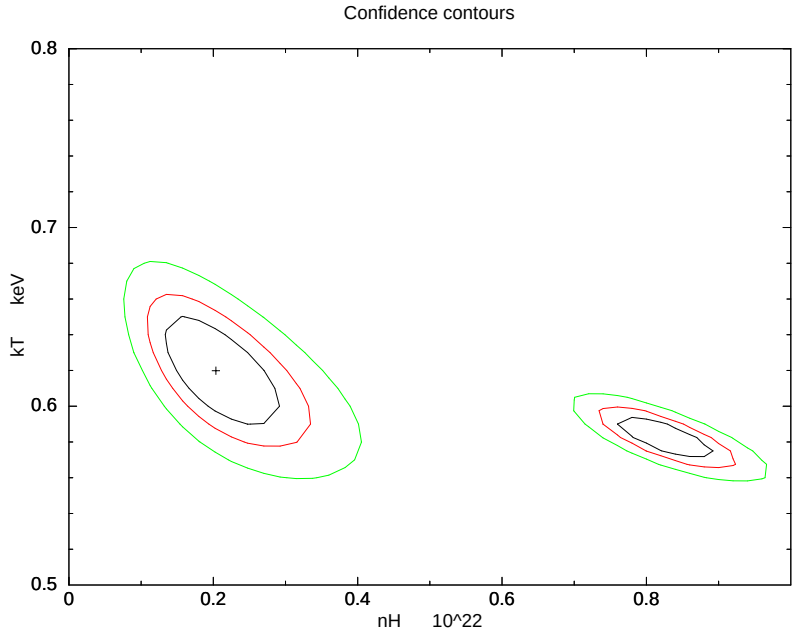

Figure 3.9: Contour plots of the hydrogen column and the blackbody temperature as derived from the one blackbody fit to the event file filtered to have a quarter of the overall counts (see figure 3.8 and table 3.9). Right: 2001 observation, left: 2005 observation. The temperatures appear totally compatible, while the hydrogen column is not.

3.4.3 Ratio of the spectra

The last test that could be performed on the *XMM-Newton* data is the comparison between the ratio of the spectra: it is another way to test what is going on in the secular variation and phase variation of the spectra. In order to do this, I first rebinned the four spectra (2001, 2005, max, min) with the rbnpha tool. The compression factor I chose is 128, to obtain 32 channel and thus increase the statistic for each channel (this was especially necessary in the min and max spectra, that have a factor 1/4 of counts compared to the 2005 spectrum). The error on each channel is poissonian, and was propagated in the ratio according to the standard error theory. The ratios I obtained are reported in figure 3.10.

One can clearly note how the trend is the same in both cases:

- at low energies the SNR emission dominates: the value of the ratios is of course 1 for figure 3.10-bottom, while for figure 3.10-top one should take into account the different duration of the observations.

- at higher energies one can note how the 'high state' spectrum is significantly harder. The ratio of the phase resolved spectra then tends to 1, but this is reasonably due to the poor statistics, as explained previously.

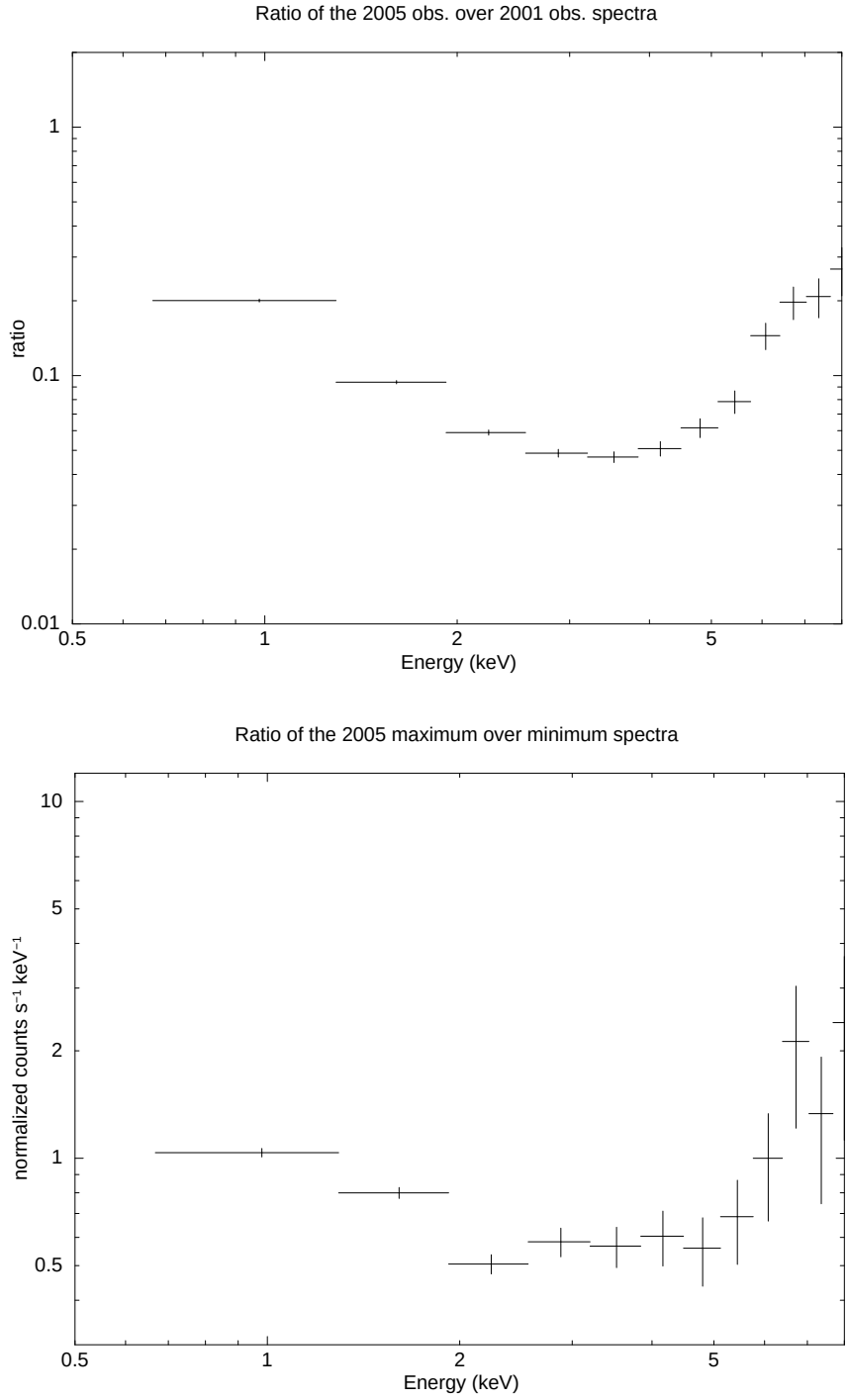

Figure 3.10: Top: ratio of the 2005 and 2001 spectra. Bottom: ratio of the minimum and maximum spectra. The trend is the same in both cases.

This result is even more powerful than the previous one, which is affected by the reduced statistic. Being the ratios of the complete models the same (just rescaling), we can reasonably affirm that the phenomenon underlying the long

time variations and the phase variations is the same.

3.4.4 First considerations

The double blackbody model is consistent with the picture of a hot spot on the stellar surface: the emitting area with hot temperature is small compared to that of the warm temperature. If the heated region only covers a small fraction of the surface, then it is responsible for the spectral variations within the different stages of the spin period.

In the isolated magnetar scenario what emerged from the spectral analysis of the *XMM-Newton* data can be easily explained: when a reconfiguration of the magnetic field happens, additional currents flow in the magnetosphere in order to produce a new equilibrium configuration, and cause a heating of the surface. In the binary system this is easily explained as well: the heating is caused by an accretion episode.

The phase resolved analysis on both the 2001 and 2005 observations gives the following information: in 2005 1E 161348-5055 was in a low state, thus the differences in the spectra of the maximum and minimum can be reproduced with different choices of the spectral parameters. The 2001 observation instead points toward a variation of the normalization of the cold blackbody. It is worth noticing that there was no ambiguity in analyzing the spectra due to the fact that the 2001 observation is shorter than a period: in fact, the regions were extracted after they were identified (see chapter 6) for being in phase with those of the 2005 observation.

Chapter 4

Chandra data

This chapter deals with the spectral analysis of all the Chandra monitoring and more recent observations. First a list of all the observations is presented and discussed (sections 4.1 and 4.2), next the simultaneous spectral analysis of the monitoring observations is explained, with the diverse models used to reproduce the data (section 4.3). Then, the long observations available were analyzed and discussed one by one, given the large diversity in the observation modes and in the status of 1E 161348-5055 at the epoch (sections 4.4 and 4.5). The chapter is concluded with the first considerations on the flux evolution (section 4.6).

4.1 Observations

There exist 22 Chandra observations of 1E 161348-5055, taken at different instrument configurations such that some of them are suitable for both spectroscopic and timing monitoring of the source, while others only contain temporal or imaging information. They are all listed in table 4.1

The first observations (Obs ID 123) was obtained before the outburst episode took place, and gives us the reference pre-outburst quiescence spectral parameters and flux of 1E 161348-5055. The following one (Obs ID 970) is the highest flux observation. The outbursting episode happened sometime in between Obs 123 and Obs 970, but was not detected by any instrument. All the subsequent observations are part of a monitoring campaign that lasted almost 5 years. They are spaced by two or three months, last $\sim$ 5 ks each (they do not provide complete coverage of the period of the source, they only sample it), and cover a wide temporal baseline, which will prove very useful for the timing analysis.

The last observation (Obs ID 7619) is very long and accurate from the imaging point of view. It was originally planned to acquire the best X-ray position of 1E 161348-5055, and look for very short (millisecond) pulsations. These piece of information were essential for the infrared ToO described in

[De Luca et al.(2008)], and to verify or exclude the hypothesis of a Binary with a millisecond pulsar as the central compact object[1]. This observation, in addition, turned out (in a different way then the monitoring observations) very important for the timing analysis too, because its later epoch puts it in the middle of the Swift observations.

Obs ID	Start time (local)	Exp. Time (ks)	Instrum.	Obs mode	Data mode
123	1999-09-26 04:19:02	13.6	ACIS-I	POINTING	VFAINT
970	2000-02-08 02:07:22	19.17	ACIS-S	POINTING	FAINT
1040	2001-01-13 19:45:26	3.87	ACIS-I	POINTING	VFAINT
2314	2001-03-18 08:09:04	4.25	ACIS-I	POINTING	VFAINT
2315	2001-04-27 17:54:31	4	ACIS-I	POINTING	VFAINT
2316	2001-06-24 05:00:04	4.08	ACIS-I	POINTING	VFAINT
2317	2001-08-18 21:16:0	3.94	ACIS-I	POINTING	VFAINT
2318	2001-10-07 13:12:44	3.81	ACIS-S	POINTING	CC33FAINT
2759	2002-03-03 04:44:52	48.83	ACIS-S	POINTING	CC33FAINT
3514	2003-03-08 09:09:11	5.25	ACIS-I	POINTING	VFAINT
3515	2003-05-04 23:51:23	5.43	ACIS-I	POINTING	VFAINT
3516	2003-07-13 11:30:14	5.66	ACIS-I	POINTING	VFAINT
3517	2003-09-21 13:11:09	5.4	ACIS-I	POINTING	VFAINT
4596	2004-01-27 17:06:46	5.16	ACIS-I	POINTING	VFAINT
4597	2004-04-26 17:50:15	4.89	ACIS-I	POINTING	VFAINT
4598	2004-08-03 20:27:46	5.18	ACIS-I	POINTING	VFAINT
4599	2004-10-19 12:58:34	5.14	ACIS-I	POINTING	VFAINT
5592	2005-01-24 13:58:33	5.68	ACIS-I	POINTING	VFAINT
5593	2005-04-21 15:22:44	5.18	ACIS-I	POINTING	VFAINT
5594	2005-07-10 03:20:19	5.18	ACIS-I	POINTING	VFAINT
5595	2005-10-09 17:22:16	4.68	ACIS-I	POINTING	VFAINT
7619	2007-07-02 20:40:33	78.18	HRC-S	POINTING	OBSERVING

Table 4.1: Net exposure time and instrument characteristics of the 22 Chandra observations used in the analysis.

4.2 Data processing

All the data were processed with the CIAO version 3.2.2, and by means of the standard analysis threads[2]. For each observation an image was created, and a region for the source data filtering was selected.

[1]This kind of object is extensively searched for, because it would be the connection between Low Mass X-ray Binaries and millisecond pulsars, when the minor star in the binary system evaporates on the accreting neutron star, whose period decreases to order of milliseconds.

[2]See also http://cxc.harvard.edu/ciao/

The ACIS-I observations were performed using a subarray (see paragraph B.1.2) of the aimpoint CCD, and offset of about $7'$ from the source position. The reason for these choices lies in the high predicted count rate of the source at the moment of the observations: using a subarray reduces the nominal full frame time, and offsetting the instrument determines a distortion and a widening of the PSF (see chapter B). Both these effects contribute to lower the probability of pileup to happen.

For the ACIS-I data mode an ellipse was used, it was centered on the peak of the emission and dimensioned accordingly. For the HRC and ACIS-S data circular regions were selected; their radius was of 6 arcsec.

Obs ID 970 deserves a special comment: as previously mentioned, it is the observation where 1E 161348-5055 was caught in its highest emission state. Its flux ($\sim 8 \times 10^{-9}$ erg / cm^2 s) is more than 100 times the quiescent flux, resulting in a heavily piled-upped observation. To obtain an accurate spectrum I used an annular region, whose internal radii are 2 arcsec and 6 arcsec respectively. According to this choice of region I generated the effective area of the instrument applying the correction described by Tsujimoto and coded into the ARFCORR tool (see http://agyo.rikkyo.ac.jp/ tsujimot/arfcorr.html). As a further test I also extracted the spectrum from the complete 6 arcsec circular region and fitted it with the pile-up model in xspec. This model is the implementation in xspec of the fast pile-up algorithm proposed by John Davis [Davis(2001)]. He improved the previous standard integral equation, which was linear while the pile-up phenomenon is inherently a nonlinear process.

The results I obtain in the two ways are perfectly consistent.

For the two observations in continuous clocking mode (Obs ID 2318 and 2759), the ACIS-S spectrometer does not provide complete spatial information: the data are collapsed into one row, so that any selection region turns out to be a rectangular, as wide as the ACIS array. I used a circular region centered on the emission peak, and a radius of 15 arcsec. The spectra, as a consequence, are highly contaminated by the supernova remnant, which holds true at low energies (< 1 keV).

All the events in the dataset were barycentered using the axbary tool, following standard procedures[3].

4.3 Spectral analysis

The spectra, together with the response and ancillary files derived, were first rebinned to have at least 30 counts per energy bin, and then analyzed simultaneously with xspec version 12.4.0, in order to trace the post-burst evolution of 1E 161348-5055. Of all the available observations we only excluded:

- Obs ID 970, the peak observation: the spectrum was analyzed on its own

[3]see, for the descriptions, http://cxc.harvard.edu/ciao/

- Obs ID 7619, the last Chandra observation: the instrument HRC does not have spectroscopic capabilities.

Thanks to the technical characteristics of the Chandra observatory, the Point Spread Function (PSF) of point-like sources is very small. For this reason, at variance with XMM-Newton, Chandra is best known for its imaging capabilities. As a consequence, Chandra sees the source separately from any surrounding background.

The source spectrum in the extraction regions chosen is only marginally (2-31%) contaminated by the supernova remnant photons. Therefore it is not necessary to background subtract the spectra, nor to model the SNR together with the source. Moreover, the hydrogen column of 1E 161348-5055 derived from this instrument is more reliable than that obtained from the fit to the XMM data, because it is not contaminated by the SNR.

The simultaneous fit of the 20 selected spectra yields very interesting results (for a discussion of the spectral models, see par. 3.3):

1. First of all, the fit to the spectra with only one blackbody gives statistically unacceptable results: χ^2/ dof = 2026.866/1771 = 1.14, but what is most important is the null hypothesis probability of 1.902×10^{-5} and the presence of high energy residuals. Adding a second blackbody model improves significantly the fit: χ^2/ dof = 1601.137/1731 = 0.92, with null hypothesis probability equal to 0.988 and no high energy residuals. The f-test shows that the second component is significant to a 100% level (F statistic value = 10.3 and probability = 0.00).

   Even from the single blackbody model (see table 4.2) it is clear that the n_H is consistent throughout all the observations: the only two that deviate from the average value 1.1-1.2 $\times10^{22}$ are the continuous clocking mode observations, but as already noticed above they are highly contaminated by the SNR. It can be noticed that the temperature shows a sort of declining trend, from 2002 when its value is $\sim$ 0.58 keV, to later epochs when it decreased to $\sim$ 0.52 keV.

2. The statistic of the spectra is not much, especially for the monitoring observations, so some of the parameters of the double blackbody model are not fully constrained. For this reason, and from the fit showing similar temperatures for the warm blackbody (while the hot is unconstrained) and similar values for the hydrogen column, I tried a spectral fit adding a constant to the model. With all the parameters linked to each other, and only the constants free to vary, the fit is surprisingly good: χ^2/ dof = 1962/1807 = 1.09. This leads to the reasonable suspicion that the variation in flux can be modeled (as a first but good approximation) with the decay in time of no more than two parameter per spectrum.

3. It is evident from the spectral parameters of the double blackbody model that the warm blackbody gives the dominant contribution to the total

Obs ID	Single Blackbody		
	n_H (10^{22} cm^{-2})	kT (keV)	Normalization
123	$0.43^{+0.11}_{-0.11}$	$0.58^{+0.04}_{-0.03}$	$0.9^{+0.3}_{-0.2}$
1040	$1.17^{+0.10}_{-0.09}$	$0.58^{+0.02}_{-0.02}$	$19.1^{+3.6}_{-3.0}$
2314	$1.26^{+0.09}_{-0.09}$	$0.58^{+0.02}_{-0.02}$	$22.6^{+4.0}_{-3.3}$
2315	$1.23^{+0.10}_{-0.09}$	$0.56^{+0.02}_{-0.02}$	$23.8^{+4.3}_{-3.6}$
2316	$1.26^{+0.11}_{-0.10}$	$0.56^{+0.02}_{-0.02}$	$20.0^{+3.9}_{-3.2}$
2317	$1.16^{+0.11}_{-0.10}$	$0.56^{+0.02}_{-0.02}$	$16.8^{+3.7}_{-3.0}$
2318	$0.72^{+0.24}_{-0.23}$	$0.57^{+0.03}_{-0.02}$	$14.7^{+4.8}_{-3.5}$
2759	$0.71^{+0.07}_{-0.07}$	$0.58^{+0.01}_{-0.01}$	$12.7^{+1.1}_{-1.0}$
3514	$1.20^{+0.21}_{-0.19}$	$0.53^{+0.04}_{-0.04}$	$10.7^{+5.3}_{-3.3}$
3515	$1.03^{+0.21}_{-0.19}$	$0.57^{+0.04}_{-0.04}$	$6.5^{+3.1}_{-2.0}$
3516	$1.01^{+0.22}_{-0.20}$	$0.55^{+0.04}_{-0.04}$	$7.0^{+3.8}_{-2.3}$
3517	$1.03^{+0.22}_{-0.19}$	$0.53^{+0.04}_{-0.04}$	$8.43^{+4.6}_{-2.8}$
4596	$1.01^{+0.22}_{-0.19}$	$0.56^{+0.05}_{-0.04}$	$6.6^{+3.5}_{-2.2}$
4597	$1.27^{+0.33}_{-0.28}$	$0.51^{+0.05}_{-0.05}$	$8.7^{+7.5}_{-3.7}$
4598	$1.14^{+0.31}_{-0.26}$	$0.53^{+0.05}_{-0.05}$	$7.0^{+5.1}_{-2.8}$
4599	$1.08^{+0.31}_{-0.26}$	$0.52^{+0.05}_{-0.05}$	$7.2^{+5.7}_{-2.9}$
5592	$1.03^{+0.21}_{-0.19}$	$0.53^{+0.04}_{-0.03}$	$4.3^{+2.1}_{-1.3}$
5593	$1.22^{+0.22}_{-0.20}$	$0.52^{+0.03}_{-0.03}$	$5.6^{+2.7}_{-1.7}$
5594	$0.86^{+0.28}_{-0.24}$	$0.52^{+0.04}_{-0.04}$	$2.7^{+1.9}_{-1.0}$
5595	$1.35^{+0.24}_{-0.22}$	$0.50^{+0.03}_{-0.03}$	$7.7^{+4.0}_{-2.5}$

Table 4.2: Fit parameters for the single blackbody model, simultaneous fit for the 20 listed spectra. All the listed errors are at 1σ confidence level. For more details and a discussion see text.

flux. Therefore I performed a double blackbody fit to the 20 spectra, with only the warm temperature allowed to vary. The choice of the temperature instead of the normalization was discussed in section 3.3, and was essentially motivated by the fact that, when taken alone, the temperature could model better than the normalization the long term variations of the spectra. Moreover, in view of the flux decay it is also motivated by the strong dependence of the flux on the temperature ($F \sim T^4$): since the flux varies of a factor ~ 100 from the peak to the quiescent state, it is more likely that the small variations of temperature, that

Obs ID	Double Blackbody				
	n_H (10^{22} cm^{-2})	kT_1 (keV)	$Norm_1$	kT_2 (keV)	$Norm_2$
123		$0.26^{+0.01}_{-0.01}$		$0.58^{+0.04}_{-0.03}$	
1040		0.45		$0.89^{+0.06}_{-0.05}$	
2314		0.46		$0.89^{+0.05}_{-0.05}$	
2315		0.46		$0.85^{+0.05}_{-0.04}$	
2316		0.44		$0.87^{+0.05}_{-0.05}$	
2317		0.43		$0.85^{+0.05}_{-0.05}$	
2318		0.44		$0.80^{+0.05}_{-0.04}$	
2759		0.44		$0.82^{+0.04}_{-0.04}$	
3514		0.36		$0.79^{+0.06}_{-0.05}$	
3515	$1.53^{+0.05}_{-0.05}$	0.34	$52.8^{+6.5}_{-5.4}$	$0.78^{+0.06}_{-0.05}$	$1.02^{+0.40}_{-0.30}$
3516		0.34		$0.76^{+0.06}_{-0.05}$	
3517		0.35		$0.74^{+0.06}_{-0.05}$	
4596		0.34		$0.77^{+0.06}_{-0.05}$	
4597		0.32		$0.73^{+0.06}_{-0.05}$	
4598		0.32		$0.74^{+0.06}_{-0.05}$	
4599		0.33		$0.71^{+0.06}_{-0.05}$	
5592		0.30		$0.68^{+0.04}_{-0.04}$	
5593		0.30		$0.68^{+0.04}_{-0.04}$	
5594		0.28		$0.61^{+0.04}_{-0.03}$	
5595		0.30		$0.68^{+0.04}_{-0.04}$	

Table 4.3: Fit parameters for the double blackbody model, simultaneous fit for the 20 listed spectra. Only the temperatures are allowed to vary. All the listed errors are at 1σ confidence level. The errors of the warm temperatures are all the same, so I reported only the first one. For more details and a discussion see text.

emerge also from the single blackbody model, can reproduce the decay in flux rather than a much bigger variation of the normalization. This is tested later (see chapter 7) by the modelization of the flux decay.

The fit is not good: reduced $\chi^2 = 1.24$ for 1807 degrees of freedom, and the spectrum is not well modeled at high energies. Allowing both the temperatures to vary gives a good fit with reduced χ^2 =1.02 for 1788 degrees of freedom (F statistic value = 20.4844 and probability 1.68919e-63). For the fit parameters see table 4.3.

It is apparent just looking at the sequence of the temperatures how it increased dramatically after the outburst, and kept declining since then, but is still above the pre-burst level. This trend is visible for both the temperatures. For a comparison, see figure 4.1.

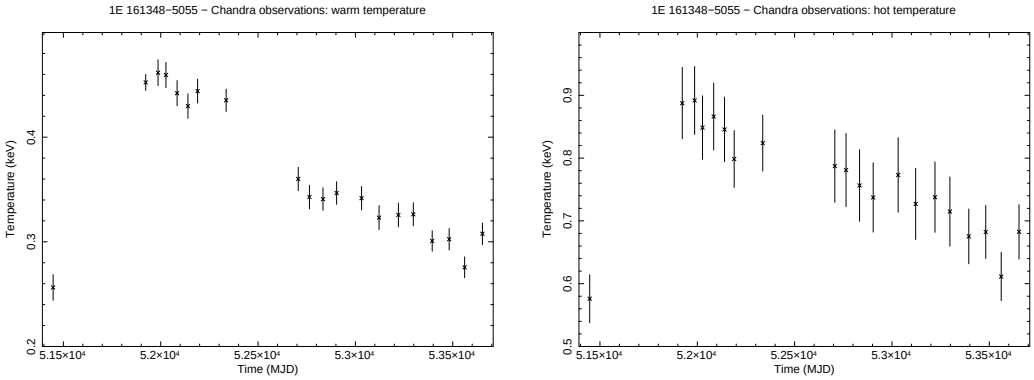

Figure 4.1: On the left: warm temperature vs time, on the right: hot temperature vs time. See text for further details.

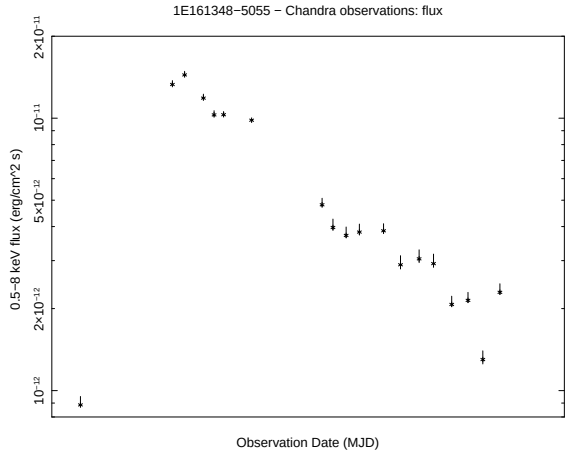

Figure 4.2: Fluxes of the 20 monitoring observations.

4. The final fit I performed is with a comptonized blackbody. This was suggested by the fact that a high energy tail always remains with a single blackbody model, but the bulk of the flux is provided by the warm blackbody. The comptonized blackbody can be physically motivated by the fact that the comptonization of photons over a population of electrons is quite common in high energy astrophysics sources. The advantage of having only one temperature for the underlying blackbody is that the fit is reasonable also when the statistic is even more reduced, as is the case with the Swift dataset (see chapter 5). In that particular situation it is impossible to fit the data with the double blackbody, even though we know that a higher energy component is necessary both from the XMM-Newton and Chandra data.

   In agreement with the previous double blackbody fit and the considerations made there, the blackbody temperature is the free parameter chosen to vary. This fit gives a good result: reduced $\chi^2 = 1.13$ for 1807 degrees of freedom, and no structurate residuals. The parameters are listed in table 4.4. The blackbody temperature, which is fully compatible with the warm temperature of the double blackbody fit, is declining, but the electronic temperature has the unlikely value of 182 keV. The probable explanation for this behavior is that the high energy photons are not enough yet to give a reasonable fit. Let's also consider that with the XMM-Newton data we were able to constrain all the parameters to physically meaning values, and the resulting blackbody temperatures are in agreement with those derived from the Chandra data (see chapter 7). At last, it must also be noted that the model is almost insensitive to the electronic temperature: being it very close to the hard limit of the parameter (200 keV), I tried some fit with different values, for example those resulting from the fit to the XMM-Newton data, or the Swift data. The other parameters do not vary, and so does the reduced χ^2 of the fit. Thus the value reported in table 4.4 has to be regarded as purely indicative.

4.4 Observation 970

The first attempt to fit observation 970 together with the other 20 used to monitor the flux of 1E 161348-5055 showed, as expected, that the spectrum of the high state is radically different from that of the following observations. As an example see figure 4.3, where I plotted the observation 1040 and 970 spectrum, with the comptonized blackbody model of 1040 multiplied by a constant free to vary for 970. The result is remarkable: even when compared to the immediately following observation, the spectrum of obs. 970 is definitely softer.

Obs ID	Comptonized Blackbody					
	n_H	kT	kTe	tau	Norm	Flux (erg/cm^2 s)
123		$0.287^{+0.004}_{-0.007}$				$8.9^{+0.7}_{-0.2} \times 10^{-13}$
1040		$0.484^{+0.005}_{-0.013}$				$1.33^{+0.04}_{-0.01} \times 10^{-11}$
2314		$0.492^{+0.007}_{-0.013}$				$1.44^{+0.04}_{-0.02} \times 10^{-11}$
2315		$0.485^{+0.008}_{-0.013}$				$1.34^{+0.04}_{-0.02} \times 10^{-11}$
2316		$0.473^{+0.007}_{-0.013}$				$1.18^{+0.04}_{-0.01} \times 10^{-11}$
2317		$0.460^{+0.007}_{-0.012}$				$1.03^{+0.03}_{-0.01} \times 10^{-11}$
2318		$0.473^{+0.005}_{-0.012}$				$1.03^{+0.03}_{-0.01} \times 10^{-11}$
2759		$0.469^{+0.006}_{-0.012}$				$9.83^{+0.09}_{-0.03} \times 10^{-12}$
3514	$1.54^{+0.04}_{-0.04}$	$0.395^{+0.006}_{-0.011}$	$182.3^{+18.6}_{-77.6}$	$0.16^{+0.04}_{-0.01}$	$56.0^{+9.7}_{-5.0}$	$4.8^{+0.3}_{-0.1} \times 10^{-12}$
3515		$0.380^{+0.007}_{-0.010}$				$3.9^{+0.3}_{-0.1} \times 10^{-12}$
3516		$0.375^{+0.006}_{-0.010}$				$3.7^{+0.3}_{-0.1} \times 10^{-12}$
3517		$0.377^{+0.007}_{-0.010}$				$3.8^{+0.3}_{-0.1} \times 10^{-12}$
4596		$0.378^{+0.006}_{-0.010}$				$3.9^{+0.2}_{-0.1} \times 10^{-12}$
4597		$0.357^{+0.007}_{-0.010}$				$2.9^{+0.2}_{-0.1} \times 10^{-12}$
4598		$0.361^{+0.007}_{-0.010}$				$3.0^{+0.2}_{-0.1} \times 10^{-12}$
4599		$0.358^{+0.007}_{-0.010}$				$2.9^{+0.2}_{-0.1} \times 10^{-12}$
5592		$0.335^{+0.005}_{-0.008}$				$2.07^{+0.15}_{-0.03} \times 10^{-12}$
5593		$0.337^{+0.005}_{-0.008}$				$2.14^{+0.15}_{-0.04} \times 10^{-12}$
5594		$0.306^{+0.005}_{-0.008}$				$1.30^{+0.10}_{-0.05} \times 10^{-12}$
5595		$0.341^{+0.006}_{-0.009}$				$2.30^{+0.17}_{-0.04} \times 10^{-12}$

Table 4.4: Fit parameters for the comptonized blackbody model, simultaneous fit for the 20 listed spectra. All the listed errors are at 1σ confidence level, and if not specified they are the same within the column. The hydrogen column is in $10^{22} cm^{-2}$ units and the temperatures are in keV. For more details and a discussion see text.

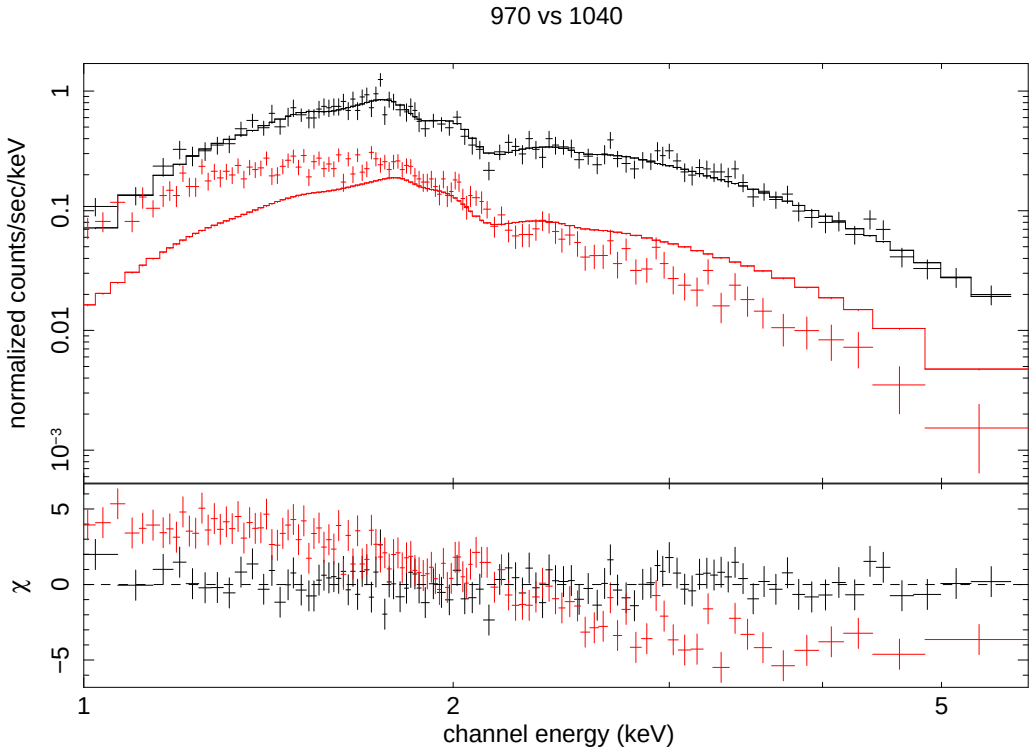

Figure 4.3: Spectra of observations 970 and 1040 for comparison. Upper panel: the spectra; lower panel: residuals. Both spectra were fitted to the model of observation 1040, with an overall normalization constant free to vary. It is evident how the observation 970 (peak) spectrum is softer than the spectrum of the first monitoring observation (in 2000).

Pile-up

As mentioned at the beginning of the chapter, this observation was severely affected by pile-up: the source in its highest state had such high luminosity that two or more photons arrive within the same detector pixel within a single ACIS frame integration time. For this reason they are detected as a single event, whose energy is approximately the sum of the pile-upped photons energy. If the summed energy of the piled event exceeds the on-board spacecraft threshold (typically 15 keV), it is rejected by the spacecraft software. For sufficiently bright sources, this can lead to a visible "hole" in the source image. This is because the count rate is sufficiently high that most piled events at the center of the PSF exceed the threshold energy and/or are assigned bad grades[4], so

[4]The grade of an event is a measure of which and how many pixels on the CCD are involved in the event. In fact, during the first step in the algorithm for detecting X-ray events, the on-board processing examines every pixel in the full CCD image and selects as events regions with bias-subtracted pixel values that both exceed the event threshold and are greater than all of the touching or neighboring pixels (i.e., a local maximum). The surrounding 3×3 neighboring pixels are then compared to the bias-subtracted split-event

they are filtered out in data processing.

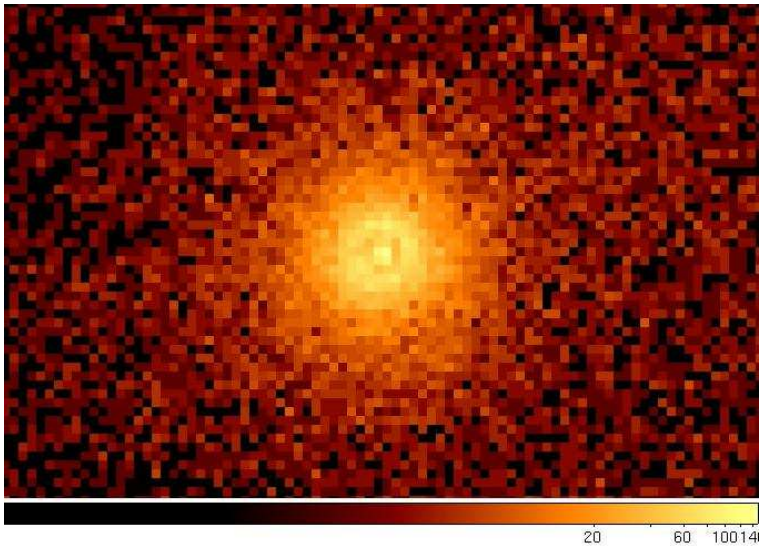

Figure 4.4: A zoom of the ACIS field of view in observation 970 to show the core of the PSF for the source. The hole due to pileup is clearly visible.

As can be seen from figure 4.4, this is te case for 1E 161348-5055. Pile-up represents a loss of information from the events. This information can be "recovered" up to a certain degree, but any corrections, however, are necessarily imperfect. This is why the errors on the derived flux are, to some extent, big.

The traditional way to overcome this problem is extracting the events from a region which is not affected by pile-up, namely an annulus that cuts out the center of the PSF. While this is straightforward with other satellites' software, for Chandra it requires some precautions: as described by Tsujimoto in the website cited before, the tool MKARF in the CIAO package assumes that the extraction region is large enough to contain the entire PSF. Moreover, as is clear from figure 4.5, the different dependence on the energy of the radius of the PSF means that the spectrum is distorted when changing from a circular to an annular region. It is possible to extract the right ARF for the region considered by means of the ChaRT and MARX simulators.

I followed the detailed instructions provided, first with sample spectra I created and then with the 970 observation spectrum. With the sample spectra and the generated ARF I was able to reproduce the original fit parameters within 3%. Seeing this good result, I went on to analyze the source spectrum on its own.

threshold; those that are above the threshold establish the pixel pattern. On the basis of this pattern, the event is assigned a grade. Depending on the grade, the data are then included in the telemetry. The grade of an event is thus a code that identifies which pixels, within the 3×3 pixel island centered on the local charge maximum, are above certain amplitude thresholds.

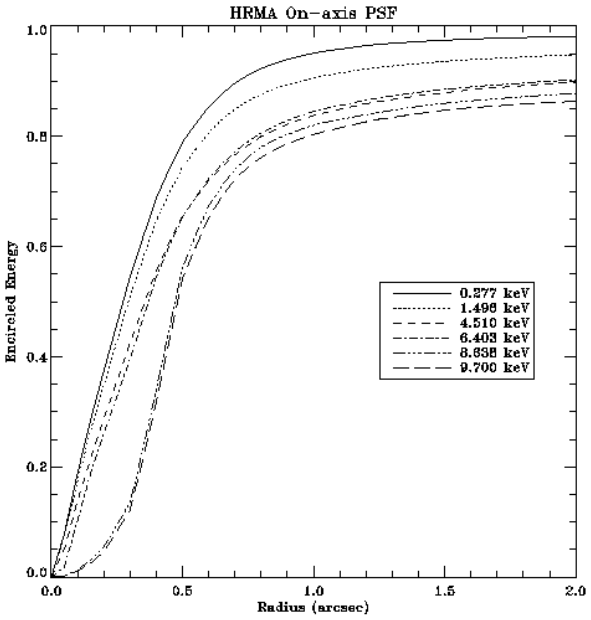

Figure 4.5: The Fractional encircled energy as a function of angular radius, calculated for an on-axis point source, at selected X-ray energies. The curves are the combined response and centered at the common focus of the full HRMA, i.e. four nested mirror pairs. For higher energies (8.638 keV and 9.700 keV), the curves are broadened at the bottom. This is because the focus of higher energies does not coincide with the the HRMA common focus, but is offset by about $0.2''$, due to a slight tilt of the HRMA mirror pair 6.

The parameters of the models I used for the fit are displayed in table 4.5. They are in good agreement with each other for the main parameters (hydrogen column and the warm temperature) and also for the flux. All the listed errors are at 1σ confidence level.

	n_H	kT_1	$Norm_1$	kT_2	$Norm_2$	Flux
1 BB	$0.87^{+0.08}_{-0.08}$	$0.42^{+0.02}_{-0.02}$	516^{+131}_{-99}	-	-	$7.53^{+0.07}_{-0.24}$
2 BB	$0.94^{+0.12}_{-0.10}$	$0.40^{+0.03}_{-0.04}$	693^{+414}_{-201}	$1.28^{198.7}_{-0.7}$	$0.45^{11.7}_{-0.45}$	$8.01^{+0.12}_{-0.30}$
CompBB	$1.00^{+0.10}_{-0.10}$	$0.36^{+0.02}_{-0.02}$	2303^{+781}_{-610}	-	-	$7.75^{+0.08}_{-0.28}$

Table 4.5: Fit parameters for the models applied on obs 970 (the peak observation). The hydrogen column is in $10^{22} cm^{-2}$ units, the temperatures are in keV and all fluxes are in 10^{-11} erg/cm^2 s.

From a statistical point of view, the single blackbody provides a very good fit: $\chi^2 = 99.748$ for 111 degrees of freedom, that corresponds to a reduced χ^2 of 0.90. The double blackbody model is valid as well, with a $\chi^2/\mathrm{dof} = 93.023/109$

= 0.85, but must be preferred since the second component is statistically significant at 94% level. Moving on to the comptonized blackbody model, it must be noticed that - as it was the case for the monitoring observations - it is not sensitive at all to the electronic temperature. For this reason I froze it and the resulting fit is almost as good as the double blackbody: reduced $\chi^2 = 0.86$.

As a last test, I checked whether the spectra were compatible with the hydrogen column found in the simultaneous fit of the 20 observations: for the single blackbody the fit is bad, while for the other two cases the fit is not as good as before, but still a good fit. See table 4.6 for all the values.

	kT_1 (keV)	$Norm_1$	kT_2 (keV)	$Norm_2$	Flux	χ^2_{red}
2 BB	$0.136^{+0.003}_{-0.003}$	$2.9^{24.2}_{-2.5} \times 10^5$	$0.38^{+0.02}_{-0.01}$	$1.01^{+0.01}_{-0.15} \times 10^3$	$7.44^{+0.12}_{-0.21}$	1.00
CompBB	$0.22^{+0.01}_{-0.01}$	$4.9^{+1.4}_{-1.0} \times 10^4$	-	-	$7.83^{+0.16}_{-0.16}$	1.10

Table 4.6: Fit parameters when the hydrogen column is forced to be the same as in the monitoring observations, that is $n_H = 1.52 \times 10^{22}$ cm^{-2} for the double blackbody, and $n_H = 1.54 \times 10^{22}$ cm^{-2} for the comptonized blackbody. The fluxes are in 10^{-11} erg/cm^2 s units.

In such events as outbursts, the spectrum at the peak of the emission is generally different from that of the following afterglow, because the emitting mechanisms are physically different. As can be seen from table 4.6, when forcing the n_H to the afterglow one would expect the temperature to be much higher than 0.5 keV if the observation is still monitoring the decay. In our case, instead, it is lower. This hints to the observation of a different emission mechanism, that is not the afterglow. We are allowed, then, to perform a separate fit for this observation, and eventually to use different models.

4.5 Observation 7619

Observation 7619 is a long observation (78 ks) that was carried on in July 2007 in order to have a dataset long enough to span a three periods of the source, in between the Swift monitoring campaign.

The instrument onboard Chandra that was used is the High Resolution Chamber that, as said before, provides excellent timing and spacial resolution, but no energy information on the collected photons. For this reason it was not used for the spectral analysis, but there is a way to obtain an estimate on the flux of 1E 161348-5055 in obs. ID 7619 by means of Pimms.

Pimms (or its online version WebPimms) is a tool developed in order to convert fluxes or count rates between instruments, keeping into account the responses of the different detectors. It performs a simulation, given a spectral model and a specified energy range, of how a source visible by an instrument

would be seen by a different instrument, under the same conditions. Pimms is then able to derive a flux of an observation, provided the count rate of the source, the instrument that carried on the observation and a spectral model. This latter request was the hardest to fulfil, because Pimms only allows for a combination of blackbodies and powerlaws, while the preferred model for 1E 161348-5055 is the comptonized blackbody (for all the Swift observations as well, see chapter 5). Moreover, the source is in its low state at the moment of the observation, which means that the statistic of the spectra of the Swift observations is poor, and choosing the double blackbody model is not possible. In fact, it is impossible to constrain the hot temperature and its normalization.

An important consideration helped to solve the problem: the flux of the Swift observations surrounding obs. 7619 is low, almost but not yet at the quiescence level. It seemed logical that the spectrum of the last Chandra observation could resemble the spectra of the last Chandra monitoring observations, namely the 04 and 05. Then the choice I made was to use a single blackbody spectrum. The flux I obtained is 1.5 $\times 10^{-12}$ erg/cm^2 s, and its associate conservative error is 2.3 $\times 10^{-13}$ erg/cm^2 s. It is still higher than the pre-burst flux, but approaching. It is also (see chapter 5) close to the average flux of the swift observations.

4.6 Considerations on fluxes

Already from figure 4.2 the decay in flux is apparent at the first glimpse: only the monitoring observations and the pre-burst level are shown, but they are enough to hint a powerlaw decay in time.

Considering, for consistency, fluxes all coming from the comptonized blackbody model, from the quiescence flux (8.9 $\times 10^{-13}$ erg/cm^2 s, see table 4.4, obs. ID 123) to the peak flux (7.75 $\times 10^{-11}$ erg/cm^2 s, see table 4.5) there is a huge increase of a factor 87! We can only set upper limits to the peak energy of the outburst, because its discovery was absolutely fortuitous and happened with obs. 970. The RXTE All Sky Monitor did not detect any burst coming from 1E 161348-5055, nor any enhancement of flux. Its sensitivity is 30 mCrab (7.2 $\times 10^{-10}$ erg/cm^2 s)[5], it will be used to establish a lower limit to the onset time of the burst, together with the model for the decay, but nothing more can be derived from it.

The absence of a bursting phase, instead, could give insight or put limits on the onset mechanism. This will be treated in chapter 7.

For what concerns the latest Chandra observation 7619, the flux I was able to derive is a reliable estimate, since it also falls in the middle of the swift flux curve (see chapter 5). It is good to remember that the swift observations are even shorter than the Chandra, they sample the highly modulated lightcurve of 1E 161348-5055. In contrast, obs. 7619 is very long, and the flux value

[5]See, for example, http://heasarc.gsfc.nasa.gov/docs/xte/rxte.html

derived must be intended as a flux averaged on the whole period of the source. Thus its agreement with the Swift fluxes is a further confirmation that the estimate is reliable.

The obs. 7619 flux is still above the pre-burst level of a factor $\sim$2.

Chapter 5

Swift data

This is the final chapter for what concerns the spectral analysis of 1E 161348-5055: all the *Swift* monitoring observations are presented and carefully analyzed. In section 5.1 and 5.2 they are listed and data reduction is explained, in section 5.3 instead the results of the spectral analysis of all the available observations are summarized. At the end of this section the fluxes are calculated and a comparison with the last *Chandra* observations is made.

5.1 Observations

The *Swift* monitoring campaign of 1E 161348-5055 is still continuing. As of August 30, 2008, there exist 22 observations.

All of them were made after the last Chandra monitoring observations, from 2006 on. They last several minutes, not enough to cover one whole period of the source. Of the dataset available for each observations, only the Photon Counting mode event file was used because two-dimensional spatial resolution is needed for the spectral analysis. At variance with some Chandra observations in continuous clocking mode, in the *Swift* windowed timing event file the contamination due to the supernova remnant is too important and the observation is too short for the fit to succeed. This is the case of the first *Swift* monitoring observations (obs. id 00035312001 and 00035312002), when the XRT was automatically switched from Photon Counting mode to Windowed Timing. It did not happen again after.

5.2 Data processing

All the data were processed with the HEASOFT, version 6.4, and by means of the standard analysis threads[1]. For each observation an image was created, and a region for the source data filtering was selected. This was not trivial, for two

[1]See for example www.heasarc.gsfc.nasa.gov/docs/swift/analysis/xrt_swguide_v1_2.pdf.

Obs ID	Start time (local)	Exposure Time (s)	Notes
00030389001	2006-04-11T05:09:03	4326	-
00030389002	2006-08-30T15:25:13	2510	-
00030389003	2006-09-03T05:52:51	2979	-
00035312001	2006-03-10T11:57:22	6484 (2292)[a]	-
00035312002	2007-02-08T05:00:52	1534 (232)	insuff stat
00035312004	2007-02-12T01:38:51	1979	-
00035312005	2007-03-06T04:05:36	2127	-
00035312006	2007-03-30T19:30:26	677	insuff stat
00035312007	2007-04-03T21:05:41	1301	-
00035312008	2007-05-06T20:07:51	2248	-
00035312009	2007-06-07T03:38:11	2405	-
00035312010	2007-07-08T13:31:47	3089	-
00035312011	2007-08-07T09:38:50	2472	-
00035312012	2007-10-07T23:52:14	2247	no cl.evt
00035312013	2008-02-07T18:18:26	1051	deadcolumn
00035312014	2008-02-19T18:12:08	795	-
00035312015	2008-03-08T03:55:36	2292	-
00035312016	2008-04-07T19:40:34	1926	-
00035312018	2008-05-10T11:43:18	3057	-
00035312020	2008-06-11T03:21:13	1899	-
00035312021	2008-07-07T12:33:22	2188	-
00035312022	2008-08-07T07:06:51	2303	-

(a) XRT total exposure; in brackets, net photon counting mode exposure. For this observation and the next, XRT was switched to windowed timing mode, thus loosing the spatial resolution needed to perform a spectral analysis.

Table 5.1: Net exposure time of the *Swift* observations.

reasons: first of all, 1E 161348-5055 is in the low state, and the modulations in flux within the period are so big (a factor ~ 3) that if an observation happens to be sampling the minimum of the intensity, the source is barely visible over the supernova remnant. Second, the XRT CCDs are affected by two badcolumns and several badpixels. In the unlucky case in which the source falls on the badcolumn, it is impossible to find the source position, and the majority of the counts is lost on the badcolumn itself, even when correcting with the exposure map (see, as an example, figure 5.1

In those cases (listed in table 5.1 as badcolumn or insufficient statistic in the "Notes" entry) I tried anyway to extract a spectrum to be used in the simultaneous fit, but the statistic was so poor that none of the parameters of the fit had a reasonable result. Moreover, those spectra compromised the whole fit itself, giving rise to pegging parameters. For this reason I decided to only use the poor statistic observations for the timing analysis in chapter 6,

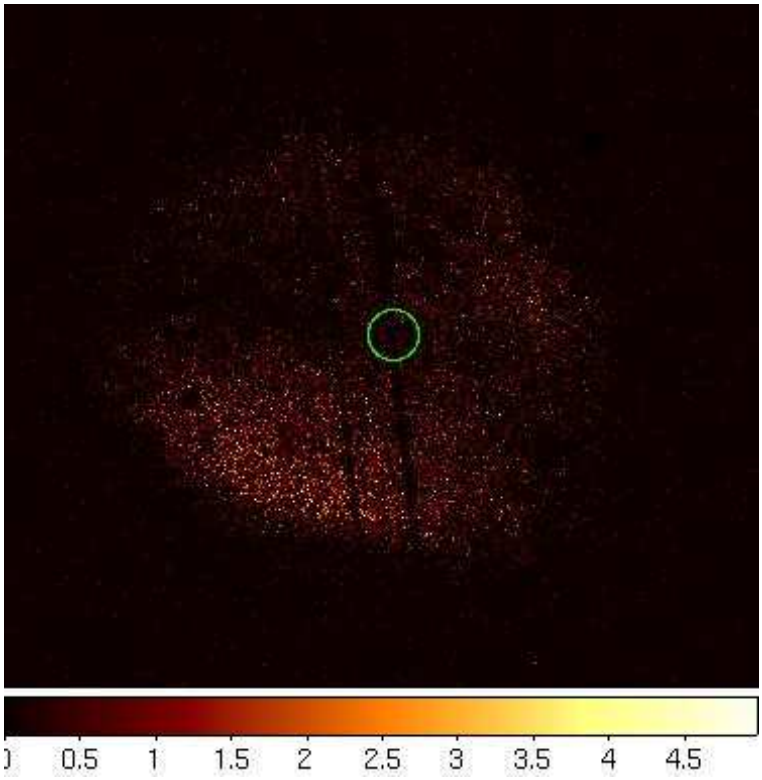

Figure 5.1: XRT field of view of observation no. 00035312013: the green circle marks the 30 arcsec circular region that should contain the source. The two deadcolumns that affect the XRT CCDs are visible, one of them overlapping the position of the point source.

and not for the spectral analysis.

The extraction region I used is a circular region, centered on the peak of the emission and with a radius of 30 arcsec, for all the observations. The response matrix used are the latest provided by the calibration database. For each observations then I generated the exposure map with the XRTEXPOMAP tool and used it to correct the ancillary files created with the XRTMKARF tool.

All the dataset were then barycentered by means of the standard tools for the timing analysis.

5.3 Spectral analysis

The *Swift* observations are useful for monitoring the flux evolution of 1E 161348-5055, but they are too short to provide enough photons to be fitted independently. For this reason, in the spectral analysis I had to exploit to the utmost the knowledge of 1E 161348-5055 acquired through XMM-Newton and Chandra.

1. The extraction region used for the *Swift* XRT observations is just the same as the one used for the XMM-Newton data analysis. This was encouraged also by the technical characteristics of the detectors: the *Swift* focal plane CCDs are the same as the XMM-Newton EPIC CCDs, and moreover the mirrors are built in a similar way as those of *XMM-Newton*, and so have similar PSFs and sensitivity. The contamination of the supernova remnant is expected to be the same, but in this situation it turns out to be helpful: only a few years passed between the 2005 XMM-Newton observation and the last *Swift* observation, a time interval that is so short compared to the SNR evolution time that allows to use the same spectral parameters found in the XMM-Newton data analysis. In fact only the normalization, temperature and hydrogen column of the supernova remnant model were left free in the fit, to account for the intrinsic differences between the detectors. All the other parameters, namely the abundances, are frozen to the XMM-Newton values.

2. For a more reliable evaluation of the supernova remnant parameters, I merged the *Swift* monitoring observations from obs. id 00035312001 to 00035312020 (including those I left out in the simultaneous fit), extracted the source spectrum, response file, ancillary file as for the individual observations, and fitted the resulting spectrum with the model described above. The best fit parameters for the supernova remnant are listed in table 5.2. As one can see, they are fully compatible with the XMM-Newton parameters. The supernova remnant was fitted simultaneously with a comptonized blackbody model for the source, whose parameters are reported below in table 5.3. The hydrogen column value comes from the Chandra monitoring observations.

3. For what concerns the source spectrum, again the statistic was so poor that it was necessary to constrain the majority of parameters with the previous analysis. As explained in chapter 4, the most reliable hydrogen column estimate is that from the Chandra observations, because they are minimally contaminated by the supernova remnant. The preferred models for the source (for a discussion of the spectral models, see par. 3.3) are a double blackbody and a comptonized blackbody, but due to the small amount of photons available, most of the parameters are derived from the XMM-Newton or Chandra analysis. I chose to let the warm blackbody temperature alone vary, because two free parameters per spectrum proved to be too much for the fit to converge. The spectral results are listed in tables 5.5 and 5.4.

4. A few comments on the fits: for the double blackbody model, it is clear from table 5.5 that the only free parameter is poorly constrained: many of the warm temperatures are consistent with zero. Nonetheless, their values are somehow correct: both the hot temperature and the warm temperatures are consistent with those of the last Chandra monitoring

Parameter	Value
N_h	$0.64^{+0.05}_{-0.03} \times 10^{22}$ cm^{-2}
kT	$0.62^{+0.04}_{-0.05}$ keV
H	1
He	4
C	0
N	0
O	1.22
Ne	0.51
Mg	1
Si	1.48
S	1.61
Ar	1
Ca	0
Fe	0.71
Ni	0
Tau	2.54×10^{11}
Redshift	0
Norm	$4.5^{+0.7}_{-0.6} \times 10^{-3}$

Table 5.2: Best fit parameters of the SNR for the merged *Swift* observations in the source extraction region. All the errors are at 1σ CL.

Comptonized Blackbody	
Parameter	Value
n_H (10^{22} cm^{-2})	1.54
kT (keV)	$0.29^{+0.04}_{-0.03}$
kTe (keV)	$2.28^{+0.10}_{-0.09}$
tau	$2.45^{+0.05}_{-0.05}$
Norm	51^{+52}_{-24}

Table 5.3: Fit parameters for the source spectrum extracted from the merged event file.

observations. The fit is quite good ($\chi^2 = 94.17$ for 85 degrees of freedom, reduced $\chi^2 = 1.11$); it improves if I let the normalization of the warm blackbody free, but in that case it is impossible to derive errors for the free parameters.

The comptonized blackbody model fit, instead, was insensitive to the electronic temperature and optical depth of the plasma, so I froze them to values I found in the fit to source spectrum from the merged *Swift* observations (See table 5.3). The fit is as good as the fit with the double blackbody: $\chi^2 = 94.19$ for 86 degrees of freedom, which means that its reduced χ^2 is equal to 1.095. This further confirms the goodness of the choices made for the spectral analysis.

Obs ID	Source	Comptonized Blackbody					
	Counts	n_H	kT	kTe	tau	Norm	Flux
00030389001	437	1.54	$0.31^{-0.01}_{+0.01}$	2.28	2.45	51	$1.9^{+0.1}_{-0.1} \times 10^{-12}$
00030389002	152		$0.30^{-0.02}_{+0.02}$				$1.7^{+0.1}_{-0.1} \times 10^{-12}$
00030389003	152		$0.31^{-0.03}_{+0.02}$				$1.9^{+0.2}_{-0.2} \times 10^{-12}$
00035312001	217		$0.31^{-0.02}_{+0.01}$				$2.0^{+0.1}_{-0.1} \times 10^{-12}$
00035312004	184		$0.32^{-0.02}_{+0.01}$				$2.3^{+0.2}_{-0.2} \times 10^{-12}$
00035312005	153		$0.28^{-0.03}_{+0.02}$				$1.2^{+0.1}_{-0.1} \times 10^{-12}$
00035312007	61		$0.27^{-0.08}_{+0.04}$				$1.0^{+0.1}_{-0.3} \times 10^{-12}$
00035312008	180		$0.30^{-0.02}_{+0.02}$				$1.6^{+0.1}_{-0.1} \times 10^{-12}$
00035312009	187		$0.29^{-0.02}_{+0.02}$				$1.5^{+0.1}_{-0.1} \times 10^{-12}$
00035312010	275		$0.30^{-0.02}_{+0.01}$				$1.6^{+0.1}_{-0.1} \times 10^{-12}$
00035312011	245		$0.31^{-0.01}_{+0.01}$				$2.1^{+0.1}_{-0.1} \times 10^{-12}$
00035312014	30		$0.31^{-0.08}_{+0.04}$				$1.9^{+0.4}_{-0.5} \times 10^{-12}$
00035312015	185		$0.28^{-0.02}_{+0.02}$				$1.08^{+0.08}_{-0.09} \times 10^{-12}$
00035312016	120		$0.32^{-0.03}_{+0.02}$				$2.5^{+0.2}_{-0.2} \times 10^{-12}$
00035312018	184		$0.27^{-0.04}_{+0.02}$				$1.0^{+0.1}_{-0.1} \times 10^{-12}$
00035312020	122		$0.28^{-0.03}_{+0.02}$				$1.2^{+0.1}_{-0.1} \times 10^{-12}$
00035312021	152		$0.32^{-0.02}_{+0.02}$				$2.4^{+0.2}_{-0.2} \times 10^{-12}$
00035312022	154		$0.25^{-0.04}_{+0.02}$				$0.69^{+0.10}_{-0.06} \times 10^{-12}$

Table 5.4: Fit parameters of the comptonized blackbody for 1E 161348-5055 in the *Swift* observations used for the spectral analysis. The hydrogen column is given in (10^{22} cm^{-2}) units, temperature is in keV and flux in erg/cm^2 s.

5. The flux values listed in table 5.4 are evaluated from the comptonized blackbody just described. A few words must be spent on the associated errors: to calculate the flux for the source, the model for the supernova remnant had to be erased first, but this prevented xspec12 from the computation of the errors. The numerical way that Xspec uses to derive

Obs ID	Comptonized Blackbody				
	n_H	kT	kTe	tau	Norm
00030389001	1.53	$0.30^{-0.02}_{+0.01}$	52.8	$0.67^{-0.02}_{+0.02}$	1.02
00030389002		$0.29^{-0.04}_{+0.02}$			
00030389003		$0.30^{-0.04}_{+0.02}$			
00035312001		$0.30^{-0.03}_{+0.02}$			
00035312004		$0.30^{-0.04}_{+0.02}$			
00035312005		$0.24^{-0.24}_{+0.05}$			
00035312007		$0.25^{-0.25}_{+0.05}$			
00035312008		$0.28^{-0.05}_{+0.03}$			
00035312009		$0.27^{-0.09}_{+0.03}$			
00035312010		$0.28^{-0.03}_{+0.02}$			
00035312011		$0.31^{-0.03}_{+0.02}$			
00035312014		$0.29^{-0.29}_{+0.05}$			
00035312015		$0.20^{-0.20}_{+0.06}$			
00035312016		$0.32^{-0.03}_{+0.02}$			
00035312018		$0.25^{-0.25}_{+0.03}$			
00035312020		$0.25^{-0.25}_{+0.04}$			
00035312021		$0.31^{-0.03}_{+0.02}$			
00035312022		$0.20^{-0.20}_{+0.06}$			

Table 5.5: Fit parameters of the comptonized blackbody for 1E 161348-5055 in the *Swift* observations used for the spectral analysis. The hydrogen column is given in (10^{22} cm^{-2}) units, temperature is in keV and flux in erg/cm^2 s. If no error is listed, the parameter was frozen to the Chandra value (see table 4.3)

the flux is this: it calculates the flux a default number of times using each time a different value (within the 1σ error) of the free parameters of the fit, and thus evaluates the confidence levels. Of course, if I erased a part of the model this procedure is not reliable any more, because the parameter values are not valid any more to reproduce the data.

It should be noted, though, that there is only one free parameter for each spectrum, which means that the relative error associated to the temperature can be propagated straightly to the flux, with one caveat. Due to the small amount of photons for the source spectra, the error

derived this way had to be compared with the statistical error associated to the number of counts: the error listed in table 5.4 is the maximum between the error coming from the temperature, and the poissonian error.

A very useful comparison can be done between table 5.4 and table 5.3: as explained before, the first one lists the properties of each observation, while the second, that lists the spectral parameters of the merged event file, can be regarded as the table of the mean values. There is a good agreement between the averaged parameters and the single parameters, which even more settles the reliability of the analysis.

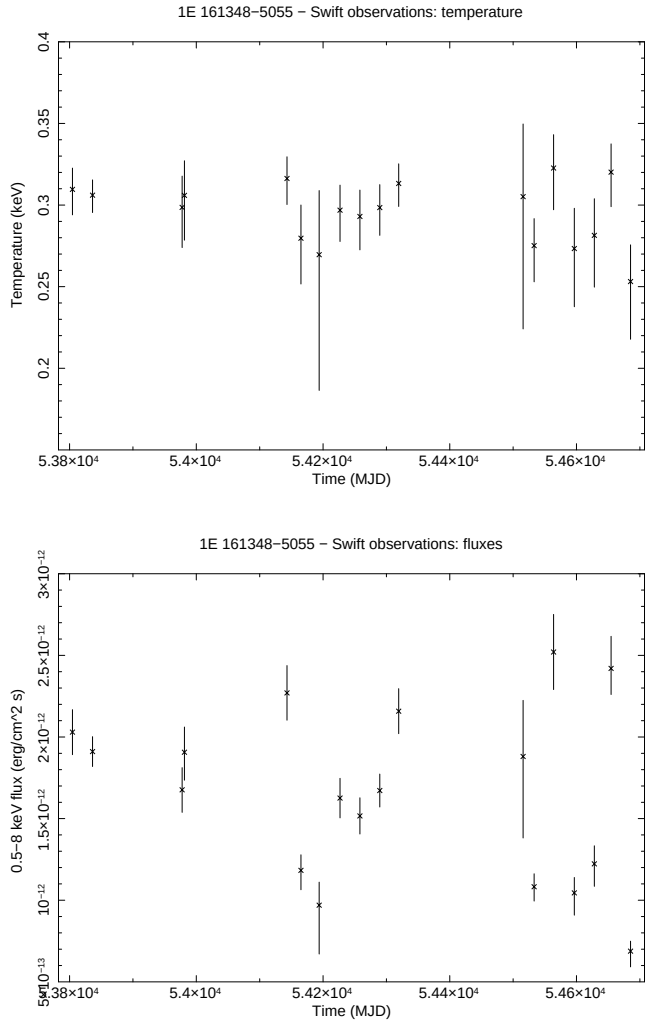

Figure 5.2: Top: temperature vs time; bottom: flux vs time. See text for further details.

Last, in figure 5.2 the graphics that show the behavior of the temperature (top) and flux (bottom) versus time are reported. The decay is not so marked as in the Chandra monitoring observations, which themselves, it is good to

remember, had almost reached the pre-outburst level (see also figure 4.2). If in the temperature vs time figure a slight decay is still visible, the flux points are very scattered, they do not follow a regular pattern. This is expected, since the modulation in flux during the period of 1E 161348-5055 is very strong (a factor $\sim$ 3 from minimum to maximum), and the more the flux is low, the more the modulation emerges.

Consider also, as a comparison, that the flux of the Chandra observation 7619 is 1.5×10^{-12} erg/cm^2 s: that observation is very long, thus the flux is an average over at least three complete periods, and it falls in the middle of the *Swift* points (see figure 5.3). This again supports the idea that the decline in flux is slowing down, but is still above the quiescence level.

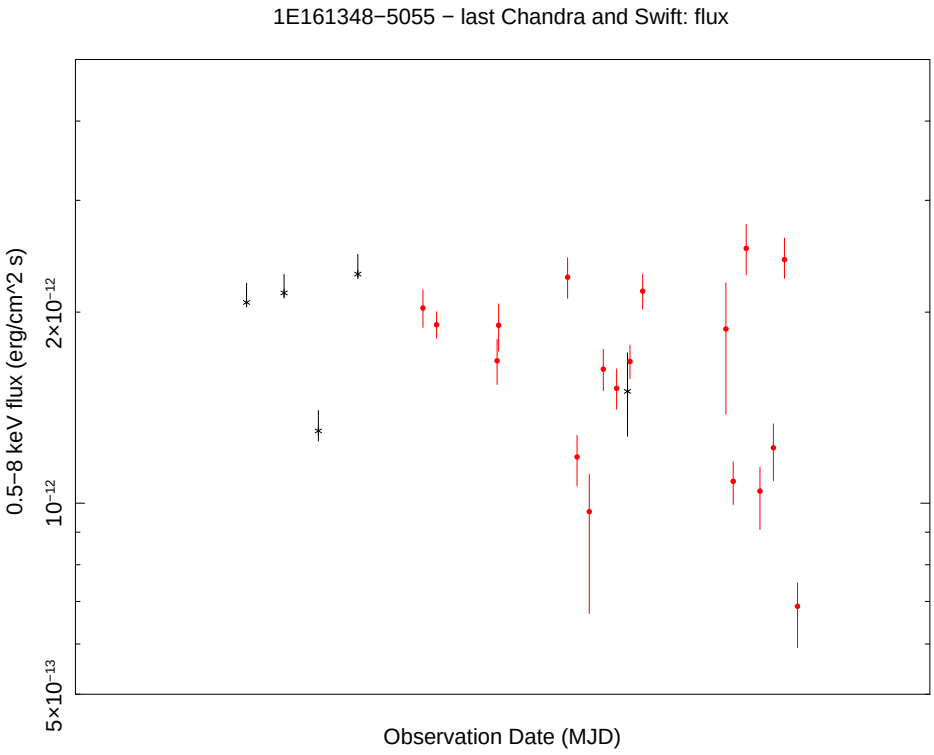

Figure 5.3: 0.5-8 keV flux of the *Chandra* observations 5592-95 (the last four monitoring observations, taken in 2005), the *Swift* observations and the last *Chandra* observation 7619 (made in 2007). See text for more details.

Chapter 6

Temporal analysis

In chapter 6 a thorough research of the temporal properties of 1E 161348-5055 is explained. After a preliminar analysis (section 6.1), the Rayleigh test is presented in section 6.2 and then used to derive a precise value for the period of the source (sections 6.2 itself, section 6.3 - 6.4). A research for temporal variability is also performed in section 6.4, and brief considerations are listed in section 6.5.

6.1 Preliminary analysis

As a first step for the temporal analysis of 1E 161348-5055, let's extract the lightcurves of the source from the XMM-Newton and longer Chandra observations, to see if any feature or variability is present. We already know that the source showed an undoubtable variability on an unusual long period (P $\simeq$ 6.67 $\pm$ 0.03 hr $\sim$ 24000 $\pm$ 100 s in the 2005 XMM-Newton observation [De Luca et al.(2006)]), but the error is not small enough to propagate it over a long baseline to look for period changes. For example, after only 20 cycles the error is 20000 s, of the same order as the period itself, and thus it is impossible to make any phase connection between observations that last more than a few hours.

It is useful anyway, even if we do not expect any particular difference from what is already known, to extract the period of 1E 161348-5055 from the Chandra 7619 lightcurve (shown in figure 6.1 together with the XMM-Newton 2005 observation). We used a constant plus sinusoidal model: the fit returns a constant of ~ 0.02 counts/s, and a sinusoidal whose period is 24000 ± 300 s, and amplitude 0.022 ± 0.002 s. Again, the error on the period is too long (even longer than that derived from the XMM-Newton 2005 observation) to permit extrapolations backward to the less recent observations.

One could think that by folding the older long lightcurves one could gain information on the period, but that is untrue: the lightcurves of the high state observations (2001 XMM-Newton observation and 2759 Chandra observation,

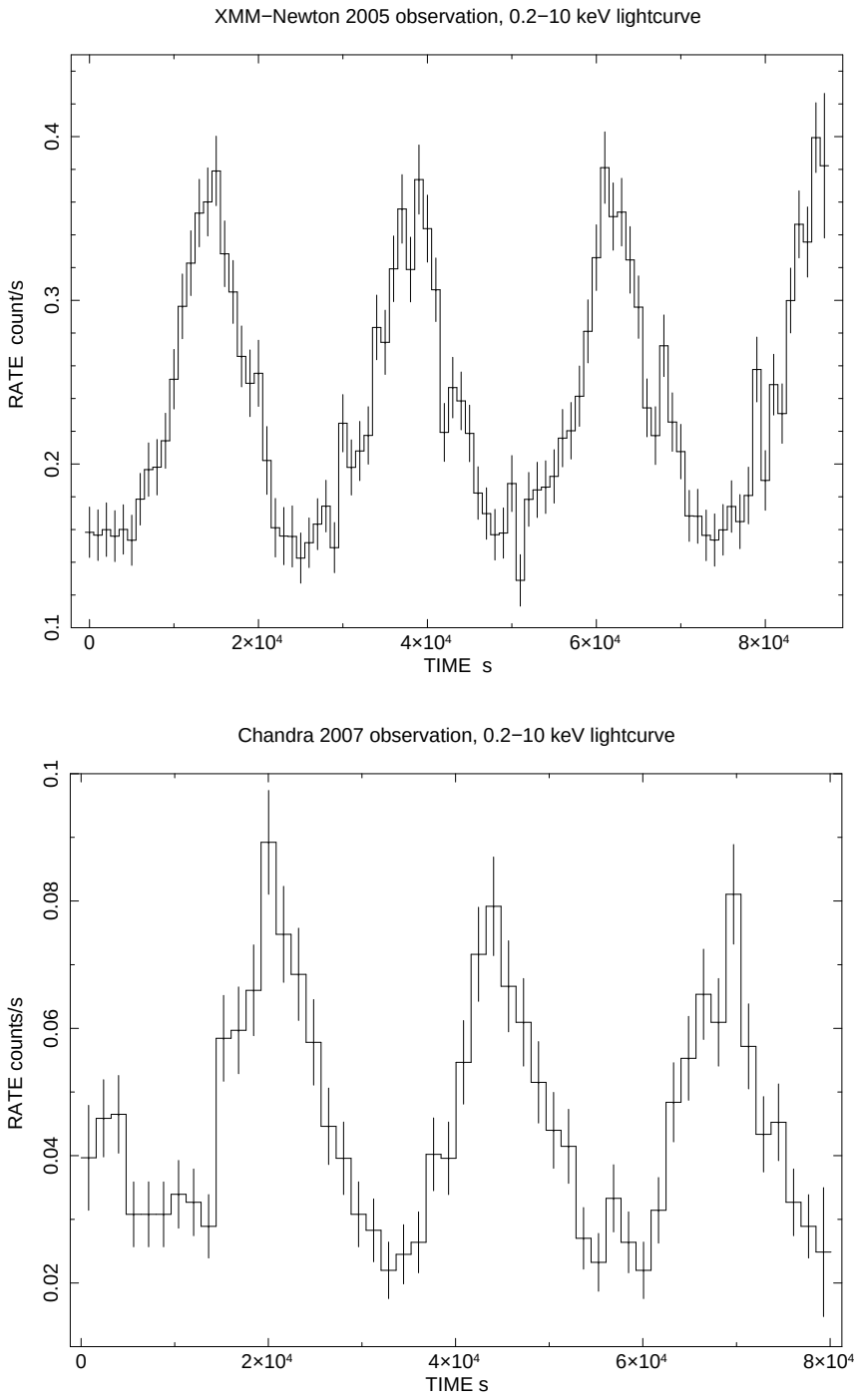

Figure 6.1: Unfolded background subtracted lightcurves of the XMM-Newton 2005 observation and Chandra 7619 observation (made in 2007), in the energy range 0.2-10 keV. The curves were rebinned with a temporal binning of 1000 s. The pulsation is clearly present in both observations, and has a smooth shape that did not show significant changes from 2005 to 2007.

see figure 6.2 for the lightcurve of the latter) are not as easy to interpret as the last XMM and Chandra observations were, since the shape of the lightcurve is not sinusoidal any more: it has a multi-peaked structure that do not even allow to associate clearly the smooth peak of the quiescent state with one of the peaks of the high state curves. Moreover, the gap between one long observation and the following long one is so big and the uncertainty on the period so large that several values of period are possible to connect the observations: namely, all those which cover the gap with an integer number of cycles, so that the peaks remain in phase. The folding technique moreover is not precise enough to determine accurately the period of 1E 161348-5055, because it depends on the assumptions made in the folding, e. g. the binning time, and it assumes as a first approximation a sinusoidal pulse shape to derive the period and its error.

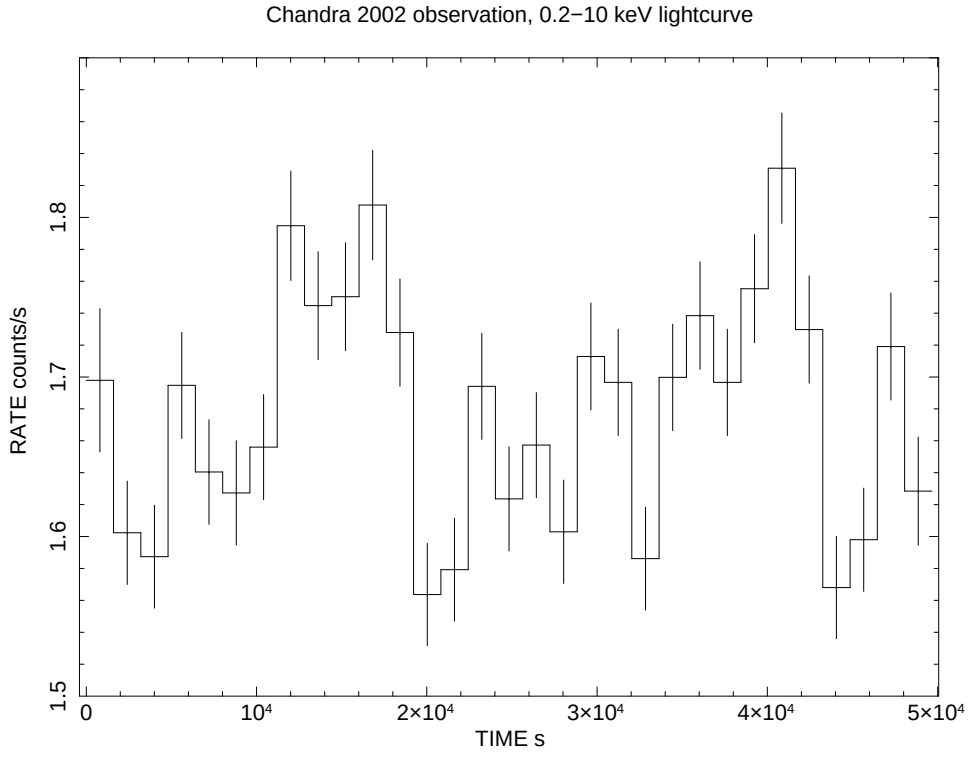

Figure 6.2: 0.2-10 keV unfolded lightcurve of the Chandra observation 2759 (made in 2002). The events were rebinned with a temporal bin of 1000 s. The shape is not any more nearly sinusoidal as it is in the quiescent state observations, but shows a multi-peaked structure.

It was necessary then to switch to a different technique, namely the Rayleigh test, that instead of looking for a period from the lightcurve, it searches it from the time of arrivals of the single photons.

6.2 Rayleigh test

The Rayleigh test (see for example [Buccheri et al.(1983)]) is a statistical test based on the analysis of the photons arrival time (Time of Arrival, TOA), after they are transformed to Solar System Barycenter time.

It needs an initial estimate of the period of the source (and eventually a period derivative), as accurate as possible, in order to associate to each photon arrival time a residual phase, whose value is usually reduced to the range 0-1 by the relation:

$$\phi_i = \text{fractional part of } (\nu \Delta t_i + \frac{1}{2} \dot{\nu} (\Delta t_i)^2 + \frac{1}{6} \ddot{\nu} (\Delta t_i)^3 + \dots), \tag{6.1}$$

where $i = 1 \dots N$ spans the total number of photons for the source, and ν is the source frequency. If with t_0 we indicate the start epoch of the observation from which the most reliable estimate of the period was made, then $\Delta t_i = t_i - t_0$ is the arrival time of the i-th photon, with respect to the start epoch.

The N phase values obtained with relation 6.1 are then Fourier analyzed by means of the statistical variable Z_n^2, defined as follows:

$$Z_n^2 = \frac{2}{N} \sum_{k=1}^{n} \left(\sum_{i=1}^{N} \cos k\phi_i \right)^2 + \left(\sum_{i=1}^{N} \sin k\phi_i \right)^2, \tag{6.2}$$

where n is the number of harmonics.

The variable Z_n^2 has a probability density function equal to that of a χ^2 with $2n$ degrees of freedom [Buccheri et al.(1977)]. In the absence of pulsations, if we choose 2 harmonics the expectation value of Z_2^2 is 4; when a periodic signal is present, due to Np "pulsed" photons, the contribution to Z_2^2 in terms of sigmas above the average is given by [Buccheri et al.(1977)]

$$n_\sigma = \frac{(Np)^2(\theta)}{N(\theta)} C, \tag{6.3}$$

where θ is the acceptance angle from the source direction, and the constant C depends on the duty cycle of the pulsations. So, the higher is the deviation of the value of Z_n^2 from its mean $2n$, the higher is the probability of pulsations with the corresponding value of the period (or frequency) used to compute the fractional phases from the times of arrival. Implementing the test means evaluating Z_n^2 for different values of period (and eventually period derivative).

The Rayleigh test thus is especially useful when the uncertainties on the rotational parameters of a star do not permit an extrapolation back to less recent observations, that are separated by a long time interval. It only needs an initial estimate of the frequency and frequency derivative, and with them it samples an interval around the initial values (chosen freely by the tester) to find the best combination for the parameters. Moreover, it is not necessary to use only the long observations, but any photon is good to be included in the

test. For this reason the Swift and Chandra monitoring observations, short but spread on a rather long baseline, are especially useful.

The natural step (see for example [Kaplan & van Kerkwijk(2005)] or [Kaplan & van Kerkwijk(2005)]), after performing the Rayleigh test and extracting the new lightcurves, is fitting them with a sinusoid (or an appropriate shape common to all of them), and refining the values of P and $\dot{P}$ found before. This is done by calculating the cycle counts (or phase) of, for example, the maximum of the folded lightcurve, through an iterative procedure. Starting with the latest and closest observations, one fits the cycle counts to:

$$\phi(t) = \phi_0 + \nu\,(t - t_0) + \frac{1}{2}\,\dot{\nu}\,(t - t_0)^2 + \frac{1}{6}\,\ddot{\nu}\,(t - t_0)^3 + \dots\ .$$

The iteration consists in using the best fit values for the period and its derivative to determine the cycle counts of the peak of the next observation, and then fitting again to refine the values. Of course the more observations are analyzed together, and the more the ephemeris is unambiguous.

Unfortunately this is not possible in this case, because the pulse shape changes dramatically during the years: for example, the observations corresponding to the high emission state show a very reduced pulsed fraction. The period variability is not marked enough (as in the last observations) to identify the emission peak. Moreover only a few observations long enough to cover the entire period are available, and it was visible at first sight whether they were in phase with each other or not.

6.2.1 Swift dataset

The first implementation of the Rayleigh test I performed is with the most recent data: the Swift monitoring observations. They are short, separated by a few months at most, and cover the last two years. Taken one by one, they do not allow a period search through a folding technique, but are perfect for an initial estimate of the period, to be used when adding more and more observations. The Swift complete dataset was barycentered, and filtered with the spatial region corresponding to the one used in the spectral analysis. The event file thus obtained was filtered one more time, to exclude most of the photons from the Supernova Remnant: from the spectral analysis (see chapter 5), they dominate the spectra at low energies, and thus a filter to exclude photons with energy below 1 keV (and above 10 keV). This later filter does not affect the test: I repeated the Rayleigh test with different lower cuts in energy, and the period value that it finds is always the same.

The result of the Rayleigh test is shown in figure 6.3, where the initial value of the period is assumed as 24000 s, and I searched in the interval [23500,24500] with null period derivative to start with. Here and in the rest of the chapter, the Rayleigh test was performed with only one harmonic.

As one can see from figure 6.3, the dominant peak is the central one; to better derive the period I run again the test but on a smaller interval, and fit

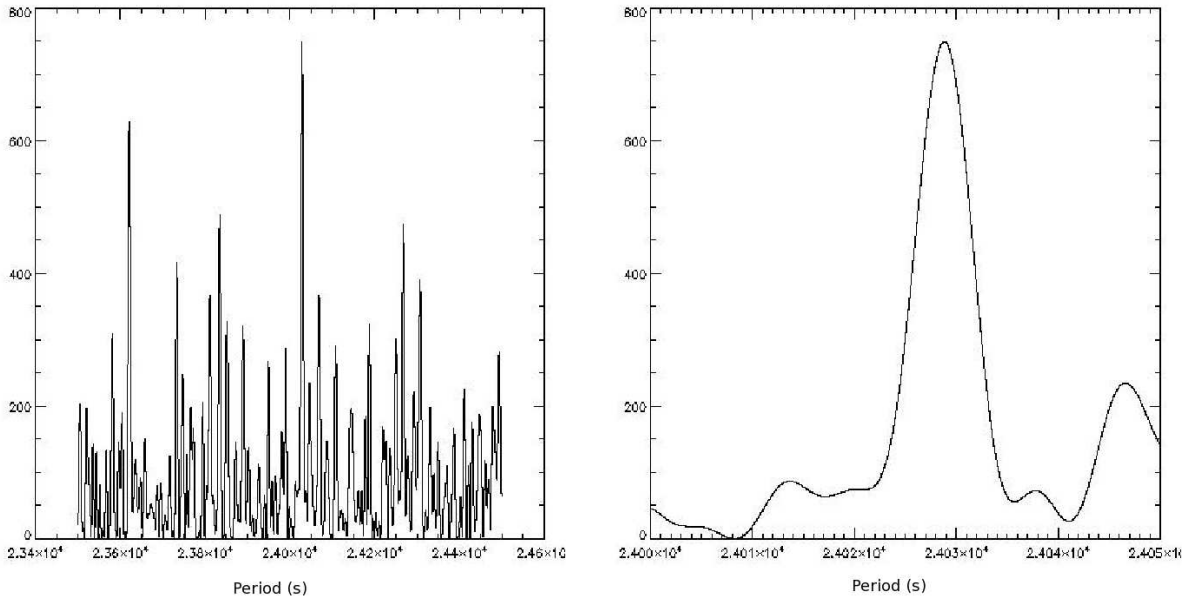

Figure 6.3: Result of the Rayleigh test for the Swift dataset, with no period derivative. On the x-axis, the values of the period; on the y-axis, the corresponding value of Z_1^2. Left figure: the period is comprised between 23500 s and 24500 s; right figure: closer look to the best period value: from 24000 to 24050 s.

it with a gaussian curve. The result of the test gives P = 24028.822 s (with $Z_1^2 = 749.734$) as the best fit period, while the Gaussian fit returns a slightly different value: P = 24028.7 ± 2.8 s[1], with epoch time the start time of the first Swift observation. One could argue that other peaks are almost as prominent as the central one, but since the XMM-Newton estimate of the period had an uncertain of 100 seconds, only the one I chose falls into the XMM-Newton uncertainty interval.

The statistically relevant error is that given by the expression:

$$\Delta P = \frac{P^2}{2\,\Delta T},$$

that is half the spacing between statistically independent values of the period. In the case of the Swift dataset, the error is: $\Delta P = 3.93$ s, which is of the same order as the half width of the gaussian fit to the peak. Furthermore, this error can be refined by the formula developed in [Leahy(1987)] by means of a

[1]The error from the any gaussian fit reported in this chapter is defined as the width (parameter A_2) of the gaussian, defined as:

$$f(x) = A_0 \exp\left(-\frac{(x - A_1)^2}{2(A_2)^2}\right).$$

simulation. The previous equation overestimates the error on the period, and a closer estimate to the real value is σ_P given by:

$$\frac{\sigma_P}{\Delta P} = 0.71(\chi^2_{red} - 1)^{-0.63} = 0.19,$$

which means that $\sigma_P = 0.75$ s.

Adding a period derivative gave uncertain results, and a value of Z^2_1 inferior to the one of the test with only a variable period. The Rayleigh test result is shown in figure 6.4, where z is plotted as a function of the period and the period derivative. The color coding is from black to white for increasing values of z. The contour plots are also displayed. It is clear that the period derivative is compatible with zero.

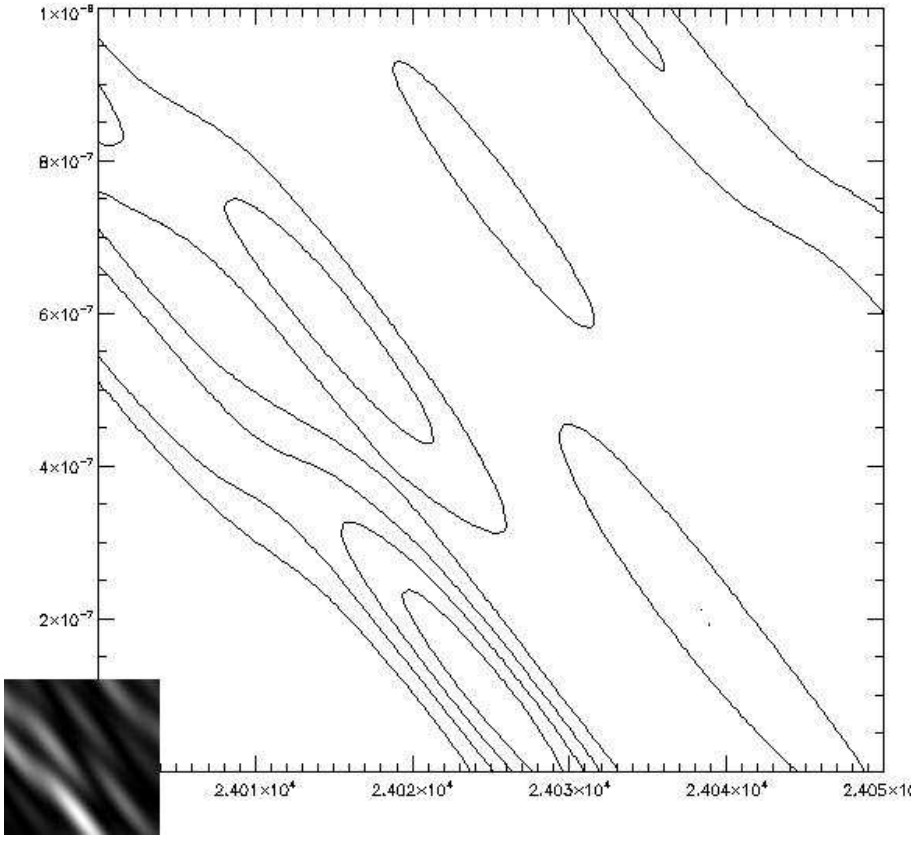

Figure 6.4: The result of the Rayleigh test with both period and its derivative free to vary, performed on the Swift dataset. The big image represents the contour plot, while the small insert is a representation of z. They both are functions of the period (on the x axis) and the period derivative (on the y axis), and the color coding for the smaller image is from black to white for increasing values of z.

The solution derived from the Swift dataset by means of the Rayleigh test

24029(3) s is (of course) fully compatible with the less precise XMM-Newton solution 24000 ± 100 s.

I then folded the longest observations available of 1E 161348-5055 with this refined period, and null period derivative, to have an overview of the evolution of the pulsed profile.

The observations I chose, even if they do not cover the entire period, are, in chronological order:

1. Chandra Obs. 123: the pre-outburst (1999) observation. It lasts 13 ks (see table 4.1).

2. Chandra Obs. 970: the peak observation, made in 2000. It lasts 19 ks.

3. XMM-Newton 2001 observation (on axis, see table 3.1): it lasts 88 ks (see table 3.1).

4. Chandra Obs. 2759: a continuous clocking observation obtained ~ 2 years after the peak (2002). It lasts 48 ks.

5. XMM-Newton 2005 observation: it lasts 19 ks.

6. Chandra Obs. 7619: the last (and longest) Chandra observation, made in 2007. It lasts 78 ks.

The folded lightcurves show intense variability over time: in figures 6.5, 6.6, 6.7 and 6.8 the lightcurves of the observations listed above are reported. No filters on energy are applied, and all of them have the same start epoch.

Keeping in mind that the first lightcurve is the pre-burst observation of 1999, the second is the peak observation of 2000, the following two are taken at short distance in 2001 and the last ones were made respectively in 2005 and 2007, one can notice that dramatic changes in the lightcurves happened during these years.

- First of all, between observation 123 and 970 the relative amplitude of the pulsations is very reduced when compared to the average value: the count rate varies of a factor 3 in the pre-outburst observation, and a factor 0.2 in the peak observation.

- The amplitude of the pulsations gradually increases, and in observation 7619 (2007) it is again close to the pre-burst level.

- The peak in the first four curves, that were obtained between 1999 and 2001, is more or less stable around phase 0.1-0.2, while after four years it moved to phase 0.4-0.5. This could a hint of a presence of a non null period derivative, in case one identifies of the only peak of the last observations with the first one of the multi-peaked observations.

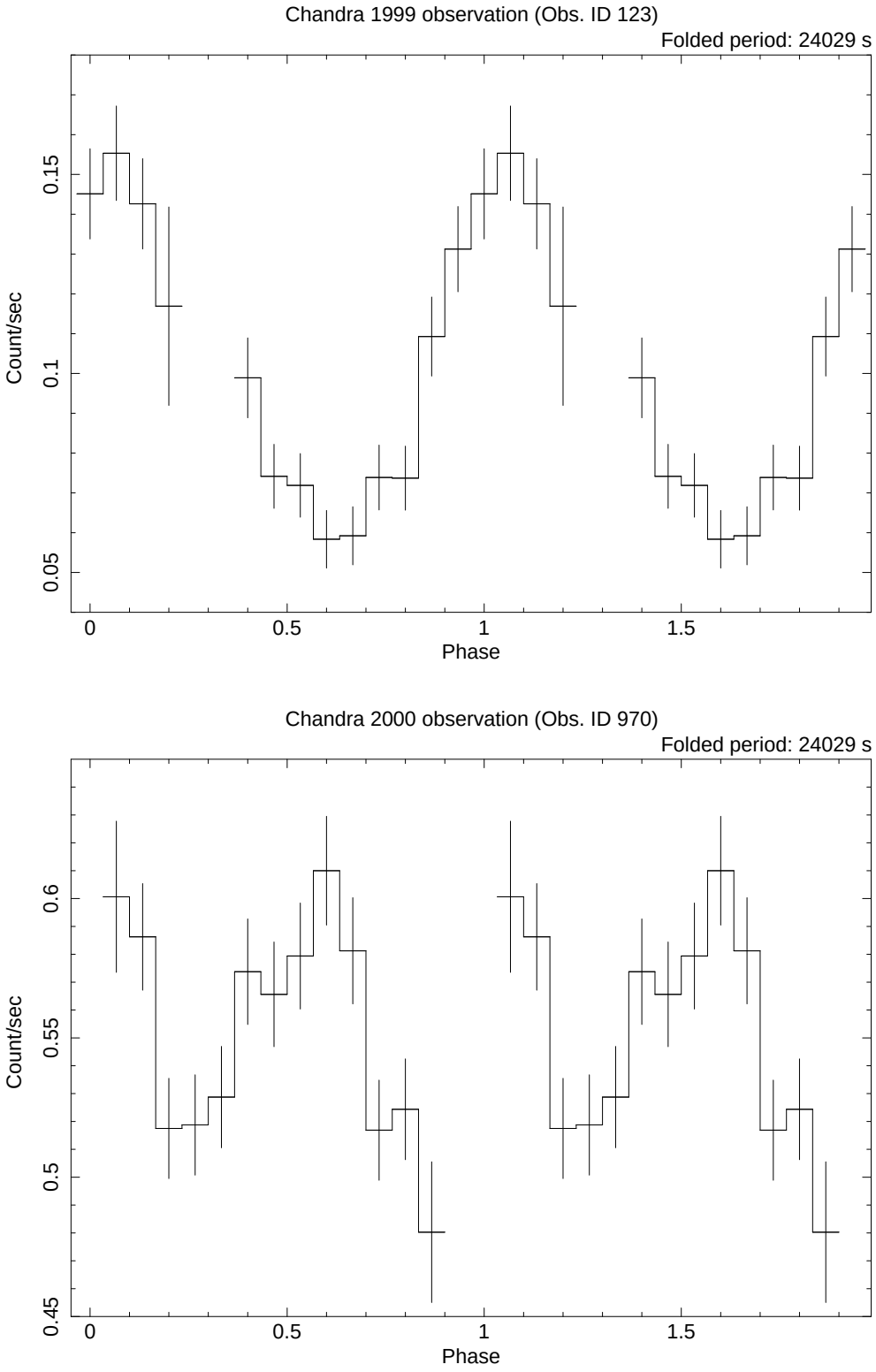

Figure 6.5: Folded lightcurves of the Chandra observations taken in 1999 (quiescence) and 2000 (peak) in the 0.2-10 keV energy range, binned to have 15 phase bins per period. The preliminary value P = 24029 s, derived from the Swift observations alone, was used for the folding.

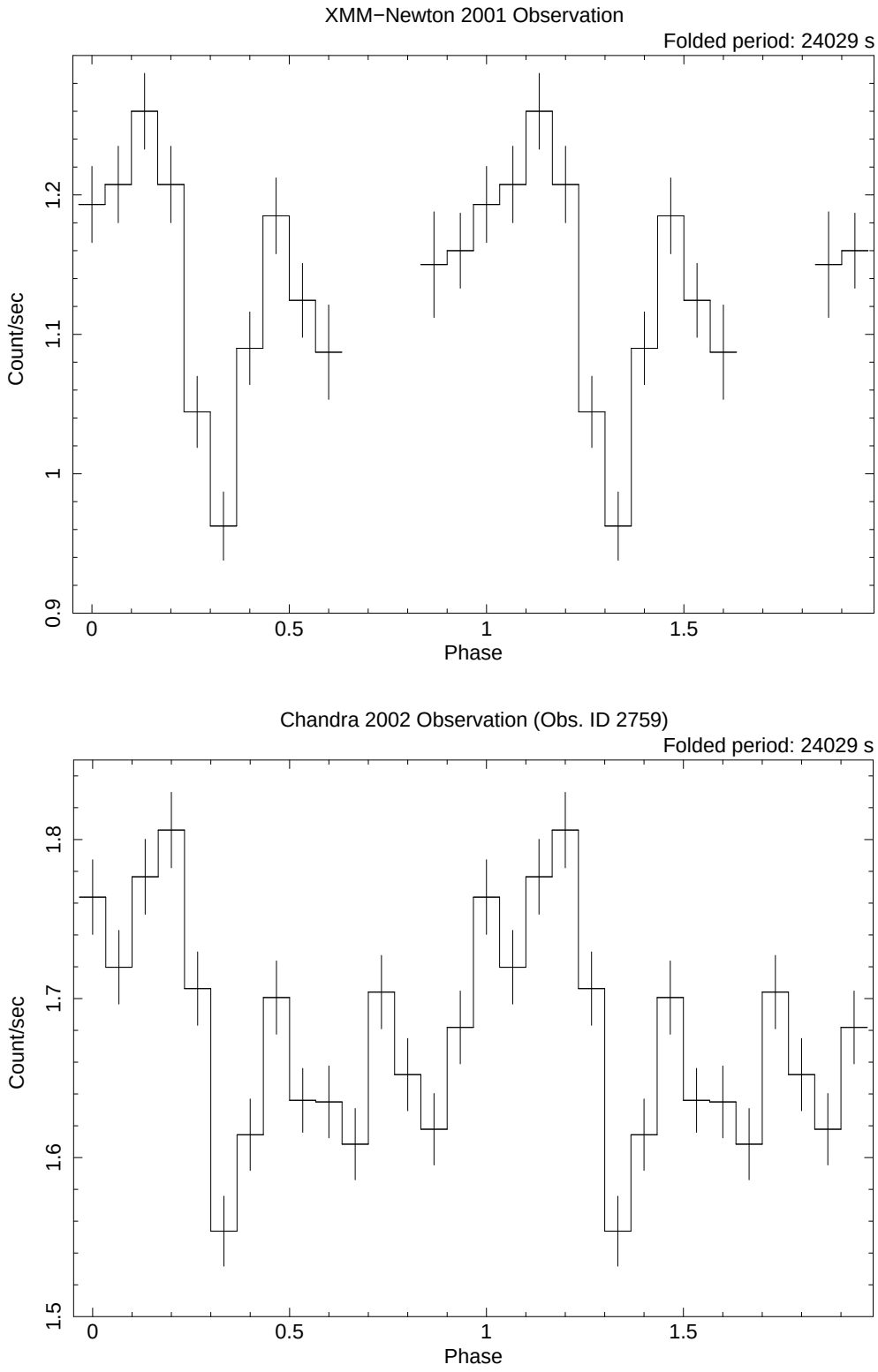

Figure 6.6: Folded lightcurves of the XMM-Newton 2001 observation and the Chandra 2002 observation in the 0.2-10 keV energy range, binned to have 15 phase bins per period. The preliminary value P = 24029 s, derived from the Swift observations alone, was used for the folding.

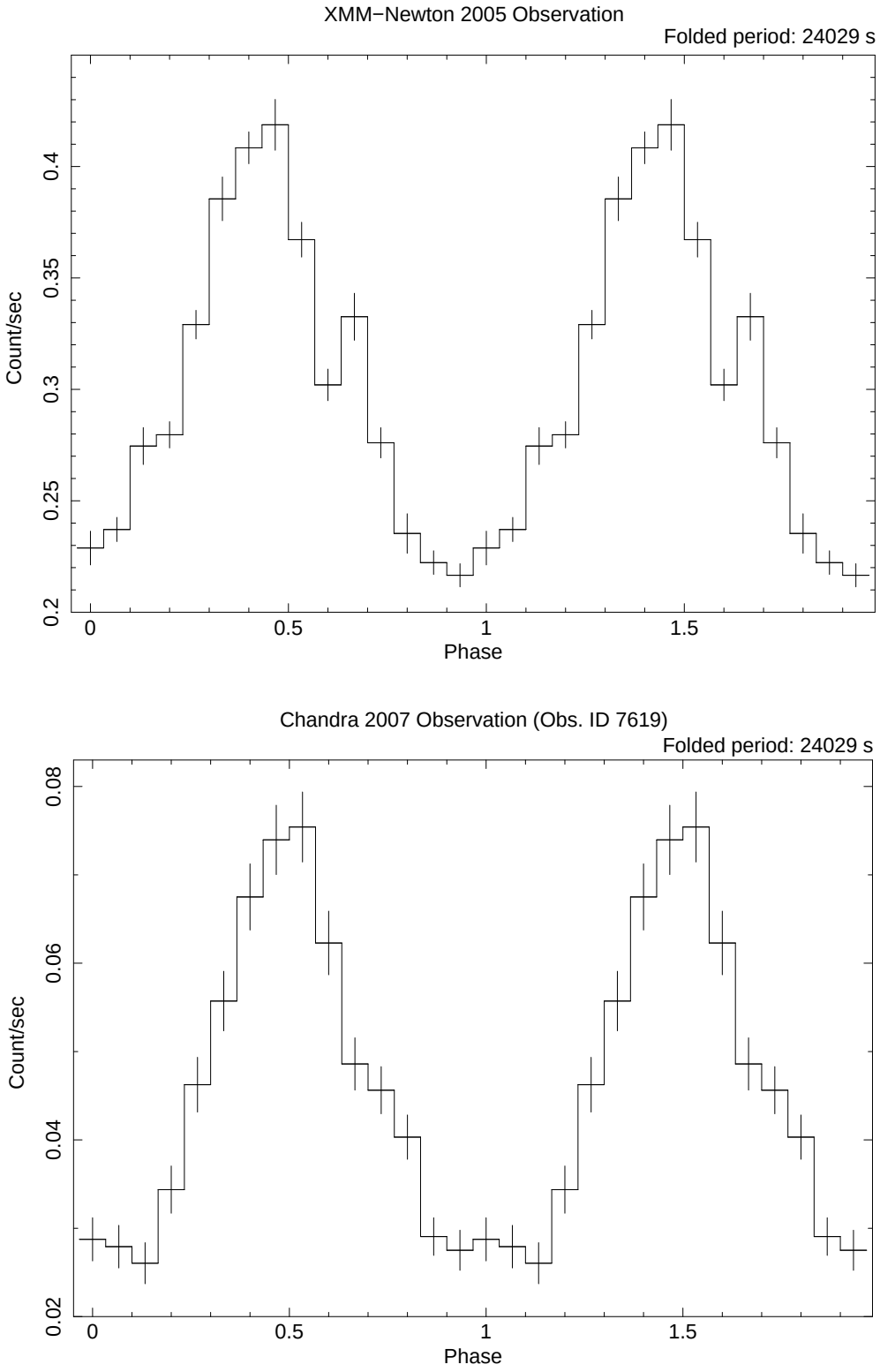

Figure 6.7: Folded lightcurves of the XMM-Newton 2005 observation and the Chandra 2007 observation in the 0.2-10 keV energy range, binned to have 15 phase bins per period. The preliminary value P = 24029 s, derived from the Swift observations alone, was used for the folding.

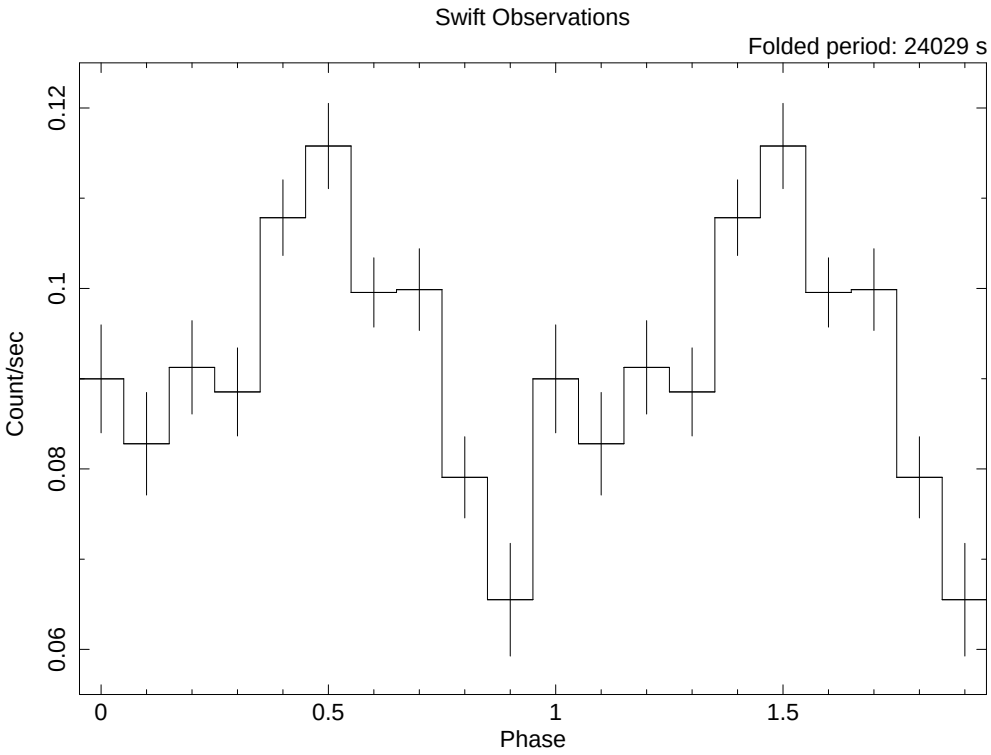

Figure 6.8: Folded lightcurve of the merged Swift observations in the 0.2-10 keV energy range, binned to have 10 phase bins per period. The preliminary value P = 24029 s, derived from the Swift observations alone, was used for the folding.

- The shape of the folded profile also shows great changes, especially from observation 123 (in 1999) to observation 970 (peak, in 2000): before the outburst, it was almost sinusoidal, at the highest flux a second peak is present, even though the hole in the profile (due to an uncomplete coverage of the period) makes it less certain.
- The Swift lightcurve shows a sinusoidal profile, but the shape is a little distorted. This could be due to a random oversampling of the minimum phase of the period.

The uncertainty on the period only allows to trace the evolution backward for a limited amount of time, because the error is transferred onto the phase: when the consequent uncertainty on the phase is greater then, for example, 0.5, it is impossible to identify without ambiguity how many cycles are there in the gap between the observations one wants to link. In fact, when the error propagated on the phase is so big, two consecutive integer values of the cycles equally connect in phase the observations. For this reason the lightcurves represented before are not to be taken as the definitive one.

The time delay between the first Swift observation and the XMM-Newton

2005 observation is less than 1 year ($\Delta t \simeq 200$ days). If we decide that the maximum phase error we can tolerate, in order to assign univocally the cycle corresponding to the first peak of the XMM-Newton 2005 observation, is $\Delta\phi = 0.25$, let's check if the error on the period derived using the Rayleigh test on the Swift dataset allows to trace the evolution back one year.

Indicating with $P_S \pm \Delta P_S$ the Swift period and its error (which was 24029 ± 3 s), the total uncertainty on the period by extrapolating back to the XMM-Newton start time is:

$$\Delta P_{tot} = \frac{\Delta t}{P_S} \times \Delta P_S \simeq 2149 \text{ s}, \tag{6.4}$$

that corresponds to a phase uncertainty of:

$$\Delta\phi = \frac{\Delta P_{tot}}{P_S} \simeq 0.1, \tag{6.5}$$

which is well below the limit uncertainty we had chosen.

For this reason we can state that among the lightcurves represented before, the XMM-Newton 2005 is valid, but the observations of 2002 and before should be taken carefully: in 2003 already, three years before the Swift first observation, the uncertainty on the phase is ~ 0.3.

By comparing figures 6.7 and 6.8, then, it is apparent that the folded profile of 1E 161348-5055 in 2005 and 2007-2008 are in phase with each other: this is a confirmation that the period derived by means of the Rayleigh test on the Swift dataset is a reliable estimate, although we cannot exclude that during the gap a variable period derivative was present, whose values were exactly the ones needed to shift the total cycle counts of an integer number. This is evidently highly improbable, nonetheless it can not be excluded.

In order to refine even more the period and to verify an eventual period derivative, a more detailed analysis is required. This can be done, first, by repeating the Rayleigh test adding to the Swift dataset also the Chandra 7619 observation, and the XMM-Newton 2005 observation, that we verified being in phase with the Swift dataset.

6.3 Refining the period with the observations from 2005 on

Adding the Chandra 2007 observation

As explained in paragraph 4.5, one of the reasons why the Chandra observation 7619 was asked is having a long and timing accurate observation very close to one of the Swift observations, so that it could be easily phase-linked to it. The result is that the statistical significance of the test is greatly improved, and the value of the period from the test is obtained with more precision.

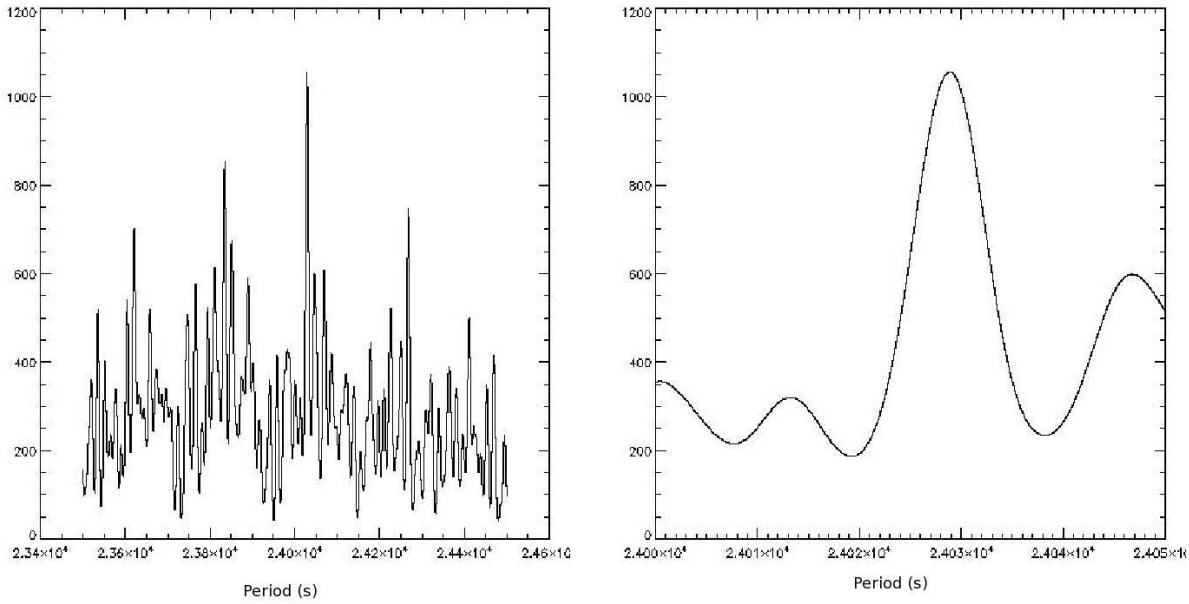

Figure 6.9: Result of the Rayleigh test for the Swift dataset plus the Chandra Obs. 7619, with no period derivative. On the x-axis, the values of the period; on the y-axis, the corresponding value of Z_1^2. Left figure: the period is comprised between 23500 s and 24500 s; right figure: closer look to the best period value: from 24000 to 24050 s.

In figure 6.9 the result of the test on the combined Swift plus Chandra 7619 data is shown: the peak is approximately at the same position (maximum is at $P = 24028.8715$ s), but now it corresponds to a much higher value of $Z_1^2 = 1056.48$. This time also the start epoch is the start time of the first Swift observation.

The gaussian fit to the highest peak leads a best value for the period of 24028.8 ± 4.1 s (the error is larger than the previous case because the central peak is larger, but its significance is improved), while:

$$\Delta P = \frac{P^2}{2\,\Delta T} = 3.93 \text{ s}$$

obviously does not change, being the Chandra 7619 Observation in between the Swift observations, but $\sigma_P = 0.2$ s is very much improved, since the reduced chi squared of the sinusoid, with respect to a fit with a constant, is much higher than the case before. Unfortunately the central value of the gaussian fit is not known precisely enough for the refined error to be used.

6.3.1 Adding XMM-Newton 2005 observation

The last XMM-Newton observation of 1E 161348-5055 was carried on in August 2005, so is separated from the first Swift observation by a gap of almost one

year. This is a quite long interval, so the Rayleigh test was able to improve from the previous case, giving as a result a best period of 24030.413 s, rather close to the first value of 24028.8, corresponding to $Z_1^2 = 2370.09$, and within the errors.

The gaussian fit to this case leads the value 24030.4 ± 2.2, and

$$\Delta P = \frac{P^2}{2\,\Delta T} = 3.18 \text{ s}$$

$$\sigma_P = 0.03\,\Delta P = 0.1 \text{ s}.$$

The results are shown in figure 6.10

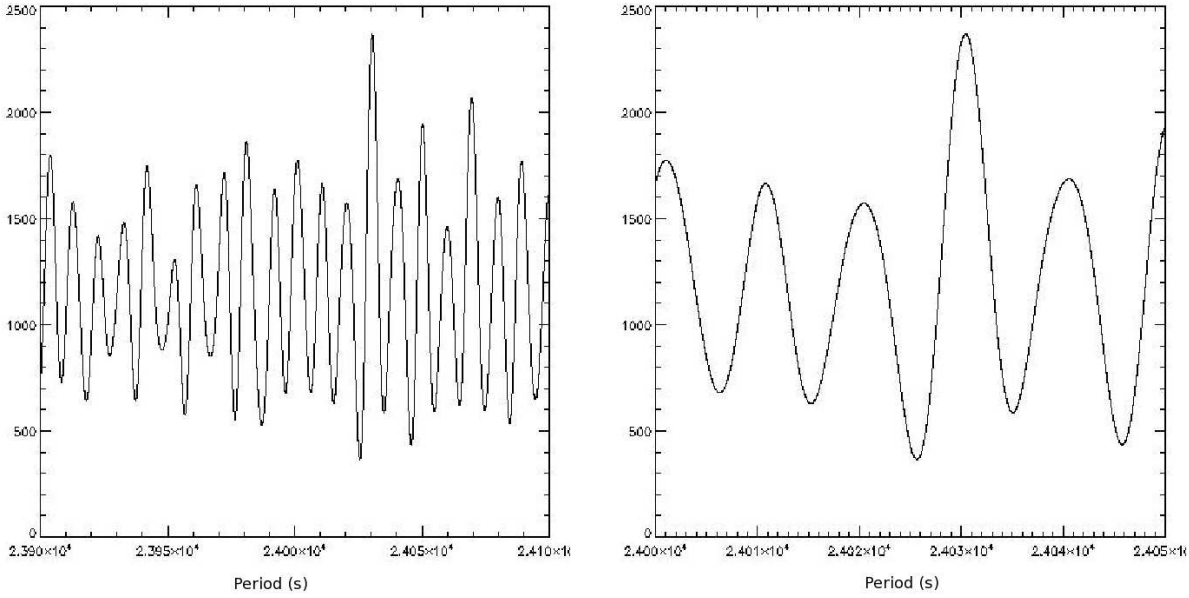

Figure 6.10: Result of the Rayleigh test for the Swift dataset plus the Chandra Obs. 7619, plus the XMM-Newton 2005 observation, with no period derivative. On the x-axis, the values of the period; on the y-axis, the corresponding value of Z_1^2. Left figure: the period is comprised between 23500 s and 24500 s; right figure: closer look to the best period value: from 24000 to 24050 s.

As one can see, the new value of the period 24030 ± 2 s is within the previous range 24029 ± 4: it is fully compatible then, and the error is smaller. This allows to extrapolate it backwards to the Chandra monitoring observations: we repeated the calculation done in equations 6.2.1 and 6.2.1 for the Chandra observations at the beginning of the year and with reference time the start time of the XMM-Newton 2005 observation, and reported the results in table 6.1.

The set of observations ACIS05 and ACIS04 are well within the limit $\Delta\phi \leqslant 0.25$, the set ACIS03 is borderline, while the ACIS02 is definitely out of the range (notice that the ACIS02 is separated by two years from the ACIS03). It

Obs. ID	Date	ΔP_{tot} (s)	$\Delta\phi$
5592	2005-01-24	1515	0.063
4596	2004-01-27	4124	0.17
3514	2003-03-08	6463	0.27
2314	2001-03-18	11639	0.48

Table 6.1: Extrapolations of the period uncertainties backward to the set of observations ACIS02, ACIS03, ACIS04, ACIS05. The time interval considered is the one between the listed observations and the XMM-Newton 2005 observation.

is possible then to extrapolate the period backward without uncertainties (or with acceptable uncertainties) until the set ACIS03 of the Chandra monitoring. Let's see how the lightcurves of the sets look like, to see whether they are still in phase with the observations studied until now.

In figure 6.11 there are the folded profiles of the dataset ACIS 03, 04 and 05, together with that of the XMM-Newton 2005 observation folded with the refined period. We used here the same start time as in the folded profiles in figure 6.5 and following, to allow direct comparison.

The Chandra sets are composed of four observations each, and as can be seen from table 4.1, for a total of about 20 ks each. The effective length of the dataset is not necessarily 20 ks though, because the observations may overlap and, as a result, the folded profile can have larger holes than expected from the sum of the exposure times of the observations. Moreover, in folding the whole set one assumes that throughout the year considered the profile does not undergo major changes.

Keeping this warnings in mind, and remembering that the phase error relative to the ACIS 03 dataset is slightly higher than the upper value accepted, one can note from the profiles that

- In 2005 and 2004 the curve was rather similar to the one extracted from the XMM-Newton 2005 observation, while in 2003 this is not so clear any more. It may just be an effect due to the fact that the peak is not sampled as clearly as it was in the ACIS 04 and 05 sets, where the rise and at least the first part of the fall are evident. Otherwise, the shape of the profile is changing towards the multipeaked curve of the 2001 and 2002 observations. This is not clear yet, because as I said the uncertainty on the phase needs one additional calculation of the period through the Rayleigh test to be extrapolated back to 2003 and before.

- For what concerns the ACIS 04 and 05 sets alone, where the peak is evident, the maximum of the profile is at phase 0.4-0.5, in total agreement with the XMM-Newton 2005 observation. In this case as well the considerations made at the end of section 6.2.1 hold as well: it can not be excluded that a variable period derivative such that the observations

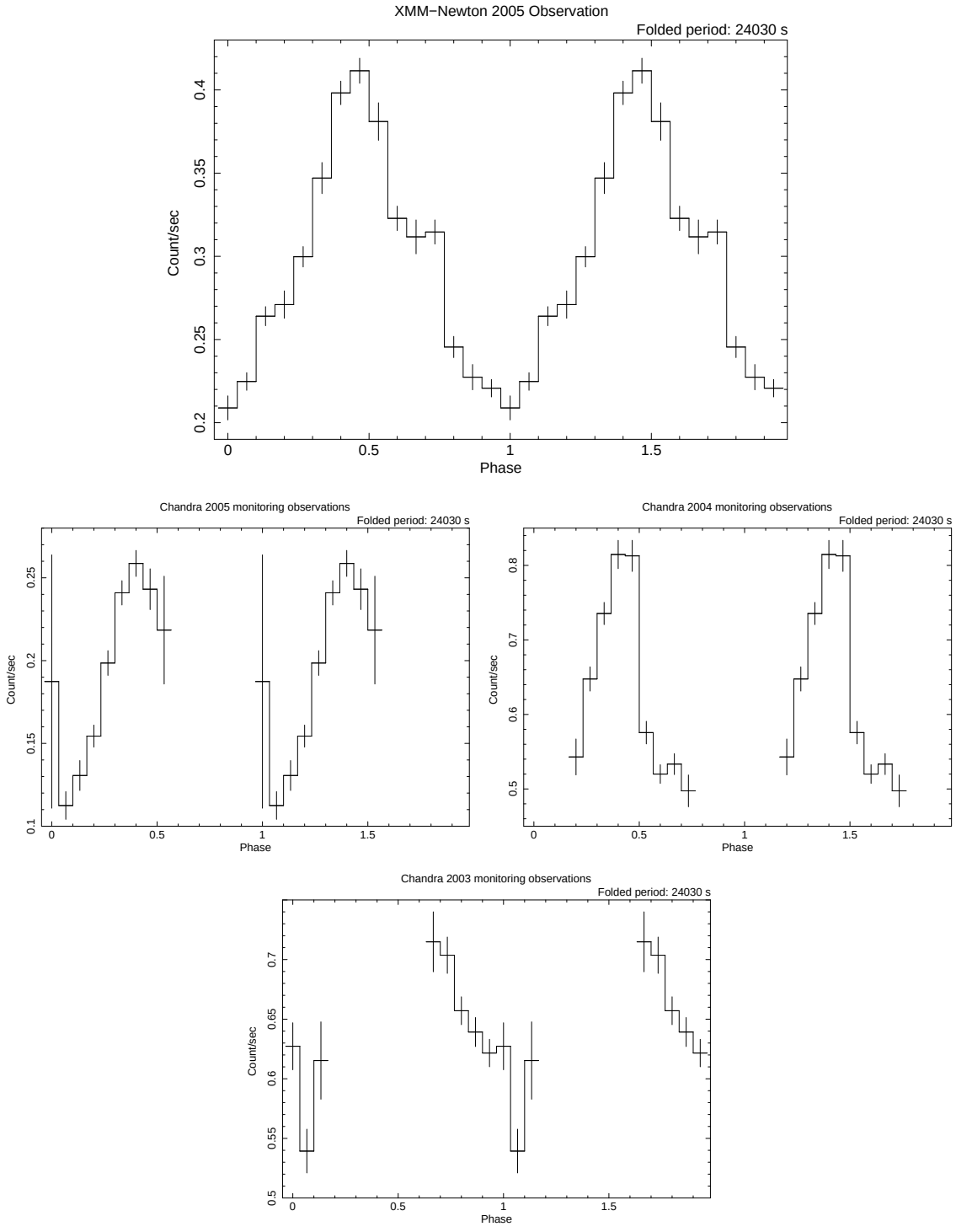

Figure 6.11: Folded lightcurves (0.2-10 keV) of the *XMM-Newton* 2005 observation (for comparison) and the Chandra 2005, 2004, 2003 observations. The start time is set as identical for all the observations, and for all the foldings the period P = 24030 s was used, as derived from the *XMM-Newton* 2005 Obs. - *Chandra* 2007 Obs. - Swift Obs. dataset. As shown in detail in the text, the error allowed propagation backwards to 2003.

remain separated by an integer number of cycles is present. At variance with the previous situation, though, this is even more implausible since the observations are many more (and not just the XMM-Newton 2005 observation in comparison with the whole Swift dataset), and separated by different time intervals. Nonetheless, it is good to say it once again, the presence of a variable period derivative cannot be ruled out.

Having verified that the ACIS 04 and 05 sets of observations are in phase with the XMM-Newton 2005 observation, and thus with the Swift dataset and the Chandra 7619 observation with no need for a period derivative, we can proceed by performing the Rayleigh test including these sets in the database. We expect to refine even more the period derivative, and once again to be able to connect in phase the 1999-2003 observations with the one considered until this point. We also want to compare the ACIS 03 set with the previous observations, to understand whether the profile is changing or the peak is experiencing a phase shift.

6.4 Chandra monitoring

6.4.1 Adding the 2005 and 2004 observations

As explained before, the Chandra monitoring observations available are added by groups of four, namely adding those done in the same year together. They are quite short, but they span a rather long baseline: the Rayleigh test is expected to improve a lot every time one year of observations is added.

For example, the images in figure 6.12 show the result of the Rayleigh test performed after the set ACIS 05 was added to the previous dataset. As a comparison, the figure for the previous test (rescaled to have the same scale on the y-axis as the new one) is shown as well.

It is immediate to notice how improved the fit is: the peak now is ~ 3 times higher than before, and it is also clearly (~ 4 times higher) above the surrounding peaks. The maximum of the test falls at:

$$P = 24030.853 \text{ s}, \quad Z_1^2 = 5074.49,$$

and the gaussian fit to the central peak leads $P = 24030.9 \pm 2.4$ s, and

$$\Delta P = \frac{P^2}{2\,\Delta T} = 2.06 \text{ s}$$

$$\sigma_P = \Delta P = 0.1 \text{ s}.$$

Next, since the ACIS 04 were in phase with the XMM-Newton 2005 observation as well, we added that dataset too and ran again the Rayleigh test. As can be seen from figure 6.13, the shape of the peak is significantly changed: it has a multipeaked structure. The test gives as best value for the period:

$$P = 24029.713 \text{ s}, \quad Z_1^2 = 12329,$$

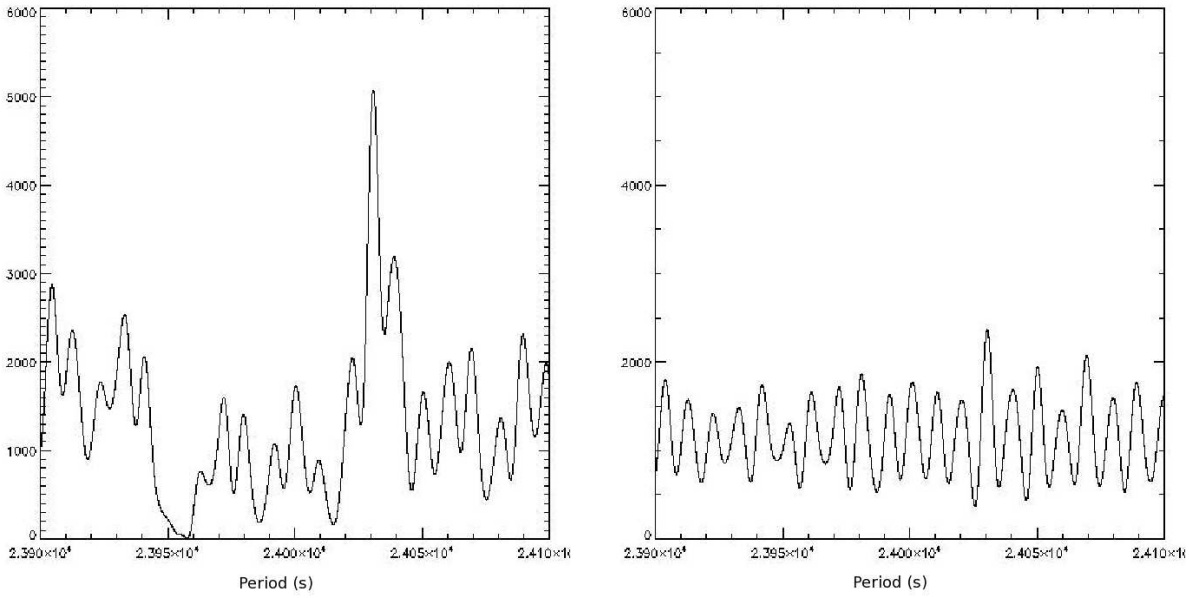

Figure 6.12: Left: result of the Rayleigh test for the dataset including all the observations from the ACIS 5592 on, with no period derivative. On the x-axis, the values of the period; on the y-axis, the corresponding value of Z_1^2. Right: the same figure as 6.10 (left) rescaled in order to have the same scale as the left figure. The improvement is evident.

while the gaussian is slightly shifted with respect to the maximum, because the shape of the original curve is not symmetric. The result is: $P = 24029.7 \pm 2.1$ s, and

$$\Delta P = \frac{P^2}{2\,\Delta T} = 2.65 \text{ s}$$
$$\sigma_P = 0.03\,\Delta P = 0.08 \text{ s}. \tag{6.6}$$

As expected, since the set ACIS 04 was in phase, the significance of the period is highly increased, because it is valid on a temporal range 1 year longer than the previous case.

In this dataset the baseline (4 years) is long enough to search for period variabilities. Since the period derivative for 1E 161348-5055 has never been studied before, there is no indication of how rapidly the period may be varying.

The Rayleigh test did not converge when large interval values of the period derivative were taken into account. To overcome this problem, we used tentative values, without specifying a variability interval, to see how such parameter affected the result of the test. We spanned the interval $\dot{P} = [1\times10^{-8}, 1.5\times10^{-7}]$ s/s, which correspond to an overall variation in period of roughly 0.3-5 s, and the results are listed in table 6.2. The introduction of a period derivative leads to an improvement of the Rayleigh test, but not a dramatic breakthrough (which was expected since the peaks of the folded profile appeared to be still

$\dot{P}$ (s/s)	P (s)	Z_1^2
0.1×10^{-7}	24029.129	12758.3
0.3×10^{-7}	24028.028	13247.9
0.4×10^{-7}	24027.477	13296.8
0.5×10^{-7}	24026.927	13217.9
0.6×10^{-7}	24026.426	13020.2
0.7×10^{-7}	24025.876	12722.2
0.8×10^{-7}	24025.425	12347
1×10^{-7}	24025.675	11495.7
1.5×10^{-7}	24026.026	10252.8

Table 6.2: Results of the Rayleigh test for tentative values (fixed) of the period derivative. The period is free to vary within [24000,24050] s.

in phase with the 2005 XMM-Newton observation): the value of Z_1^2 passes from $\sim$ 12300 up to $\sim$ 13300. From table 6.2, moreover, one can deduce that the most probable value of the period derivative is in the range $0.1 - 0.8 \times 10^{-7}$ s/s. Having restricted the interval of variability for the period derivative, we can now proceed to a Rayleigh test with both the period and its derivative free to vary. In order to have more reliable results, we fractioned the interval for $\dot{P}$ into smaller intervals: [0.1-0.3], [0.3-0.6] and [0.6-0.8] $\times 10^{-7}$ s/s. The results are listed in table 6.3. Even though the highest value of Z_1^2 is in correspondence

P range (s)	$\dot{P}$ range ($\times 10^{-7}$ s/s)	P (s)	$\dot{P}$ ($\times 10^{-7}$ s/s)	Z_1^2
	[0.1-0.3]	24050.0	0.3	13195.5
[24000 − 24050]	[0.3-0.6]	24050.0	0.6	13287.3
	[0.6-0.8]	24026.263	0.705	12996.4

Table 6.3: Results of the Rayleigh test for some variability intervals of both period and its derivative. See text for details and discussion.

of $\dot{P} = 0.6 \times 10^{-7}$ s/s, clearly that result is unacceptable, because the period is shifted of $\sim$ 20 s from the original, while we were looking for variations of no more than a few seconds. The physically more significative result is the couple $P = 24026.3$ s and $\dot{P} = 0.705 \times 10^{-7}$ s/s.

This is just an indication of a possible period derivative, but will not be taken into account at the moment because the datasets used until now did not show phase shifts of the peaks of the folded profile. It will eventually be checked in the next larger datasets, if phase shifts occur, but for completeness I reported in figure 6.13 the central peak in two cases: left, $\dot{P} = 0$ and right with $\dot{P} = 0.705 \times 10^{-7}$ s/s. With the selected value of the period derivative, the shape of the period peak is a little more definite.

Gaussian fit to the peaks gives the following results:

$$P = 24029.7 \pm 2.1 \text{ s}, \quad \dot{P} = 0 \text{ s/s (fixed)};$$

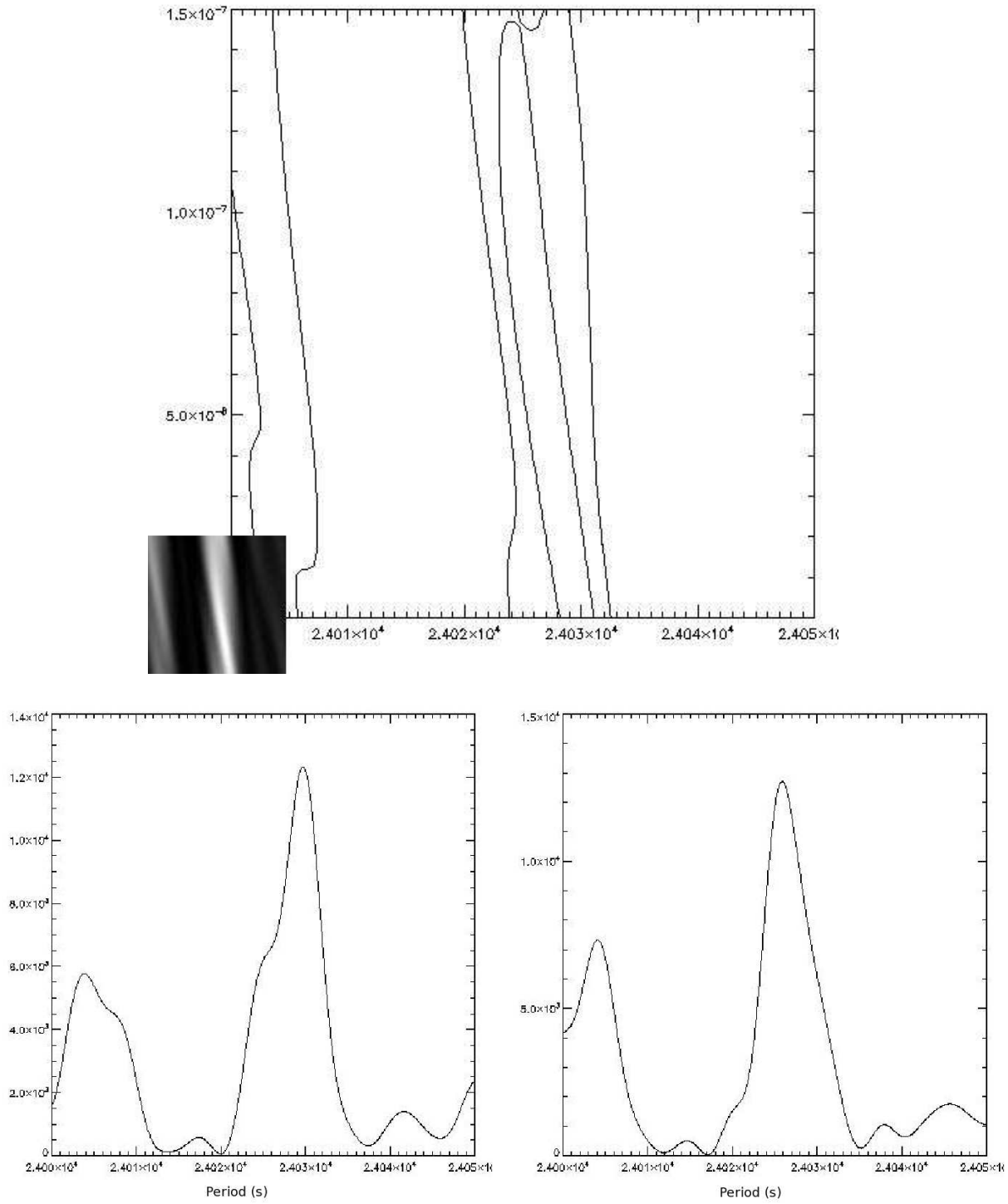

Figure 6.13: Top: contour plot and corresponding color image of the result of the Rayleigh test with both the period and its derivative free to vary; the color coding for the smaller image is from black to white for increasing values of z. Bottom: result of the Rayleigh test for the dataset comprising all the observations since the Chandra 2004 monitoring observations. On the x-axis, the values of the period; on the y-axis, the corresponding value of Z_1^2. Left figure: the period derivative is set to zero; right figure: the period derivative has the best fit value of 0.705×10^{-7} s/s.

$$P = 24025.9 \pm 2.6 \text{ s}, \quad \dot{P} = 0.705 \times 10^{-7} \text{ s/s (fixed)}.$$

6.4.2 Lightcurves

Considering the refined value of the period as $P = 24030 \pm 2$, the same calculation made above applied here on the propagation of the error backward mean that this value is valid for at least 2 years (maybe three, keeping in mind that the phase error is slightly above the limit we required). Thanks to the refined error through the formula from [Leahy(1987)], reported in equation 6.4.1 we are absolutely sure that propagating it backwards to the Chandra Obs. 123 we are well below the maximum uncertainty on the phase.

We can now fold the lightcurves of the major observations of 2001 and 2002, together with the set ACIS 02, the peak observation and the pre-outburst observation. To have a better idea of how the profile evolves, all the folded profiles, together with the incomplete ones, are reported in figure 6.14 and 6.15. All of them were calculated with the same start time in order to compare the phase of the peaks.

- The folded profile of the ACIS 03 set, that already before raised some problems of 'incompatibility' with the following observations, remains sort of unclear, since the refined calculation of the period gave as a result the same value used before. It must be noticed though that 2003 is the transition year between the multi-peaked curves of 2001 and 2002, and the smooth profile visible in the XMM-Newton 2005 observation, but already in the 2004 folded profile. The clear feature of the curve is the minimum, which is at phase 0.1, in perfect agreement with all the previous profiles where that phase interval was covered. For all these reasons, then, and in addition with the fact that the peak is not complete, we prefer to think of a transition shape of the folded profile rather then a change of the period. This is even more confirmed by the considerations made below.

- The Chandra 2759 observation: the multi-peaked structure is dominant. Two deeps are present, the one at phase 0.1 which is common to all the previous observations (even if not that thin), and an additional one at phase 0.5-0.65. The equal deeps separate the period into two almost equal intervals, both of which have substructures. The first part is the highest one, with two peaks: the first one is at phase 0.2, and the second, that reaches the maximum, at phase 0.45. The second half reaches half of the height (in amplitude from the minima) of the first part, has again a two peaked substructure but this time the peaks are equally high; they are located at phase 0.7 and 0.95 respectively. This profile points towards a sub-periodicity. It will be investigated further on.

- The XMM-Newton 2001 observation, which is unfortunately incomplete, has a rather similar profile to that of the Chandra 2759 observation.

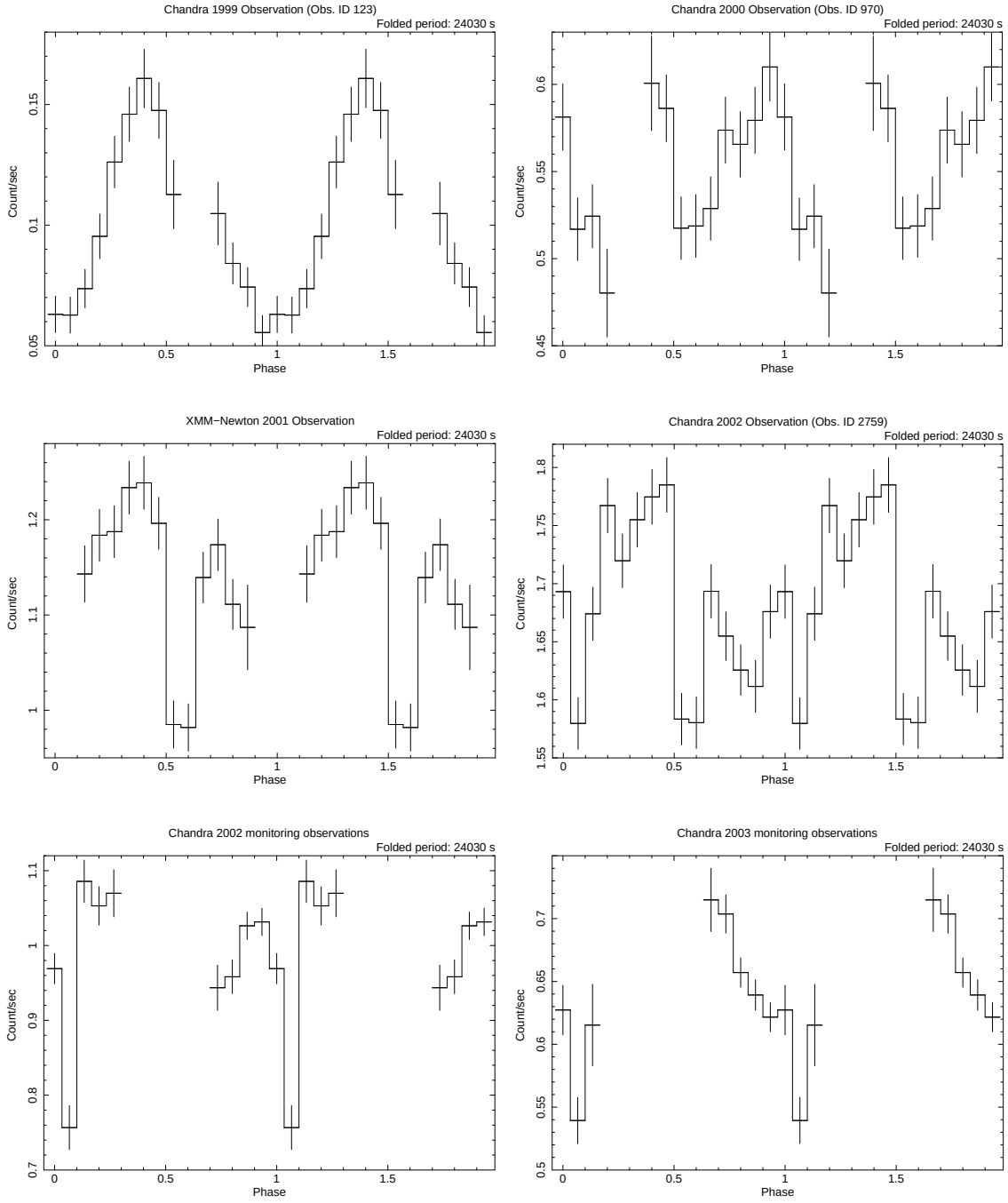

Figure 6.14: Folded lightcurves (0.2-10 keV) of the observations from 1999 to 2003. The start time is set as identical for all the observations, and for all the foldings the period P = 24030 s was used. As shown in detail in the text, the error allowed the period to be valid throughout the 10 years of observations. The profiles appear to be in phase.

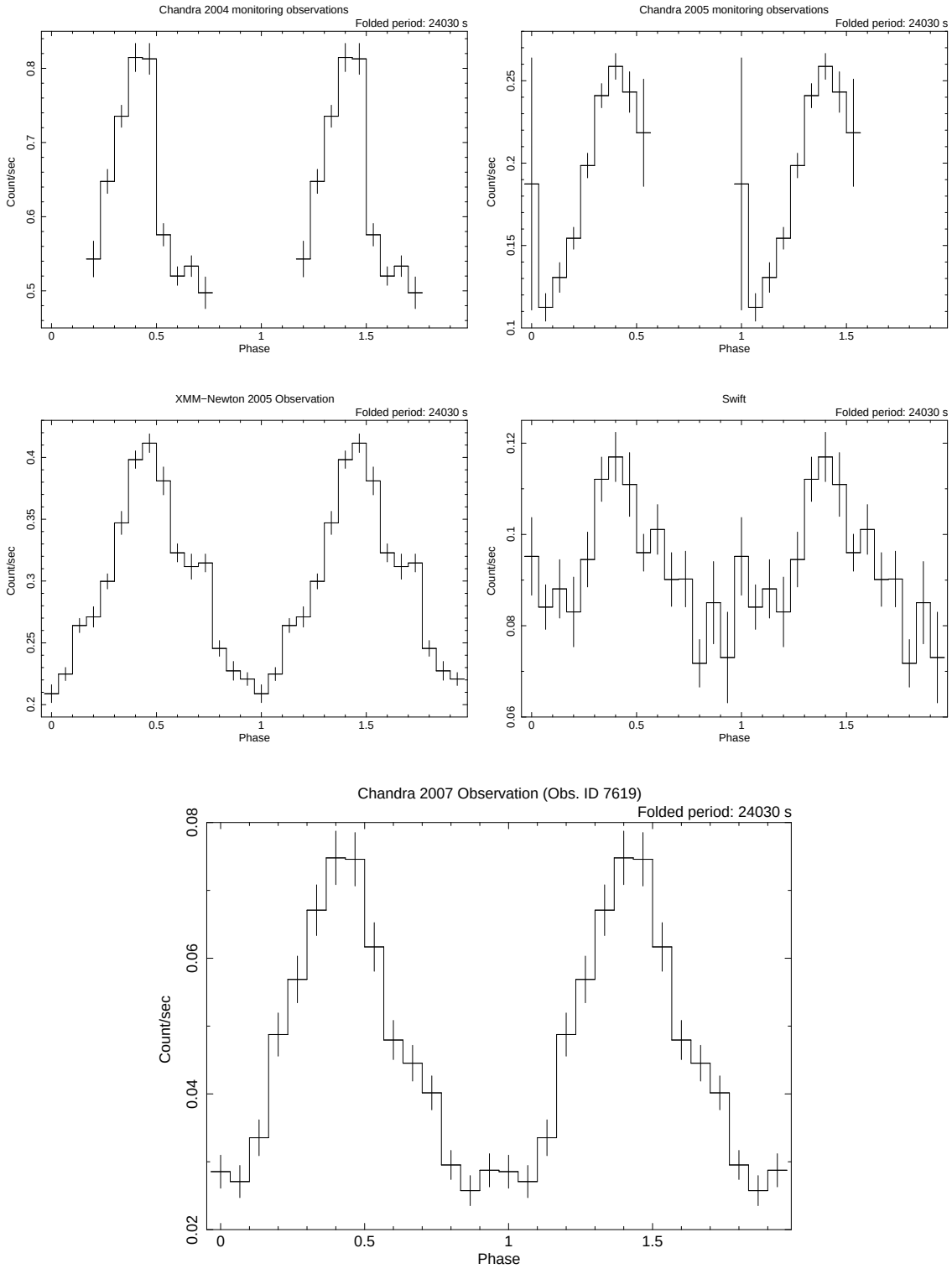

Figure 6.15: Folded lightcurves (0.2-10 keV) of the observations from 2003 to present. The start time is set as identical for all the observations, and for all the foldings the period P = 24030 s was used. As shown in detail in the text, the error allowed the period to be valid throughout the 10 years of observations. The profiles appear to be in phase.

The deep at 0.5-0.65 is present as well while the first one falls into the uncovered phase interval. For this reason, in comparison with the 2759 observation one can recognize the two parts in which the period was divided by the two deeps, but no information are available on the deepness of the missing minimum. One could infer that, since the minimum at phase 0.1 is present in all the observations, it should be there as well, but it is not certain according to only this observation. For what concern the peaks, the first part of the curve has a simpler structure: only one broad peak is present, while for the second part only the first peak is visible. The second, if present, was not sampled by this observation.

- The ACIS 02 dataset, at variance of what one could think, is composed of observations not done in 2002 but in 2001: it is immediately before the XMM-Newton 2001 observation, and accordingly it shows the same complex structure. The period is not completely covered by the set: the deep at phase 0.1 is present, as well as the second peak at phase 0.8-0.9.

- Moving back in time we reach observation 970, made in 2000, when 1E 161348-5055 was in its highest state. This observation is incomplete as well, nonetheless both of the deeps are present: the one at phase 0.5-0.65 is clear, while the first one is a little more ambiguous. It is expected at phase 0.1, where the curve is declining, but the minimum here appears at phase 0.2. This could just be an effect of the hole, that could cover part of the last phase bin; in this situation the two minima would have the same deepness. The two peaks are present, without significant substructures (but one is incomplete).

- Observation 123 is the pre-outburst observation, where 1E 161348-5055 shows the quiescence smooth and near sinusoidal profile. The only peak in the period is at phase 0.4, in agreement with the late folded profiles. The observation is not complete as well, but the hole is in the declining phase, thus it does not affect the identification of the peak or the minimum.

Being the pre-burst observation (Chandra 123) in phase with all the ones analyzed until now, we performed again the Rayleigh test adding this last observation to the dataset that included the sets ACIS 04, ACIS 05, XMM-Newton 2005 observation, obs. ID 7619 (Chandra) and the Swift dataset. The result is represented in figure 6.16.

The best period value is:

$$P = 24029.993 \text{ s}, \quad Z_1^2 = 12243.2,$$

and the gaussian fit to the peak leads:

$$P = 24029.9 \pm 1.8 \text{ s}, \quad \dot{P} = 0\text{s/s (fixed)}.$$

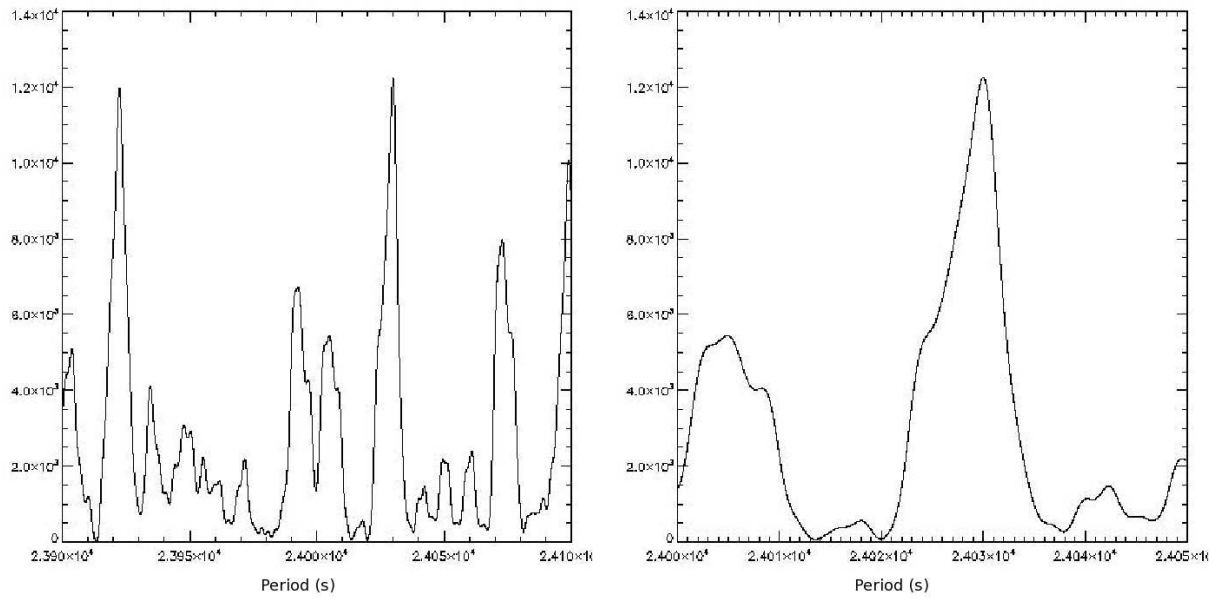

Figure 6.16: Result of the Rayleigh test for the dataset comprising all the observations since the ACIS 2004, plus the Chandra observation 123. On the x-axis, the values of the period; on the y-axis, the corresponding value of Z_1^2. Left figure: the period is comprised between 23500 s and 24500 s; right figure: closer look to the best period value: from 24000 to 24050 s.

The period is in agreement with the previous values, but as is clear from figure 6.16 this was not necessary to be expected: the gap between obs. 123 and the ACIS 04 dataset is important, ~ 5 years, and the effect of more values of the period plausibly reproducing that gap and the smaller ones between the single observations is visible by the presence of multiple peaks, all of them with comparable height. These peaks, though are clearly an emergence of aliases: they are far from the central peak, that was selected by the *Swift* dataset to be the more probable. This highlights even more the importance of the *Swift* and *Chandra* monitoring observations in order to identify unambiguously the correct period of 1E 161348-5055: short but regularly spaced observations are more fundamental than long observations but very distant from each other to constrain the period.

6.5 Considerations

The evolution of 1E 161348-5055 is remarkable: without presence of a period derivative, the pulsed profile changes dramatically both as a consequence of the outburst, and during the evolution, but does not show any phase shifts. As pointed out before, it is impossible to exclude the presence of a variable period derivative that modifies the cycle counts in the temporal gaps between the observations of integer numbers, but this eventuality is highly improbable.

Seen how dramatically the shape of the pulsed profile changes, we decided not to proceed further on with the Rayleigh tests: adding the older observations, in fact, could lead to a distortion of the results because of the presence of the intermediate peaks. Table 6.4 summarizes then all the results of the Rayleigh test performed until now.

Observations	Epoch[a]	Period	Z_1^2
Swift	2006-04-11 05:09:03	24028.822	749.734
Swift + Chandra 7619	2006-04-11 05:09:03	24028.8715	1056.48
Swift + Chandra 7619 + XMM05	2005-08-24 07:53:58.0	24030.413	2370.09
From ACIS 05	2005-01-24 13:58:33	24030.933	5074.49
From ACIS 04	2004-01-27 17:06:46	24029.735	12329

[a]In seconds, from the Chandra MJD reference (MJD=518).

Table 6.4: Results of all the Rayleigh tests done before.

Chapter 7

Discussion and Conclusions

This final chapter is an overview and summarization of the analyzes described in the previous chapters. The overall flux evolution is presented in section 7.1, followed by the relative spectral evolution (section 7.2) and the cooling models (section 7.3) under the several different scenarios available for 1E 161348-5055. Next, the temporal properties are also summarized, with the extraction of the lightcurves with the revised value of the period (section 7.4), and a few considerations on the pulsed fraction. The last section (7.5) briefly compares the results with the plausible models for 1E 161348-5055, and draws conclusions.

7.1 Flux evolution

The evolution of the X–ray flux of 1E 161348-5055 in the energy band $0.5 - 8$ keV, between 1999 and 2008 is plotted in Figure 7.1. This light curve has been computed from the array of *Chandra*, *XMM-Newton* and *Swift* observations described in detail in chapters 3, 4 and 5. As explained there, two models (double blackbody and comptonized blackbody) could equally well describe the spectral properties and evolution of 1E 161348-5055, but the first one of the two required some parameters to be frozen or linked for the fit to be successful. It was necessary then to choose a framework for the flux calculation, homogeneous for all the datasets. The choice fell on the comptonized blackbody model, and the flux reported in figure 7.1 are those derived from this model. Of course if instead we choose the double blackbody scenario, the values of the flux are perfectly compatible within the 1σ errors.

The first *Chandra* observation caught the source in quiescence in 1999. The outburst occurred between the first and the second observation (spaced out by 134.8 days), but unfortunately no activity in correspondence with the onset was detected by any of the instruments in orbit at the time.

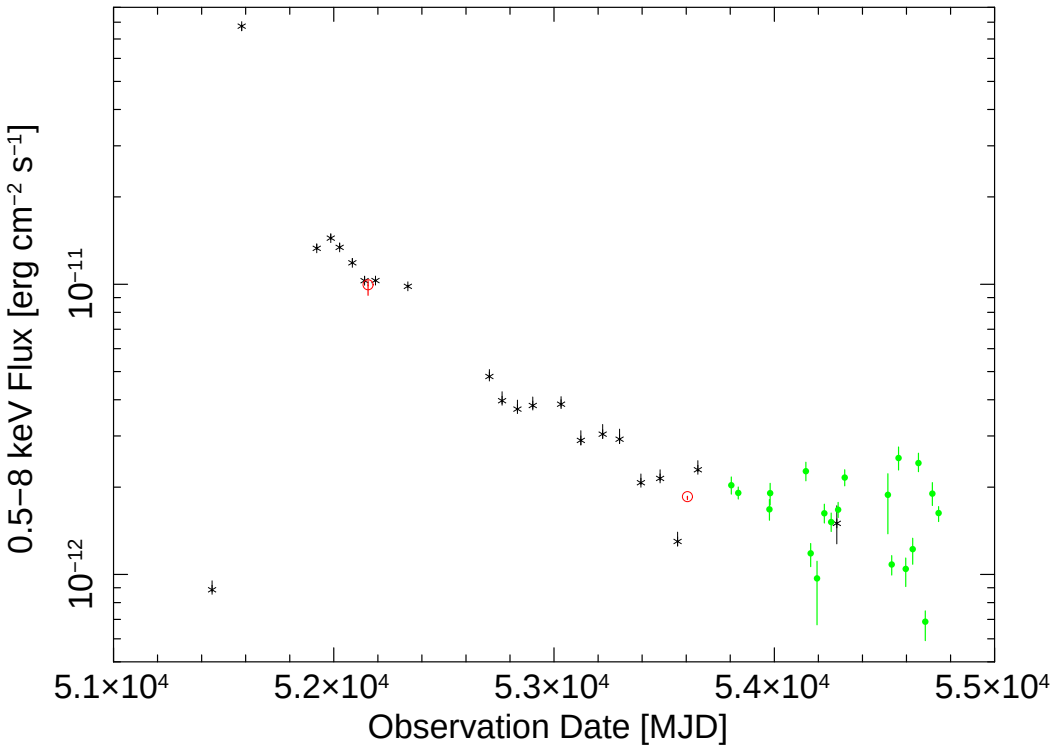

Figure 7.1: The X-ray flux of 1E in the energy band $0.5 - 8$keV. The plot spans the time interval from 26th September, 1999 to 7th October 2008. The symbols refer to different instruments: black asterisks, *Chandra*; red hollow circles, *XMM-Newton*; green full circles, *Swift*.

7.1.1 The Light Curve of 1E 161348-5055: Emitted Energy

After the outburst, the light curve has been steadily declining, almost approaching the 1999 level. It is easy to estimate the energy radiated by the outburst: if we assume that the 1999 luminosity is a fair and reliable estimate of the quiescent flux of 1E 161348-5055, a simple integration over time of the flux in excess with respect to the 1999 observation provides a reliable estimate of the total emitted energy in the X-ray spectral band we are considering. Assuming an isotropic emission from a distance of 3.3 kpc, we find $E_{\rm tot} = 3.5 \times 10^{42}$ erg in the spectral band $0.5 - 8.0$ keV.

This is clearly a lower estimate of the total energy output. First of all, our X-ray data only covers a limited spectral energy band: we cannot rule out that the bulk of the energy was emitted in a spectral band inaccessible to us, e.g. in γ-rays. Moreover, we do not know when the X-ray emission peaked, so the energy emitted soon after the outburst peak is probably missing from the count. In view of these uncertainties, and keeping into account that no detection was

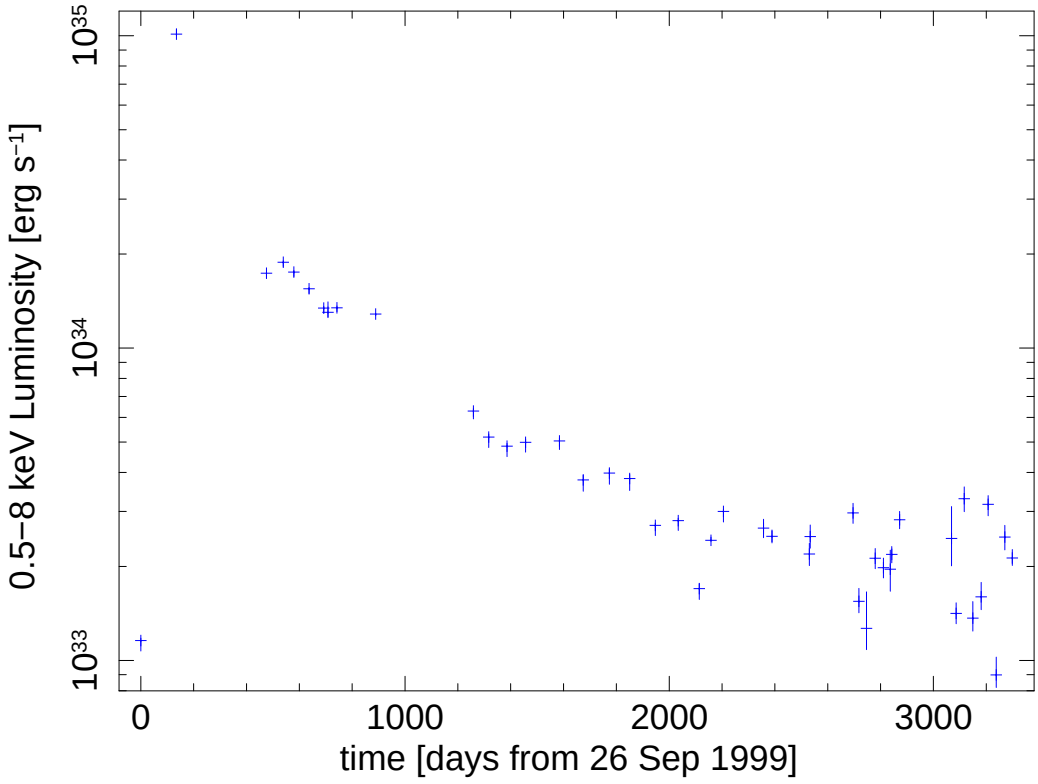

Figure 7.2: The luminosity in the energy band $0.5 - 8.0$keV, converted from the flux of Figure 7.1, assuming that the source emits isotropically from a distance $D = 3.3$ kpc.

claimed of 1E 161348-5055 in other energy bands in correspondence to the peak, we consider the estimate 3.5×10^{42} erg to be not far from the real value of the energy output.

In order to address the evolution of the light curve of 1E 161348-5055 it is easier to work with the fluence (or the energy $E(< t)$ emitted before a given time t) instead of the instantaneous value $F(t)$ of the flux (or the luminosity). The cumulant energy in fact is more regular, because its derivative (the flux or luminosity) is known, so for numerical reasons it is better to deal with.

Figure 7.3 plots the energy $E(< t)$ of the outburst emitted before the time t, as measured from the 1999 pre-outburst observation. The outburst emitted $\sim 30\%$ of the total energy (as of June 2008) before the peak *Chandra* observation (ID. 970), i.e. within 134.8 d from the outburst onset. At the time the *Chandra* monitoring started (with obs. ID 1040, in 2001; in figure 7.3 it corresponds to the first point of the first group of observations close to each other), the energy output had already reached $\sim 70\%$ of the total. The remaining $\sim 30\%$ has been emitted in the following ~ 8.4 yr, in a much gentler fashion.

We pass to analyze in some detail the light curve of 1E 161348-5055. In

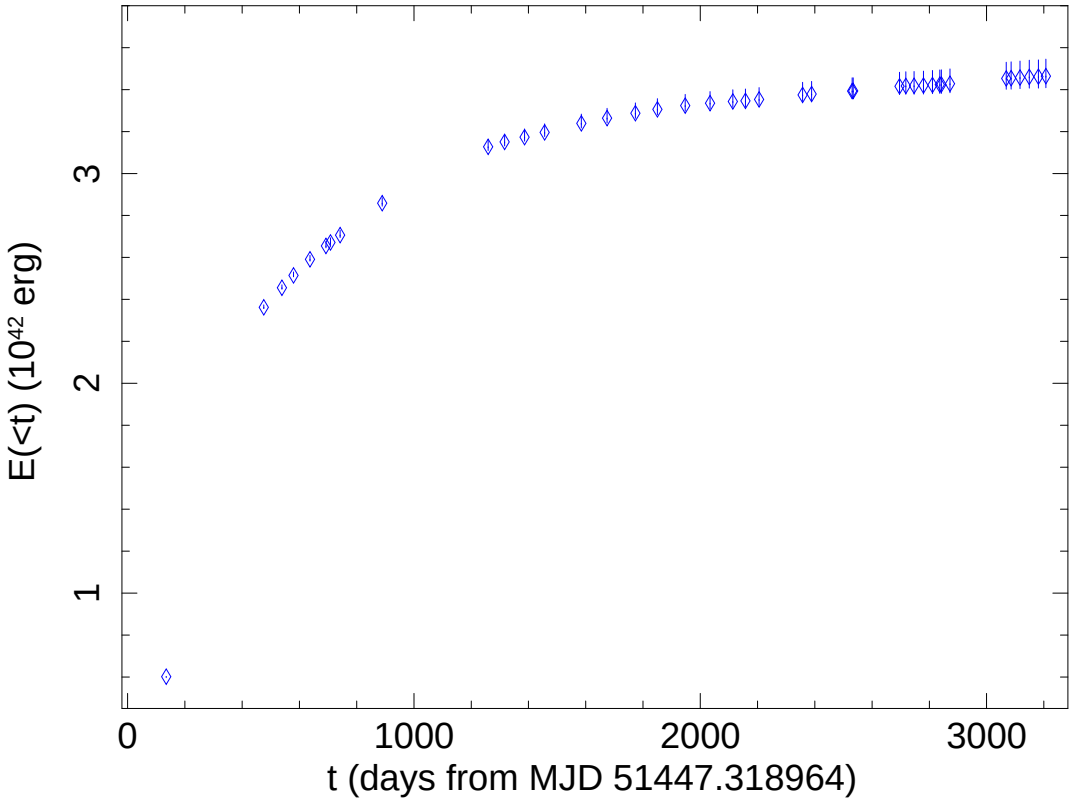

Figure 7.3: Cumulant energy output $E(< t)$ in excess with respect to the pre-outburst luminosity in the spectral band $0.5 - 8.0$ keV.

particular, we aim to find a suitable fitting function able to reproduce the evolution of $E(< t)$ with time. With trial and error, we find that the best fit is provided by the following function:

$$E(<t) = \begin{cases} 0 & \text{if } t < t_0 \\ K_0 & \text{if } t_0 < t < t_1 \\ K_0 + K_1(t-t_1)^{\alpha_1} & \text{if } t_1 < t < t_2 \\ K_0 + K_1(t_2-t_1)^{\alpha_1} + K_2(t-t_2)^{\alpha_2} & \text{if } t > t_2 \end{cases} , \qquad (7.1)$$

where the time t is measured from the first *Chandra* observation.

Despite its appalling look, the meaning of this function is quite simple. The outburst onset occurs at the time t_0. Before it, $E = 0$. The outburst injects an impulsive energy load $E_0 = K_0$ at $t = t_0$. Later on, the new power-law component $E_1 = K_1(t - t_1)^{\alpha_1}$ sets in. It remains active until the later time $t = t_2$, when it quenches and is replaced by the new power law component $E_2 = K_2(t-t_2)^{\alpha_2}$. It is very important to remark that the components E_1 and E_2 are not simultaneously active. E_2 turns on only after E_1 has switched off.

The data, as well as the best fitting function 7.1.1 are plotted in Figure 7.4. The quality of the fit is satisfactory: $\chi^2/\text{dof} = 1.8/33$. Note that if we allow

the components E_1 and E_2 to be active together, the fit worsens significantly: $\chi^2/\mathrm{dof} = 68.4/33$. In particular, the fitting procedure fails to model the points at $t \gtrsim 1000$ d, since the best-fit value of the exponent α_2 is too high.

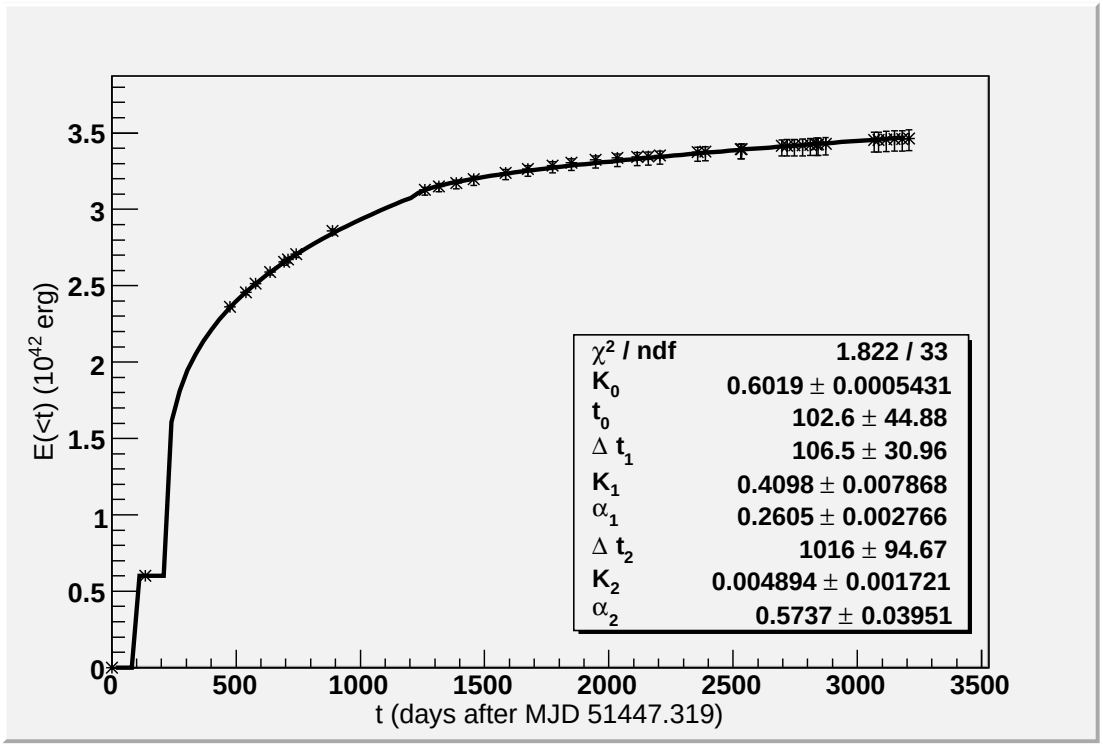

Figure 7.4: Best fit parameters of the function 7.1.1 to the energy cumulant. The parameters meaning is discussed in the text: here $\Delta t_1 = t_1 - t_0$ and $\Delta t_2 = t_2 - t_1$.

According to the best-fit parameters, the outburst occurred $t_0 = 103 \pm 45$ d after the first *Chandra* observation. According to our model, it was an impulsive episode; it is impossible to further refine this part of the model, on account of the poor coverage of the early outburst evolution. This impulsive component emitted about 6×10^{41} erg in a very short time interval.

At the instant t_1, $\Delta t_1 = 106 \pm 31$ d after the outburst, a new component of the flux emerged. This component behaves as an offset power law of index $\alpha_1 = 0.260 \pm 0.003$. The energy flux associated to this component decays as $F_1 \propto (t - t_1)^{\alpha_1 - 1}$, i.e. with an exponent $\beta_1 = \alpha_1 - 1 \sim -0.74$. This component lasted for $\Delta t_2 = 1016 \pm 95$ d, and it injected $E_1 = 2.5 \times 10^{42}$ erg. At $t = t_2$, i.e about 1122 d after the outburst, the component E_1 died out, and was replaced by the component E_2. The flux decay after this time varies as $(t - t_2)^{\beta_2}$, where $\beta_2 = \alpha_2 - 1 = -0.42$. In other words, the decay of this component is slower. This component, still active, has radiated the energy 3.8×10^{41} erg as of June 2008.

As the source has been observed with different telescopes, in principle some

cross-miscalibration may mimic the effect of a new component on the light curve, so it is straightforward to dispute about the reliability of the result. This though does not appear to be the case, because the dataset were analyzed with the same model, and before proceeding to a new analysis the results were verified to be compatible with those obtained before. Moreover, in chapter 5 it is explained how the modelization of the supernova remnant is obtained from the *XMM-Newton* data, and transferred to the Swift data. As an additional prove, in that occasion the fluxes of corresponding regions of the SNR were calculated from the 2005 *XMM-Newton* observation and some of the *Swift* observations, and they were found to be in agreement within the calibration errors.

All the possible "discontinuities" of the fit function lie within the range of observations covered by *Chandra*, and not between observations obtained through different instruments, so they are not due to this latter effect. The *XMM-Newton* observations, moreover, are situated one between the *Chandra* observations of 2001 and 2002, and the second at the end of the Chandra monitoring; their flux is in fair agreement with that of the *Chandra* observations which, it is useful to remember, being short only sample a part of the periodic emission, and thus are subjected to modulation. Finally, the *Swift* observations sample the tail of the light curve, and the last *Chandra* observation (ID. 7619) falls in between them. It is a very long observation, so its flux should correspond to the average of the *Swift* observations flux, and this is what appears already at first sight from figure 7.1, where more in general there is no jump between the fluxes estimate from the different instruments.

7.2 Spectral evolution

The reanalysis of 1E 161348-5055 spectra from all the available observations made in chapters 3, 4 and 5 allowed us to better model each spectrum, and the secular evolution during a baseline lasting as long as 9 years. In particular, we chose to study the supernova remnant together with the source, keeping the abundances parameters equal for all the observations. This, as a consequence, freed us from the background subtraction, which is very dangerous in this case since the supernova remnant shows marked spatial variability. The estimates for the neutron star parameters are thus more reliable, because the do not depend on the particular choice of the background in the observations.

In detail, the parameters that are more affected by a wrong background subtraction are the hydrogen column and, as a consequence, the temperature of the comptonized blackbody model (or the cold temperature of the double blackbody).

The hydrogen column is $1.2-1.5\times10^{22}$ cm^{-2}, consistent for both the XMM-Newton observations (that are strongly affected by the supernova remnant) and the Chandra observations. The importance of determining as most precisely as possible the hydrogen column in the direction of 1E 161348-5055 is due to the

fact that the study of the hydrogen column is a very powerful tool to distinguish between the isolated magnetar and the binary scenario. In particular, the phase resolved analysis and the comparison between the 2001 and 2005 spectra of 1E 161348-5055 could spread light: if the hydrogen column were found to vary between the minimum and the maximum, or between 2001 and 2005, this would be an uncontrovertible proof in favor of the binary system.

Unfortunately this is not the case: even though in chapter 3 a careful spectral analysis of the 2001-2005 spectra, and of the maximum and minimum of the folded lightcurve was performed, the situation remained ambiguous. For what concerns the time-integrated spectra, the variation could not be reproduced by a change of the n_H alone, and when two parameters were let free to vary, also situations where the hydrogen column was constant led good results. Examining the phase resolved spectra, instead, turned out not to be so straightforward: first of all the reduced statistic implied that a single component model was enough to describe the spectra, but in that case no variability could be claimed because it was likely to be an artifact due to the different model. Next I introduced a second blackbody, allowing only the hydrogen column to vary, but the fit could not satisfactorily reproduce the spectral variations ($\chi^2_{red} = 2.09$ for 166 degrees of freedom). Conversely, allowing all the parameters to vary but the n_H yielded to a good spectral fit, but inconsistent results: the hot blackbody had temperature compatible with zero. The physically meaning trials had either the normalizations linked to each other, or the temperature frozen to the values derived from the time integrated spectrum, and showed both that constant and variable n_H between the maximum and the minimum could reproduce the data. It is likely then that the n_H variations depend very much on the choice made to parameterize the spectra.

When the n_H varied, this was in opposite way as one could expect from a standard accreting scenario (see table 3.10). Instead of showing an increase of n_H with the minimum phase, it decreased compared to the maximum. This instead could have been compatible with a Low Mass X-ray Binary in which the neutron star accretes from the wind of the companion, if it were not ruled out by the infrared observations: it was found, in fact, that the companion mass consistent with its non-detection is too small to produce enough wind to power the X-ray emission.

For all these reasons the evidence of a hydrogen column variations had to be rejected, concluding with no answers about the n_H variability: none of the two scenarios can be excluded.

The rationale of our next modelization with a comptonized blackbody is that we would like to associate one single temperature to the NS surface. We therefore assume that the hard component in the spectrum is due to the Compton scattering of the source's thermal photons due to their interaction with a cloud of hot plasma surrounding 1E 161348-5055. The spectral fit is in broad agreement with the data.

In figure 7.5 the evolution of the blackbody temperature of the comptonized blackbody model is reported: the temperature decay is smooth and without jumps or apparent discontinuities in between the datasets, that are represented in black for *Chandra*, red for *XMM-Newton* and green for *Swift*. One caveat: the temperature of the Chandra Obs. ID 970 is missing because, as discussed in chapter 4, its spectrum is radically different compared to those of the monitoring observations. This was partially expected because the outburst is likely to have changed (at least temporarily) the physical properties of the neutron star. As a matter of fact, we are in front of an event that changed dramatically the phenomenology of 1E 161348-5055: first of all, the peak is softer with respect to the rest of the emission. After the soft intense peak observations, the monitoring ones reveal a harder blackbody whose temperature is slowly returning back to the pre-outburst value.

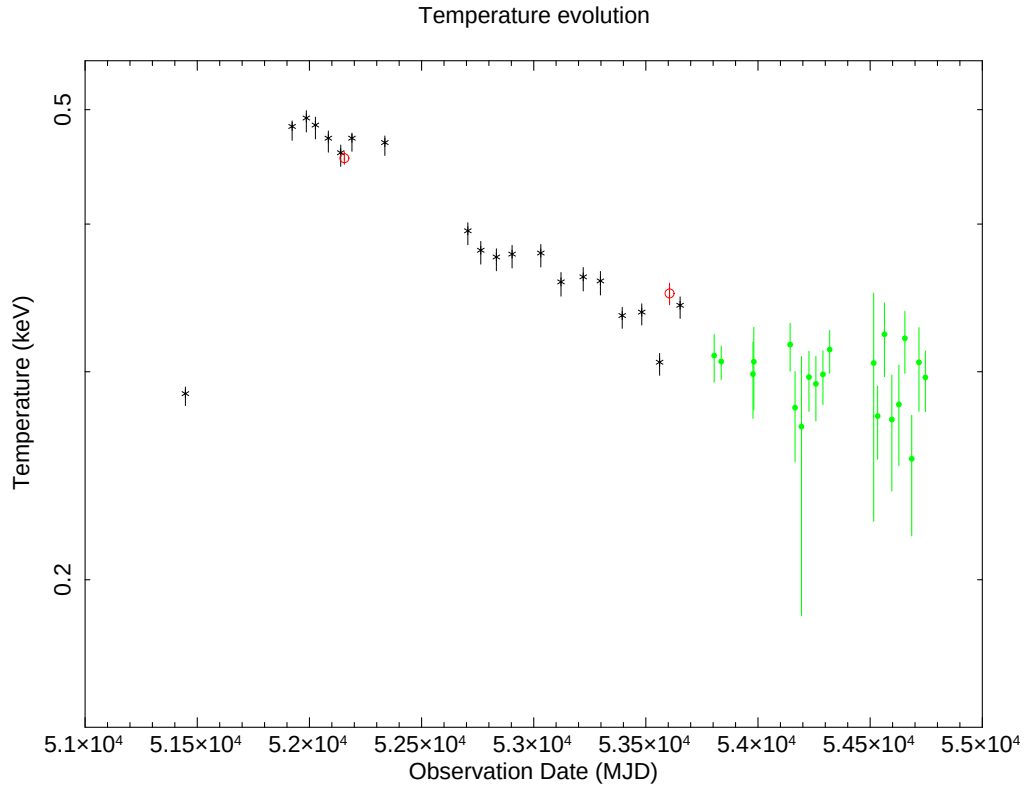

Figure 7.5: Evolution of the NS surface temperature from the comptonized blackbody model, as of June 2008.

In the case where it was possible to perform a reliable fit with a double blackbody model, an analogous plot for the temperature evolution was built (see chapter 4), but since in that case only a limited set of observations was available, we preferred to go on with the analysis with the complete dataset.

The temperature of the blackbody is smoothly declining with time, suggesting that a portion of the crust of the magnetar was heated and now is releasing

energy fast through a cooling process. Since there was no trace of the event that originated the brightening of 1E 161348-5055, no a priori knowledge on the mechanism that caused this phenomenon is available. Nonetheless, no or little doubts arise on this interpretation, seeing how smooth the decline of the temperature is. This is also compatible with the phase-resolved analysis: in chapter 3 we studied both the phase resolved spectra of the 2001 and the 2005 *XMM-Newton* observations. In 2001 the peak and dip differ for the normalization of the warm blackbody, while the hot blackbody alone is not sufficient to explain the variations, nor the hydrogen column was. For what concerns the 2005 observation, the spectral differences between the maximum and the minimum of the folded profile of 1E 161348-5055 are well modeled by an increase in either the normalizations or the temperatures corresponding to the maximum. This signature is likely to be originated from a rotating hot spot on the surface of 1E 161348-5055, the modulation arising with more portion of the hot spot visible from the Earth's line of sight.

For a distance of the source of 3.3kpc we find that the radius of the black body emitting area in the *Swift* monitoring observations is:

$$R_{\rm BB} \sim 2.5 \text{ km}, \tag{7.2}$$

smaller than the radius of a neutron star.

In order to gain insight in what really happened between 1999 and 2000 on 1E 161348-5055 it is especially important to try and model the decay of the flux (and temperature) curve as a function of time.

7.3 Cooling

In this section I present in some detail the results of the analysis of the light curve decay of 1E 161348-5055 after the 1999 outburst.

The exact physical mechanism driving the outburst is still unknown. As outlined in chapter 2, both the two models available for 1E 161348-5055 predict it is endowed with a magnetar-like magnetic field ($10^{15} - 10^{16}$ G).

According to Li, 1E 161348-5055 is an isolated magnetar braked to its current period by a relic disc left over by the supernova explosion [Li(2007)]. In this model the X-ray outburst is similar in nature to the outburst observed in other magnetars as well, i.e. the sudden release of a hefty amount of magnetic energy.

An alternative model put forward by Pizzolato et al. suggests that 1E 161348-5055 is a system akin to a *Polar* (a.k.a *AM Herculis*) cataclysmic variable, where a magnetar is in synchronous (or nearly synchronous) orbit with a lower main sequence star [Pizzolato et al.(2008)]. According to this model, the outburst may still have been triggered by the release of magnetic energy, but also by a sudden accretion episode from the companion star.

Studying and modelizing the decay is very important because it can give us insight in what actually happened on 1E 161348-5055: this is especially needed

in view of the fact that we do not even know what kind of object is hosted inside RCW103, whether it is an isolated magnetar or a magnetar in a binary system. In all these cases one has to distinguish whether the energy released during the process was first stored in the magnetosphere or in the crust of the magnetar itself, and if the phenomenon was magnetically driven or accretion driven.

In particular, what we can learn from the decay is:

1. assuming that all the injected energy has been (or will be) radiated, we may evaluate the total energy involved in the outburst.

2. In the magnetic release scenario, we may estimate the involved magnetic field and/or the volume of the NS interested by the energy release. We can then check for consistency with the expected structure of magnetic fields in a magnetar. This is the case if the energy *before* outburst was stored in the NS crust. If instead it was stored in the magnetosphere (e.g. Lyutikov, [Lyutikov(2006)]), this is a different situation that needs to be treated aside.

3. In the accretion framework, the enhanced luminosity follows an accretion episode. It may be either impulsive or slow. In the first case, the decay of the light curve is due to an internal relaxation process. In the second case, the light curve closely follows the decay of the mass accretion rate.

4. Still in the accretion framework, we can evaluate the accreted mass required by the total radiated energy. We can check if it is consistent with a stellar outburst from the companion (impulsive load) or an enhanced stellar wind (slow load).

5. In the impulsive load model, we can estimate the volume of the NS interested by the episode. We will check if it is more consistent with the release of magnetic energy or with heating by accretion.

Admittedly, the best-fit parameters are quite sensitive to the precise choice of the spectral model. For this reason we do not claim that the results presented in this thesis do not leave room for alternatives. We just conclude that the scenario we envisage is probable, and *consistent* with the available data.

The evolution of the X–ray flux of 1E 161348-5055 in the energy band $0.5 - 8.0$ keV, between 26th September 1999 and 7th October 2008 is plotted in figure 7.1. The first *Chandra* observation (taken in 1999) caught the source in quiescence. The outburst occurred before the second observation, obtained 134.8 days after the first one. After the outburst, the light curve has been steadily declining, slowly approaching the 1999 level.

We estimated in paragraph 7.1 the energy radiated by the outburst by assuming that in 1999 1E 161348-5055 was quiescent. A simple integration over time of the flux in excess with respect to the 1999 observation provides a reliable estimate of the total emitted energy in the X–ray spectral band we

are considering. Assuming an isotropic emission from a distance of 3.3 kpc, we find the radiated energy $E_{\rm rad} \sim 3.5 \times 10^{42}$ erg in the spectral band $0.5-8.0$keV. In the next paragraph we investigate on the possible origin of this energy.

7.3.1 Magnetic vs. Accretion-powered Outburst

In view of the available models, the energy source of the outburst can be explained in two ways:

1. The energy is due to the accretion of a lump of matter, ejected from the companion star, or possibly released by an instability in an accretion disc (fossil or fed by the companion).

2. The energy has been released by a magnetic reconnection episode. The pre-outburst energy may be stored either in the NS crust, or in the magnetosphere. It is to be seen if the energy released by the outburst is buffered in the NS crust as heat, or is immediately radiated away. Clearly, in the first case the X-ray flux is expected to be decaying much slower than in the second case.

Accretion-powered Outburst

If the luminosity is accretion-powered, then the amount of accreted mass ΔM required to generate the energy $E_{\rm tot}$ with efficiency η_A is:

$$E_{\rm tot} = \eta_A \, \Delta M \, c^2, \tag{7.3}$$

where

$$\Delta M = 4 \times 10^{22} \, {\rm g} \, \left(\frac{\eta_A}{0.1}\right)^{-1} \, \left(\frac{E_{\rm tot}}{3.5 \times 10^{42} \, {\rm erg}}\right). \tag{7.4}$$

If the luminosity of 1E 161348-5055 is accretion-powered, it is quite clear that the responsible of the outburst is some instability in the mass accretion rate. The occurrence of such an instability is quite unlikely in a fossil disc, but may occur in a binary system. Current models for the donor stars in CVs predict that their mass loss rate may increase by a factor $\sim 10^2$ (corresponding to the luminosity leap in 1E 161348-5055) over $\sim 10^5$ s, to slowly settle back to quiescence (see e.g. Frank [Frank et al.(2002)], and references therein).

We then face two possibilities within this framework:

1. the binary system has no disc, but the neutron star directly accretes from the donor star; in this case the rise time has the same temporal scale of the development of the mass instability. The decay time instead can have two origins: it has to be compared with either the mass transfer rate, in case the accretion is direct (and emission is originated from the mass itself), or with the relaxation time of the crust, in case the transferred mass hits and heats the surface of the neutron star and the emission is coming from the surface.

2. The binary is wide enough to have room for an accretion disc around the neutron star, and we can be facing a transient accretion disc, or a disc instability where a fraction of the inner disc mass is suddenly accreted onto the star.

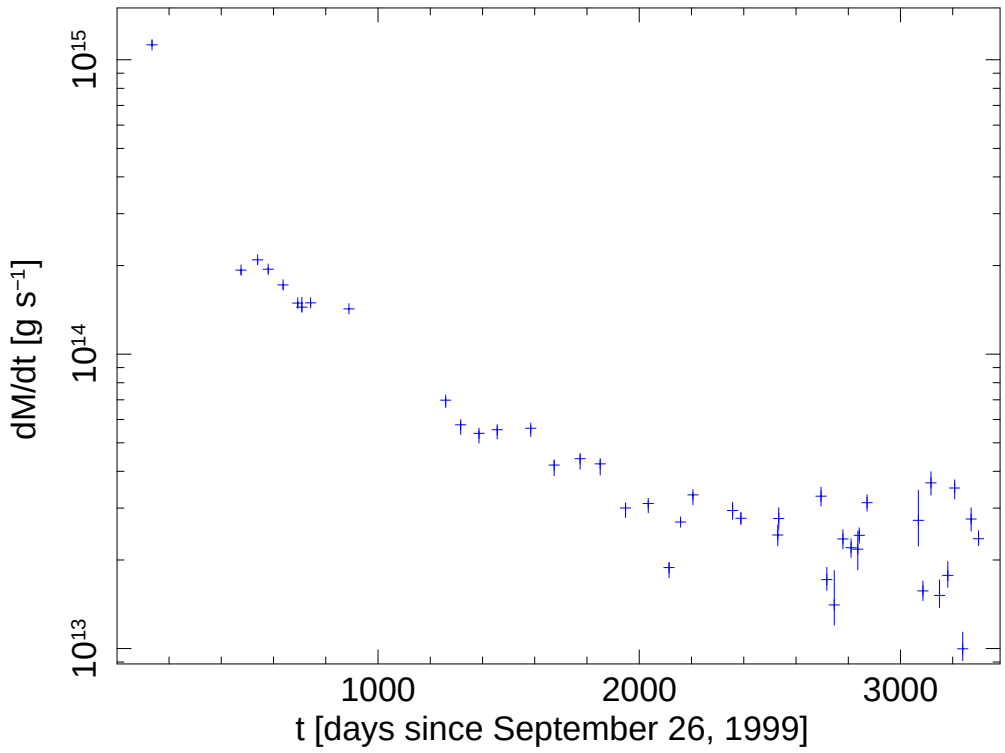

Figure 7.6: The accretion rate $\dot{M}$ on the NS, under the assumption that the light curve tracks the instantaneous accretion rate.

In case 1) (**direct accretion**) the outburst rise time is clearly the characteristic time scale for the development of the mass transfer instability (MTI) from the donor star. The decay of the light curve takes ~ 10 yr, much longer than the relaxation time of any reasonable MTI. We must then conclude that the decaying light curve does not track the declining mass accretion rate, but follows a relaxation process, most likely in the NS crust, heated by the impulsive accretion of the mass ejected by the donor star.

Is this scenario viable? The best argument against it is the huge amount of mass (7.4) which must have been transferred from the donor star in a single instability episode. The required mass (7.4) exceeds by seven orders of magnitude the mass of an average solar coronal mass ejection. It is quite unlikely that an amount of mass as large as 4×10^{22} g may accrete on the neutron star *in a single shot*. For this reason, the direct accretion from the companion star is not very likely, and we shift to consider the case 2), i.e. the NS **accretes from a disc**.

Some constraints on the possible existence of a disc are set by the size of the binary system. As outlined and discussed by [Pizzolato et al.(2008)], we assume that the companion is a $0.4\,M_\odot$ star, and that the NS harbors a magnetic field of 10^{15} G. Within the *Polar* star model for 1E 161348-5055, the maximum allowed orbital period is ~ 12 hr. These constraints leave little room for an accretion disc, which (if any) must be bounded between the inner radius $R_{\rm in} \sim 2 \times 10^{10}$ cm (the Alfvén radius) and $R_{\rm out} \sim 10^{11}$ cm (the size of the NS Roche lobe).

The evolution of truncated discs like this has been studied e.g. by [Lipunova & Shakura(2000)], and the fundamental characteristic of this scenario is that the mass is slowly accreted onto the neutron star. For this reason the X-ray luminosity is related to the mass transfer rate.

For our set of parameters such a disc has a mass of $M_{\rm disc} \sim 10^{25}$ g, so it may provide enough mass to power the source. According to [Lipunova & Shakura(2000)], after a transient time the disc mass decreases as $M_{\rm disc} \propto t^{-\zeta}$, where the index ζ depends on the opacity of the disc matter, being $\zeta = 3/2$ for Thomson scattering and $\zeta = -7/3$ for free–free opacity. As this mass accretes on the neutron star surface, it powers the *bolometric* luminosity $L_{bol} \propto |\dot{M}_{\rm disc}| \propto t^{-\zeta-1}$.

At a first glance, then, it would seem that also the X-ray luminosity would decay with time as a power law, in agreement with the observations. Actually, this is not the case. Assuming that the impinging matter powers a black-body radiation, its effective temperature is of a fraction of keV, and decays as $T_{\rm eff} \propto t^{-\zeta/4}$. The X-ray spectral window $0.5 - 8.0$keV, therefore, only may capture the photons emitted in the Wien tail of the black body; the X-ray spectral luminosity in the Wien tail is:

$$L_X(E) \propto \mathrm{e}^{-E/T_{\rm bb}} \propto \mathrm{e}^{-K\,t^{\zeta/4}}, \tag{7.5}$$

(where K is a constant), i.e. the luminosity decays faster than an exponential in in the relevant X-ray window. We may therefore conclude that the available X-ray data do not support the scenario of a transient accretion disc, since it is expected to decay much faster than observed.

The accretion model for the outburst may encompass a further case: the **disc instability**. In this scenario, the inner rim of the disc becomes unstable (due to some unspecified reason), and suddenly accretes on the neutron star. In this case the impinging matter may impulsively heat the crust, and the long decay of the X-ray luminosity is due to the crust thermal relaxation to its pre-outburst state, and not to a continuous mass transfer as in the transient accretion disc case. The instability develops on the thermal diffusion time of the inner disc. We assume that the fraction of the disc involved is the innermost ring, with radial thickness d.

The mass of this ring is

$$M_{\rm ring} \sim 2\,\pi R_{\rm in}^2\, d\, \Sigma, \tag{7.6}$$

where Σ is the ring surface density. The instability develops on a thermal

diffusion time (see e.g. [Frank et al.(2002)])

$$t_{\rm th} \sim \frac{c_s^2}{v_K^2}\,\frac{R_{\rm in}^2}{\nu}, \tag{7.7}$$

where c_s is the sound speed in the ring, v_K is its keplerian velocity, and ν is the disk kinematic viscosity.

Since the instability propagates as a diffusion process,

$$d^2 \sim \nu\, t_{\rm th}. \tag{7.8}$$

Inserting the expression (7.7) we find

$$d \sim c_s\, R_{\rm in}/v_K, \tag{7.9}$$

and the ring mass

$$M_{\rm ring} \sim 2\,\pi\, R_{\rm in}^2\, \Sigma\, c_s/v_K. \tag{7.10}$$

Inserting some typical values, we obtain an estimate of the mass an instability may accrete before dying out:

$$M_{\rm ring} \sim 3{\times}10^{20}\ {\rm g}\ \left(\frac{M_{\rm ns}}{1.4\,M_\odot}\right)^{-1/2}\ \left(\frac{R_{\rm in}}{2\times10^{10}\ {\rm cm}}\right)^{5/2}\ \left(\frac{T}{10^4\ {\rm K}}\right)^{1/2}\ \left(\frac{\Sigma}{10\ {\rm g\ cm^{-2}}}\right), \tag{7.11}$$

where T is the temperature of the ring. This mass is still two orders of magnitude less than the amount ($\sim 4\times10^{22}$ g) required to power the observed fluence. We may conclude, therefore, that a disc instability followed by an intrinsic thermal relaxation of the NS crust is not in agreement with the observed light curve of 1E 161348-5055after its outburst.

In summary, accretion does not seem the correct explanation for the decaying light curve of 1E 161348-5055. We must revert to another mechanism, which is most likely connected to the magnetic energy stored in the strong field of the neutron star.

Magnetically Triggered Outburst

We pass to analyze the second scenario to explain the outburst of 1E 161348-5055. We assume that the energy freed by the outburst was initially stored in the star magnetic field. As a first step, we evaluate the field required to power the observed energy.

We consider a field of strength B distributed over a volume V, which we parameterize in terms of the star volume $V_{\rm ns}$ as:

$$V = f\, V_{\rm ns}. \tag{7.12}$$

The place the energy is initially stored in may be either the NS magnetosphere, or the NS crust. In any case, we do expect $f \sim 1$ in equation (7.12).

If the magnetic energy is converted to radiation with an efficiency η_B

$$E_{\rm tot} = \eta_B \, \frac{B^2}{8\,\pi} \, f \, V_{\rm ns}. \tag{7.13}$$

Inserting the appropriate figures, we estimate the strength of the field powering the outburst

$$B = 6.5 \times 10^{12}\ {\rm G} \, \left(\frac{\eta_B}{1}\right)^{-1/2} \, \left(\frac{f}{0.5}\right)^{-1/2} \, \left(\frac{R_{\rm ns}}{10\ {\rm km}}\right)^{-3/2} \, \left(\frac{E_{\rm tot}}{3.5 \times 10^{42}\ {\rm erg}}\right)^{1/2}. \tag{7.14}$$

The above formula with the factor $f = 0.5$ is *exact* if the magnetic energy is initially stored in a dipolar field outside the star. The key result is that –even for small f– the field required to power the observed outburst is a fraction of the overall NS field, estimated in $10^{15} - 10^{16}$ G.

7.3.2 Where Was the Outburst Energy Stored?

This analysis of course does not tell anything about the place the magnetic energy is initially stored in. The two alternatives are

1. The NS magnetosphere
2. The NS crust

NS Magnetosphere

If the magnetic field is outside the star, the outburst was most likely triggered by magnetic reconnection, whose characteristic time scale –if comparable to what observed in the Sun– is of few minutes up to a hour. The energy is then loaded impulsively, and it may accelerate the surrounding plasma, which is swept away, similarly to what occurs in a solar coronal mass ejection. This is unlikely to occur in the present case. First of all, the ejected matter must keep optically thick for a long time ($\sim$ 3000d), since the X-ray emission is always roughly described by a black body. Second, the ejected mass would dissipate within days, and this is at variance with the long duration of the post-outburst X-ray emission. Finally, the normalization of the black body (calculated on the spectra with sufficient statistics) never increases with time, which would be expected for an expanding "fireball" started by a magnetic flare. We conclude that the pre-outburst energy cannot be initially stored in the NS magnetosphere. The only alternative, therefore, is that it was stored in the NS crust.

NS Crust

In this case we assume –as before– that some impulsive event freed a large amount of energy. The important difference with respect to the previous case

is that the energy may heat the NS crust, which only gradually releases it, as it relaxes back to its pre-outburst thermal configuration. In this scenario the long tail of the light curve of 1E 161348-5055 is explained as a relaxation process of the NS crust after an impulsive heating. In this section we elaborate a straightforward model for this kind of cooling and compare it to the data.

We assume a simple model for the NS. First of all, we neglect any relativistic effect. Then, we consider the NS as composed by two layers only. The outermost layer is a thin skin of degenerate matter, which radiates as a black body at the effective temperature $T_{\rm e}$. Below this we find a crust of nuclear matter, few hundred meters thick. This crust harbored the pre-outburst field, which due to some catastrophic event released its own energy.

The heat balance of the crust is quite simple:

$$C_V \, \frac{dT}{dt} = -L_\gamma + E \, \delta(t - t_{\rm ob}). \tag{7.15}$$

The left-hand side is the variation of the crust heat content per unit time: C_V is the crust specific heat and T is the crust temperature.

The causes of this variation are on the right-hand side of the equation. First, we have the photon emission rate L_γ. If the NS atmosphere is optically thick, it emits as a black body with the temperature $T_{\rm e}$, which does *not* coincide with the crust temperature T. If the heat deposition occurs over a fraction ϕ of the stellar surface, we may assume that the emission occurs from the same area, so the total luminosity reads

$$L_\gamma = 4\,\pi \, R_{\rm ns}^2 \, \phi \, \sigma_{\rm SB} \, T_{\rm e}^4, \tag{7.16}$$

where $\sigma_{\rm SB}$ is the Stefan-Boltzmann constant. The effective temperature is related to the temperature of the underlying envelope by a relation which can be approximated by a power law

$$T = T_K \, (T_{\rm e}/T_0)^w, \tag{7.17}$$

where for non-magnetic neutron stars $w \sim 1.82$ [Yakovlev & Pethick(2004)].

The last term on the right-hand side of Equation (7.15) is the heat loaded by the field. The amount of energy E is impulsively injected at the instant $t = t_{\rm ob}$ of the outburst onset. For simplicity we neglect any possible thermal coupling of the crust with the deeper layers of the neutron star.

We assume that the crust is made by N non-relativistic neutrons. The Fermi statistics yields the total specific heat (see e.g. [Reif(1965)])

$$C_V = \frac{\pi^2}{2} \, k_B^2 \, \frac{N\,T}{\epsilon_F}, \tag{7.18}$$

where k_B is the Bolzmann constant, and

$$\epsilon_F = \frac{\hbar^2}{2\,m_N} \, \left(3\,\pi^2 \, n_N\right)^{2/3} \tag{7.19}$$

is the neutrons' Fermi energy; here n_N is the neutrons' number density and m_N is the neutron mass. The total specific heat reads

$$C_V = 2\,\pi^3 R_{\rm ns}^2\; H\;\phi\;\frac{k_B^2\,T}{\epsilon_F}\;\left(\varrho/m_N\right). \tag{7.20}$$

Plugging Equations (7.16), (7.17) and (7.20) into the heat equation (7.15) we may write it in dimensionless form

$$Y^w \frac{d\,Y^w}{d\tau} = -Y^4 + q\;\delta(\tau - \tau_{\rm ob}), \tag{7.21}$$

where we have introduced the variables

$$Y = T_{\rm e}/T_0 \tag{7.22}$$

$$\tau_{\rm rel} = \frac{(\pi\,k_B\,T_K)^2\;H\;(\varrho/m_N)}{2\,\epsilon_F\;\sigma_{\rm SB}\;T_0^4} \tag{7.23}$$

$$q = \frac{2}{\pi^2}\;\left(\frac{Q}{k_B\,T_K}\right)\;\left(\frac{\epsilon_F}{k_B\,T_K}\right), \tag{7.24}$$

the dimensionless times $\tau = t/\tau_{\rm rel}$, $\tau_{\rm ob} = t_{\rm ob}/\tau_{\rm rel}$, and the energy deposed by the outburst for each particle (neutron) $Q = E/N$. Equation (7.21) must be supplemented by the initial condition

$$Y(\tau = 0) = Y_{\rm in}, \tag{7.25}$$

where the time $\tau = 0$ is The relaxation time is

$$\tau_{\rm rel} = 9.5\times 10^9\;{\rm s}\;\left(\frac{T_K}{10^8\;{\rm K}}\right)^2\;\left(\frac{H}{10^4\;{\rm cm}}\right)\;\left(\frac{\varrho}{10^{10}\;{\rm g\;cm^{-3}}}\right)^{1/3}\;\left(\frac{T_0}{10^6\;{\rm K}}\right)^{-4}. \tag{7.26}$$

Notice that –as expected– the relaxation time does not depends on the fraction ϕ over which the heat has been deposed by the field.

The analytical solution of the initial value problem (7.21)-(7.25) is straightforward. It is split in two branches due to the delta function on the right-hand side of Equation (7.21):

$$Y = \left[Y_{\rm in}^{-\zeta} + (\zeta/w)\;\tau\right]^{-1/\zeta} \qquad \tau < \tau_{\rm ob} \tag{7.27a}$$

$$Y = \left[Y_{+}^{-\zeta} + (\zeta/w)\;(\tau - \tau_{\rm ob})\right]^{-1/\zeta} \qquad \tau > \tau_{\rm ob}, \tag{7.27b}$$

where

$$\zeta = 4 - 2\,w, \tag{7.27c}$$

Y_+ is the value of Y immediately after the outburst, linked to the value

$$Y_{-} = \left[Y_{\rm in}^{-\zeta} + (\zeta/w)\;\tau_{\rm ob}\right]^{-1/\zeta} \tag{7.27d}$$

immediately before the outburst by the relation set by the delta function in Equation (7.21)

$$Y_+^{2\,w} - Y^{2\,w} = 2\,q \tag{7.27e}$$

We have fitted the solution (7.27) to the evolution of the effective temperature, obtained by the spectra as described in Section 7.2. The results are presented in Figures 7.7 and 7.8. In the first case, the index w of the $T - T_{\rm e}$ relation is a free parameter; in the second, it has been frozen to the value $w \sim 1.82$ provided by [Yakovlev & Pethick(2004)] (and references therein).

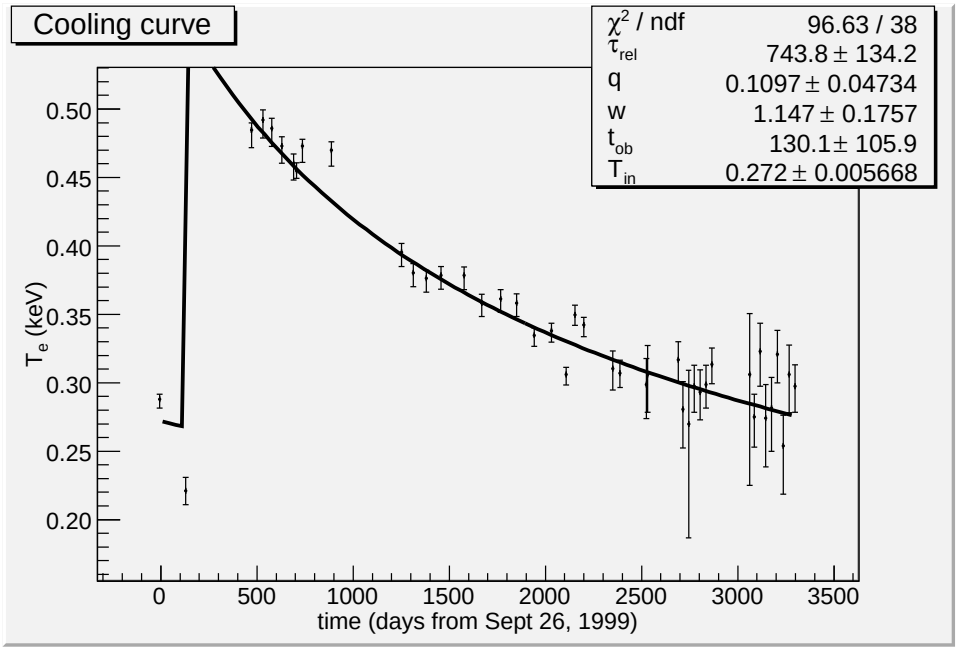

Figure 7.7: Best fit parameters for the crustal cooling following an impulsive heat load. The index w of the $T - T_e$ relation is left free

Formally, the first fitting model is better than the second (The Fisher test yields a null-hypothesis probability of $\sim 6 \times 10^{-3}$), but –also in view of our approximations– their results are similar, giving a thermal relaxation time $\tau_{\rm rel} \approx 10^3$ d, and a $q \approx 0.04 - 0.1$. The observed thermal relaxation time is consistent with the theoretical value (7.23) and $T_{\rm e} \sim 3 \times 10^6$ K, $T_K \sim 10^9$ K if $H \sim 10^2$ cm, i.e the release of magnetic energy occurs in a relatively thin layer of the crust.

Reverting to the estimate (7.14), the fraction f of the stellar volume over which the magnetic energy was stored is then $f \sim H/R \sim 10^{-4}$, we find that the field required to power the outburst is $B \sim 5 \times 10^{14}$ G, consistent with a magnetar.

In summary, we conclude that the energy budget, as well as the post-outburst thermal history of 1E 161348-5055 are consistent with a sudden injection of magnetic energy, followed by a thermal relaxation of the outer envelope

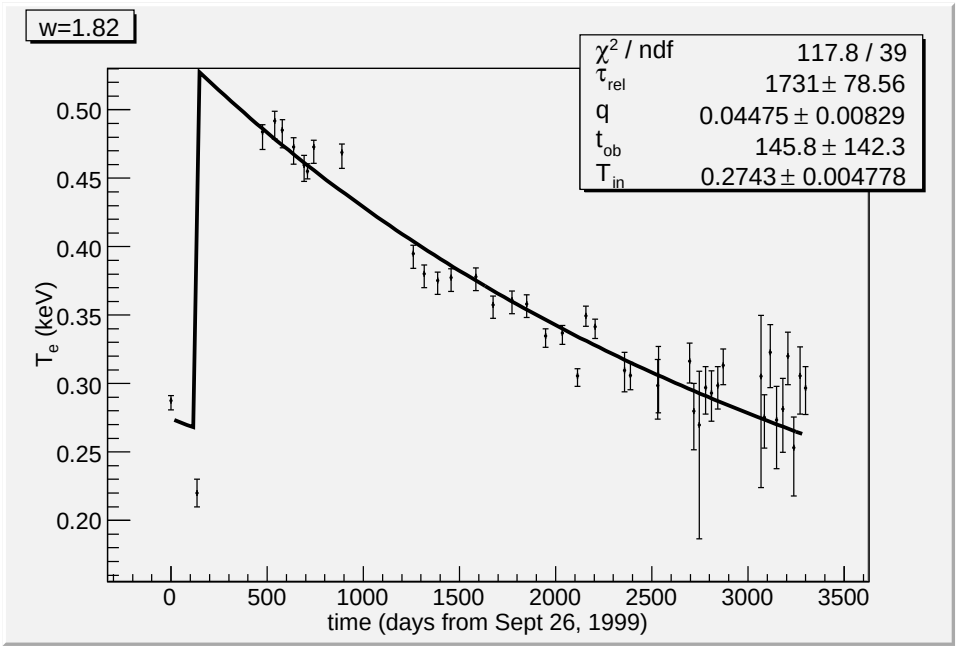

Figure 7.8: Best fit parameters for the crustal cooling following an impulsive heat load. The index w of the $T - T_e$ relation is frozen to the value $w \simeq 1.82$ given by [Yakovlev & Pethick(2004)].

of the crust.

7.4 Timing properties

Chapter 6 was dedicated to the study of the timing properties of 1E 161348-5055: after a detailed and careful analysis, we showed that the time evolution of 1E 161348-5055 is consistent with a constant period $P = 24030 \pm 2$ s, derived by means of the Rayleigh test on a dataset formed by all the observations from 2004 on: it includes 8 *Chandra* monitoring observations, plus the XMM-Newton 2005 observation, the *Chandra* observation ID 7619 made in 2007, in between the complete dataset of the *Swift* observations, used as starting point. All the observations were barycentered with each dedicated tool.

The $\sim$ 20 *Swift* observations in particular were important despite being very short, because span a wide baseline of two years: at variance with the Chandra monitoring observations, they are closer to each other (spaced by one month instead of two), and sampled the source in a long lasting period of quiescence. They are homogeneous to each other, then, allowing for a research of the period using the time of arrivals of each photon.

A reliable value and an estimate of the error was obtained, and propagated back in time towards the *XMM-Newton* 2005 observation; it was refined and, after verifying that the new error was small enough to trace the evolution

back of some more years, the whole procedure was repeated to include the ACIS 05 and ACIS 04 dataset (that is the *Chandra* observations made in 2004 and 2005). At that point all the lightcurves were extracted again, to look for eventual phase shifts in the earlier observations, that had not showed out in the years 2004-2008. Since none was present as well, the logical conclusion was that no period derivative was present, even though it still can not be excluded that there was a variable period derivative such that the gap between the observations could be fitted by an integer number of cycles. This seems a very unlikely eventuality. To be even more sure, we performed another Rayleigh test on the 2004-2008 dataset, and searched for a period derivative, but the result is perfectly compatible with null period variations.

With the refined value of the period the lightcurves have the shape outlined in figures 7.9 and 7.10.

7.4.1 Constant period

The accurate and repeated tests we performed on several datasets of observations of 1E 161348-5055 allowed to derive a precise value of the period of 1E 161348-5055: 24030 ± 2 s (see chapter 6, and the even smaller refined error of 0.1 s gave us the opportunity to trace the evolution of 1E 161348-5055 back 9 years without ambiguities, and showed that the evolution of 1E 161348-5055 from before the outburst to nowadays is reproducible by means of a constant period. Let's see what this result means with respect to the isolated magnetar vs binary system models. We are not expecting any stringent limit to be set: the binary system model generally foresees a rather large period derivative, that should be non compatible with our upper limit by several orders of magnitude. In the isolated neutron star scenario, instead, the very slow rotation of 1E 161348-5055 gives as a consequence that the period derivative has to be very small.

- In an isolated magnetar scenario, the dipole magnetic field leads to a magnetic braking that can be estimated by equating the rotational energy loss (given by equation 7.28) and the dipole magnetic braking (in equation 7.29):

$$\dot{E}_{rot} = -I\omega\dot{\omega} = -4\pi^2 I \frac{\dot{P}}{P^3} \tag{7.28}$$

and

$$\dot{E}_{brak} = -\frac{32\pi^4}{3c^3} B^2 R^6 P^{-4}, \tag{7.29}$$

where I is the neutron star momentum of inertia, assumed as $I = 10^{45}$ g cm^3, $R = 10^6$ cm is the stellar radius, P is the spin period. Equating the previous equations with a dipolar magnetic field of $B \sim 10^{14} - 10^{15}$ G and spin period $P = 24030$ s, the corresponding value of the period derivative is:

$$\dot{P} \lesssim 4 \times 10^{-14} \text{ s/s}. \tag{7.30}$$

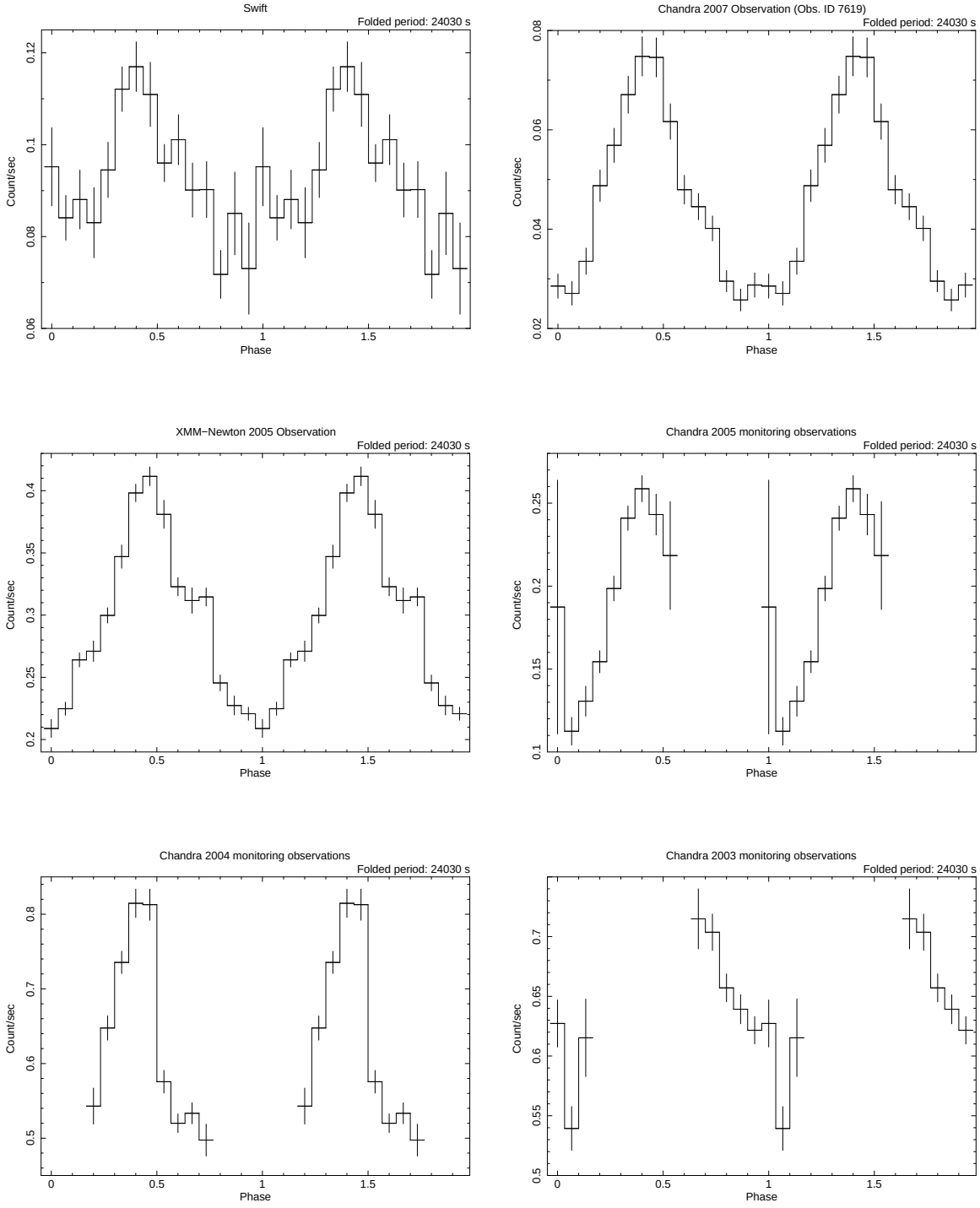

Figure 7.9: Folded lightcurves (0.2-10 keV) of the observations from 2003 to 2008. The start time is set as identical for all the observations.

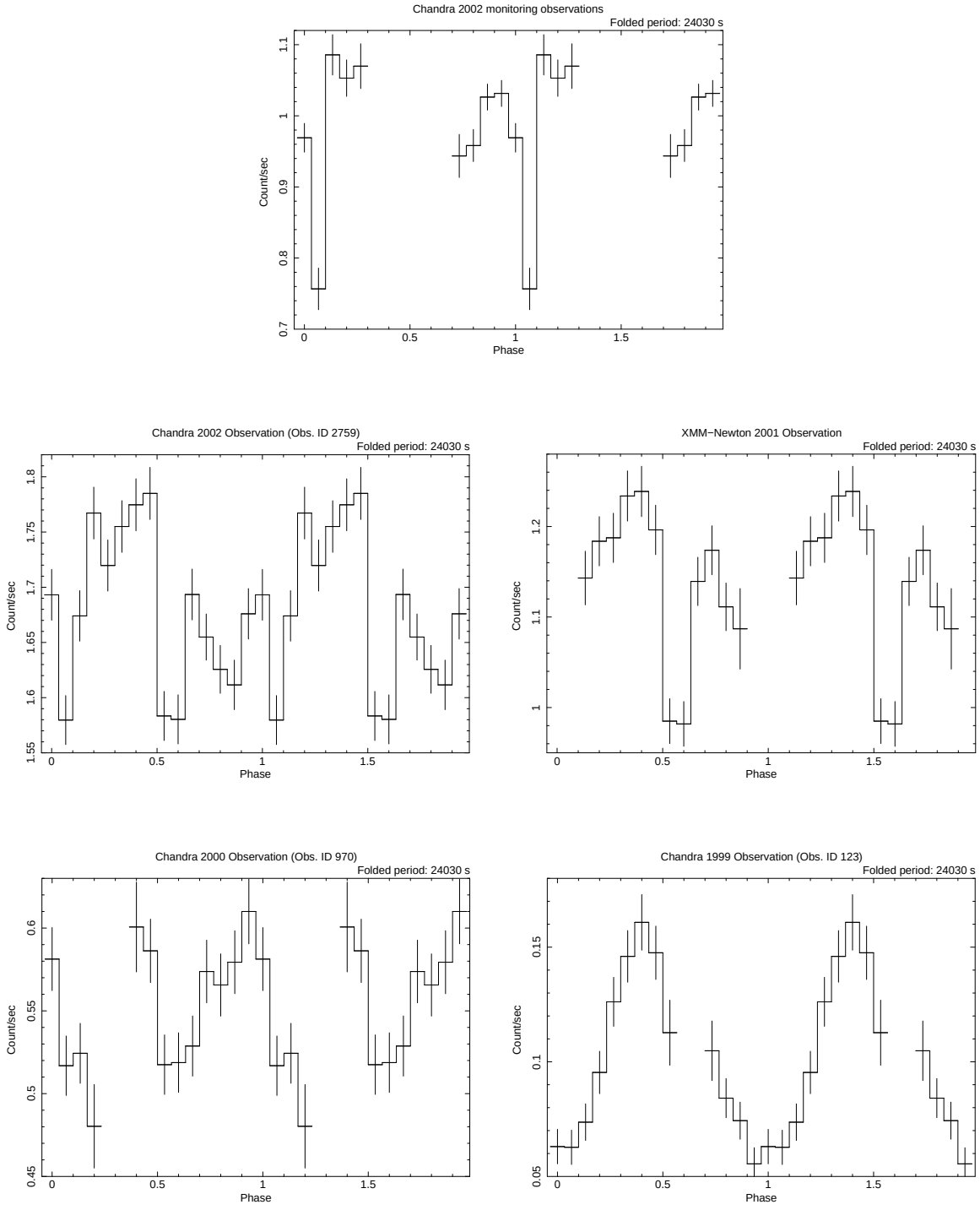

Figure 7.10: Folded lightcurves (0.2-10 keV) of the ACIS 02 dataset, the Chandra observations 2759, 970 and 123, and the XMM-Newton Observation 2001. The start time is set as identical for all the observations.

Conversely, from the evidence that the period is constant throughout the almost 10 years of data analyzed in the previous chapters, one can derive a conservative upper limit on the period derivative by allowing the period to vary within 5 times the refined error on a time baseline starting with the Chandra 123 observation and ending with the last Swift monitoring observation:

$$\dot{P} \lesssim 5\frac{\sigma_P}{\Delta t} \sim 3 \times 10^{-10} \text{ s/s}. \tag{7.31}$$

This upper limit is consistent with the hypothesis of an isolated magnetar whose period changes by means of magnetic dipole braking.

- For what concerns a binary system origin, a few scenarios should be distinguished: the case of a Low Mass X-ray Binary turns out to be inconsistent with the upper limit derived in equation 7.31. As described by [Ghosh & Lamb(1979)] an accreting scenario in a traditional LMXB that does not contain a magnetar, a relation links the luminosity produced by accretion with the period derivative induced by accretion itself:

$$-\dot{P} = 5.0 \times 10^{-5} \mu_3 0^{2/7}\, n(\omega_S)\, S_1(M)\, (P L_{37}^{3/7})^2 \text{ s/yr}, \tag{7.32}$$

where $n(\omega_S)$ is a function depending on the stellar spin angular velocity, $S_1(M)$ is a structure function depending only on geometrical properties of the star, $\mu_3 0$ is the magnetic moment in units of 10^{30} G cm^3 and L_{37} is the star luminosity in units of 10^{37} erg/s. Taking into account the peak luminosity $L \sim 10^{35}$ erg/s, canonical values for the star's geometrical properties and a magnetic field $B \sim 10^{12}$ G, the period derivative is of order $\sim 10^{-5}$ s/s, incompatible with our stringent upper limit. The situation worsens even more when allowing the magnetic moment to be as high as $\mu \sim 10^{33}$ G cm^3, value that corresponds to a magnetar-like magnetic field: the period derivative becomes $\sim 10^{-4}$ s/s. For this reason a Low Mass X-ray Binary hypothesis for 1E 161348-5055 is ruled out.

7.4.2 Pulsed profile changes

It is remarkable how the folded profiles of 1E 161348-5055 undergo such dramatic changes during the 9 years of observations. Thanks to the *Swift*, *Chandra* and *XMM-Newton* observations available, that sample the 9 year baseline, we were able to reconstruct the evolution of the period from 2008 back to 1999, obtaining as a result a very precise value of 24030 s (see chapter 6 and discussions therein), and that the value remained constant throughout the decade. This phase coherent solution allowed to compare the pulsed profiles without uncertainties due to the changing shape. The profiles of only the long observations are reported in figure 7.11, to allow a better comparison.

From an almost sinusoidal profile in 1999, the rebrightening modified the curve to have two peaks in the period, almost resembling a sinusoidal curve with period half of the original. After the outburst, in 2001 when the declining

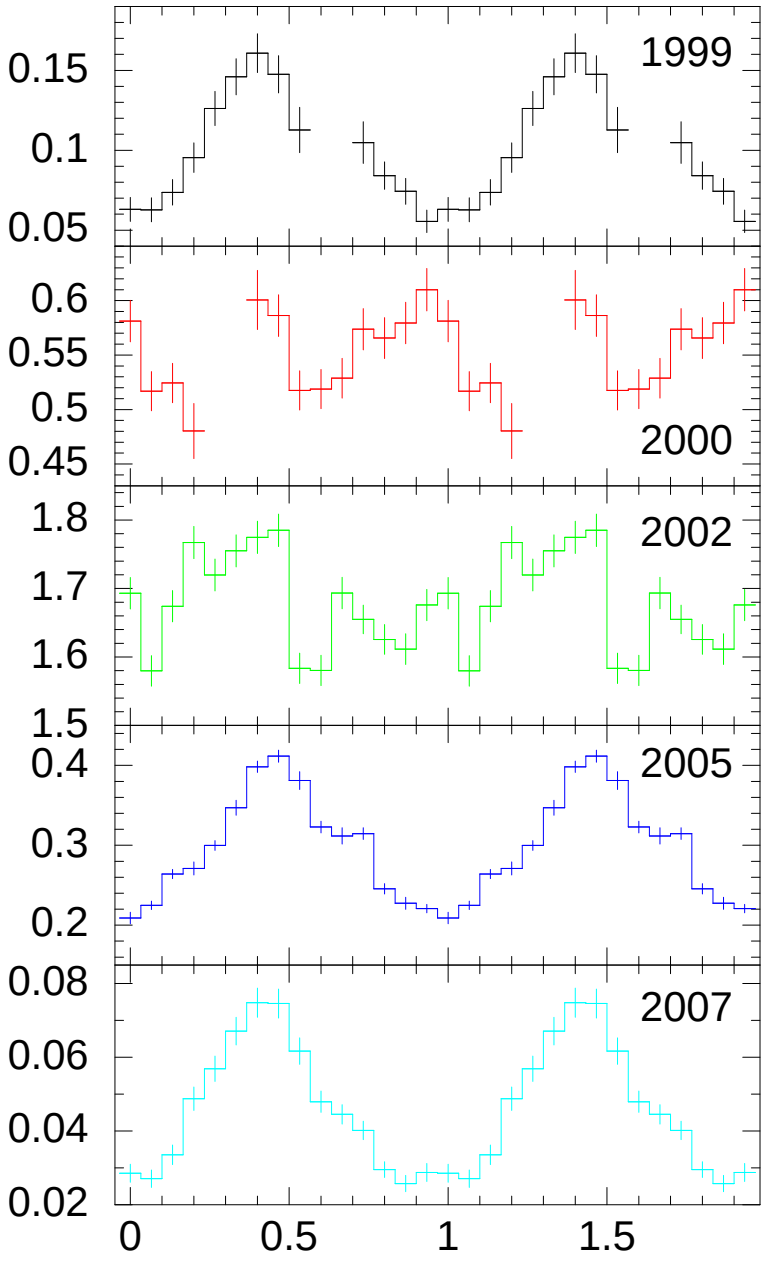

Figure 7.11: 0.2-10 keV folded profiles of the long observations available for 1E 161348-5055, from top to bottom in chronological order. The top window is the pre-burst observation, the second one is the peak detection, the intermediate ones show how different the profile became in 2001 and 2002. The last windows instead show the recover to the quiescence shape.

phase started, the profile becomes even more complicated, with four peaks per period, well visible in the *Chandra* 2002 observation (Obs. ID 2759) and partially in the *XMM-Newton* 2001 observation. In 2003 the curve has an intermediate profile, but the ACIS 03 set did not sample the part of the period where the peaks fall, so it is not possibile to check whether in 2003 the pulse profile was as complicated as in 2001 and 2002. The profile then gradually recovers the pre-outburst shape, with the same almost sinusoidal profile, but with larger minima.

In all the profiles where the phase interval [0-0.2] was covered, a minimum at phase 0.1 is always present: it is larger at the quiescence level, but very deep and narrow in the high state and declining phases. Moreover, a maximum at phase 0.4 is again always there, with variable shape and in 2001 and 2002 accompanied by a second peak.

Even though we cannot exclude that the correspondence between the positions of the minimum and maximum of the folded profiles during the years is serendipitous, and it is only by chance that we see a phase-locked evolution of the curve, this seems a really unlikely situation, and the simpler and more realistic explanation is that the correspondence is real and not a chance happening. This implies that the overall flux increased, maintaining the same pulsation period, but new phenomena superimposed to the 24030 s sinusoidal shape emerged: in particular, in the highest state a second peak (that appears to be in phase opposition with the permanent one) is present. What happens in the decay could be that the overall emission decreases, and thus the multi-peaked structure surfaces with a fragmentation of the two main peaks. Gradually then the second peak disappears, and the profile recovers the simple sinusoidal profile.

This scenario is supported by the evolution of the pulsed fraction PF[1] of 1E 161348-5055 in time too (see figure 7.12). In fact, in the pre-burst observation (*Chandra*, 1999) the PF was $50 \pm 12\%$, but as a consequence of the outburst it became $7 \pm 4\%$. In the years 2001 and 2002, when the lightcurve was very complicated, the pulsed fraction was respectively $42 \pm 3\%$ and $35 \pm 2\%$, and with the passing of time it returned to the quiescence value: $PF = 63 \pm 7\%$ in 2005, and $PF = 60 \pm 12\%$ in 2007. Even though this might not be so clear in figure 7.12, due to the long error bars in the observations taken when 1E 161348-5055 was in low state, the trend is evident: the brightening caused a reduction of the pulsed fraction, that later gradually recovered its quiescence level.

Such great evolution of the folded profile is not uncommon in magnetars: for example in chapter 2 some cases of transient AXPs and SGRs that underwent

[1]The pulsed fraction is defined as the ratio of the the counts above the minimum of the lightcurve, with the total counts:

$$PF = \frac{\text{counts above the minimum}}{\text{total counts}} \tag{7.33}$$

and it was calculated in the energy band 0.2-10 keV.

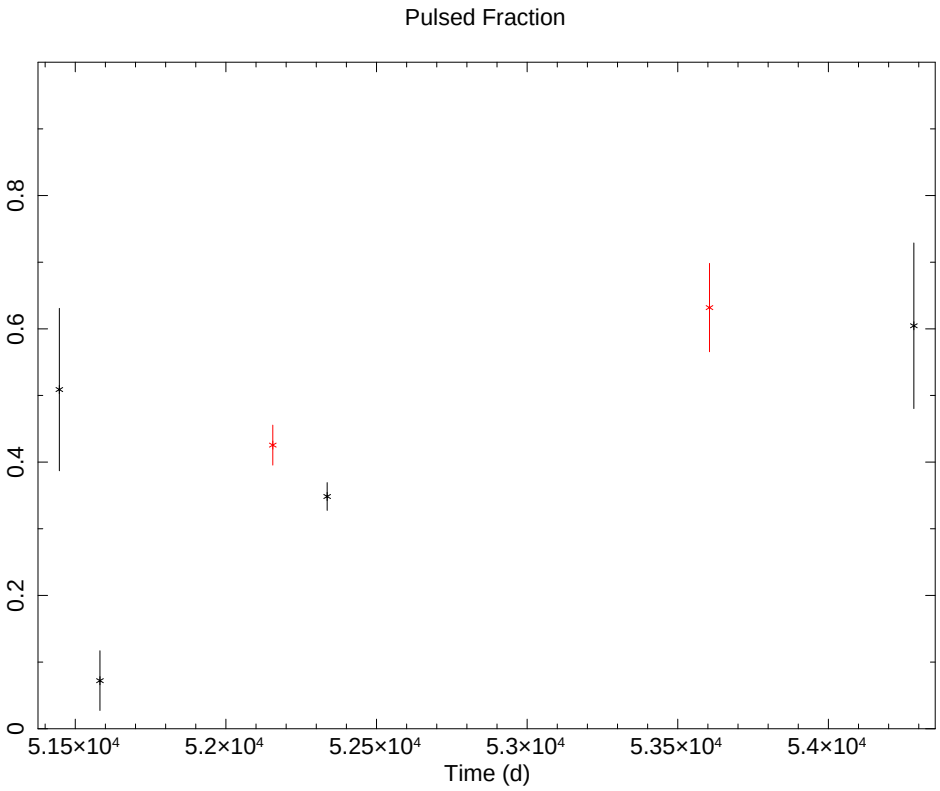

Figure 7.12: Evolution of the pulsed fractions of the long observations listed in figure 7.11. Red: *XMM-Newton* observations, black: *Chandra* observations. The pulsed fraction is defined as the ratio of the counts above the minimum of the lightcurve, with the total counts, and it was calculated in the energy band 0.2-10 keV.

similar remarkable changes in the pulse profile were listed. There are very well known cases of both simplification of the profile (SGR 1627−41, SGR 1900+14) and evolution toward a more complex structure (CXOU J1647−45), and also cases of changes of the relative amplitude of the pre-existing peaks (1E 2259+586). In the magnetar hypothesis this is ascribed to modifications of the structure of the magnetic field, that either reduces the multipolar field to an almost dipolar configuration, or that injects a twist and multipolar structures into a simpler field.

The changes showed by 1E 161348-5055 in an isolated magnetar scenario can be interpreted as a change of the magnetic configuration of the star toward a more complicated configuration, and then a slow decay in order to recover the pre-outburst simple dipolar configuration and smooth almost sinusoidal profile. This evolution resembles more closely those already detected in AXPs rather then SGRs.

Conversely, the same evolution can be easily interpreted in a totally different scenario: the *Chandra* and *XMM-Newton* observations of 1E 161348-5055 in 2001 and 2002 see the source in a highly complicated state, temporally speaking. The folded profiles show multi-peaked structures, but what is more striking is the presence of two very narrow deeps. Already at the time of their discovery it was suggested that they could be interpreted in a binary framework as an eclipse from the companion star [Becker & Aschenbach(2002)], or as extra-absorption due to accretion curtains in the polar model [Kuulkers et al.(2006)] (see also chapter 2). A typical polar lightcurve as that reported in figure 2.8 in chapter 2 also has some broad absorption features, like those shown by 1E 161348-5055 in the 2001 lightcurve, that in particular could be responsible of the multi-peaked structure.

The polar model is appealing to explain the high variability of the profile of the lightcurve, even though some common properties of Intermediate Polars may not match those of 1E 161348-5055: for example, the predicted spectrum should show abundant emission lines, and the slow rotators (and highly magnetized) accretors are predicted to have sinusoidal profiles, together with sideband modulation at some time in their evolution. Nonetheless, with the present data one additional consideration could shed some light on the possibility of the polar model as the explanation for 1E 161348-5055: the narrow dips, as explained, are induced by extra absorption, and this could be visible when analyzing the spectra corresponding to the dips in comparison with those of the maximum of the emission. This was researched when performing the phase-resolved analysis on the *XMM-Newton* observations, but as already explained in chapter 3, for the *XMM-Newton* 2005 observation no evidence of variability of the hydrogen column is present, while the 2001 observation highlights that what is responsible for the spectral variations is the normalization of the warm blackbody.

A hardness ratio diagram could be of some use: due to extra absorption on the dips, the hardness ratio should show an evolution to harder spectrum in

the dip phase bins, and to softer spectrum in the maximum bins. Of course, in absence of an evidence from the spectral analysis an eventual modulation of the hardness ratio as described can only be an indication in favor of the polar model. Conversely, if no modulations appear one can conclude that the polar model does not apply in the case of 1E 161348-5055. A preliminary analysis is shown in figure 7.13, where the folded profiles of the *Chandra* 2002 observation (Obs. ID 2759) in two different energy bands are shown (top: 0.5-2 keV, intermediate: 2-8 keV). The bottom window of the image represents the ratio of the folded profiles, hard over soft. A hint of hardening of the maxima and softening of the minima can be noticed, but the variations are not significative: the ratio is not very different from being a constant. In case extra-absorption were present, the ratio should be very different than a constant. Moreover, as said before, we found that the spectral variations have to be ascribed not to the hydrogen column, but to the warm blackbody normalization.

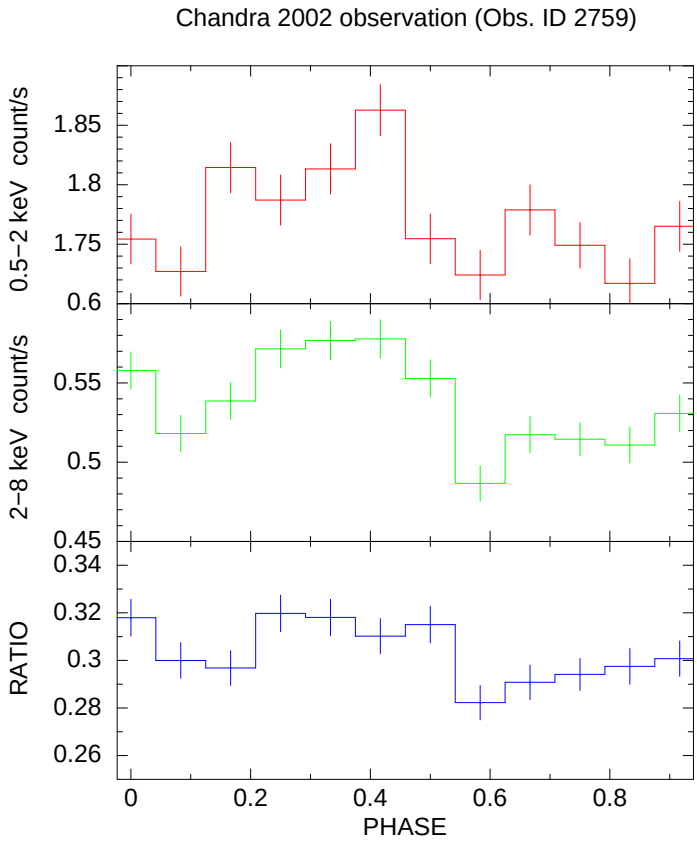

Figure 7.13: 2002 *Chandra* observation (Obs. ID 2759). Top: 0.5-2 keV folded profile. Intermediate: 2-8 keV folded profile. Bottom: ratio of the folded profiles (hard over soft).

The above considerations apparently would argue against accretion in a polar-like system, but one should also keep in mind that when episodes of ac-

cretion of a large mass happen, the star is occultated by the companion, giving as a signature an overall reduction of the photons detected by the observer. Nonetheless, in the previous paragraph the mass accretion as the origin of the outburst was discussed, and somehow ruled out due to the too big amount of matter needed to power the rebrightening.

In addition to a variability in the hydrogen column, the polar model predicts that the size of the accreting spot on the star surface can be derived from the amplitude of the dips; it can be compared with the radial estimates from the double blackbody models. Moreover, the multi-peaked structure can be searched for the sub-periodicities the polar model predicts, and eventually we could derive an estimate of the orbital period, and thus of the mass transfer rate. The *Chandra* 2007 observation, though, ruled out the presence of subperiodicities in the lightcurve down to a timescale of a fraction of second.

We also extracted the energy resolved lightcurves, that are shown in figures 7.14 and 7.15. Some changes between the hard and the soft band are actually visible: in all the profiles but that in 2005 the maxima appear to be broader in high energies than in low energies. In 2005, instead, the maxima occupy the same phase range, but in lower energies the decline is sharper. The 2002 profile shows the biggest changes: in addition to the maximum at phase 0.4 being large enough to level up the subpeaks into one, and the same changes affected the two subpeaks in phase opposition. They now resemble a plateau with an enhanced peak at phase 0.9. The overall profile then seems smoother at higher energies than it is at low energies. For what concerns the 2005 observation, no major changes are found between the energy ranges. At variance with figure 7.11, the Chandra 2007 observation is not present here because, as explained in chapter 4, the experimental setup during that observation did not allow energy resolution to be achieved. Further analysis is at the moment ongoing to assess how statistically important the changes in the pulsed profiles, that are visible at first sight, are, and to compare them to what models foresee.

7.5 Conclusions

Alongside this thesis work a thorough analysis of the properties of 1E 161348-5055 during the last decade was performed: the amount of observations collected by *Chandra*, *XMM-Newton* and *Swift* allowed to study with great detail the spectral and timing properties of 1E 161348-5055 (the results were presented in chapters 3, 4, 5 and 6).

1E 161348-5055 is classified as a central compact object (see chapter 1), and shares the common properties of having thermal spectrum and lack of optical/IR or radio counterparts, and of being positioned close to the geometrical center of a supernova remnant.

But at variance with the other CCOs it does show pulsated emission, with pulsed fraction up to $\sim 60\%$. Moreover, 1E 161348-5055 is endowed with a ultra-high magnetic field (1E 161348-5055 in fact is a magnetar) and is very

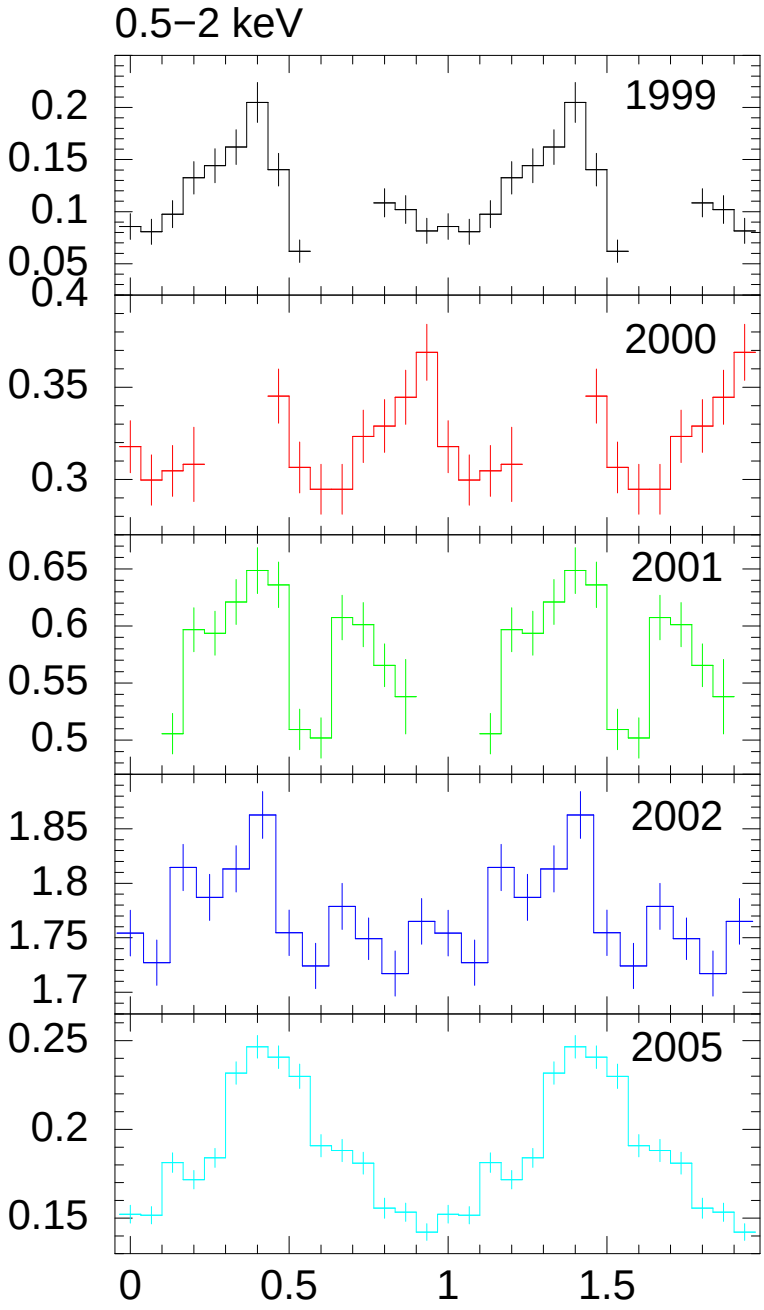

Figure 7.14: 0.5-2 keV folded profiles of the long observations available for 1E 161348-5055, from top to bottom in chronological order. The top window is the pre-burst observation, the second one is the peak detection, the intermediate ones show how different the profile became in 2001 and 2002. The last window (2005) instead shows the recover to the quiescence shape. The 2007 Chandra observation, at variance with figure 7.11, is not present because due to the technical setup during the observation the energy resolution was not possible to be obtained.

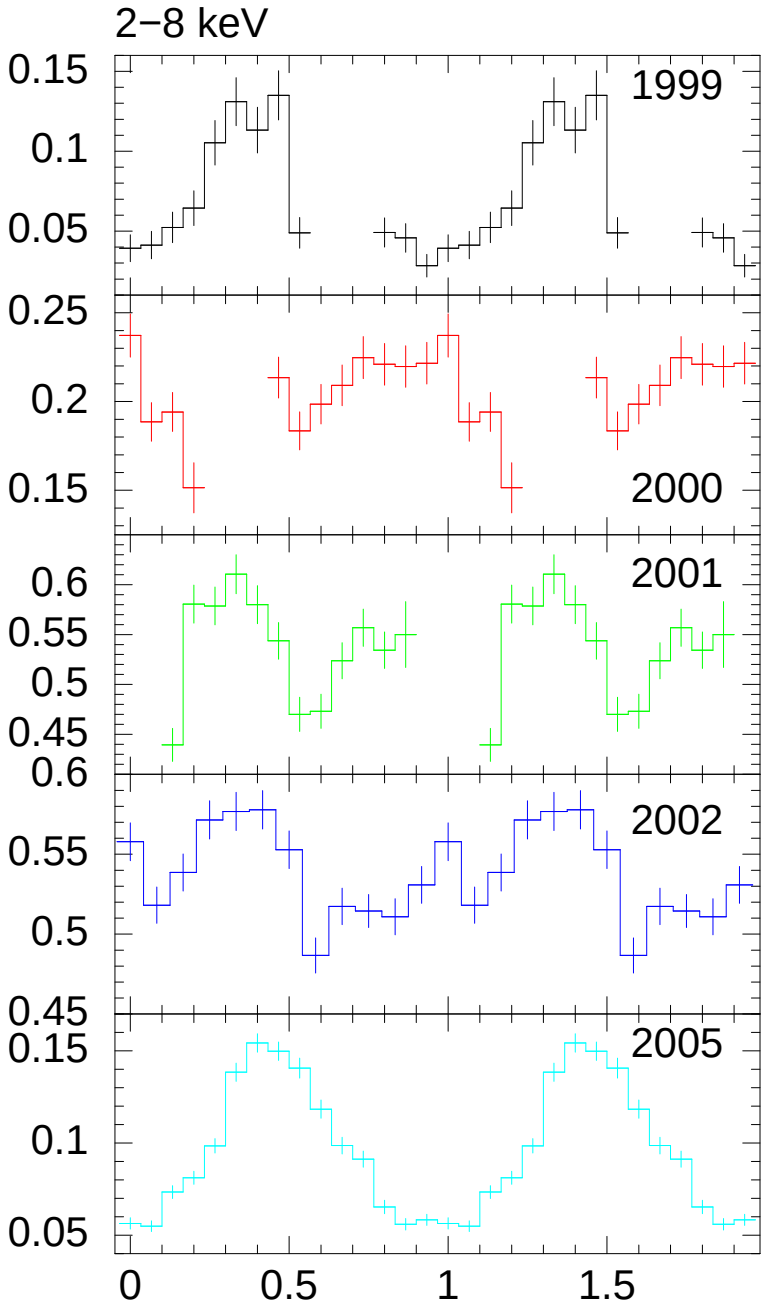

Figure 7.15: 2-8 keV folded profiles of the long observations available for 1E 161348-5055, from top to bottom in chronological order. The top window is the pre-burst observation, the second one is the peak detection, the intermediate ones show how different the profile became in 2001 and 2002. The last window (2005) instead shows the recover to the quiescence shape. The 2007 Chandra observation, at variance with figure 7.11, is not present because due to the technical setup during the observation the energy resolution was not possible to be obtained.

active, giving rise to rebrightenings on the 10 year timescale together with dramatic changes in the pulsed profiles and pulsed fraction.

1E 161348-5055 shows the longest rotation period among all known pulsars and, as was showed in chapter 6, null period derivative. As one can see in figure 7.16, as a result in the period-period derivative diagram 1E 161348-5055 is positioned outside the region usually occupied by traditional pulsars (the central black bulk), binary systems (bottom left) or magnetars (red triangles): it is the only object known as far that is in the top right corner of the period-period derivative diagram. All these evidences make 1E 161348-5055 a unique object, and even more stressed the importance of knowing with more details the physic mechanisms that provoked the last decade X-ray emission.

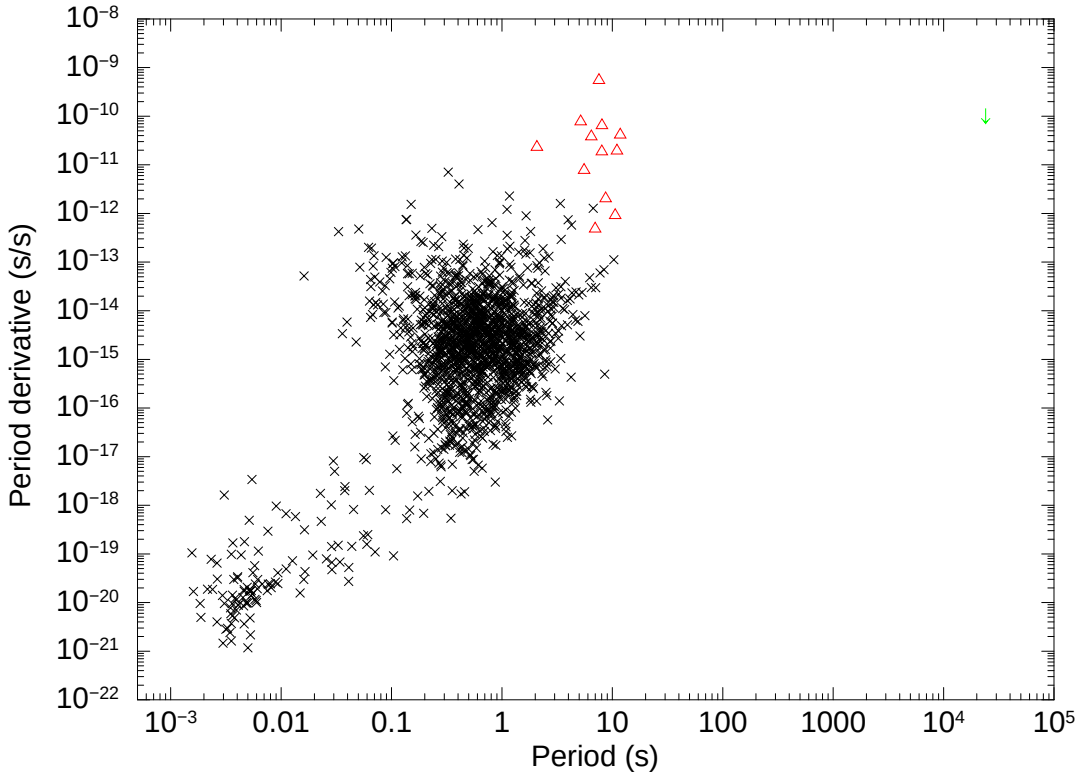

Figure 7.16: Period vs Period derivative diagram for all the known pulsars. In red the magnetars are highlighted, and in green 1E 161348-5055 is represented: it's clearly out of the region where pulsars and 'classical' magnetars are found, making it a unique object.

Several new evidences emerged: thanks to a comparative analysis of the long *XMM-Newton* observations, the spectrum of this peculiar source was modeled as a thermal spectrum, most likely with a double blackbody, and the whole evolution from 1999 to 2008 was traced as a decay in temperature (and eventually emitting areas). The double blackbody model is likely to be

produced by a hot spot on the star's surface, arised after an injection of energy in the neutron star's magnetosphere, whose origin is a priori unknown. This scenario could compatible with both the isolated magnetar and the binary system origin, since from the spectral analysis no conclusive evidence for a variation of the hydrogen column was found, not in the secular spectral variations nor in the analysis of the phase-resolved spectrum of the 2005 or 2001 *XMM-Newton* observation.

The modelization shown in section 7.3 gives a very important indication on the possible origin of the brightening. Even though this is not definitive, since a global spectral analysis on the complete dataset of 1E 161348-5055 is not possible due to the intrinsic differences in all the instruments that observed the source, the comparison between the expected decay times from an accretion driven episode or a magnetospheric injection and the flux decay time *rule out* these scenarios. De facto, the only viable way to explain the long duration decay of the emission is that the energy was stored in the crust (that is a magnetic origin), and its release into the magnetosphere induced a heating of the crust that gave rise both to the distortion of the pulsed profile, and to the hot spot that determines the spectral variations between the maximum and minimum of the profile.

The timing analysis showed remarkable results: the temporal evolution of 1E 161348-5055 was connected in phase throughout the last 9 years of observations, leading to a precise (but still conservative) measurement of the spin period $P = 24030.0 \pm 0.1$ s and the evidence that it does not vary, with upper limit placed at $|\dot{P}| \lesssim 3 \times 10^{-10}$ s/s. Thanks to this accurate result, we recognized that there is a remarkable correspondence between the minima and maxima of the sinusoidal profile and the dips and highest peaks of the multi-peaked curve, that is recognizable before and after the rebrightening. This points toward an explanation of an AXP-like behavior of 1E 161348-5055 in an isolated magnetar scenario, or a polar-like interpretation in a binary system. Preliminary calculations show that the isolated magnetar spun down by dipolar magnetic field is consistent with the upper limit derived, while the Low Mass X-ray Binary model is not. More detailed calculations are ongoing to derive constraints on the propeller stage given by the presence of a disk, or on a polar-like system.

The remarkable changes in the pulse shape can be easily interpreted in an isolated magnetar scenario, with the presence of a field configuration such that a hot spot is created in phase opposition with the sinusoidal modulation. From this hypothesis an important consideration on the pulsed profiles evolution comes: in the case we favor, 1E 161348-5055 is an AXP and the formation of a multi-peaked structure is due to a re-arrangement of the magnetosphere. This means that when the next outburst happens it will produce a different pulse profile than the one observed in 2001. If instead we observe that a pulse profile will emerge similar to the one recorded in 2000 and 2001, the polar scenario has to be reconsidered. In the polar scenario, in fact, the pulse shape is only

determined by the accretion geometry around the star, which clearly does not change: in case 1E 161348-5055 is a polar, then, a pulsed profile similar to the multi-peaked structure shown in 2001 will emerge.

The importance of detecting promptly a new rebrightening of 1E 161348-5055 justifies even more the *Swift* monitoring program: thanks to the unique capabilities of the *Swift* satellite, we will be able to detect it and follow the decay in luminosity not only on a monthly time scale (that is already provided by the monitoring) but also during the first few days. This way it is possible to check whether the peak emission and immediate decay actually is governed by a different time scale than the long term evolution (like 1E 2259+586) or not. This is particularly important to model the flux and temperature decay.

A real time detection of the next 1E 161348-5055 rebrightening must be followed by a multi-wavelength observation campaign: X-ray observations with *XMM-Newton* and *Chandra*will acquire important data to perform spectral and temporal analysis, while optical and infrared observations are needed to finally detect the counterpart and eventually a companion. One should keep in mind, in fact, that the magnetic origin of the 2000 outburst does not rule out the presence of a binary system: it just states that the particular episode was magnetically driven. An infrared observation simultaneous with a new *XMM-Newton* observation, in case 1E 161348-5055 will have another rebrightening, will be essential in order to single out the IR counterpart of 1E 161348-5055 by means of a search of correlated X-ray/IR variability. Whatever the result of the new search is, 1E 161348-5055 is a unique source: in case it is an isolated magnetar, this is the first object of a new class of slowly rotating isolated magnetars. If instead it has a companion, the unique characteristics of 1E 161348-5055 single it out also among the binary systems class.

Appendix A

XMM-Newton

The European Space Agency's (ESA) X-ray Multi-Mirror Mission (XMM-Newton) was launched by an Ariane 504 on December 10th 1999. It carries 3 high throughput X-ray telescopes with an unprecedented effective area, and an optical monitor, the first flown on a X-ray observatory. The large collecting area and ability to make long uninterrupted exposures provide highly sensitive observations.

Each of the three X-ray telescopes on board XMM-Newton consists of 58 Wolter I grazing-incidence mirrors which are nested in a coaxial and cofocal configuration. The design of the optics was driven by the requirement of obtaining the highest possible effective area over a wide range of energies, with particular emphasis in the region around 7 keV. Thus, the mirror system had to utilize a very shallow grazing angle of $30'$ in order to provide sufficient reflectivity at high energies. The telescopes focal length is 7.5 meters and the diameter of the largest mirrors is 70 cm, to be compatible with the shroud of the launcher. Each telescope consists includes, apart from the mirror modules, baffles for visible and X-ray stray-light suppression and an electron deflector for diverting soft electrons.

XMM-Newton provides the following three types of science instrument:

1. **European Photon Imaging Camera (EPIC)** 3 CCD cameras for X-ray imaging, moderate resolution spectroscopy, and X-ray photometry; the two different types of EPIC camera, MOS and pn, are described in paragraph A.1.3 XMM-Newton carries 2 MOS cameras and one pn.

2. **Reflection Grating Spectrometer (RGS)** 2 essentially identical spectrometers for high-resolution X-ray spectroscopy and spectro-photometry, see par. A.1.5

3. **Optical Monitor (OM)** for optical/UV imaging and grism spectroscopy; par. A.1.6 provides an overview.

The three EPIC cameras and the two detectors of the RGS spectrometers reside in the focal planes of the X-ray telescopes, while the OM has its own

telescope. A sketch of the XMM-Newton payload is displayed in figure A.1. There are in total six science instruments on board XMM-Newton, which are operated simultaneously (unless prohibited by constraints, for example, excessive target brightness). The instruments can be operated independently and each in different modes of data acquisition. Observers will receive data from all science instruments.

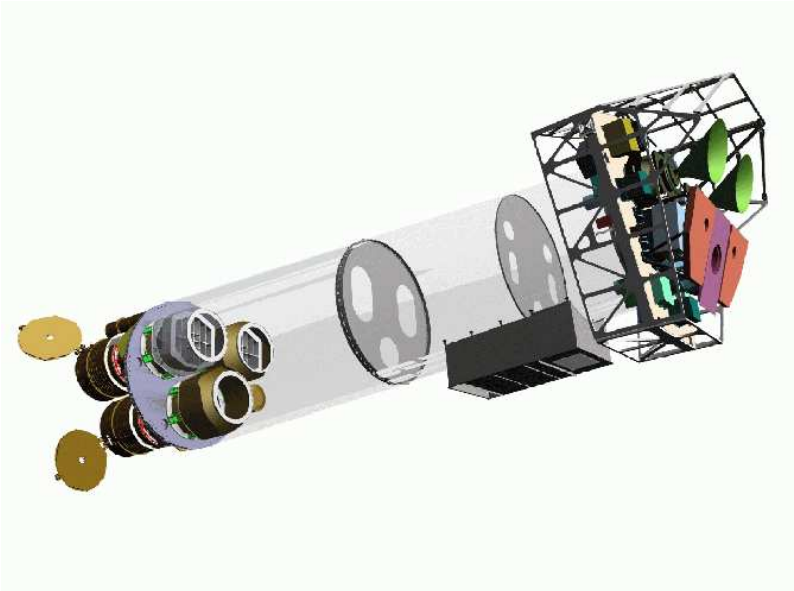

Figure A.1: Sketch of the XMM-Newton payload. The mirror modules, two of which are equipped with Reflection Grating Arrays, are visible at the lower left. At the right end of the assembly, the focal X-ray instruments are shown: The EPIC MOS cameras with their radiators (black/green "horns"), the radiator of the EPIC pn camera (violet) and those of the (light blue) RGS detectors (in pink). The OM telescope is obscured by the lower mirror module.

The most important characteristics of XMM-Newton are compiled in table A.1. The following description is mostly based on the information contained in the papers [Gondoin et al.(1998)], [Gondoin et al.(1998)], [Jansen et al.(2001)] and from the XMM-Newton Users' Handbook.

The basic characteristics of XMM-Newton are:

- **Simultaneous operation of all science instruments**: if not prohibited, e.g. by target brightness constraints, all six XMM-Newton science instruments operate simultaneously. They work independently (i.e., exposures of the individual instruments do not necessarily start and end at the same time).
- **High sensitivity**: XMM-Newton carries the X-ray telescopes with the largest effective area of a focusing telescope ever: the total mirror geometric effective area at 1.5 keV energy is ca. 1550 cm^2 for each telescope, i.e., 4650 cm^2 in total.

	EPIC MOS	EPIC pn	RGS	OM
Bandpass	0.15-12 keV	0.15-15 keV	0.35-2.5 keV[a]	180-600 nm
Target vis.[b]	5-135 ks	5-135 ks	5-135 ks	5-145 ks
Sensitivity [c]	$\sim 10^{-14}$ [d]	$\sim 10^{-14}$ [d]	$\sim 8 \times 10^{-5}$ [e]	20.7 mag [f]
Field of view	$30'$	$30'$	$\sim 5'$	$17'$
PSF[g]	$5''/14''$	$6''/15''$	-	$1.4''$-$2.0''$
Pixel size	40 μm ($1.1''$)	150 μm ($4.1''$)	81 μm (9×10^{-3} Å) [h]	$0.476513''$
Timing res [i]	1.75 ms	0.03 ms	0.6 s	0.5 s
Spectral res [j]	$\sim$70 eV	$\sim$80 eV	0.04/0.025 Å	350

[a] In the -1. grating order (wavelength range: 5-35 Å; λ [Å] $\times$ E [keV] = 12.3984).

[b] Total time available for science per orbit; minimum of 5 ks in order to ensure observatory efficiency. XMM-Newton science observations can only be performed outside the Earth's radiation belts.

[c] After 10 ks.

[d] In the range 0.15-15.0 keV, in units of erg s^{-1} cm^{-2}

[e] OVII 0.57 keV line flux in photons cm^{-2} s^{-1}, for an integration time of 10 ks and a background of 10^{-4} photons cm^{-2} s^{-1} keV^{-1}.

[f] 5-σ detection of an A0 star in 1000 s.

[g] Full Width Half Maximum, Half Energy Width (FWHM/HEW).

[h] In spectroscopy mode (standard 3×3 pixel on-chip binning applied).

[i] In fast data acquisition mode (i.e., fast mode for OM and timing mode for EPIC, spectroscopy mode for RGS, reading out only one of nine CCDs). The EPIC pn burst mode offers an even higher timing resolution of 7μs, but has a very low duty cycle of 3%.

[j] At 1 keV energy. At the energy of Fe Kα (6.4 keV), the energy resolution of both EPIC cameras is ca. 150 eV.

Table A.1: Most important characteristics of XMM-Newton.

- **Good angular resolution**: XMM-Newton's high sensitivity is achieved by using 58 thin nested mirror shells in each X-ray telescope. The achieved point-spread function (PSF) has a full width at half maximum (FWHM) on the order of $6''$ and a HEW, at which 50% of the total energy are encircled, of ca. $15''$.

- **Moderate and high spectral resolution**: the EPIC CCD cameras have moderate spectral resolution (with a resolving power, E/ΔE, of ca. 20-50). The RGS spectrometers offer much higher spectral resolution, with a resolving power in the range of 200-800.

- **Simultaneous optical/UV observations**: observations with the co-aligned OM optical/UV telescope render possible the monitoring and identification of optical/UV counterparts of X-ray sources seen by the X-ray telescopes as well as imaging of the surrounding field.

- **Long continuous target visibility**: a highly elliptical orbit offers continuous target visibility of up to about 40 hours, with a minimum height for science observations of 46,000 km. This is very favourable for studies

of source variability and also in order to achieve a high overall observatory efficiency.

To highlight even more the potentialities of the XMM-Newton in comparison with other observatories, see table A.2, where a basic comparison of XMM-Newton's properties with those of Chandra and Swift is made. It is visible immediately that Chandra and XMM-Newton have complementary characteristics.

Satellite	PSF FWHM	PSF HEW	E range [keV]	A_e at 1 keV [a] [cm^2][a]	Target visib [hr]	Energy resol at 1 keV [eV]
XMM-Newton	6″	15″	0.15 - 15	4650 [b]	36.7 [c]	4 (RGS)
Chandra	0.2″ [d]	0.5″ [d]	0.1 - 10	555 (ACIS-S)	44.4[c]	1 (HETG)
Swift (XRT)	8.8″	18″ [e]	0.2-10	133.5	∼0.8 [f]	70

[a]Mirror effective area.
[b]Note that the EPIC detector responses is included as well.
[c]Orbital visibility outside the particle-radiation dominated zone.
[d]The Chandra High Resolution Camera (HRC) spatial response is well matched to the mirror resolution and the intrinsic on-axis PSF of the HRC is well modelled by a Gaussian with a FWHM of 0.4 arcsec. The spatial resolution for on-axis imaging with the ACIS instrument is limited by the physical size of the CCD pixels (0.492 arcsec) and not the mirrors.
[e]At 1.5 keV.
[f]Low orbit with Earth occultation.

Table A.2: A basic comparison of XMM-Newton's properties with those of Chandra and Swift.

A.1 X-ray telescopes

XMM-Newton's three X-ray telescopes are co-aligned with a relative astrometry between the three EPIC cameras calibrated to better than 1-2″ across the full FOV. One telescope has a light path; the two others have grating assemblies in their light paths, diffracting part of the incoming radiation onto their secondary focus. The performance of each X-ray telescope is characterised by the image quality, and the effective area.

A.1.1 Point Spread Function

The first critical parameter determining the quality of an X-ray mirror module is its ability to focus photons. Here lies one of XMM-Newton's major strong points: the core of its on-axis point-spread function (PSF) is narrow and varies little over a wide energy range (0.1-6 keV). Above 6 keV, the PSF becomes only slightly more energy dependent.

Each of the three Wolter-type X-ray telescopes on board XMM-Newton has its own point-spread function (PSF). As an example, figure A.2 shows the in orbit on-axis PSF of the MOS1, MOS2 and pn X-ray telescopes, registered on the same source. This figure is primarily provided to show the shape of the PSF, with for example the radial substructures caused by the spiders holding the mirror shells. Values for the full width at half maximum ($FWHM$) and half energy width (HEW) of the PSFs (both in-orbit and ground measurements) are listed in table A.3.

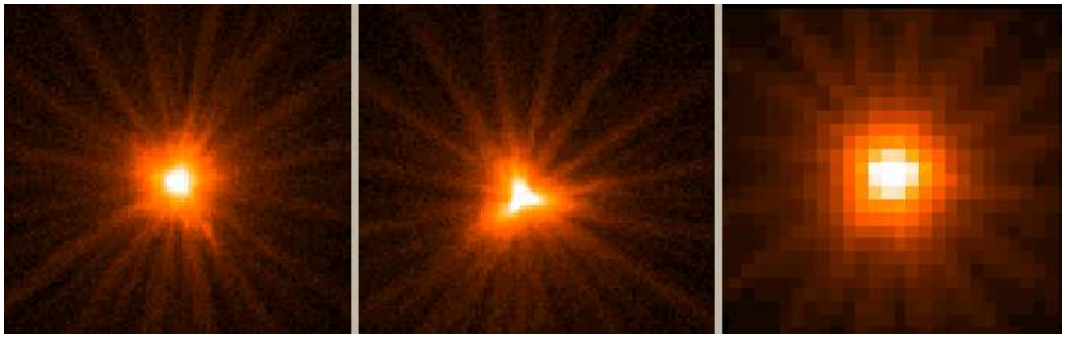

Figure A.2: On axis point spread function of the MOS1, MOS2 and pn X-ray telescopes (left to right) registered on the same source with each MOS camera in Small Window Mode, and the pn camera in Large Window mode. The pixel size is 1.1 arcsec square for the MOS, and 4.1 arcsec square for the pn. A square root scale has been used to visualize the wings of the point spread function. The core of the PSF is piled-up for this source, with a different factor for the MOS and the pn. The star-like pattern is created by the spider which supports the 58 co-axial Wolter I mirrors of the telescope. The shape of the point spread function core is slightly different for all cameras, with MOS2 having a somewhat triangular shape.

Mirror module	2	3	4
Instr. chain [a]	pn orbit/ground	MOS1 + RGS1 orbit/ground	MOS2 + RGS2 orbit/ground
FWHM [″]	< 12.5 [b]/6.6	4.3/6.0	4.4/4.5
HEW [″]	15.2/15.1	13.8/13.6	13.0/12.8

[a]The instruments located behind the mirror module.

[b]The core of mirror module 2 cannot be better resolved in orbit because of the large pn-CCD pixel size.

Table A.3: The on-axis in orbit and on ground 1.5 keV PSFs of the different X-ray telescopes.

Figure A.3 shows the fractional encircled energy as a function of radius

from the centre of the PSF for several different energies as it is currently implemented in the current calibration file (CCF).

Note that the PSF measurements by the EPIC cameras might depend on the instrument readout mode, through combinations of out-of-time event smearing and/or pile-up. The PSF can be severely affected by pile-up effects when the count rate exceeds a few counts per frame: a hole can even appear in the core of the PSF due to the lack of isolated events under high flux conditions.

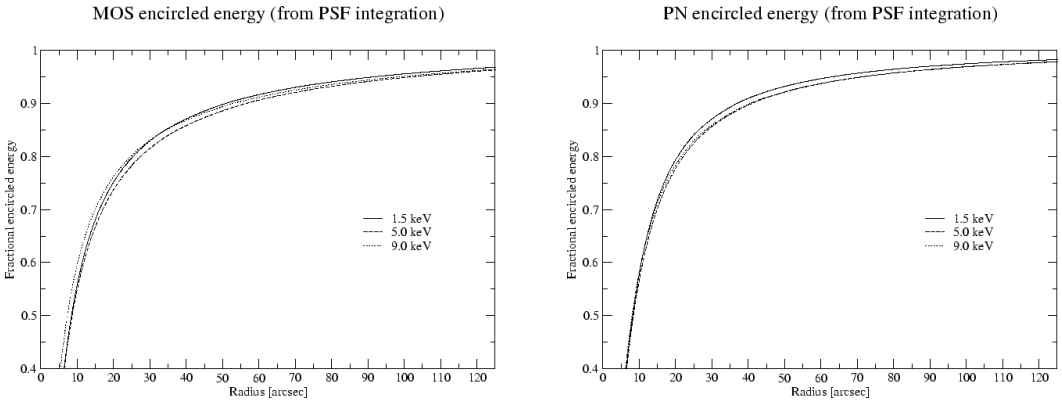

Figure A.3: Left the MOS1 and right the pn fractional encircled energy as a function of angular radius (on-axis) at different energies. The curves were calculated integrating the PSFs that currently are implemented in the calibration files.

The PSF of the X-ray telescopes depends on the source off-axis angle, i.e., its distance from the centre of the field of view (FOV). It is important to know the encircled energy fraction at different positions in the FOV, e.g., to use the correct extraction areas for source photons. In figure A.4 the dependence of the radius at which 90% of the total energy is encircled ($W90$) on the off-axis angle is shown. Note that as the off-axis angle increases the energy dependence of the PSF changes as focusing of high energy photons is no longer confined to the inner shells. A large fraction of these high energy photons are redistributed into the wings of the PSF by X-ray scattering hence $W90$ is larger at high energies than at soft energies for large off-axis angles.

A.1.2 Effective Area

The second important characteristic of the mirror performance is their effective area, A_e, which reflects the ability of the mirrors to collect radiation at different photon energies.

The mirror effective area, folded through the response of the different focal instruments, is shown in figure A.5.

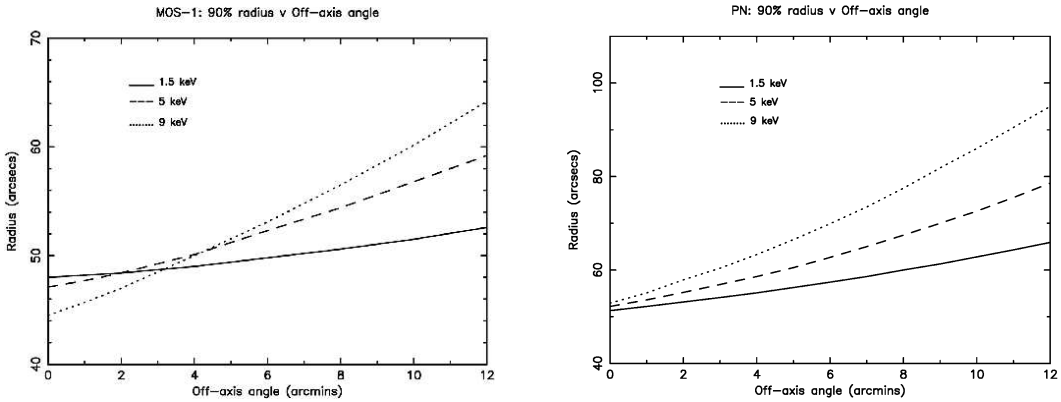

Figure A.4: The $W90$ radius of a point source observed with the MOS camera (left) and the pn camera (right) as a function of off-axis angle at different energies. The curves were calculated assuming a fractional encircled energy of 100% at a radial distance of 5 arcmin, independent of the off-axis angle.

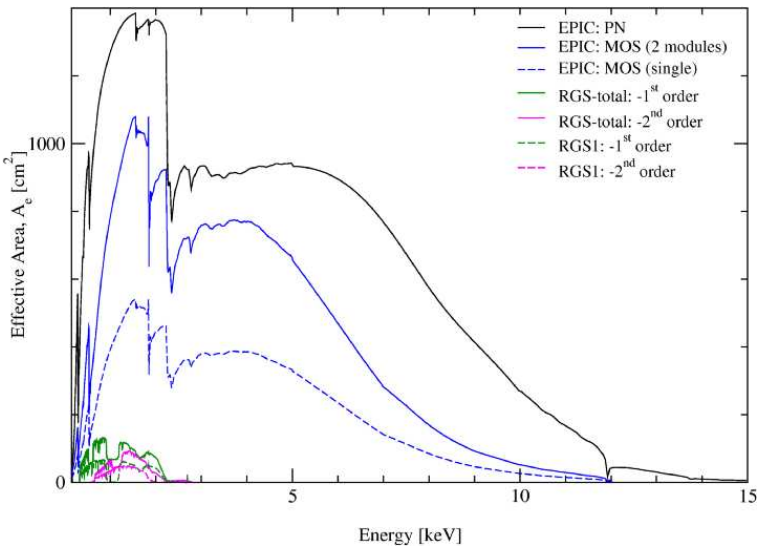

Figure A.5: The net effective area of all XMM-Newton X-ray telescopes, EPIC and RGS (linear scale).

One can see that the XMM-Newton mirrors are most efficient in the energy range from 0.1 to 10 keV, with a maximum at about 1.5 keV and a pronounced edge near 2 keV (the Au M edge). The effective areas of the two MOS cameras are lower than that of the pn, because only part of the incoming radiation falls onto these detectors, which are partially obscured by the RGAs (fig. A.5).

Not only the shape of the X-ray PSF, but also the effective area of the mirrors is a function of off-axis angle within the mirrors' 30′ FOV. With increasing off-axis angle, less of the photons entering the telescopes actually reach the focal plane. This effect is called "vignetting". The vignetting of

the XMM-Newton telescopes, which is reflected by the decline of the X-ray telescope's effective area as a function of off-axis angle, can be quantified by a function that has the value 1 for an on-axis source, and decreases to 0.2-0.4 at $15'$ off-axis

A.1.3 European Photon Imaging Camera (EPIC)

Two of XMM-Newton's X-ray telescopes are equipped with EPIC MOS (Metal Oxide Semi-conductor) CCD arrays, the third carries a different CCD camera called EPIC pn. In a nutshell, the XMM-Newton EPIC cameras offer the possibility to perform extremely sensitive imaging observations over a field of view of $30'$ and the energy range from 0.15 to 15 keV, with moderate spectral ($E/\Delta E \sim 20 - 50$) and angular resolution ($6''$ FWHM; $15''$ HEW). The pn type camera can be operated with very high time resolution down to 0.03 ms in the timing mode and 0.007 ms (but with a very low duty cycle of 3%) in the burst mode. The detector layout and the baffled X-ray telescope FOV of both types of EPIC camera are shown in figure A.6

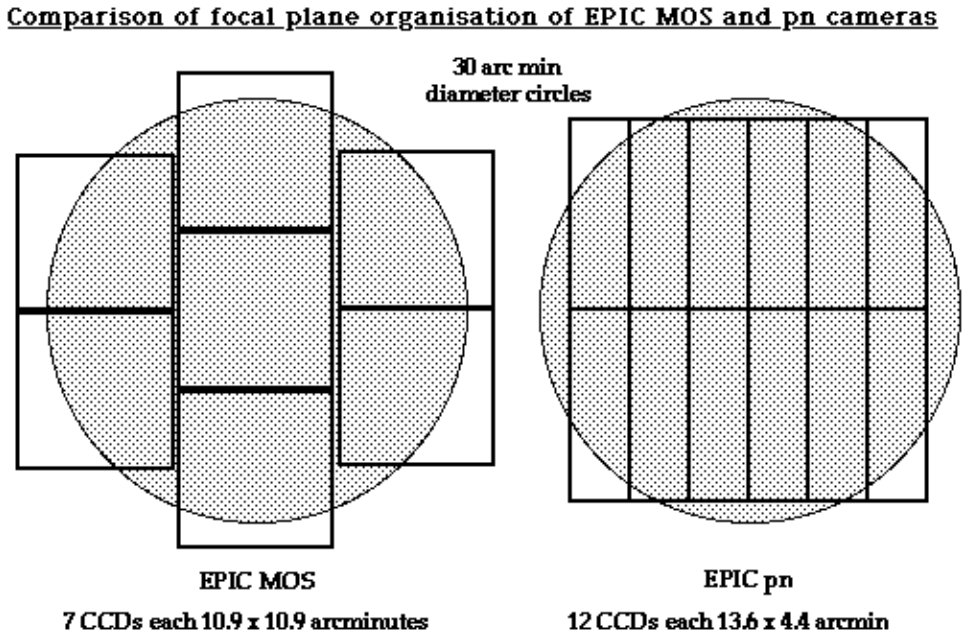

Figure A.6: A rough sketch of the field of view of the two types of EPIC camera; MOS (left) and pn (right). The shaded circle depicts a $30'$ diameter area. This figure does not take into account the real alignment of the cameras with respect to each other.

The following details should be noted:

- The pn chip array is slightly offset with respect to the optical axis of its X-ray telescope so that the nominal, on-axis observing position does not

fall on the central chip boundary (see approximate boresight position for pn marked in Fig. 19). This ensures that $\geq 90\%$ of the energy of an on-axis point source are collected on one pn CCD chip.

- The two EPIC MOS cameras are rotated by 90° with respect to each other.
- The dead spaces between the MOS chips are not gaps, but unusable areas due to detector edges (the MOS chips physically overlap each other, the central one being located slightly behind the ones in the outer ring).
- At about 01:30 hrs. UT on 09 March, 2005, during XMM-Newton revolution 961, an event was registered in the focal plane of the EPIC MOS1 instrument. The characteristics of the event might be attributed to a micrometeoroid impact scattering debris into the focal plane. In the period immediately following a light flash it became apparent that MOS1 CCD6 was no longer recording events, and that all CCD6 pixels were, in effect, returning signal at the saturation level raising the possibility that CCD6 had sustained significant damage. At the time of writing, scientific observations are continuing normally with XMM-Newton, including MOS1, but with the peripheral CCD6 switched off. [1]

All EPIC CCDs operate in photon counting mode with a fixed, mode dependent frame read-out frequency, producing event lists. This allows for simultaneous imaging and non-dispersive spectroscopy due to the intrinsic energy resolution of the pixels.

The two types of EPIC camera are fundamentally different. This does not only hold for the geometry of the MOS chip array and the pn chip array (Fig. A.6), but other properties as well, like their readout times. The readout of the pn chips is much faster than that of the MOS cameras, because each pixel column has its own readout node. Another important difference is that the MOS chips are front-illuminated, while the pn CCDs are back-illuminated, which affects the detector quantum efficiencies decisively.

The MOS chip arrays consist of 7 individual identical, front-illuminated chips. The individual CCDs are not co-planar, but offset with respect to each other, following closely the slight curvature of the focal surface of the Wolter telescopes. Technically, this leaves space for the connections to the central CCD. The MOS chips have a frame store region which serves as a data buffer for storage before they are read out through the readout nodes, while the rest of the chip is obtaining the next exposure. As said before, the MOS cameras are mounted on those X-ray telescopes that also carry RGS instruments. Therefore, they receive only 44% of the reflected light.

The heart of the pn camera, instead, is a single Silicon wafer with 12 CCD chips integrated.

[1] For more details regarding this event, see:
http://xmm.esac.esa.int/external/xmm_news/items/MOS1-CCD6/.

A.1.4 Science modes of the EPIC cameras

Operating Modes The EPIC cameras allow several modes of data acquisition. Note that in the case of MOS the outer ring of 6 CCDs remain in standard full-frame imaging mode while the central MOS CCD can be operated separately. The pn camera CCDs can be operated in common modes in all quadrants for full frame, extended full frame and large window mode, or just with one single CCD for small window, timing and burst mode.

1. **Full frame and extended full frame** (pn only): in this mode, all pixels of all CCDs are read out and thus the full FOV is covered.

2. **Partial window**: in a partial window mode the central CCD of both **MOS** cameras can be operated in a different mode of science data acquisition, reading out only part of the CCD chip: in small window mode an area of 100 x 100 pixels is read out, whereas in large window mode an area of 300 x 300 pixels is active.

   For what concerns the **pn**, in large window mode only half the area of all 12 CCDs is read out, whereas in small window mode only a part of the CCD at the focal point is used to collect data.

3. **Timing**: when the pn and mos cameras are operated simultaneously, in timing mode imaging is made only in one dimension, along the column axis. Along the row direction, data from a predefined area on one CCD chip are collapsed into a one-dimensional row to be read out at high speed. A special flavour of the timing mode of the EPIC pn camera is the burst mode, which offers very high time resolution, but has a low duty cycle of 3%.

The properties of each camera in the different science modes are summarized in table A.4

As one can see, one of the major differences between the two types of camera is the high time resolution of the pn. With this camera high-speed photometry of rapidly variable targets can be conducted, down to a minimum integration time of 30 (7) μs in the timing (burst) mode.

For what concerns the angular resolution, instead, one must note that the EPIC's angular resolution is basically determined by the PSF of the mirror modules. This is due to the fact that the EPIC MOS and pn cameras have pixels with sizes of 40 and 150 μm, respectively. For the focal length of the X-ray telescopes (7.5 m), this corresponds to 1.1″ (4.1″) on the sky. Given the FWHM of the PSF of ca. 6″ (see table A.1), for the MOS cameras the images are fully sampled. The pixel size of the pn camera slightly undersamples the core of the PSF.

The CCD pixels of the EPIC cameras are energy sensitive, enabling non-dispersive spectroscopy. The resolving power of these cameras is determined by the intrinsic energy resolution of the individual pixels. The spectral resolution for a point source located at the nominal pointing position of both

MOS (central CCD) (1 pixel = 1.1″)	Time resol	Live time[a] (%)	Max.[b] point source count rate [s^{-1}] (flux [mCrab][c])
Full frame (600×600)	2.6 s	100.0	0.70 (0.24)
Large window (300×300)	0.9 s	99.5	1.8 (0.6)
Small window (100×100)	0.3 s	97.5	5 (1.7)
Timing uncompressed (100×600)	1.75 ms	100.0	100 (35)
pn (array or 1 CCD) (1 pixel = 4.1")			
Full frame (376×384)	73.4 ms	99.9	6 (0.7)
Extended full frame [d] (376×384)	200 ms	100.0	2 (0.25)
Large window (198×384)	48 ms	94.9	10 (1.1)
Small window (63×64)	6 ms	71.0	100 (11)
Timing (64×200)	0.03 ms	99.5	800 (85)
Burst (64×180)	7 μs	3.0	60000 (6300)

[a]Ratio between the time interval during which the CCD is collecting X-ray events (integration time, including time needed to shift events towards the readout) and the frame time (which in addition includes time needed for the readout of the events).

[b]"Maximum" to avoid deteriorated response due to photon pile-up.

[c]1 mCrab = 2.4×10^{-11} erg s^{-1} cm^{-2} (in the energy range 2-10 keV).

[d]"Extended" means that the image collection time (i.e. the frame time) is longer than in the normal full frame mode.

Table A.4: Basic numbers for the science modes of EPIC.

the EPIC MOS and pn CCDs, as a function of energy, shows a degradation of approximately 13% in the energy resolution of the MOS since the launch of XMM-Newton. The degradation is due to an increase in the CTI (Charge Transfer Inefficiency) of the CCDs with time in orbit. For the pn camera, no significant degradation of the $FWHM$ has been found.

A.1.5 Reflection Grating Spectrometers (RGS)

Behind two of the three telescopes, about half of the X-ray light is utilized by the Reflection Grating Spectrometers (RGS). Each RGS consists of an array of reflection gratings which diffracts the X-rays to an array of dedicated charge coupled devices (CCD) detectors. The RGS instruments achieve high resolving power (150 to 800) over a range from 5 to 35 Å [0.33 to 2.5 keV] (in the first spectral order). The effective area peaks around 15 Å [0.83 keV] (first order) at about 150 cm^2 for the two spectrometers.

The RGS design incorporates an array of reflection gratings placed in the converging beam at the exit from the X-ray telescope. The grating stack intercepts roughly half of the X-ray light and deflects it to a strip of CCD detectors offset from the telescope focal plane. The undeflected light passes through and is intercepted by EPIC-MOS in the telescope focal plane. Nine large format back-illuminated CCDs are operated in single photon counting and frame

transfer mode at a temperature of -80 C. For each photon, the position and the energy is measured: the position to determine the high resolution X-ray spectrum as diffracted by the grating module, and the energy and position to separate the contributions from the various overlapping grating orders (and from the in-flight calibration source) and to reduce the background.

A.1.6 Optical Monitor

The Optical/UV Monitor Telescope (XMM-OM) is mounted on the mirror support platform of XMM-Newton alongside the X-ray mirror modules. It provides coverage between 170 nm and 650 nm of the central 17 arc minute square region of the X-ray field of view, permitting routine multiwavelength observations of XMM targets simultaneously in the X-ray and ultraviolet/optical bands.

The XMM-OM consists of a Telescope Module and a separate Digital Electronics Module, of which there are two identical units for redundancy. The Telescope Module contains the telescope optics and detectors, the detector processing electronics and power supply. There are two distinct detector chains, again for redundancy. The Digital Electronics Module houses the Instrument Control Unit, which handles communications with the spacecraft and commanding of the instrument, and the Data Processing Unit, which pre-processes the data from the instrument before it is telemetered to the ground.

The Telescope Module consists of a modified 30 cm Ritchey-Chretien telescope with a focal ratio of f/12.7, i.e. a focal length of ca. 3.8 m. The incoming light is reflected by a mirror inclined at an angle of 45ï¿½ to one of two redundant detectors. The OM telescope tube is ca. 2 m long. Incoming light falls onto the primary mirror, which reflects it onto the secondary, from where it goes to the inclined mirror that reflects it onto the detector. A filter wheel is mounted immediately in front of the detectors . This does not only contain filters, but also other optical elements, like grisms and a magnifier (i.e. optics for a longer focal length and thus higher resolution on the sky).

Appendix B

Chandra

The Chandra X-Ray Observatory (CXO), successfully launched by NASA's Space Shuttle Columbia on July 23, 1999 and subsequently placed in a high elliptical orbit, is the X-Ray component of NASA's four Great Observatories, together with the Hubble Space Telescope, the late Compton Gamma-Ray Observatory and the Spitzer Space Telescope. Chandra combines an efficient high-resolution ($\leqslant$ 0.5 arcsecond) X-ray telescope with a suite of advanced imaging and spectroscopic instruments.

Chandra was designed to provide order-of-magnitude advances over previous X-ray astronomy missions with regards to spatial and spectral resolution. The High Resolution Mirror Assembly (HRMA), that consists of a nested set of four paraboloid-hyperboloid (Wolter-1) grazing-incidence X-ray mirror pairs, produces images with a half-power diameter (HPD) of the point spread function (PSF) of < 0.5 arcsec.

Thus Chandra is complementary to XMM-Newton: their characteristics allow Chandra to be extremely precise, while XMM-Newton has a much higher effective area, which makes it more suitable to spectroscopic analyses.

B.1 Instruments

Chandra carries on board two focal plane instruments, that are imaging-readout devices: the High Resolution Camera (HRC), the Advanced CCD Imaging Spectrometer (ACIS). In addition, it also has two diffractors: High Energy and Low Energy Transmission Grating Spectrometer (HETGS and LETGS). They can be positioned behind the mirrors, in order to diffract the incoming X-rays according to their energy. Both grating systems offer resolving powers well in excess of 500 over much of their bandwidth which, together, cover the range from 0.1 to 10 keV.

In the following sections I will give a brief description of the two instru-

ments.[1]

B.1.1 High Resolution Camera

The High Resolution Camera (HRC) is a microchannel plate (MCP) instrument comprised of two detectors, one optimized for imaging (HRC-I), and one (HRC-S) which serves as a readout for the Low Energy Transmission Grating (LETG) (see figure B.1. The HRC-I provides the largest field-of-view ($\sim 30' \times 30'$) of any detector aboard Chandra, and its response extends to energies below the sensitivity of ACIS. The time resolution of the HRC detectors (16 μsec) is the best on the observatory, but can only be utilized under certain conditions as discussed later. Moreover, it has minimal intrinsic energy resolution.

The HRC is a direct descendant of the Einstein [Giacconi et al.(1979)] and ROSAT High Resolution Imagers (HRIs) [David et al.(1999)]. The ROSAT HRI had the same coating (CsI) as the HRC. The primary components of the HRC are two Micro-Channel Plates (MCP). They each consist of a 10 cm square cluster of 69 million lead-oxide glass tubes that are about 10 micrometers in diameter (1/8 the thickness of a human hair) and 1.2 millimeters long. The tubes have a special coating that causes electrons to be released when the tubes are struck by X-rays. These electrons are accelerated down the tube by a high voltage, releasing more electrons as they bounce off the sides of the tube. By the time they leave the end of the tube, they have created a cloud of 2×10^7 electrons. A crossed grid of wires detects this electronic signal and allows the position of the original X-ray to be determined with high precision by calculating the centroid of the charge cloud exiting the rear MCP.

The aimpoints are the positions on the instrument where the flux from a point source with no commanded offsets is placed. Note that the on-axis position is offset of about 20 arcsec from the aimpoint. There are two nominal aimpoints as indicated in figure B.1 - one at the approximate center of the HRC-I, and the other slightly off-center on HRC-S.

Other characteristics of the instruments:

- Field of view HRC-I: $\sim 30' \times 30'$, HRC-S: $6' \times 99'$.
- Spatial resolution: FWHM $\sim 20\mu$m, ~ 0.4 arcsec.
- Pixel size (electronic readout): 6.42938 μm [0.13175 arcsec per pixel].
- Energy range: 0.08-10.0 keV.
- Spectral resolution: ΔE/E ~ 1 at 1 keV.
- On-Axis Effective Area: HRC-I, 133 cm^2 at 0.277 keV, 227 cm^2 at 1 keV.

[1] For more details see, for example, http://cxc.harvard.edu/proposer/POG/html/index.html.

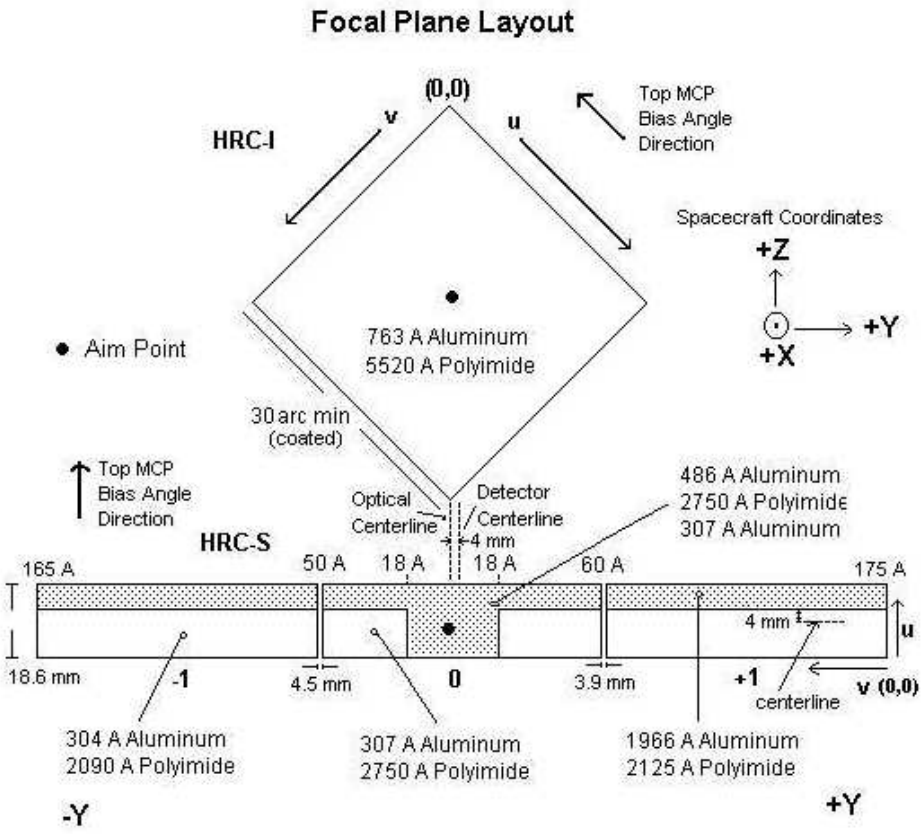

Figure B.1: A schematic of the HRC focal plane geometry as viewed along the optical axis from the telescope towards the focal plane.

- Limiting Sensitivity for a point source, 3σ detection in 3×10^5 s: 9×10^{-16} erg/cm^2 s (power law spectrum: $\alpha = 1.4$, $N_H = 3\times10^{20}$ cm^{-2}.

Imaging with the HRC is best performed with the HRC-I because of the much lower background[2] and larger field of view. The intrinsic PSF of the HRC is well modeled by a gaussian with a FWHM of ~ 20 μm (~ 0.4 arcsec). The HRC pixels, determined by the electronic readout are 6.42938 μm (0.13175 arcsec). The HRC response is thus well matched to the intrinsic HRMA resolution. The measured PSF is as good or better than the simulations because a very conservative pre-flight estimate of the aspect solution was used in the simulations. The imaging resolution of the HRC-I degrades off-axis for two reasons: the HRMA PSF increases in size with increasing off-axis angle, and the deviation increases between the flat HRC-I detection surface and the curved HRMA focal surface.

Approximately 90% of the encircled energy lies within a 14 pixel diameter

[2]The anti-coincidence shield of the HRC-S does not work because of a timing error in the electronics. The error is not correctable.

region (1.8 arcsec) from the center pixel.

Instrument Anomalies

- Initial observations with the HRC-I showed a faint secondary "ghost" image. This "ghost" image was a displaced, weaker ($\sim 3\%$) image ~ 10 arcsec on one side of every source in the HRC-I field of view. The cause of this imaging anomaly is saturation of the fine position amplifiers. A change in the HRC-I operating high-voltage reduced the occurrence of saturating events and the processing algorithms, which are now part of the CXO/HRC data pipeline, label these events and filter them out. The combination of the HV change and filtering have reduced the relative intensity of the ghost image to < 0.1 %, effectively eliminating it. A similar ghost image existed in the HRC-S but at a much reduced intensity.

- A wiring error in the HRC causes the time of an event to be associated with the following event, which may or may not be telemetered. The result is an error in HRC event timing that degrades accuracy from about 16 microseconds to roughly the mean time between events. For example, if the trigger rate is 250 events/sec, then the average uncertainty in any time tag is less than 4 milliseconds. The HRC team has developed a special operating mode that allows high precision timing to be achieved: this timing mode uses only the central segment of the HRC-S. Disabling the outer two segments lowers the total count rate by two-thirds, dropping it below the telemetry saturation limit for most sources. Thus, there is a high probability that all events will be telemetered. In this case, once the time tag of each event has been appropriately shifted in ground processing, the original timing accuracy (16 microseconds) can be recovered. When using this approach, it is prudent to be sure that the total count rate (source plus background) is somewhat below the telemetry saturation limit to avoid telemetry saturation due to statistical fluctuations in the count rate.

Operating Modes

- **Timing Mode**: the HRC-S is normally operated in spectroscopy mode, where signals from any of the three MCP segments can be recognized as triggers. An alternate mode of operation (timing) ties the signals from the outer segments to ground so that only signals from the center MCP generate triggers. A key distinction of this mode from using an edge-blanked region (described below) to select only the center MCP segment is that the timing mode selects events without using the on-board veto logic. This preferred method of doing high-precision timing observations reduces the active detector area, minimizing the total trigger rate. Provided that this rate is below telemetry saturation, all events will

then be telemetered and the event time tags can be correctly assigned in ground processing.

- **Edge and Center Blanking**: it is possible to define a rectangular region, other than the default region, on both the HRC-I and the HRC-S. Events from either inside (edge-blanking) or outside (center-blanking) the defined regions are telemetered. This could be done, for example, to prevent events from a nearby bright source from contributing to telemetry.

- **Zero-order Blocking**: the HRC shutters can be used to block selected portions of the field, but this option is not currently implemented.

B.1.2 Advanced CCD Imaging Spectrometer

The Advanced CCD Imaging Spectrometer (ACIS) offers the capability to simultaneously acquire high-resolution images and moderate resolution spectra. The instrument can also be used in conjunction with the High Energy Transmission Grating (HETG) or Low Energy Transmission Grating (LETG) to obtain higher resolution spectra. It is the instrument of choice for studying temperature variations across X-ray sources such as vast clouds of hot gas in intergalactic space, or chemical variations across clouds left by supernova explosions.

ACIS contains 10 planar, 1024 × 1024 pixel CCDs, four arranged in a 2×2 array (ACIS-I) used for imaging, and six arranged in a 1×6 array (ACIS-S) used either for imaging or as a grating readout. Aimpoints are on S3 for ACIS-S and I3 for ACIS-I. The highest (sub-arcsecond) resolution is obtained within 1-2 arcmin from the aimpoints, depending on the energy of the source. The layout is shown in Figure B.2.

Currently any combination of up to 6 CCDs may be operated simultaneously. Prior popular combinations include an extended ACIS-I imaging mode, using chips I0-I3 plus S2 and S3; and an ACIS-S imaging mode, using chips S1-S4 plus I2 and I3. Two CCDs (S3 and S1) are back-illuminated (BI) and eight are front-illuminated (FI). The response of the BI devices extends to energies below that accessible to the FI chips. The chip-average energy resolution of the BI devices is better than that of the FI devices. Radiation damage suffered by the FI chips has had a negative impact on their energy resolution - the BI devices were not impacted - thus impacting the basic considerations as to how to make best use of the instrument. The low energy response of ACIS has also been affected by the build-up of a contaminant on the optical blocking filters.

Other characteristics of the instruments:

- Chip size: $8' \times 8'$ with a pixel size of $0.49''$.

- Array size: 16.9 by 16.9 arcmin for ACIS-I, 8.3 by 50.6 arcmin for ACIS-S.

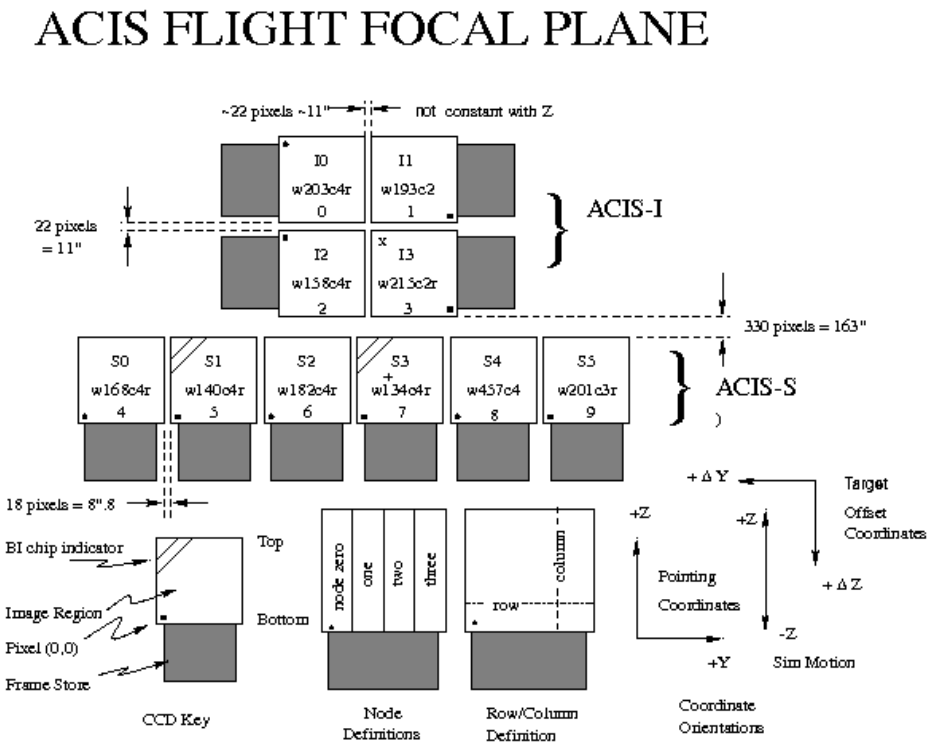

Figure B.2: A schematic drawing of the ACIS focal plane; insight to the terminology is given in the lower left. Note the nominal aimpoints: on S3 (the "+") and on I3 (the "×"). It is standard practice to add an offset to all observations on S3 to move the source away from the node 0-1 boundary. Note the differences in the orientation of the I and S chips, important when using Subarrays. The numerous ways to refer to a particular CCD are indicated: chip letter+number, chip serial number, and ACIS chip number. The node numbering scheme is illustrated lower center. Any combination of up to 6 CCDs may be operated simultaneously. Prior popular combinations include an extended ACIS-I imaging mode, using chips I0-I3 plus S2 and S3; and an ACIS-S imaging mode, using chips S1-S4 plus I2 and I3.

- On-axis effective Area (integrated over the PSF to $> 99\%$ encircled energy): 110 cm^2 at 0.5 keV (FI), 600 cm^2 at 1.5 keV (FI), 40 cm^2 at 8.0 keV (FI).
- Nominal frame time is 3.2 sec (full frame), allowable frame times span 0.2 to 10.0 s. The frame transfer time is 40 μsec (per row).
- Point-source sensitivity: 4 $\times 10^{-15}$ ergs/cm^2 s in 10^4 s (0.4-6.0 keV).

The CCDs have an "active" or imaging section, which is exposed to the incident radiation, and a shielded "frame store" region. A typical mode of the ACIS CCD operation is: (1) the active region is exposed for a fixed amount of

time (full frame is 3.2 s); (2) at the end of the exposure, the charge in the active region is quickly (41 ms) transferred in parallel into the frame store; (3) the next exposure begins; (4) simultaneously, the data in the frame store region is transferred serially to a local processor which, after removing bias, identifies the position and amplitude of any "events" according to a number of criteria depending on the precise operating mode. These criteria always require a local maximum in the charge distribution above the event threshold. The position and the amount of charge collected, together with similar data for a limited region containing and surrounding the pixel are classified ("graded") and then passed into the telemetry stream.

The spatial resolution for on-axis imaging with HRMA/ACIS is limited by the physical size of the CCD pixels (24.0 μm square $\sim$ 0.492 arcsec) and not the HRMA. This limitation applies regardless of whether the aimpoint is selected to be the nominal point on I3 or S3. Approximately 90% of the encircled energy lies within 4 pixels (2 arcsec) of the center pixel at 1.49 keV and within 5 pixels (2.5 arcsec) at 6.4 keV. Figure B.3 shows an in-flight calibration. There is no evidence for any differences in data taken with either S3 or I3 at the nominal focus.

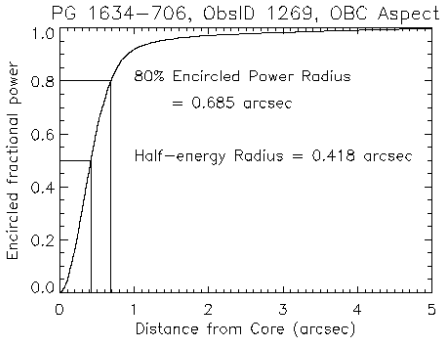

Figure B.3: The on-orbit encircled broad-band energy versus radius for an ACIS observation of point source PG1634-706 (ObsID 1269). The effective energy is 1 keV.

In the following paragraphs I will give a short description of the ACIS operating modes. Note that the selected operating mode (TE/CC) discussed below for the ACIS CCDs applies to all selected CCDs. It is not possible to simultaneously operate individual CCDs in different modes.

Operating Modes: Timed Exposure (TE) Mode

A timed exposure refers to the mode of operation wherein a CCD collects data (integrates) for a preselected amount of time - the Frame Time. Once this time interval has passed, the charge from the 1024 $\times$ 1024 active region is quickly ($\sim$ 41 ms) transferred to the framestore region and subsequently read out through (nominally) 1024 serial registers.

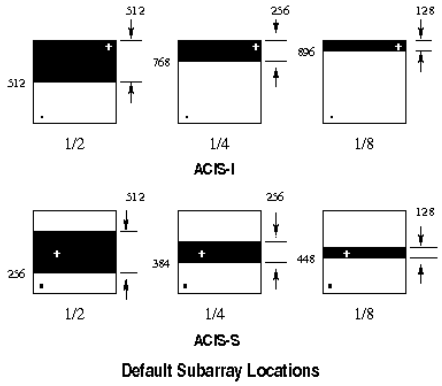

Figure B.4: Examples of various subarrays. The heavy dot in the lower left indicates the origin.

- **Frame Times - Full Frames**: frame times are selectable within a range of values spanning the time interval from 0.2 to 10.0 seconds. If the data from the entire CCD are utilized (full frame) then the nominal (and optimal!) frame time is 3.2 s. Selecting a frame time shorter than the nominal value (e.g. to decrease the probability of pileup) has the consequence that there will be a time during which no data are taken, "deadtime", as 3.2 s are required for the frame store readout process regardless of the frame time. The fraction of time during which data are taken is simply the ratio of the selected frame time to the sum of the nominal frame time and the 41 msec transfer time. The full-frame time depends on how many CCD s are on - see the equation below - but the differences are very small. Finally, we note that selecting a frame time longer than the most efficient value increases the probability of pileup occurring

- **Frame Times and Subarrays**: It is also possible for one to select a subarray - a restricted region of the CCD in which data will be taken. A subarray is fully determined by specifying the number of rows separating the subarray from the framestore region (q) and the number of rows in the subarray (n).

  Examples of standard subarrays are shown in figure B.4 and B.1. The nominal frame time for a subarray depends on (q), (n), and the total number of CCDs that are activated (m); it is given by:

$$T(msec) = 41.12 \times m + 0.040 \times (m \times q) + 2.85 \times n - 32.99.$$

  Thus subarrays are a way to diminish the frame time for bright sources but, as with full frames, selecting a frame time less than the most efficient value results in loss of observing efficiency.

Subarray	ACIS-I		ACIS-S	
No. of chips	1	6	1	6
1	3.0	3.2	3.0	3.2
1/2	1.5	1.8	1.5	1.8
1/4	0.8	1.2	0.8	1.1
1/8	0.5	0.8	0.4	0.7

Table B.1: CCD Frame Time (seconds) for Standard Subarrays.

Operating Modes: Alternating Exposures

In some instances, it is desireable to have both long and short frame times. If the exposure time is made very short, pile-up may be reduced, but the efficiency of the observation is greatly reduced by the need to wait for the full 3.2 seconds (if six chips are clocked) for the framestore array processing. With alternating exposure times, all CCDs are clocked in unison, but have two exposure times. One (typically short) primary exposure is followed by 0 to 15 standard exposures.

Operating Modes: Continuous Clocking (CC) Mode

The continuous clocking mode is provided to allow 3 msec timing at the expense of one dimension of spatial resolution. In this mode, one obtains 1 pixel x 1024 pixel images, each with an integration time of 2.85 msec. Details as to the spatial distribution in the columns are lost.

B.1.3 Comparison

ACIS is most often used for imaging combined with low resolution spectroscopy. The pixel size is such that the core of the point spread function (PSF) of an on-axis source falls mostly into one pixel. The HRC has smaller pixels that oversample the PSF of an on axis point source: it therefore has the highest spatial resolution. The HRC-I detector has the largest field of view. It is somewhat less sensitive than ACIS, and has very little sensitivity above 2keV.

The LETG is optimized for high resolution spectra in the 0.08-0.2 keV region. It is most often used with HRC-S as the readout instrument. The HETG was designed primarily for use with ACIS-S, where the intrinsic energy resolution of the CCDs can be used for order sorting.

B.1.4 High Resolution Mirror Assembly offset Point Spread Function

Finally, a subsection must be dedicated to what happens to the PSF of the Chandra mirror assembly when the source is offset from the pointing.

Instrument	FOV arcmin	Pixel size arcsec	Energy Res eV at 1 keV	Timing Res s	Effective Area cm^2 at 1 keV, on axis
ACIS-I	16.9×16.9	0.492	60[a]	3.2[b]	367 (FI)
ACIS-S	8.3×18.3	0.492	120(BI), 60(FI)	3.2	367(FI) 555 (BI)
HRC-I	30×30	0.13	∼1000[c]	[d]	227
HRC-S	6×99	0.13	∼1000[c]	16×10^{-6}	227

[a]Energy resolution of FI chips is energy dependent.
[b]For full frame.
[c]Only with gratings applied.
[d]For the timing problems concerning HRC-I see text.

Table B.2: Chandra ACIS and HRC capabilities.

The PSF broadens for off-axis sources, and there is considerable distortion in the image even if the HRMA were perfect. This distortion is due to the aberrations of Wolter type I optics and to the different focal surfaces for the four mirror pairs. The increase in image size with off-axis angle is greatest for the inner shell, and hence is larger for higher X-ray energies.

Figure B.5 shows the dependence of encircled energy radii on off-axis angle on the HRC-I with the HRMA focus at the HRC-I aimpoint. Because the HRC-I is axially symmetric with respect to the HRMA optical axis, the off-axis encircled energy radii are almost azimuthally symmetric, except some small asymmetry due to the imperfect HRMA as mentioned above. The figure gives the averaged radii for 1.49 keV and 6.40 keV at 50% and 90% encircled energy. The blurs due to the HRC-I spatial resolution and the aspect solution, estimated to be FWHM: 0.22″, are included.

The ACIS-I surface is not axially symmetric with respect to the HRMA optical axis, because the HRMA aimpoint is located near the inner corner of one of the four ACIS-I chips - I3. Thus the off-axis encircled energy radii are not azimuthally symmetric. Figure B.5 shows the dependence of encircled energy radii on off-axis angle on the four ACIS-I chips. The figure gives the encircled energy radii for 1.49 keV and 6.40 keV at 50% and 90% encircled energy in four azimuthal directions - from the aimpoint to the outer corners of the four ACIS-I chips. The blurs due to the ACIS-I spatial resolution and the Chandra aspect error are included.

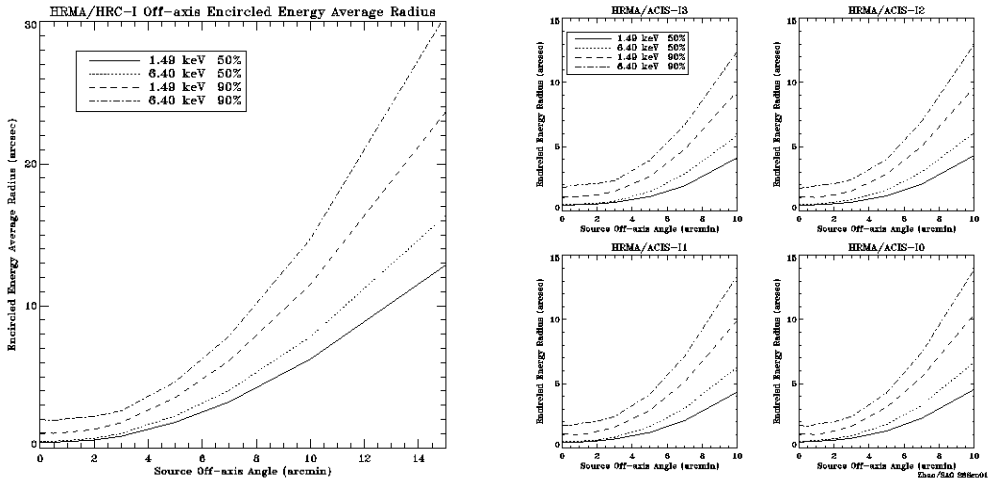

Figure B.5: Left: the HRMA/HRC-I. Right: the HRMA/ACIS-I encircled energy average radii for circles enclosing 50% and 90% of the power at 1.49 and 6.40 keV as a function of off-axis angle. The HRC-I surface is a flat plane perpendicular to the optical axis, which does not follow the curved Chandra focal plane. The ACIS-I surface is composed by four tilted flat chips which approximate the curved Chandra focal plane. The HRMA optical axis passes near the aimpoint which is located near the inner corner of chip I3. Thus the off-axis encircled energy radii are not azimuthally symmetric. The four panels show these radii's radial dependence in four azimuthal directions - from the aimpoint to the outer corners of the four ACIS-I chips. All these curves include the blurs due to the spatial resolution and the Chandra aspect error.

Appendix C

Swift

The Swift Gamma-Ray Burst mission by NASA [Gehrels et al.(2004)] is a multi-wavelength observatory dedicated to the study of gamma-ray burst (GRB) science. Its three instruments work together to observe GRBs and afterglows in the gamma-ray, X-ray, ultraviolet, and optical wavebands. Swift was launched into a low-Earth orbit on November 20, 2004, and since then it provided data on an average of 100 Gamma Ray Bursts per year.

The Swift telescope payload is composed of three instruments which work in team to provide rapid identification and multiwavelength follow-up of GRBs and their afterglows. Within 20 to 75 seconds of a detected burst, the telescope slews autonomously so that the fields-of-view of the pointed instruments are directed towards the location of the burst. The afterglows are monitored over their durations, and the data rapidly made available to the public. For this reasons Swift is particularly suitable to study sudden bursting events, being them gamma ray bursts or not, but they are not its only scientific aim: Swift will also use the BAT to perform an all-sky survey of low-energy gamma-rays that will be significantly more sensitive than any previous survey. Moreover, during the time between one burst and another, Swift is a capable X-ray instrument for the scientific community, and can perform observations like the follow up to 1E 161348-5055.

Let's have a closer look to the instruments carried onboard.

C.1 Instruments

As mentioned before, Swift has a complement of three co-aligned instruments for studying gamma-ray bursts and their afterglow: the Burst Alert Telescope (BAT), the X-ray Telescope (XRT), and the Ultraviolet/Optical Telescope (UVOT), see figure C.1 The largest instrument on-board Swift is the BAT, which can view approximately a sixth of the entire sky at one time. It will detect approximately 100 or more gamma-ray bursts per year. Within seconds of detecting a burst, the spacecraft will slew and autonomously repoint itself

to aim the XRT and UVOT at the burst to enable high-precision X-ray and optical positions and spectra to be determined.

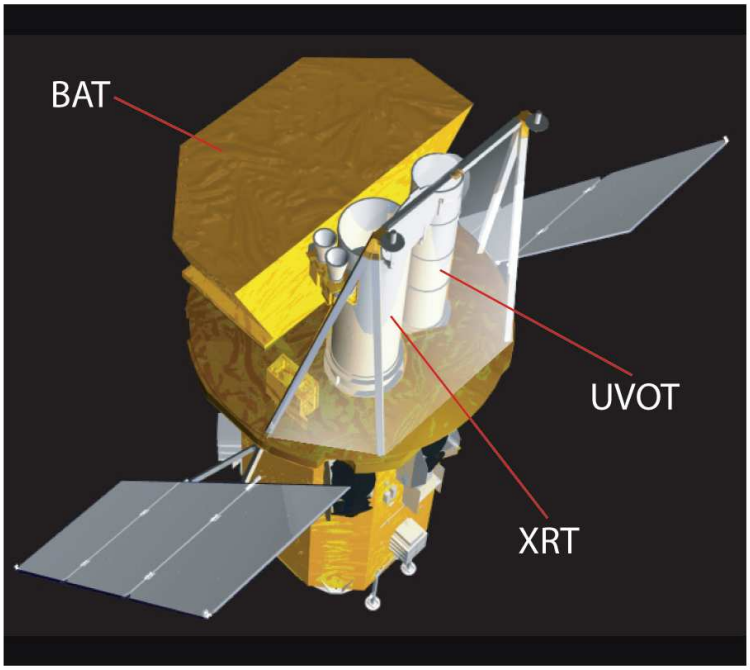

Figure C.1: Swift schematic view.

C.1.1 Burst Alert Telescope

The Burst Alert Telescope (BAT) is a highly sensitive, large field of view (FOV) instrument designed to provide critical GRB triggers and 4-arcmin positions. It is a coded aperture imaging instrument with a 1.4 steradian field-of-view (half coded). The energy range is 15-150 keV for imaging with a non-coded response up to 500 keV. Within several seconds of detecting a burst, the BAT calculates an initial position, decides whether the burst merits a spacecraft slew and, if so, sends the position to the spacecraft. Since the BAT coded aperture field of view always includes the XRT and UVOT fields-of-view, long duration gamma-ray emission from the burst can be studied simultaneously with the X-ray and UV/optical emission. Further information on the BAT is given by [Barthelmy et al.(2005)].

While searching for bursts, the BAT performs an all-sky hard X-ray survey and monitor for hard X-ray transients. The BAT accumulates detector plane maps every 5 minutes. These sky images are searched to detect and position sources. The sensitivity of the survey is about 1 mCrab in the 15-150 keV band for 2 years. For regions where there are perpetually numerous strong sources in the BAT FOV (i.e. the Galactic Plane), the limiting sensitivity will be $\sim$3 mCrab.

BAT Table of Instrument Parameters	
Aperture	Coded mask
Detecting Area	5200 cm^2
Detector Operation	Photon counting
Field of View	1.4 sr (partially-coded)
Detection Elements	256 modules of 128 elements
Detector Size	4 mm × 4 mm × 2 mm
Telescope PSF	17 arcmin
Location Accuracy	1-4 arcmin
Energy Range	15-150 keV
Burst Detection Rate	> 100 per year

Table C.1: Burst Alert Telescope: instrumental parameters.

C.1.2 X-Ray Telescope

Swift's X-Ray Telescope (XRT) is designed to measure the fluxes, spectra, and lightcurves of GRBs and afterglows over a wide dynamic range covering more than 7 orders of magnitude in flux. The XRT can measure GRBs direction of provenience to 5-arcsec accuracy within 10 seconds of target acquisition for a typical GRB, and can study the X-ray counterparts of GRBs beginning 20-70 seconds from burst discovery and continuing for days to weeks. Table C.2 summarizes the instrument's parameters. Further information on the XRT is given by [Burrows et al.(2005)] and [Hill et al.(2005)]

XRT Table of Instrument Parameters	
Telescope	JET-X Wolter I
Focal Length	3.5 m
Effective Area	110 cm^2 at 1.5 keV
Field of view	23 arcmin
Telescope PSF	18 arcsec HPD[1] at 1.5 keV
Detector	EEV CCD-22, 600 x 600 pixels (XMM EPIC CCD)
Detector Operation	Imaging, Timing, and Photon-counting
Detection Element	40 x 40 micron pixels
Pixel Scale	2.36 arcsec/pixel
Energy Range	0.2-10 keV
Sensitivity	2 $\times 10^{-14}$ erg/cm^2 s in 10^4 seconds

Table C.2: X-Ray Telescope: instrumental parameters.

The complete mirror module for the XRT consists of the X-ray mirrors,

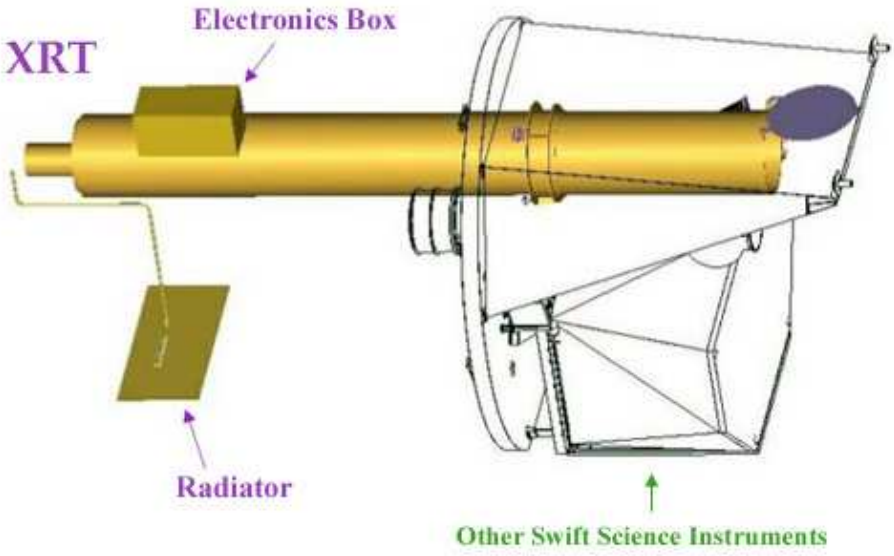

Figure C.2: XRT schematic view.

thermal baffle, a mirror collar, and an electron deflector. To prevent on-orbit degradation of the mirror module's performance, it is being maintained at 20 $\pm$ 5 °C with gradients of <1 °C. A composite telescope tube holds the focal plane camera, containing a single CCD-22 detector, designed for the EPIC MOS instruments on the XMM-Newton mission, to achieve a useful bandpass of 0.2-10 keV [Short et al.(1998)].

The XRT supports three readout modes to enable it to cover the dynamic range and rapid variability expected from GRB afterglows, and autonomously determines which readout mode to use.

- Imaging Mode: produces an integrated image measuring the total energy deposited per pixel and does not permit spectroscopy, so it is only used to position bright sources.

- Timing Mode: sacrifices position information to achieve high time resolution and bright source spectroscopy through rapid CCD readouts.

- Photon-counting Mode: uses sub-array windows to permit full spectral and spatial information to be obtained for source fluxes ranging from the XRT sensitivity limit of 2 $\times 10^{-14}$ erg/cm^2 s to 9 $\times 10^{-10}$ erg/cm^2 s.

The XRT mirrors point spread function has a 15 arcsec half-energy width, and, given sufficient photons, the centroid of a point source image can be determined to sub-arcsec accuracy in detector coordinates. The mean afterglow flux should allow the XRT to obtain source positions to better than 1 arcsec

in detector coordinates, which will increase to ~ 5 arcsec when projected back into the sky due to alignment uncertainty between the star tracker and the XRT.

Charge Transfer Inefficiency

CCD detectors provide good X-ray imaging and spectroscopic performance. However, the CCD energy resolution and gain degrade with time due to the increase of the Charge Transfer Inefficiency (CTI). The main origin of CTI is the increase of charge traps, which are mainly due to the irradiation of high-energy protons on the CCD passing through the shielding. Although the low-Earth orbit of Swift and the thick Al shielding around the CCD detector reduce the proton flux, the frequent passages of the spacecraft through the South Atlantic Anomaly (SAA) can cause formation of charge traps, and hence an increase of CTI.

Since the launch, the FWHM measured using the four ^{55}Fe calibration sources (located in each corner of the CCD; the area of the detector covered by these corner sources being small and outside the imaging area) increased from 146 eV at 5.9 keV in Feb 2005 to 210 eV in March 2007 [Godet et al.(2007)] when using the bad and good columns (i.e. columns with and without significant traps), respectively. The broadening of the line is due to the energy scale shifting effect of traps in the pixels through which the charge has to be transported. The increase of traps in the CCD imaging area, the serial register and the frame-store area also causes an energy scale offset. To avoid this effect, one must use the CTI-corrected gain file when processing the data.

C.1.3 Ultraviolet/Optical Telescope

Ground observations of GRBs have shown that optical afterglows typically decline in brightness as $t^{-1.1}$ to $t^{-2.1}$. Therefore, rapid response is required to observe these counterparts and determine their redshift while they are still bright. The Ultraviolet/Optical Telescope (UVOT) [Roming et al.(2005)] is uniquely capable for afterglow studies. It has UV capability which is not possible from the ground. It cannot be clouded out. It is also much more sensitive than any other quick reaction telescope. The UVOT also enables optimal ground based observations by providing rapid optical images of the GRB field so that any optical or IR counterpart can be quickly identified and studied. Stars in the FOV of the UVOT provide an astrometric grid for the GRB field.

When a new GRB is acquired by the spacecraft, the UVOT goes through a predetermined program of exposure times and filter combinations. The initial images are immediately sent to the ground for use as a finding chart by ground-based observers, and for comparison to archival observations of the same patch of sky to detect a variable source that could be the optical counterpart. The filtered observations give the temporal behavior as a function of wavelength.

UVOT Table of Instrument Parameters	
Telescope	Modified Ritchey-Chretien
Aperture	30 cm diameter
Focal Ratio	12.7
Detector	Intensified CCD
Detector Operation	Photon counting
Field of View	17 × 17 arcmin
Detection Element	2048 × 2048 pixels
Telescope PSF	2.0 arcsec at 350 nm
Wavelength Range	170-650 nm
Colors	6
Sensitivity	B = 24 in white light in 1000 s
Pixel Scale	0.48 arcsec
Spectral Resolution (grism)	$\lambda/\Delta\lambda$ ∼350 at 400 nm
Brightness limit	V = 7.4 mag
Camera Speed	11 ms

Table C.3: Ultraviolet/Optical Telescope: instrumental parameters.

If the GRB is at a distance greater than z $\sim$ 1, the filtered observations can also measure the redshift of the GRB.

The UVOT can detect a mB = 24 point source in 1000 s using the open filter. A comparable 30 cm ground-based telescope is limited to 20th mag due to sky brightness and seeing. Observing from space, the UVOT has very low sky brightness, better spatial resolution and a zero read-noise detector, making it competitive with a 4 m ground-based telescope.

Bibliography

[Aharonian et al.(2004)] Aharonian, F. A., et al. 2004, Nature, 432, 75

[Baade & Zwicky(1934)] Baade, W., & Zwicky, F. 1934, Proceedings of the National Academy of Science, 20, 259

[Barthelmy et al.(2005)] Barthelmy, S. D., et al. 2005, Space Science Reviews, 120, 143

[Becker & Aschenbach(2002)] Becker, W., & Aschenbach, B. 2002, Neutron Stars, Pulsars, and Supernova Remnants, 64

[Becker et al.(2006)] Becker, W., Hui, C. Y., Aschenbach, B., & Iyudin, A. 2006, ArXiv Astrophysics e-prints, arXiv:astro-ph/0607081

[Beloborodov & Thompson(2007)] Beloborodov, A. M., & Thompson, C. 2007, ApJ, 657, 967

[Bendat and Piersol (1071)] Bendat, J.S., Piersol, A.G: 1971, Random data: Analysis and Measurement Procedures, Wiley, New York

[Buccheri et al.(1977)] Buccheri, R., Damico, N., Scarsi, L., Kanbach, G., & Masnou, J. L. 1977, Recent Advances in Gamma-Ray Astronomy, 124, 309

[Buccheri et al.(1983)] Buccheri, R., et al. 1983, A&A, 128, 245

[Burrows et al.(2005)] Burrows, D. N., et al. 2005, Space Science Reviews, 120, 165

[Camilo et al.(2007)] Camilo, F., Ransom, S. M., Halpern, J. P., & Reynolds, J. 2007, ApJL, 666, L93

[Caswell et al.(1975)] Caswell, J. L., Murray, J. D., Roger, R. S., Cole, D. J., & Cooke, D. J. 1975, A&A, 45, 239

[Chatterjee et al.(2000)] Chatterjee, P., Hernquist, L., & Narayan, R. 2000, ApJ, 534, 373

[Cordes & Lazio(2002)] Cordes, J. M., & Lazio, T. J. W. 2002, ArXiv Astrophysics e-prints, arXiv:astro-ph/0207156

[Cordes et al.(2004)] Cordes, J. M., Bhat, N. D. R., Hankins, T. H., McLaughlin, M. A., & Kern, J. 2004, ApJ, 612, 375

[David et al.(1999)] David, L.P., Harnden, F.R. Jr., Kearns, K.E, and Zombeck, M.V., The ROSAT High Resolution Imager (HRI) Calibration Report, revised (1999). http://hea-www.harvard.edu/rosat/hricalrep.html

[Davies & Pringle(1981)] Davies, R. E., & Pringle, J. E. 1981, MNRAS, 196, 209

[Davis(2001)] Davis, J. E. 2001, ApJ, 562, 575

[De Luca & Molendi(2004)] De Luca, A., & Molendi, S. 2004, A&A, 419, 837

[De Luca et al.(2006)] De Luca, A., Caraveo, P. A., Mereghetti, S., Tiengo, A., & Bignami, G. F. 2006, Science, 313, 814

[De Luca(2008)] de Luca, A. 2008, 40 Years of Pulsars: Millisecond Pulsars, Magnetars and More, 983, 311

[De Luca et al.(2008)] De Luca, A., Mignani, R. P., Zaggia, S., Beccari, G., Mereghetti, S., Caraveo, P. A., & Bignami, G. F. 2008, ApJ, 682, 1185

[Dickel et al.(1994)] Dickel, J. R., Milne, D. K., Kennicutt, R. C., Chu, Y.-H., & Schommer, R. A. 1994, AJ, 107, 1067

[Duncan & Thompson(1992)] Duncan, R. C., & Thompson, C. 1992, ApJL, 392, L9

[Duncan & Thompson(1994)] Duncan, R. C., & Thompson, C. 1994, Gamma-Ray Bursts, 307, 625

[Ekşİ & Alpar(2005)] Ekşİ, K. Y., & Alpar, M. A. 2005, ApJ, 620, 390

[Esposito et al.(2008)] Esposito, P., et al. 2008, MNRAS, L84

[Faucher-Giguère & Kaspi(2006)] Faucher-Giguère, C.-A., & Kaspi, V. M. 2006, ApJ, 643, 332

[Ferrario & Wickramasinghe(2006)] Ferrario, L., & Wickramasinghe, D. 2006, MNRAS, 367, 1323

[Fesen et al.(2006)] Fesen, R. A., Pavlov, G. G., & Sanwal, D. 2006, ApJ, 636, 848

[Fesen et al.(2006)] Fesen, R. A., et al. 2006, ApJ, 645, 283

[Francischelli et al.(2002)] Francischelli, G. J., Wijers, R. A. M. J., & Brown, G. E. 2002, ApJ, 565, 471

[Frank et al.(2002)] Frank, J., King, A., & Raine, D. J. 2002, Accretion Power in Astrophysics, by Juhan Frank and Andrew King and Derek Raine, pp. 398. ISBN 0521620538. Cambridge, UK: Cambridge University Press, February 2002.,

[Garmire et al.(2000)] Garmire, G. P., Garmire, A. B., Pavlov, G., & Burrows, D. N. 2000, Bulletin of the American Astronomical Society, 32, 1237

[Garmire et al.(2000)] Garmire, G. P., Pavlov, G. G., Garmire, A. B., & Zavlin, V. E. 2000, IAU Circ. , 7350, 2

[Garnavich et al.(1994)] Garnavich, P. M., Szkody, P., Robb, R. M., Zurek, D. R., & Hoard, D. W. 1994, ApJL, 435, L141

[Gehrels et al.(2004)] Gehrels, N., et al. 2004, ApJ, 611, 1005

[Gelfand & Gaensler(2007)] Gelfand, J. D., & Gaensler, B. M. 2007, ApJ, 667, 1111

[Ghosh & Lamb(1979)] Ghosh, P., & Lamb, F. K. 1979, ApJ, 234, 296

[Giacconi et al.(1979)] Giacconi, R., et al. 1979, ApJ, 230, 540

[Godet et al.(2007)] Godet, O., et al. 2007, Proc. SPIE, 6686,

[Gondoin et al.(1998)] Gondoin, P., Aschenbach, B. R., Beijersbergen, M. W., Egger, R., Jansen, F. A., Stockman, Y., & Tock, J.-P. 1998, Proc. SPIE, 3444, 290

[Gondoin et al.(1998)] Gondoin, P., Aschenbach, B. R., Beijersbergen, M. W., Egger, R., Jansen, F. A., Stockman, Y., & Tock, J.-P. 1998, Proc. SPIE, 3444, 278

[Gotthelf et al.(1997)] Gotthelf, E. V., Petre, R., & Hwang, U. 1997, ApJL, 487, L175

[Gotthelf et al.(1999)] Gotthelf, E. V., Petre, R., & Vasisht, G. 1999, ApJL, 514, L107

[Gotthelf & Halpern(2005)] Gotthelf, E. V., & Halpern, J. P. 2005, ApJ, 632, 1075

[Gotthelf & Halpern(2007)] Gotthelf, E. V., & Halpern, J. P. 2007, AP&SS, 308, 79

[Gotthelf & Halpern(2007)] Gotthelf, E. V., & Halpern, J. P. 2007, ApJL, 664, L35

[Haberl(2007)] Haberl, F. 2007, AP&SS, 308, 181

[Hack et al.(1993)] Hack, M., La Dous, C., Jordan, S. D., Thomas, R. N., Goldberg, L., & Pecker, J.-C. 1993, Monograph Series on Nonthermal Phenomena in Stellar Atmospheres - NASA SP, Paris: Centre National de la Recherche Scientifique; Washington, D.C.: NASA, |c1993,

[Halpern et al.(2005)] Halpern, J. P., Gotthelf, E. V., Becker, R. H., Helfand, D. J., & White, R. L. 2005, ApJL, 632, L29

[Halpern & Gotthelf(2005)] Halpern, J. P., & Gotthelf, E. V. 2005, ApJ, 618, 874

[Halpern et al.(2007)] Halpern, J. P., Gotthelf, E. V., Camilo, F., & Seward, F. D. 2007, ApJ, 665, 1304

[Heyl & Hernquist(1998)] Heyl, J. S., & Hernquist, L. 1998, MNRAS, 300, 599

[Hewish et al.(1968)] Hewish, A., Bell, S. J., Pilkington, J. D., Scott, P. F., & Collins, R. A. 1968, Nature, 217, 709

[Hill et al.(2005)] Hill, J. E., et al. 2005, Proc. SPIE, 5898, 325

[Hui & Becker(2006)] Hui, C. Y., & Becker, W. 2006, A&A, 454, 543

[Hurley et al.(1994)] Hurley, K. J., McBreen, B., Rabbette, M., Steel, S. 1994. The lognormal properties of the soft gamma-ray repeater SGR 1806-20 and the VELA pulsar. Astronomy and Astrophysics 288, L49-L52.

[Ibrahim et al.(2004)] Ibrahim, A. I., et al. 2004, ApJL, 609, L21

[Illarionov & Sunyaev(1975)] Illarionov, A. F., & Sunyaev, R. A. 1975, A&A, 39, 185

[Israel et al.(2007)] Israel, G. L., Campana, S., Dall'Osso, S., Muno, M. P., Cummings, J., Perna, R., & Stella, L. 2007, ApJ, 664, 448

[Jansen et al.(2001)] Jansen, F., et al. 2001, A&A, 365, L1

[Kalogera(1996)] Kalogera, V. 1996, ApJ, 471, 352

[Kaplan & van Kerkwijk(2005)] Kaplan, D. L., & van Kerkwijk, M. H. 2005, ApJL, 635, L65

[Kaplan & van Kerkwijk(2005)] Kaplan, D. L., & van Kerkwijk, M. H. 2005, ApJL, 628, L45

[Kaplan(2008)] Kaplan, D. L. 2008, Astrophysics of Compact Objects, 968, 129

[Kaspi et al.(2003)] Kaspi, V. M., Gavriil, F. P., Woods, P. M., Jensen, J. B., Roberts, M. S. E., & Chakrabarty, D. 2003, ApJL, 588, L93

[Kaspi et al.(2004)] Kaspi, V. M., Roberts, M. S. E., & Harding, A. K. 2004, ArXiv Astrophysics e-prints, arXiv:astro-ph/0402136

[King & Lasota(1979)] King, A. R., & Lasota, J. P. 1979, MNRAS, 188, 653

[King & Wijnands(2006)] King, A. R., & Wijnands, R. 2006, MNRAS, 366, L31

[Knight(2006)] Knight, H. S. 2006, Chinese Journal of Astronomy and Astrophysics Supplement, 6, 020000

[Kouveliotou et al.(1998)] Kouveliotou, C., Kippen, M., Woods, P., Richardson, G., Connaughton, V., & McCollough, M. 1998, IAU Circ. , 6944, 2

[Kuulkers et al.(2006)] Kuulkers, E., Norton, A., Schwope, A., & Warner, B. 2006, Compact stellar X-ray sources, 421

[Leahy(1987)] Leahy, D. A. 1987, A&A, 180, 275

[Li(2007)] Li, X.-D. 2007, ApJL, 666, L81

[Lipunova & Shakura(2000)] Lipunova, G. V., & Shakura, N. I. 2000, A&A, 356, 363

[Lyubarsky et al.(2002)] Lyubarsky, Y., Eichler, D., & Thompson, C. 2002, ApJL, 580, L69

[Lyutikov(2006)] Lyutikov, M. 2006, MNRAS, 367, 1594

[Mazets & Golenetskii(1981)] Mazets, E. P., & Golenetskii, S. V. 1981, AP&SS, 75, 47

[Mereghetti et al.(1996)] Mereghetti, S., Bignami, G. F., & Caraveo, P. A. 1996, ApJ, 464, 842

[Lazendic et al.(2003)] Lazendic, J. S., Slane, P. O., Gaensler, B. M., Plucinsky, P. P., Hughes, J. P., Galloway, D. K., & Crawford, F. 2003, ApJL, 593, L27

[Lipunov(1992)] Lipunov, V. M. 1992, Berlin ; New York : Springer-Verlag, c1992., 5713

[McLaughlin et al.(2006)] McLaughlin, M. A., et al. 2006, Nature, 439, 817

[Mereghetti et al.(2002)] Mereghetti, S., De Luca, A., Caraveo, P. A., Becker, W., Mignani, R., & Bignami, G. F. 2002, ApJ, 581, 1280

[Mereghetti et al.(2006)] Mereghetti, S., et al. 2006, A&A, 450, 759

[Mereghetti(2008)] Mereghetti, S. 2008, A&A Rev. , 15, 225

[Mignani et al.(2004)] Mignani, R. P., de Luca, A., & Caraveo, P. A. 2004, Young Neutron Stars and Their Environments, 218, 391

[Muno et al.(2006)] Muno, M. P., et al. 2006, ApJL, 636, L41

[Muno et al.(2007)] Muno, M. P., Gaensler, B. M., Clark, J. S., de Grijs, R., Pooley, D., Stevens, I. R., & Portegies Zwart, S. F. 2007, MNRAS, 378, L44

[Nishimura et al.(1986)] Nishimura, J., Mitsuda, K., & Itoh, M. 1986, Publ. Astr. Soc. Japan, 38, 819

[Norton et al.(1999)] Norton, A. J., Beardmore, A. P., Allan, A., & Hellier, C. 1999, A&A, 347, 203

[Nugent et al.(1984)] Nugent, J. J., Pravdo, S. H., Garmire, G. P., Becker, R. H., Tuohy, I. R., & Winkler, P. F. 1984, ApJ, 284, 612

[Page et al.(2006)] Page, D., Geppert, U., & Weber, F. 2006, Nuclear Physics A, 777, 497

[Pavlov et al.(2004)] Pavlov, G. G., Sanwal, D., & Teter, M. A. 2004, Young Neutron Stars and Their Environments, 218, 239

[Pizzolato et al.(2008)] Pizzolato, F., Colpi, M., De Luca, A., Mereghetti, S., & Tiengo, A. 2008, ApJ, 681, 530

[Reif(1965)] Reif, F. 1965, Fundamentals of Statistical and Thermal Physics, New York: McGraw-Hill, 1965,

[Roming et al.(2005)] Roming, P. W. A., et al. 2005, Space Science Reviews, 120, 95

[Sanwal et al.(2002)] Sanwal, D., Garmire, G. P., Garmire, A., Pavlov, G. G., & Mignani, R. 2002, Bulletin of the American Astronomical Society, 34, 764

[Short et al.(1998)] Short, A. D., Keay, A., & Turner, M. J. 1998, Proc. SPIE, 3445, 13

[Thompson & Duncan(1993)] Thompson, C., & Duncan, R. C. 1993, ApJ, 408, 194

[Thompson & Duncan(1995)] Thompson, C., & Duncan, R. C. 1995, MNRAS, 275, 255

[Thompson & Duncan(1996)] Thompson, C., & Duncan, R. C. 1996, ApJ, 473, 322

[Thompson et al.(2002)] Thompson, C., Lyutikov, M., & Kulkarni, S. R. 2002, ApJ, 574, 332

[Treves & Colpi(1991)] Treves, A., & Colpi, M. 1991, A&A, 241, 107

[Tuohy & Garmire(1980)] Tuohy, I., & Garmire, G. 1980, ApJL, 239, L107

[van Paradijs et al.(1995)] van Paradijs, J., Taam, R. E., & van den Heuvel, E. P. J. 1995, A&A, 299, L41

[Vink & Kuiper(2006)] Vink, J., & Kuiper, L. 2006, MNRAS, 370, L14

[Wang et al.(2006)] Wang, Z., Chakrabarty, D., & Kaplan, D. L. 2006, Nature, 440, 772

[Wang et al.(2007)] Wang, Z., Kaplan, D. L., & Chakrabarty, D. 2007, ApJ, 655, 261

[Warner(1995)] Warner, B. 1995, Cambridge Astrophysics Series, Cambridge, New York: Cambridge University Press, |c1995,

[Woelk & Beuermann(1996)] Woelk, U., & Beuermann, K. 1996, A&A, 306, 232

[Woods et al.(1999)] Woods, P. M., et al. 1999, ApJL, 519, L139

[Woods et al.(2001)] Woods, P. M., Kouveliotou, C., Göğüş, E., Finger, M. H., Swank, J., Smith, D. A., Hurley, K., & Thompson, C. 2001, ApJ, 552, 748

[Woods et al.(2004)] Woods, P. M., et al. 2004, ApJ, 605, 378

[Woods et al.(2005)] Woods, P. M., et al. 2005, ApJ, 629, 985

[Woods & Thompson(2006)] Woods, P. M., & Thompson, C. 2006, Compact stellar X-ray sources, 547

[Yakovlev & Pethick(2004)] Yakovlev, D. G., & Pethick, C. J. 2004, ARA&A, 42, 169

Acknowledgements

At the end of this thesis work I'd like to thank some persons:

Dott. Caraveo, to have made possible this PhD and Dott. Hurley, for the support he gave me when I was in Berkeley.

Dott. De Luca, because you've always been present and you could find time to teach, listen and help.

Dott. Mignani, for carefully reading the thesis and giving me some very good pieces of advice.

My office mates: Gio, Fabio, Mario, Fabrizio, for your presence during these years and the moments we shared.

My PhD colleagues, present and past: what a crew!